PUBLISHED VERSION

Aoki, Y.;...; Zanotti, James Michael; ... et al.; RBC Collaboration; UKQCD Collaboration Continuum limit physics from 2+1 flavor domain wall QCD Physical Review D, 2011; 83(7):074508

© 2011 American Physical Society

http://prd.aps.org/abstract/PRD/v83/i7/e074508

PERMISSIONS

http://publish.aps.org/authors/transfer-of-copyright-agreement

"The author(s), and in the case of a Work Made For Hire, as defined in the U.S. Copyright Act, 17 U.S.C.

§101, the employer named [below], shall have the following rights (the "Author Rights"):

[...]

3. The right to use all or part of the Article, including the APS-prepared version without revision or modification, on the author(s)' web home page or employer's website and to make copies of all or part of the Article, including the APS-prepared version without revision or modification, for the author(s)' and/or the employer's use for educational or research purposes."

26th April 2013

http://hdl.handle.net/2440/76519

PHYSICAL REVIEW D **83,** 074508 (2011)

Continuum limit physics from 2 + 1 flavor domain wall QCD

Y. Aoki,[1] R. Arthur,[2] T. Blum,[3,1] P. A. Boyle,[2] D. Brömmel,[4,5] N. H. Christ,[6] C. Dawson,[7] J. M. Flynn,[4] T. Izubuchi,[1,8] X-Y. Jin,[6] C. Jung,[8] C. Kelly,[2] M. Li,[6] A. Lichtl,[1] M. Lightman,[6] M. F. Lin,[9] R. D. Mawhinney,[6] C. M. Maynard,[10] S. Ohta,[11,12,1] B. J. Pendleton,[2] C. T. Sachrajda,[4] E. E. Scholz,[13] A. Soni,[8] J. Wennekers,[2] J. M. Zanotti,[2] and R. Zhou[3]

(RBC and UKQCD Collaborations)

[1]*RIKEN-BNL Research Center, Brookhaven National Laboratory, Upton, New York 11973, USA*
[2]*SUPA, School of Physics, The University of Edinburgh, Edinburgh EH9 3JZ, Scotland*
[3]*Physics Department, University of Connecticut, Storrs, Connecticut 06269-3046, USA*
[4]*School of Physics and Astronomy, University of Southampton, Southampton SO17 1BJ, England*
[5]*Jülich Supercomputing Centre, Institute for Advanced Simulation, Forschungszentrum Jülich GmbH, 52425 Jülich, Germany*
[6]*Physics Department, Columbia University, New York, New York 10027, USA*
[7]*Department of Physics, University of Virginia, 382 McCormick Road Charlottesville, Virginia 22904-4714, USA*
[8]*Brookhaven National Laboratory, Upton, New York 11973, USA*
[9]*Department of Physics, Yale University, Sloane Physics Laboratory, New Haven, Connecticut 06511, USA*
[10]*EPCC, School of Physics, The University of Edinburgh, Edinburgh EH9 3JZ, Scotland*
[11]*Institute of Particle and Nuclear Studies, KEK, Tsukuba, Ibaraki, 305-0801, Japan*
[12]*Department of Particle and Nuclear Physics, Sokendai Graduate University of Advanced Studies, Hayama, Kanagawa 240-0193, Japan*
[13]*Institute for Theoretical Physics, University of Regensburg, 93040 Regensburg, Germany*

(Received 10 November 2010; revised manuscript received 22 February 2011; published 22 April 2011)

We present physical results obtained from simulations using 2 + 1 flavors of domain wall quarks and the Iwasaki gauge action at two values of the lattice spacing a, [$a^{-1} = 1.73(3)$ GeV and $a^{-1} = 2.28(3)$ GeV]. On the coarser lattice, with $24^3 \times 64 \times 16$ points (where the 16 corresponds to L_s, the extent of the 5th dimension inherent in the domain wall fermion formulation of QCD), the analysis of C. Allton *et al.* (RBC-UKQCD Collaboration), Phys. Rev. D **78** is extended to approximately twice the number of configurations. The ensembles on the finer $32^3 \times 64 \times 16$ lattice are new. We explain in detail how we use lattice data obtained at several values of the lattice spacing and for a range of quark masses in combined continuum-chiral fits in order to obtain results in the continuum limit and at physical quark masses. We implement this procedure for our data at two lattice spacings and with unitary pion masses in the approximate range 290–420 MeV (225–420 MeV for partially quenched pions). We use the masses of the π and K mesons and the Ω baryon to determine the physical quark masses and the values of the lattice spacing. While our data in the mass ranges above are consistent with the predictions of next-to-leading order SU(2) chiral perturbation theory, they are also consistent with a simple analytic ansatz leading to an inherent uncertainty in how best to perform the chiral extrapolation that we are reluctant to reduce with model-dependent assumptions about higher order corrections. In some cases, particularly for f_π, the pion leptonic decay constant, the uncertainty in the chiral extrapolation dominates the systematic error. Our main results include $f_\pi = 124(2)_{\text{stat}}(5)_{\text{syst}}$ MeV, $f_K/f_\pi = 1.204(7)(25)$ where f_K is the kaon decay constant, $m_s^{\overline{\text{MS}}}(2\text{ GeV}) = (96.2 \pm 2.7)$ MeV and $m_{ud}^{\overline{\text{MS}}}(2\text{ GeV}) = (3.59 \pm 0.21)$ MeV ($m_s/m_{ud} = 26.8 \pm 1.4$) where m_s and m_{ud} are the mass of the strange quark and the average of the up and down quark masses, respectively, $[\Sigma^{\overline{\text{MS}}}(2\text{ GeV})]^{1/3} = 256(6)$ MeV, where Σ is the chiral condensate, the Sommer scale $r_0 = 0.487(9)$ fm and $r_1 = 0.333(9)$ fm.

DOI: 10.1103/PhysRevD.83.074508 PACS numbers: 11.15.Ha, 11.30.Rd, 12.15.Ff, 12.39.Fe

I. INTRODUCTION

For several years now, the RBC and UKQCD Collaborations have been undertaking a major programme of research in particle physics using lattice QCD with domain wall fermions (DWF) and the Iwasaki gauge action. In the series of papers, [1–3], we studied general properties of ensembles with an inverse lattice spacing of $a^{-1} = 1.73(3)$ GeV (corresponding to $\beta = 2.13$) and with unitary pion masses $m_\pi \geq 330$ MeV (partially quenched $m_\pi \gtrsim 240$ MeV). The number of points in these ensembles are $16^3 \times 32 \times 8$ [2], $16^3 \times 32 \times 16$ [3], and $24^3 \times 64 \times 16$ [1], where the fifth dimension is a feature of DWF and is not visible to low-energy physics which remains four-dimensional. We do not review the properties of DWF here, beyond underlining their physical chiral and flavor properties which we exploit in much of our wider scientific programme. We have used these ensembles to investigate a

 © 2011 American Physical Society

broad range of physics, including studies of the hadronic spectrum, mesonic decay constants, and light-quark masses [1], the evaluation of the B_K parameter of neutral-kaon mixing [1,4], the calculation of the form-factors of $K_{\ell 3}$ decays [5,6], studies in nucleon structure [7–9] and proton decay matrix elements [10], and very recently the first lattice study of the masses and mixing of the η and η' mesons [11] as well as a determination of the matrix elements relevant for neutral B-meson mixing in the static limit [12]. A key limiting factor in the precision of these results was that the simulations were performed at a single lattice spacing. In this paper we remove this limitation, by presenting results for the spectrum, decay constants and quark masses obtained with the same lattice action using ensembles generated on a $32^3 \times 64 \times 16$ lattice at a second value of the lattice spacing corresponding to $\beta = 2.25$, for which we will see below that $a^{-1} = 2.28(3)$ GeV. Now that we have results for the same physical quantities with the same action at two values of the lattice spacing we are able to perform a continuum extrapolation and below we will present physical results in the continuum limit.

Since the most precise results at $\beta = 2.13$ were obtained on the $24^3 \times 64 \times 16$ [1] lattices, as a shorthand throughout this paper we will refer to these lattices as the 24^3 ensembles and label the new lattices at $\beta = 2.25$ as the 32^3 ensembles.

The new 32^3 ensembles at $\beta = 2.25$ will, of course, be widely used also in our studies of other physical quantities. In this first paper however, we discuss their properties in some detail (see Sec. II). In this section we also discuss *reweighting* which allows us to eliminate one source of systematic uncertainty. While at present we cannot simulate with physical u and d quark masses, there is no reason, in principle, why we cannot simulate with the physical strange-quark mass. The difficulty, however, is that we do not know *a priori* what this mass is and so in practice the simulations are performed with a strange-quark mass which is a little different from the physical one. As explained in Sec. II D, the technique of reweighting allows us to correct *a posteriori* for the small difference in the simulated and physical strange-quark masses. In Sec. III, we present updated raw results for the pion and kaon masses and decay constants and the mass of the Ω baryon on the 24^3 ensembles which have been extended beyond those discussed in Ref. [1]. Section IV contains the corresponding results on the 32^3 ensembles. In these two sections we also present the raw results for the masses of the nucleon and Δ baryons from the two ensembles, but in contrast to the mesonic quantities a description of their chiral behavior and extrapolation to the continuum limit are postponed to a future paper.

The price we pay for using a formulation with good chiral and flavor properties is the presence of the fifth dimension and the corresponding increase in computational cost. The lightest unitary pion which we have been able to afford to simulate has a mass of 290 MeV and so, in addition to the continuum extrapolation we need to perform the chiral extrapolation in the quark masses. In Sec. V we present a detailed explanation of how we combine the chiral and continuum extrapolations in an attempt to optimize the precision of the results, exploiting the Symanzik effective theory approach as well as chiral perturbation theory and other ansatze for the mass dependence of physical quantities. Having explained the procedure, we then proceed in Sec. V E to discuss the results, to determine the physical bare masses and lattice spacings as well as to make predictions for the pion and kaon decay constants. In particular we find that the ratio of kaon and pion decay constants [13]

$$\frac{f_K}{f_\pi} = 1.204 \pm 0.026, \tag{1}$$

where the error is largely due to the uncertainty in the chiral behavior of f_π as explained in Sec. V E 3. From the chiral behavior of the masses and decay constants we determine the corresponding low-energy constants (LECs) of SU(2) chiral perturbation theory (ChPT).

Among the most important results of this paper are those for the average u and d quark mass and for the strange-quark mass which are obtained in Sec. VI:

$$m_{ud}^{\overline{\rm MS}}(2\ {\rm GeV}) = (3.59 \pm 0.21)\ {\rm MeV} \quad \text{and}$$
$$m_{s}^{\overline{\rm MS}}(2\ {\rm GeV}) = (96.2 \pm 2.7)\ {\rm MeV}. \tag{2}$$

The masses are presented in the $\overline{\rm MS}$ scheme at a renormalization scale of 2 GeV, after the renormalization to symmetric momentum schemes has been performed non-perturbatively [14,15] and the conversion to the $\overline{\rm MS}$ scheme has been done using very recent two-loop results [16,17].

Section VII contains a discussion of the topological charge and susceptibility of both the 24^3 and 32^3 ensembles and in Sec. VIII we summarize our main results and present our conclusions. There are three appendices. Appendix A contains the chiral extrapolations performed separately on the 24^3 and 32^3 ensembles. This is in contrast with the procedure described in Sec. V E in which the chiral and continuum extrapolations were performed simultaneously with common fit parameters at the two spacings. Appendix B contains a detailed analysis of a subtle issue, the normalization of the partially conserved axial current. For domain wall fermions this is expected to deviate from the conventionally normalized continuum current by terms of order $am_{\rm res}$, where a is the lattice spacing and $m_{\rm res}$ is the residual mass [1,18]. Current simulations are now becoming sufficiently precise that these effects need to be understood and quantified and the method proposed in Appendix B, in which the $O(am_{\rm res})$ effects are absent, is implemented in the numerical analyses throughout the paper. Finally Appendix C contains a

discussion of the expected statistical errors when reweighting is performed on Monte Carlo data to obtain results with a different action from that used to generate the data.

We end the Introduction with an explanation of our notation for quark masses [1]. When discussing unitary computations, with the valence and sea quarks degenerate, we call the bare light (u or d) quark mass m_l and the bare heavy (strange) quark mass m_h. m_{ud} and m_s refer to the physical values of these masses (we work in the isospin limit so that the up and down quarks are degenerate). For the partially quenched computations we retain the notation m_l and m_h for the sea-quark masses, but use m_x and m_y for the valence quarks. A tilde over the mass indicates that the *residual mass* has been added, $\tilde{m}_q = m_q + m_{\rm res}$; it is $\tilde{m}$ which is multiplicatively renormalizable.

II. SIMULATION DETAILS AND ENSEMBLE PROPERTIES

As described in Refs. [1,3,19], we generate ensembles using a combination of the DWF formulation of Shamir [20] and the Iwasaki gauge action [21]. For the fermionic action we use a value of 1.8 for the "domain wall height" M_5 and an extension of the 5th dimension of $L_s = 16$. In addition to the new ensembles generated on a $32^3 \times 64$ lattice volume and a gauge coupling $\beta = 2.25$, we have also significantly extended the $24^3 \times 64$, $\beta = 2.13$ ensembles generated in our previous study [1]. As indicated in Table I we have extended the $m_l = 0.005$, $24^3 \times 64$ ensemble from 4460 to 8980 molecular dynamics (MD) units while the $m_l = 0.01$ ensemble has been extended from 5020 to 8540 MD units. The three $32^3 \times 64$ ensembles that are first reported here are also shown in Table I and those with light-quark masses of 0.004, 0.006 and 0.008 contain 6856, 7650 and 5930 MD units, respectively.

A. Ensemble generation

For the generation of both the $24^3 \times 64$ and $32^3 \times 64$ ensembles, we employ the "RHMC II" algorithm described in Ref. [1]. More specifically, the simulation of two light quarks and one strange quark is carried out using a product of three separate strange-quark determinants each evaluated using the rational approximation. The 2 flavors of light quarks are preconditioned by the strange-quark determinant [22]. While the preconditioning mass does not have to be the same as the strange-quark mass, we found that the strange-quark mass is close to being optimal in DWF simulations in tests on smaller volumes.

Using the notation $\mathcal{D}(m_l) = D^\dagger_{DWF}(M_5, m_l) D_{DWF} \times (M_5, m_l)$, the fermion determinant including the contribution from the Pauli-Villars fields and evaluated on a fixed gauge configuration can be written as

$$\det\left[\frac{\mathcal{D}(m_s)^{1/2}\mathcal{D}(m_l)}{\mathcal{D}(1)^{3/2}}\right] = \det\left[\frac{\mathcal{D}(m_s)}{\mathcal{D}(1)}\right]^{3/2} \cdot \det\left[\frac{\mathcal{D}(m_l)}{\mathcal{D}(m_s)}\right] \tag{3}$$

$$= \det\left[\mathcal{R}_{1/2}\left(\frac{\mathcal{D}(m_s)}{\mathcal{D}(1)}\right)\right] \cdot \det\left[\mathcal{R}_{1/2}\left(\frac{\mathcal{D}(m_s)}{\mathcal{D}(1)}\right)\right] \cdot \det\left[\mathcal{R}_{1/2}\left(\frac{\mathcal{D}(m_s)}{\mathcal{D}(1)}\right)\right] \cdot \det\left[\frac{\mathcal{D}(m_l)}{\mathcal{D}(m_s)}\right]. \tag{4}$$

In Eq. (4) we explicitly show how this ratio of determinants is implemented using the rational approximation. Here $\mathcal{R}_a(x)$ denotes x^a evaluated using the rational approximation and each determinant is evaluated using a separate set of pseudofermion fields. An Omelyan integrator [23] with the Omelyan parameter $\lambda = 0.22$ was used in each part of evolution.

Given the disparate contributions to the molecular dynamics force coming from the gauge action and the different factors in Eq. (4) we follow the strategy of Ref. [24] and increase performance by simulating these different contributions with different molecular dynamics time step granularities. In particular, the suppression of the force from the light-quark determinant that results from the Hasenbusch preconditioning allows us to evaluate the computationally expensive force from the light quark using the largest time step among the different terms, decreasing the computational cost significantly. As a result, we divide our simulation in such a way that $\Delta t_{\rm light}$:$\Delta t_{\rm heavy}$:$\Delta t_{\rm gauge}$ = 1:1:1/6

TABLE I. Simulation parameters as well as the average acceptance, plaquette ($\langle P \rangle$), and value for the light-quark chiral condensate [$\langle \bar{\psi}\psi(m_l) \rangle$] for the ensembles studied in this paper. The fifth column shows the number of time units in the ensembles that were included from Ref. [1]. The residual masses given explicitly and those appearing in the ratio $\tilde{m}_l/\tilde{m}_s$ are taken from Table VII appearing in Sec. III below.

$m_s a$	$m_l a$	$\tilde{m}_s/\tilde{m}_l$	$\Delta t_{\rm light}$	τ (Ref. [1])	τ (MD)	Acceptance	$\langle P \rangle$	$\langle \bar{\psi}\psi(m_l) \rangle$
$V/a = 24^3 \times 64$, $L_s = 16$, $\beta = 2.13$, $a^{-1} = 1.73(3)$ GeV, $m_{\rm res} a = 0.003\,152(43)$, $\tau/{\rm traj} = 1$								
0.04	0.005	5.3	1/6	4460	8980	73%	0.588 053(4)	0.001 224(2)
	0.01	3.3	1/5	5020	8540	70%	0.588 009(5)	0.001 738(2)
$V/a = 32^3 \times 64$, $L_s = 16$, $\beta = 2.25$, $a^{-1} = 2.28(3)$ GeV, $m_{\rm res} a = 0.000\,666\,4(76)$, $\tau/{\rm traj} = 2$								
0.03	0.004	6.6	1/8	—	6856	72%	0.615 587(3)	0.000 673(1)
	0.006	4.6	1/8	—	7650	76%	0.615 585(3)	0.000 872(1)
	0.008	3.5	1/7	—	5930	73%	0.615 571(4)	0.001 066(1)

which gave a good performance, measured in flops per accepted trajectory in tuning runs performed separately. (Note, the nature of the Omelyan integrator makes Δt_{heavy} effectively half of Δt_{light}.) This ratio of time steps was used for all the ensembles studied here. However Δt_{light} was varied from ensemble to ensemble to reach an approximate acceptance of 70%. The precise numbers that were used are listed in Table I.

In addition, we chose to simulate with a trajectory length $\tau = 2$ for the 32^3 ensembles, twice that used for the 24^3 ensembles. While a longer trajectory length may be expected to reduce the autocorrelation between configurations, the time for a trajectory scales very nearly linearly in the trajectory length. In comparisons between $\tau = 1$ and $\tau = 2$ trajectory lengths we were not able to recognize any statistically significant reduction in autocorrelations, especially in those for the topological charge, in terms of wall-clock time used to generate the configurations.

A final optimization was used for the simulations run on the IBM BG/P machines at the Argonne Leadership Computing Facility (ALCF). Instead of using double precision throughout, the BAGEL-generated assembly routines [25] keep the spin-projected spinors in single precision in the conjugate gradient (CG) inverters during the molecular dynamics evolution to decrease the amount of communication needed per CG iteration. (Full precision is used in the accept-reject step.) While this kind of improvement is expected to make the molecular dynamics integrator unstable for sufficiently large volumes, the effect on the acceptance turned out to be minimal for all the ensembles presented in this paper while improving the performance of the CG by up to 20% compared to a full double precision CG with the same local volume.

B. Ensemble properties

In Fig. 1 we show the evolution of the plaquette and the chiral condensate for the 32^3 ensembles. Both quantities suggest that 500 MD units is enough for the thermalization of each of the 32^3 ensembles. We have thus begun measurements at 1000 MD units for $m_l = 0.006$ (except for the measurements of the chiral condensate which started after 3304 MD units) and 520 MD units for the other 32^3 ensembles. (The starting points for measurements on the three $24^3 \times 64$ ensembles are given in Table I of Ref. [1].)

Figure 2 shows the integrated autocorrelation time for various quantities measured on the 32^3 ensembles. As can be seen the plaquette, chiral condensate and even the light pion propagator for a separation of 20 time units show a short autocorrelation time of 5–10 MD units. However, the measured autocorrelation times for the topological charge are much larger, on the order of 80 MD units. In fact, as is discussed in Sec. VII, the evolutions shown in Fig. 52 suggest even longer autocorrelation times implying that the autocorrelation times shown in Fig. 2 may be underestimated because of insufficient statistics.

In Sec. VII this issue of the autocorrelation time for the topological charge is discussed in greater detail and the $\beta = 2.13$ and 2.25 evolutions are compared. The 32^3, $\beta = 2.25$ ensembles (with finer lattice spacing) are shown to evolve topology more slowly. This suggests that the change from the DBW2 gauge action used in earlier 2-flavor work [26] to the Iwasaki gauge action used here may have been a wise one. While the DBW2 gauge action gives smaller residual DWF chiral symmetry breaking, it does this by suppressing the tunneling which changes topological charge. Thus, the use of the DBW2 gauge action may have resulted in a topological charge evolution for our current finest lattice spacings that would have been unacceptably slow.

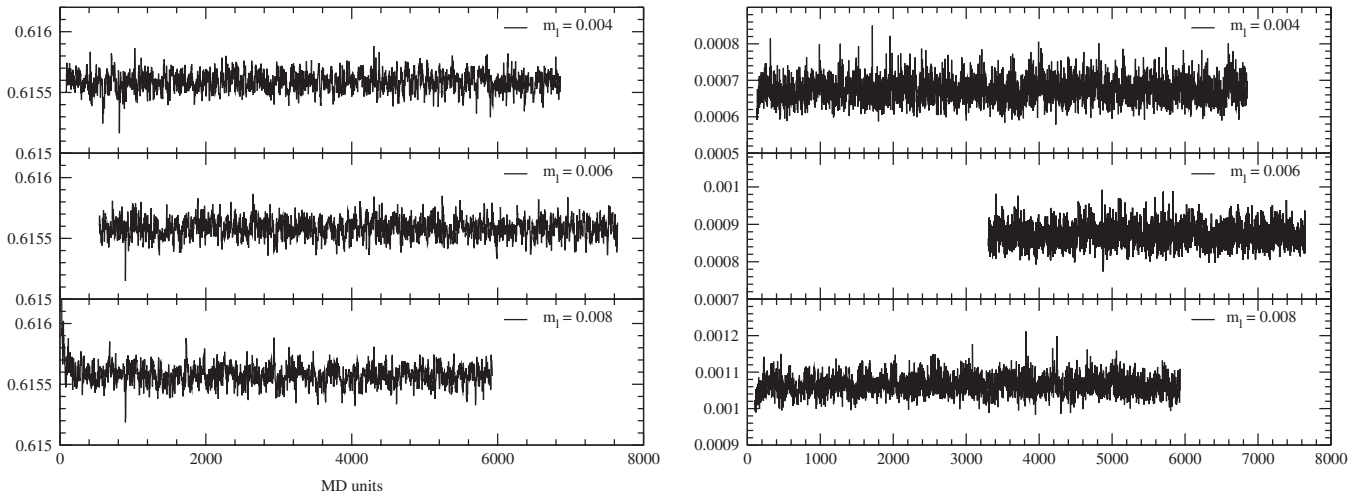

FIG. 1. Evolution of the average plaquette (left panel) and the chiral condensate (right panel) for the $\beta = 2.25$, $32^3 \times 64$, $L_s = 16$ ensembles. The chiral condensate is normalized such that $\langle \bar{\psi}\psi \rangle \sim 1/\text{m}$ in the heavy-quark limit.

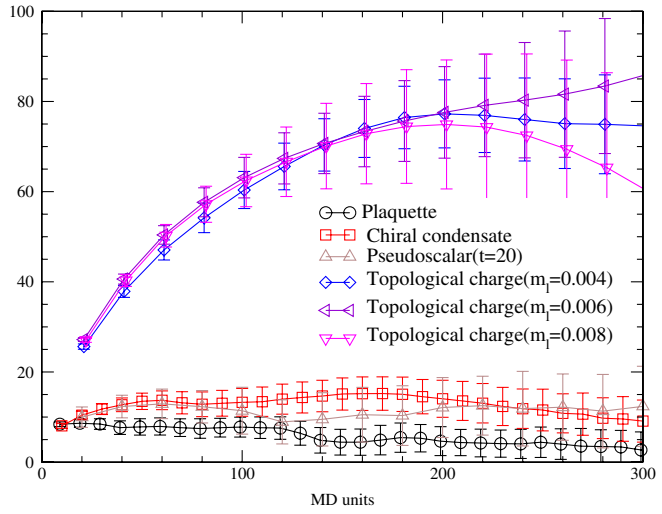

FIG. 2 (color online). The integrated autocorrelation time is shown for the average plaquette, chiral condensate $\langle \bar{\psi}\psi \rangle$, pseudoscalar propagator at time separation 20 from a Gaussian source, and point sink, all computed from the 32^3, $m_l = 0.004$ ensemble and the global topological charge for all three 32^3 ensembles. The chiral condensate and plaquette are measured every two MD units and the averages within sequential blocks of 10 MD units have been analyzed. The topological charge is measured every 4 MD units and the averages within sequential blocks of 20 MD units have been analyzed. All other quantities were measured every 20 MD units and no averaging has been performed. Further discussion of the topological charge is given in Sec. VII.

C. Fitting procedure

In the analysis described in this paper it is important to take into account the fact that the various quantities computed on a single gauge configuration may be correlated. To do this we apply the jackknife technique to simple uncorrelated fits. While there is no proof, or even expectation, that this is an optimal procedure, the jackknife will provide a good estimate of the error except in the unlikely event of large deviations of our result from a normal distribution. While we could attempt to perform a "textbook" correlated fit (again, using a jackknife procedure), this would not be sensible: such fits assume that the data should exactly follow the functional form used in the fit. In the case of a fit to chiral perturbation theory or a simpler analytic ansatz for the quark mass dependence of physical quantities we know that this is not the case. While this complaint applies to both correlated and uncorrelated fits, for the highly correlated lattice data with which we are dealing, small deviations (which in this procedure are assumed to be statistical, but in our case are likely to be systematic) are penalized by many orders of magnitude more for the correlated than uncorrelated fits. Nevertheless, we have performed correlated fits, where the correlation matrix is obtained by taking increasing numbers of the leading eigenvectors. Within our limited ability to estimate the correlation matrix, we find no significant difference in the results and errors with those obtained using uncorrelated fits. Therefore, in this paper (as was also the case in Ref. [1]) we present our main results from the uncorrelated fits, but with a full jackknife procedure for estimating the errors. However, it must be borne in mind that for such uncorrelated fits the resulting χ^2 may not be a reliable indicator of goodness of fit. Therefore, we present a sample set of our fits graphically.

D. Reweighting in the mass of the sea strange quark

The sea strange-quark mass value used in our ensemble generation, $m_h^{(\mathrm{sim})}$, differs from the one in nature, which we determine only after performing our final analysis. In this subsection, we describe the reweighting method used to correct this strange-quark mass from $m_h^{(\mathrm{sim})}$ to the target mass m_h. Various target heavy-quark masses are determined in Sec. V through interpolation/extrapolation to yield meson masses which match either unphysical values present in a different ensemble or which reproduce those from experiment. Recently, several large-scale QCD simulations have been reported using a reweighting technique [27–29]. The various uses of this method include obtaining sea-quark mass derivatives in Ref. [30], tuning the light and strange-quark masses in Ref. [31], tuning the strange and charm quark masses in Ref. [32] and going to larger L_s for the DWF action in Ref. [33].

An observable, such as the meson propagator, at the target strange sea-quark mass m_h is obtained by measuring that observable on the ensemble generated using $m_h^{(\mathrm{sim})}$, multiplied by the reweighting factor w:

$$\langle \mathcal{O} \rangle_{m_h} = \frac{\langle \mathcal{O}w \rangle_{m_h^{(\mathrm{sim})}}}{\langle w \rangle_{m_h^{(\mathrm{sim})}}}. \tag{5}$$

Here the reweighting factor $w[U_\mu]$ for a particular ensemble of gauge links U_μ is the ratio of the square root of the two-flavor Dirac determinant evaluated at the mass m_h divided by that same rooted determinant evaluated at $m_h^{(\mathrm{sim})}$,

$$w[U_\mu] = \frac{\det \mathcal{D}(m_h)^{1/2}}{\det \mathcal{D}(m_h^{(\mathrm{sim})})^{1/2}}. \tag{6}$$

This factor must be calculated for each configuration on which measurements will be performed in the ensemble generated using the sea strange mass $m_h^{(\mathrm{sim})}$.

Among the many possible ways of computing the determinant ratio in Eq. (6), we have chosen to use the Hermitian matrix $\Omega(m_h, m_h^{(\mathrm{sim})})$, whose determinant is $w[U_\mu]$,

$$\Omega(m_h, m_h^{(\mathrm{sim})}) = [D(m_h^{(\mathrm{sim})})^\dagger]^{1/2}[D(m_h)^\dagger]^{-1/2}[D(m_h)]^{-1/2} \times [D(m_h^{(\mathrm{sim})})]^{1/2}. \tag{7}$$

The square root of these matrices is implemented using the same rational polynomial approximation, $\mathcal{R}_{1/2}(x)$, and multishift conjugate gradient algorithm, which are used in the ensemble generation. The order of the matrix products in Ω assures that in the limit of $m_h \to m_h^{(\mathrm{sim})}$, Ω goes to the unit matrix, so that the method described below for evaluating w has vanishing stochastic error in this limit.

To obtain w on each configuration, the determinant of Ω is stochastically evaluated using a complex random Gaussian vector ξ of dimension $L_s \times 12$. Each complex element is drawn from a random distribution centered at zero with width σ_ξ in both the real and imaginary directions:

$$w = \langle\langle e^{-\xi^\dagger[\Omega - 1/(2\sigma_\xi^2)]\xi}\rangle\rangle_\xi \equiv \frac{\int \mathcal{D}\xi\mathcal{D}\xi^\dagger e^{-\xi^\dagger[\Omega - 1/(2\sigma_\xi^2)]\xi} e^{-\xi^\dagger\xi/(2\sigma_\xi^2)}}{\int \mathcal{D}\xi\mathcal{D}\xi^\dagger e^{-\xi^\dagger\xi/(2\sigma_\xi^2)}}. \quad (8)$$

We set $\sigma_\xi^2 = 1/2$ and sample using N_ξ Gaussian vectors per configuration. For one sample, two multimass inversions, one for m_h and another for $m_h^{(\mathrm{sim})}$, are performed.

One needs to be careful in evaluating Eq. (8) to avoid a large and difficult to estimate statistical error. When the eigenvalues of Ω, λ_Ω, are far from $1/(2\sigma_\xi^2)$, the large shift in the width of the Gaussian in the integrand will cause poor sampling in this stochastic evaluation of w, as can be seen if Eq. (8) is rewritten with Ω diagonal:

$$w = \prod_{\lambda_\Omega \in \mathrm{spect}(\Omega)} \int d\xi_\lambda \xi_\lambda^\dagger e^{-\xi_\lambda^\dagger[\lambda_\Omega - 1/(2\sigma_\xi^2)]\xi_\lambda} e^{-\xi_\lambda^\dagger\xi_\lambda/(2\sigma_\xi^2)} \Big/ \prod_{\lambda_\Omega \in \mathrm{spect}(\Omega)} \int d\xi_\lambda \xi_\lambda^\dagger e^{-\xi_\lambda^\dagger\xi_\lambda/(2\sigma_\xi^2)}. \quad (9)$$

The first exponential function in the integrand (9) will be a rapidly decreasing function of $\xi^\dagger\xi$ when $[\lambda_\Omega - 1/(2\sigma_\xi^2)]$ is large, with most of the Gaussian samples generated according to the second exponential function in Eq. (9) falling in a region where the first factor is very small. In this sense, Eq. (8) may provide a statistically noisy estimate of the ratio of the determinants in Eq. (6). The fluctuations in this estimate will be rapidly reduced when $[\lambda_\Omega - 1/(2\sigma_\xi^2)] \to 0$ or, for our choice of σ_ξ, when Ω becomes close to the unit matrix, $\Omega \to 1$.

To reduce the stochastic noise in our estimate, $\det\Omega$ is divided into N_{rw} factors [28]

$$w = \det\Omega = \prod_{i=0}^{N_{rw}-1} \det\Omega_i = \prod_{i=0}^{N_{rw}-1} \langle\langle e^{-\xi_i^\dagger[\Omega_i - 1/(2\sigma_\xi^2)]\xi_i}\rangle\rangle_{\xi_i}. \quad (10)$$

Each of Ω_i needs to be close to the unit matrix while keeping the determinant of the product the same as the original determinant. Each factor $\det\Omega_i$ in the product is evaluated using Eq. (8) with N_ξ Gaussian vectors. We note that all Gaussian vectors, ξ_i, must be *statistically independent* otherwise there will be unwanted correlation among contribution from the N_{rw} steps. A similar decomposition of the reweighting factor is also possible by using the n-th root of the operators [33].

In this work, Ω_i is chosen by uniformly dividing the interval $[m_h, m_h^{(\mathrm{sim})}]$ into smaller pieces:

$$\Omega_i = \Omega(m_h^{(i+1)}, m_h^{(i)}), \quad (11)$$

$$m_h^{(i)} = m_h^{(\mathrm{sim})} + i\frac{m_h - m_h^{(\mathrm{sim})}}{N_{rw}}, \quad (i = 0, 1, \ldots, N_{rw}). \quad (12)$$

In that way, reweighting factors for the intermediate masses $m_h^{(i)}$ are also obtained, which will be used in our analysis too.

For a given difference between the target and the simulation masses, $m_h - m_h^{(\mathrm{sim})}$, N_{rw} needs to be sufficiently large that Ω_i is close to the unit matrix, suppressing the statistical noise in estimating each of the determinants. We have checked whether N_{rw} is large enough in our calculation of the reweighting factor. Figure 3 shows the logarithm of the full reweighting factor, $-\ln(w)$, as a function of the number of divisions in strange-quark mass, N_{rw}, on the $\beta = 2.13$, $24^3 \times 64$, $m_l = 0.005$ lattices, the 2000th trajectory in the left panel and the 4000th trajectory in the

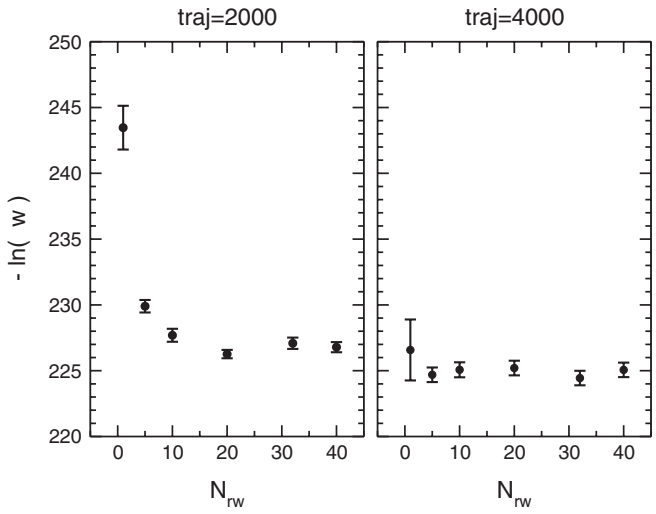

FIG. 3. Logarithm of the reweighting factor, $-\ln(w)$, as a function of the number of divisions in the strange-quark mass, N_{rw} on the $\beta = 2.13$, $24^3 \times 64$, $m_l = 0.005$ lattices, the 2000th trajectory on the left panel and the 4000th trajectory on the right panel. The target and simulation quark masses are $m_h = 0.035$ and $m_h^{(\mathrm{sim})} = 0.040$. For $N_{rw} = 1, 5, 10, 20, 32, 40$, the number of Gaussian samples per mass steps is set to $N_\xi = 40, 8, 4, 4, 2, 2$, respectively. The error bars shown are the standard deviations resulting from $N_{rw} \times N_\xi$ samples for $\det\Omega_i$. We interpret the inconsistency between the values for $N_{rw} = 1$, 5, and 10 and those with larger N_{rw} in the left-hand panel as resulting from insufficient statistics leading to underestimated errors for these three cases where the stochastic sampling is very poor.

right panel. The target and simulation quark masses are $m_h = 0.035$ and $m_h^{(\mathrm{sim})} = 0.040$.

For $N_{rw} \leq 10$, the reweighting factor w appears inconsistent with the results obtained for larger N_{rm} by a large amount [note that $-\ln(w)$ is plotted] for the left case (2000th trajectory). We believe this is caused by the poor stochastic sampling in our method to compute w when $N_{rw} \leq 10$ and that for these cases the statistics are insufficient to estimate the error accurately.

We also check the relative difference between the reweighting factors for $N_{rw} = 20$ and $N_{rw} = 40$ in Fig. 4 for five lattices. This plot indicates that $N_{rw} = 20$ is sufficient to estimate the reweighting factor and its error for changing from $m_h^{(\mathrm{sim})} = 0.040$ to $m_h = 0.035$ on this ensemble. We summarize the values of N_{rw} and N_ξ used in estimating the reweighting factors for the sea strange-quark mass in Table II.

Is the N_{rw} dependence, described above, all one needs to check to assure the correctness of the reweighting procedure? The answer is clearly no. So far, we have only established that Eq. (10) estimates w to some degree of accuracy, on each configuration for large N_{rw}. One needs further checks to see whether or not the reweighted observable in Eq. (5) has an accurately estimated statistical error. A highly inaccurate estimate of the statistical errors could easily result from a poor overlap between the reweighted ensemble and the original ensemble generated by the RHMC simulation. In addition, because the reweighted observable in Eq. (5) is given by a ratio of averages it is a biased estimator of the observable of interest. In this circumstance, a large statistical error, even if well determined, may lead to a systematic error of order $1/N_{\mathrm{conf}}$ enhanced by this large statistical error.

We have attempted the following checks: In Fig. 5, w is plotted as a function of trajectory. If the fluctuation among

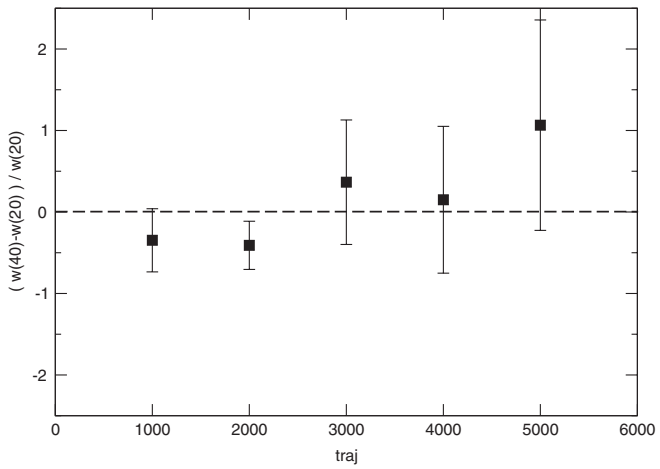

FIG. 4. The relative differences between the reweighting factors for $N_{rw} = 20$, $N_\xi = 4$ and $N_{rw} = 40$, $N_\xi = 2$ on five lattices. The target and simulation quark masses are $m_h = 0.035$ and $m_h^{(\mathrm{sim})} = 0.040$.

TABLE II. Parameters chosen for the sea strange-quark mass reweighting calculation are shown.

Ensemble	$m_h^{(\mathrm{sim})}$	m_h	N_{rw}	N_ξ
$32^3 \times 64$	0.030	0.025	10	4
$24^3 \times 64$	0.040	0.030	40	2

different configurations is large, Eq. (5) might be dominated by a small number of measurements made on those configurations with large w, and the measurement efficiency for the reweighted observable would be very poor. Using the reweighting factor, w_i, obtained on the i-th configuration, the reweighted observable $\mathcal{O}$ can be written from Eq. (5) as

$$\langle \mathcal{O} \rangle_{m_s} = \sum_{i=1}^{N_{\mathrm{conf}}} O_i \hat{w}_i, \tag{13}$$

$$\hat{w}_i = \frac{w_i}{\sum_{i=1}^{N_{\mathrm{conf}}} w_i}. \tag{14}$$

Because the process of reweighing selectively samples the original distribution, even with precisely determined reweighting factors we should expect the effective number of samples to be reduced and the statistical errors to increase. In Appendix C this effect is analyzed in the case that correlations between the data and the reweighting factors can be neglected when estimating these statistical errors, including the effects of autocorrelations. For the case of no autocorrelations, we obtain the following expression for the effective number of configurations after reweighting:

$$N_{\mathrm{eff}} = \frac{(\sum_{n=1}^{N_{\mathrm{conf}}} w_n)^2}{\sum_{n=1}^{N_{\mathrm{conf}}} w_n^2}. \tag{15}$$

The quantity N_{eff} goes to N_{conf} if there is no fluctuation in the w_i while it goes to 1 if the largest w_i completely

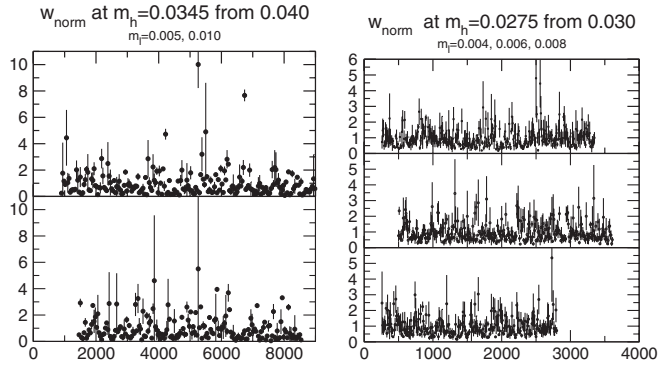

FIG. 5. The normalized reweighting factor $\hat{w}_i$ as a function of trajectory number i for the $24^3 \times 64$, $m_l = 0.005$, 0.010 ensembles (left-hand plot) and the $32^3 \times 64$, $m_l = 0.004$, 0.006, 0.008 ensembles (right-hand plot). The sea-quark masses m_l are plotted in ascending order from top to bottom. The target sea strange-quark mass and that of simulation are $m_h = 0.0345$, $m_h^{(\mathrm{sim})} = 0.040$ ($m_h = 0.0275$, $m_h^{(\mathrm{sim})} = 0.030$) for the left-hand (right-hand) plot.

TABLE III. The maximum and minimum reweighting factors, the effective number of samples, $N_{\rm eff}$, according to the formula derived in this paper, [Eq. (15)], the corresponding number, $N^*_{\rm eff}$ given by the formula of Ref. [34] [defined in Eq. (16)] and the actual number of configurations $N_{\rm conf}$ in each ensemble. The target sea strange-quark mass and that of the simulation are $m_h = 0.0345$, $m_h^{(\rm sim)} = 0.040$ ($m_h = 0.0275$, $m_h^{(\rm sim)} = 0.030$) for $24^3 \times 64$ ($32^3 \times 64$).

Ensemble	$\max(w_i)$	$\min(w_i)$	$N_{\rm Eff}$	$N^*_{\rm Eff}$	$N_{\rm conf}$
$24^3 \times 64$, $m_l = 0.005$	10.0	0.078	90.3	20.3	203
$24^3 \times 64$, $m_l = 0.010$	5.50	0.049	97.0	32.4	178
$32^3 \times 64$, $m_l = 0.004$	4.77	0.17	228	63.9	305
$32^3 \times 64$, $m_l = 0.006$	3.45	0.23	234	90.4	312
$32^3 \times 64$, $m_l = 0.008$	5.36	0.16	183	47.0	252

dominates the reweighted ensemble. We summarize the statistical features of the reweighting factors for each ensemble in Table III. For completeness we also compare the definition of $N_{\rm eff}$ given in Eq. (15) with the more pessimistic estimate used in Ref. [34]:

$$N^*_{\rm eff} = \frac{\sum_{i=1}^{N_{\rm conf}} w_i}{\max_j(w_j)}. \tag{16}$$

As can be seen from Table III, our choice gives a somewhat more optimistic view of the effects of reweighting on the effective size of our ensembles.

As the numbers in Table III indicate, for our ensemble and reweighting settings, the ensembles are not overwhelmed by a small number of configurations.

The efficiency of the reweighting procedure is also observable dependent. It is influenced by the fluctuations of the reweighted observable within the ensemble and the strength of the correlation between the reweighted observable and the reweighting factor. Sanity checks of the statistical properties of the most important observables, m_π and f_π, have been performed and are summarized in Fig. 6. The observables reweighted to $m_h = 0.0250$ from $m_h^{(\rm sim)} = 0.030$ are calculated using the first half and the second half of the ensemble (circle symbols), which are compared to that of the full statistics (square symbols). The number of the Gaussian vectors, N_ξ, is also varied from $N_\xi = 1$ (first 12 points from left to right in each panel denoted by blue symbols) to $N_\xi = 2$ (next 6 points denoted by green symbols) to $N_\xi = 4$ (next 3 points denoted by red symbols) in the same plot. The rightmost (black) 3 points are the unweighted observables. In the case of m_π, all the statistical samples are within $1 \times \sigma$, while for f_π the deviations are less than $\sim 2 \times \sigma$.

To probe the m_h dependence of the observables, we show in Fig. 7 the correctly reweighted m_π and f_π as a function of m_h along with the results obtained from randomly permuting the $\{w_i\}$ in Eq. (13). The random permutation is done for each reweighted mass m_h to show the difference from the correctly reweighted observables. While the randomly reweighted observables are almost flat in m_h, the correctly reweighted observables have a positive slope in m_h. Finally in Fig. 8 we plot the reweighted observables f_π and f_K as a function of the target reweighted mass m_h for three example parameter points. Note that in both Figs. 7 and 8 we observe an increase in statistical errors which appears roughly consistent with what should be expected from the decrease in $\sqrt{N_{\rm eff}}$. We should emphasize that further careful studies may be needed to establish a more accurate estimate of possible errors in the reweighting procedure.

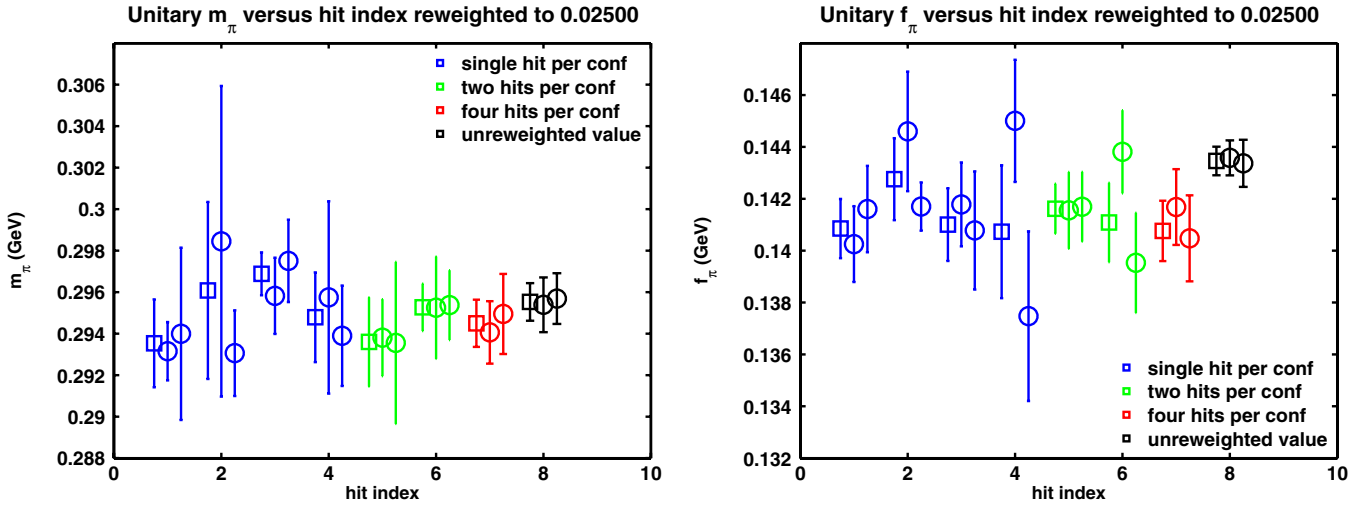

FIG. 6 (color online). Reweighted values for m_π (left) and f_π(right) for various numbers of reweighting hits, $N_\xi = 1$ (leftmost 12 points in each panel denoted by blue symbols), $N_\xi = 2$ (next 6 points denoted in green), $N_\xi = 4$ (next 3 points denoted in red), on each ensemble. The squares are for the full data set (300 configurations) and the circles are for the first and second half of the data (150 configurations.) The data is from the $32^3 \times 64 \times 16$, $(m_l, m_h) = (0.004, 0.03)$ ensemble with a light valence quark of mass 0.004. The rightmost 3 (black) points are the unreweighted observables.

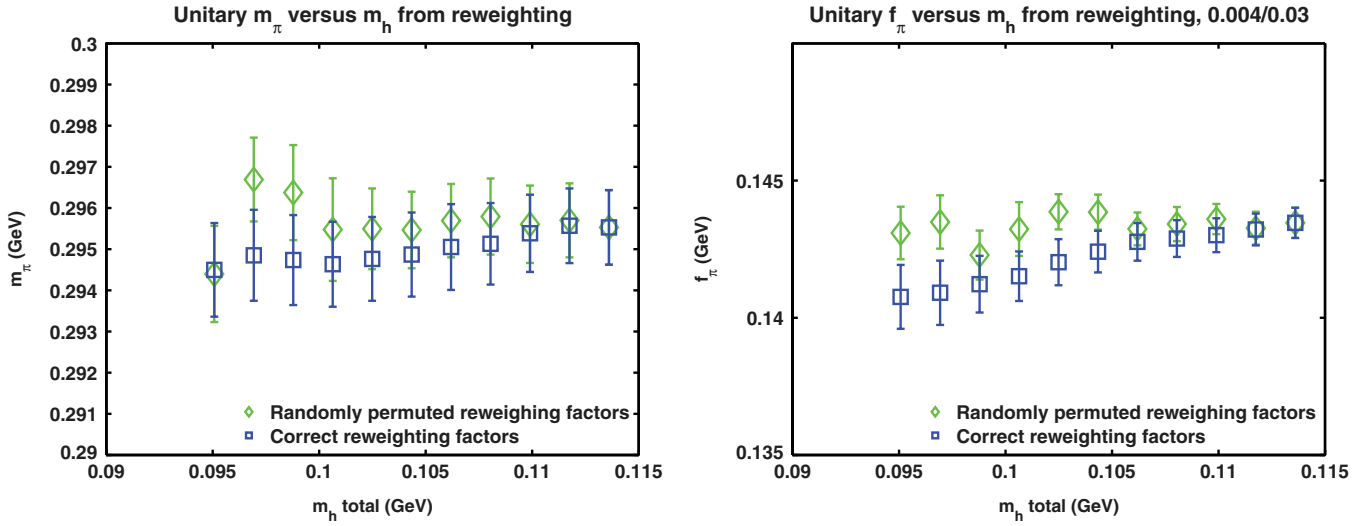

FIG. 7 (color online). The left figure gives m_π with correct reweighting factors (blue squares) and with randomly permuted reweighting factors (green diamonds). The right figure is the same but for f_π.

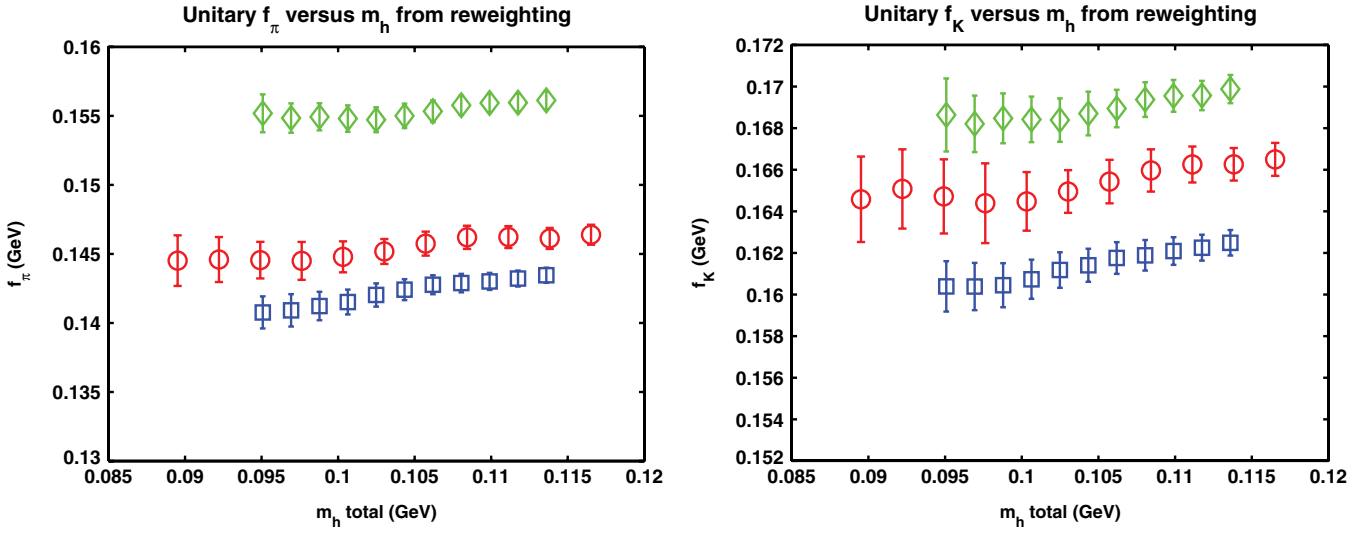

FIG. 8 (color online). Reweighted results for f_π (left) and f_K (right) as functions of m_h at three parameter sets (β, m_l): green diamonds: (2.25, 0.008), red circles: (2.13, 0.005), blue squares: (2.25, 0.004).

III. UPDATED RESULTS FROM THE 24^3 ENSEMBLES

In this section we update the results presented on the 24^3 ensembles in [1] to the extended data set described in Sec. II, and in Table I in particular. For this extended data set we make measurements of pseudoscalar quantities on a total of 203 configurations for the $m_l = 0.005$ ensemble and 178 configurations for the $m_l = 0.01$ ensemble. These configurations were separated by 40 trajectories as documented in the first two rows of Table IV. In our previous work we used 92 of these measurements on each ensemble [1,4]. Before performing the analyses we binned the data into blocks of either 80 or 400 trajectories and the measurements from each bin were then treated as being statistically independent. No statistically significant increase in the error was observed with the analysis using bins of 400 trajectories compared to that with bins of 80 trajectories.

In the following sections the results from the 24^3 lattices, combined with those obtained on the 32^3 ensembles, will be input into global chiral and continuum fits in order to determine physical quantities; here we simply tabulate the fitted pseudoscalar masses and decay constants as obtained directly from the correlation functions at our simulated quark masses. In addition, since we use the mass of the Ω baryon in the definition of the scaling trajectory, we also present the results for m_{hhh} here together with those for the

TABLE IV. A summary of the five ensembles used in this work are shown.

Volume	(m_l, m_h)	Total MD time	Measurement range	Measurement total
24^3	(0.005, 0.04)	0-8980	900–8980 every 40	203
24^3	(0.01, 0.04)	1455-8540	1460–8540 every 40	178
32^3	(0.004, 0.03)	0-6756	520–6600 every 20	305
32^3	(0.006, 0.03)	0-7220	1000–7220 every 20	312
32^3	(0.008, 0.03)	0-5930	520–5540 every 20	252

Sommer scale r_0 and also the scale r_1. Finally, we give the results for the masses of the nucleons and Δ baryons from the 24^3 ensembles, although the chiral and scaling behavior of these masses will not be studied in this paper. We present these baryon masses partly for completeness and partly to share our experience in the use of different sources.

On the 24^3 lattices discussed in this section, the measurements are presented for the two values of the sea light-quark mass, $m_l = 0.005$ and 0.01, and for the full range of valence-quark masses $m_{x,y} = 0.001$, 0.005, 0.01, 0.02, 0.03, and 0.04. The ensembles with $m_l = 0.02$ and 0.03, presented in [1], are not included in this paper because such values of m_l were found to be too large for SU(2) chiral perturbation theory to describe our data. The value of the sea strange-quark mass in these simulations is $m_h = 0.04$. After completing the global chiral and continuum fits described in Sec. V below, we find that the physical value of the bare strange-quark mass, obtained using the chiral perturbation theory ansatz, is $m_s = 0.0348(11)$. In this section we anticipate this result and use reweighting to obtain results also at this value of the strange-quark mass.

For the 24^3 ensembles, we placed Coulomb gauge-fixed wall sources at $t = 5$ and at $t = 57$. From each source, we calculated two quark propagators, one with periodic and the other with antiperiodic boundary conditions. From the periodic propagators for the two sources, denoted by $D^{-1}_{P,5}$ and $D^{-1}_{P,57}$, and the antiperiodic propagators, written as $D^{-1}_{A,5}$ and $D^{-1}_{A,57}$, we form the combinations

$$D^{-1}_{P+A,5} = \tfrac{1}{2}(D^{-1}_{P,5} + D^{-1}_{A,5}) \quad \text{and}$$
$$D^{-1}_{P+A,57} = \tfrac{1}{2}(D^{-1}_{P,57} + D^{-1}_{A,57}). \tag{17}$$

The use of periodic plus antiperiodic boundary conditions in the time direction doubles the length of the lattice in time, which markedly reduces the contamination from around-the-world propagation in the time direction. For two-point functions, such as the propagator of a pseudoscalar meson given by

$$\langle \pi(t)\pi(0)\rangle = \sum_{\vec{x}} \mathrm{Tr}\{[D^{-1}_{P+A,5}(t,\vec{x})]^\dagger D^{-1}_{P+A,5}(t,\vec{x})\}, \tag{18}$$

on a lattice of time extent N_t the time dependence of the contribution of the ground state is given by

$$\langle \pi(t)\pi(0)\rangle = A[\exp(-m_\pi(t-5)) + \exp(-m_\pi(2N_t - (t-5))]. \tag{19}$$

Here A is a t-independent constant. For our 24^3 ensembles, we find that around-the-world propagation is not visible in two-point functions. This is not the case, however, for three-point functions, as we now explain (although we do not analyze three-point functions in this paper, they are being evaluated in the computation of B_K, for example [35]).

For three-point functions of the form $\langle P(x)O(y)P(z)\rangle$, where $P(x)$ and $P(z)$ are pseudoscalar interpolating fields and $O(y)$ is an operator whose matrix element we wish to measure, we use the wall source at $t = 5$ as the source for $P(z)$ and the wall source at $t = 57$ as the source for $P(x)$. We only consider y_0 in the range $5 \le y_0 \le 57$, so we do not perform any measurements in the doubled lattice. The doubling of the lattice is important to reject around-the-world propagation in time for such measurements. For kaons, we found that a time separation of 52 between the sources gave us a broad plateau, with sufficiently small errors. This measurement strategy was chosen to optimize the measurement of the kaon bag parameter [4,35].

Before presenting our results for masses, decay constants and r_0 and r_1, we discuss the values of the residual mass and the renormalization constant of the local axial current. The residual mass $m'_{\mathrm{res}}(m_f)$ at each partially quenched valence mass used in this work is measured using the ratio [36]

$$m'_{\mathrm{res}}(m_f) = \frac{\langle 0|J^a_{5q}|\pi\rangle}{\langle 0|J^a_5|\pi\rangle}, \tag{20}$$

where J^a_{5q} is the usual DWF midpoint pseudoscalar density composed of fields of each chirality straddling the midpoint in the fifth dimension, and J^a_5 is the physical pseudoscalar density at the surfaces of the fifth dimension composed of surface fields in the fifth dimension. The results are given in Table V. For completeness we also present the corresponding residual masses obtained after reweighting to the physical strange mass in Table VI. The residual mass in the two-flavor chiral limit $m_{\mathrm{res}} = m'_{\mathrm{res}}(m_x = m_l = 0)$ is given in Table VII and in the left-hand plot of Fig. 9.

We define Z_A to be the renormalization constant of the local axial current, A_μ, composed of the physical surface

TABLE V. $m'_{\rm res}(m_x)$ measured on the 24^3 ensembles at the simulated strange-quark mass $m_h = 0.04$ is shown.

m_x	m_l	
	0.005	0.01
0.001	0.003 194(16)	0.003 286(28)
0.005	0.003 154(15)	0.003 259(26)
0.01	0.003 079(14)	0.003 187(24)
0.02	0.002 939(12)	0.003 042(21)
0.03	0.002 822(12)	0.002 919(19)
0.04	0.002 725(11)	0.002 818(17)

TABLE VI. $m'_{\rm res}(m_x)$ on the 24^3 ensembles at the physical strange-quark mass is shown.

m_x	m_l	
	0.005	0.01
0.001	0.003 146(27)	0.003 224(33)
0.005	0.003 099(27)	0.003 191(32)
0.01	0.003 025(26)	0.003 120(31)
0.02	0.002 889(24)	0.002 981(26)
0.03	0.002 774(23)	0.002 863(23)
0.04	0.002 680(21)	0.002 765(21)

TABLE VII. $m_{\rm res}$ in the two-flavor chiral limit on the 24^3 and 32^3 ensembles at the simulated and physical strange sea-quark masses are shown.

m_h	$m_{\rm res}^{24^3}$	$m_{\rm res}^{32^3}$
$m_h^{\rm sim}$	0.003 152(43)	0.000 666 4(76)
$m_h^{\rm phys}$	0.003 076(58)	0.000 664 3(82)

fields. Here we have determined Z_A through two methods. In the first, Z_A is determined for each valence mass using the improved ratio [37] of the matrix element $\langle \mathcal{A}_4(t)P(0)\rangle$ to $\langle A_4(t)P(0)\rangle$, where $\mathcal{A}_\mu$ is the conserved DWF axial current and the results are presented in Table VIII. This method assumes $Z_{\mathcal{A}} = 1$, and we find $Z_A = 0.716\,51(46)$ in the two-flavor chiral limit with the simulated sea strange mass, and $Z_A = 0.716\,89(51)$ when reweighted to the nearby physical strange mass. This determination of Z_A is illustrated in the plots of Fig. 10. As pointed out in [1], we expect $Z_{\mathcal{A}} = 1 + O(am_{\rm res})$, and in [1] we added a $\sim$1% error to account for the size of this correction. As part of our current work, we have investigated the consequences of this correction, which is discussed in detail in Appendix B. From this analysis, we find $Z_A = 0.7041(34)$, a 1.8% difference from the result with our previous method. Although, as we will see, this error is smaller than our current combined errors on the decay constants and other physical quantities, we choose to use this value of $Z_A = 0.7019(26)$, coming from $Z_V/Z_{\mathcal{V}}$ as defined in Eq. (B19), as the normalization factor for the local axial current when quoting all our central values below. Here V and $\mathcal{V}$ are the local and conserved vector currents.

TABLE VIII. Z_A on the 24^3 ensembles at the simulated and physical strange sea-quark masses are shown.

m_h	Z_A (chiral)	$Z_A(m_l = 0.005)$	$Z_A(m_l = 0.01)$
$m_h^{\rm sim} = 0.04$	0.71651(46)	0.71732(14)	0.71783(15)
$m_h^{\rm phys}$	0.71689(51)	0.71746(17)	0.71781(17)

We now turn to the measurements of the meson masses and decay constants. In order to illustrate the quality of the fits, we start by presenting some sample plots for the unitary pion and kaon on the $m_l = 0.005$, $m_h = 0.04$ ensemble. The pion effective masses obtained using different sources and sinks are shown in Fig. 11. The mass and decay constant is obtained from a simultaneous fit with a single, constrained mass to five correlation functions. These are the $\langle P|P\rangle$, $\langle A|A\rangle$, and $\langle A|P\rangle$ correlation functions

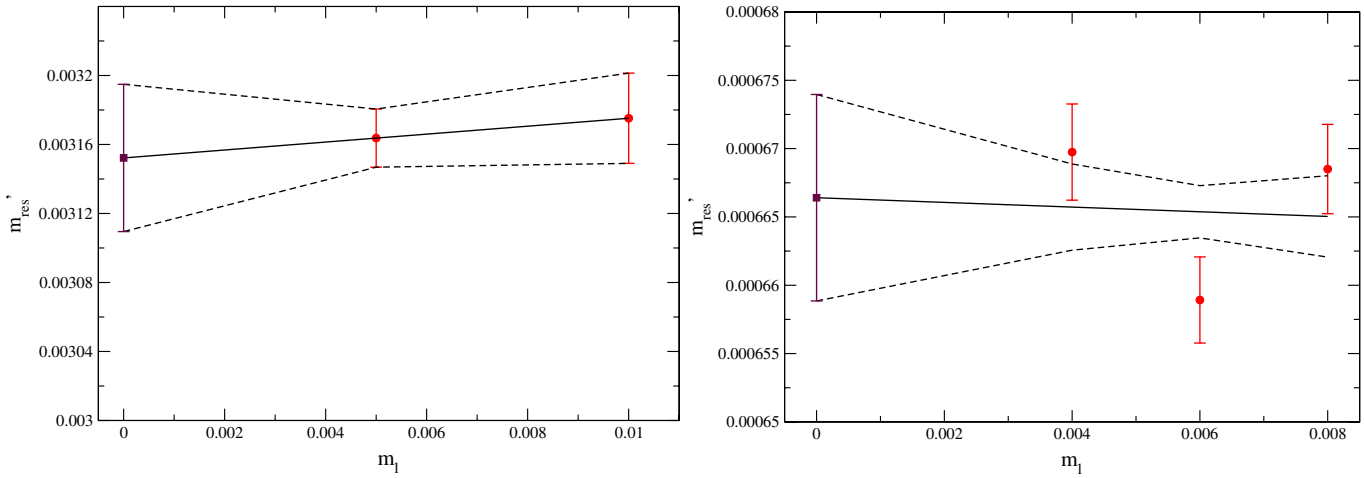

FIG. 9 (color online). Chiral extrapolation of the unitary values of $m'_{\rm res}$ for the 24^3 (left) and 32^3 (right) ensembles. While the fit is only marginally acceptable for the 32^3 lattices, an additional uncertainty of $O(5 \times 10^{-6})$ is negligible.

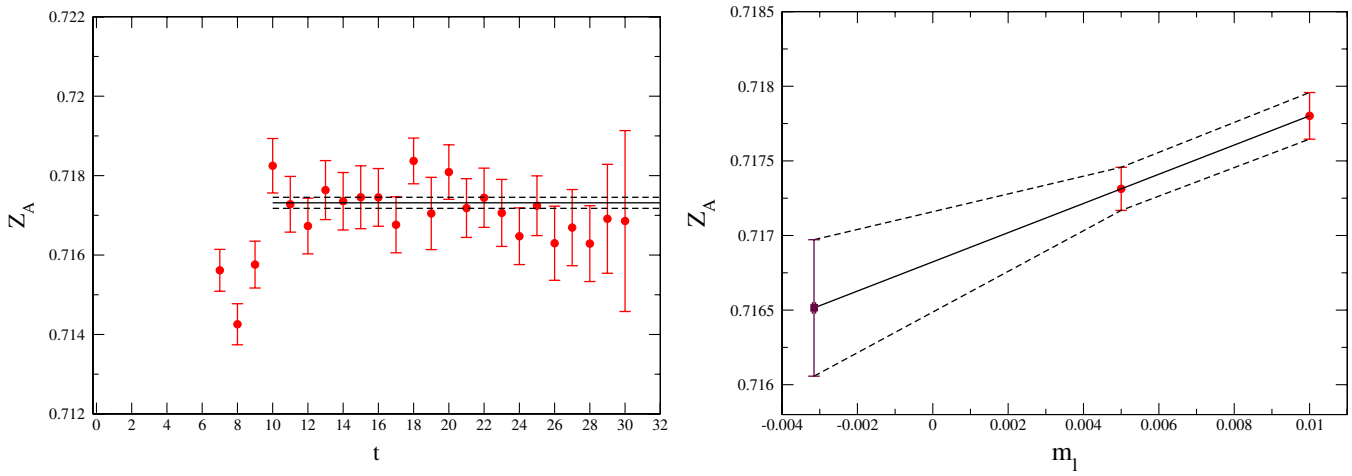

FIG. 10 (color online). Measurement of Z_A for $m_f = 0.005$ on the $m_l = 0.005$, $m_h = 0.04$ ensemble (left panel) and the unitary chiral extrapolation of Z_A for the 24^3 ensembles (right panel). The results do not change significantly under reweighting to the physical strange mass.

(denoted in the figure by PP, AA, and AP, respectively) with gauge-fixed wall sources and local (LW) or wall (WW) sinks (we do not use the AA-WW combination because it is noisier). The long time extent $N_t = 64$ on our lattices together with the noise properties of pseudoscalar states allow for long plateaux and the results are insensitive to the choice of $t_{\rm min}$, the starting point of the fits. Figure 12 displays the effective masses for the unitary kaon, together with the results obtained from a simultaneous constrained fit. We give an example of the m_h dependence of the unitary pion and kaon masses in Fig. 13. This dependence is obtained by reweighting.

We normalize the states so that, for periodic boundary conditions, the time-dependence of the correlators for large times is given by

$$\mathcal{C}^{s_1 s_2}_{O_1 O_2}(t) = \frac{\langle 0|O_1^{s_1}|\pi\rangle\langle\pi|O_2^{s_2}|0\rangle}{2m_{xy}V}[e^{-m_{xy}t} \pm e^{-m_{xy}(2N_t - t)}], \quad (21)$$

where the superscripts specify the type of smearing and the subscripts denote the interpolating operators. The sign in the square brackets in Eq. (21) is + for PP and AA correlators and − for AP ones. We therefore define the amplitude of the correlator to be

$$\mathcal{N}^{s_1 s_2}_{O_1 O_2} \equiv \frac{\langle 0|O_1^{s_1}|\pi\rangle\langle\pi|O_2^{s_2}|0\rangle}{2m_{xy}V}. \quad (22)$$

For each correlator included in the simultaneous fit

$$\mathcal{N}^{LW}_{AA}, \mathcal{N}^{LW}_{PP}, \mathcal{N}^{LW}_{AP}, \mathcal{N}^{WW}_{PP}, \quad \text{and} \quad \mathcal{N}^{WW}_{AP},$$

we determine the amplitude and obtain the decay constant f_{xy} using

$$f_{xy} = Z_A\sqrt{\frac{2}{m_{xy}}\frac{\mathcal{N}^{LW2}_{AP}}{\mathcal{N}^{WW}_{PP}}}. \quad (23)$$

Table IX contains the measured pseudoscalar masses and decay constants at the simulated strange-quark mass $m_h = 0.04$. After reweighting to the estimated physical strange-quark mass $m_s = 0.0348(11)$ the masses and decay constants of the pions are presented in Table X and those for the kaons in Table XI.

The Ω baryon, being one of the quantities included in the definition of our scaling trajectory (see Sec. V), plays an important rôle in our analysis. We have performed measurements on the same configurations using a gauge-fixed box source of size 16 lattice units that gives a good plateau for the Ω state for valence-quark masses $m_x = 0.04$ and $m_x = 0.03$ to enable interpolation to the physical strange-quark mass. We display the fit to the $m_x = 0.04$ Ω baryon mass on the $m_l = 0.005$, $m_h = 0.04$ ensemble in Fig. 14, along with the dependence of this mass on the dynamical strange mass using reweighting.

The results for the Ω mass, m_{hhh}, obtained directly at the simulated strange-quark mass ($m_h = 0.04$) with valence strange-quark masses $m_y = 0.04$ and 0.03 are presented in Table XII. In this table we also present the results for m_{hhh} obtained after reweighting to the physical strange-quark mass. In Table XIII we display the values of the Sommer scale r_0, r_1 and their ratio at both the simulated and physical strange-quark masses. These quantities were determined using Wilson loops formed from products of temporal gauge links with Coulomb gauge-fixed closures in spatial directions, with an exponential fit to the time dependence of the Wilson loop $W(r, t)$ from $t = 3$ to $t = 7$ for each value of the separation r. The resulting potential $V(r)$ was then fit over the range $r = 2.45 - 8$ to the Cornell form [38]

$$V(r) = V_0 - \frac{\alpha}{r} + \sigma r, \quad (24)$$

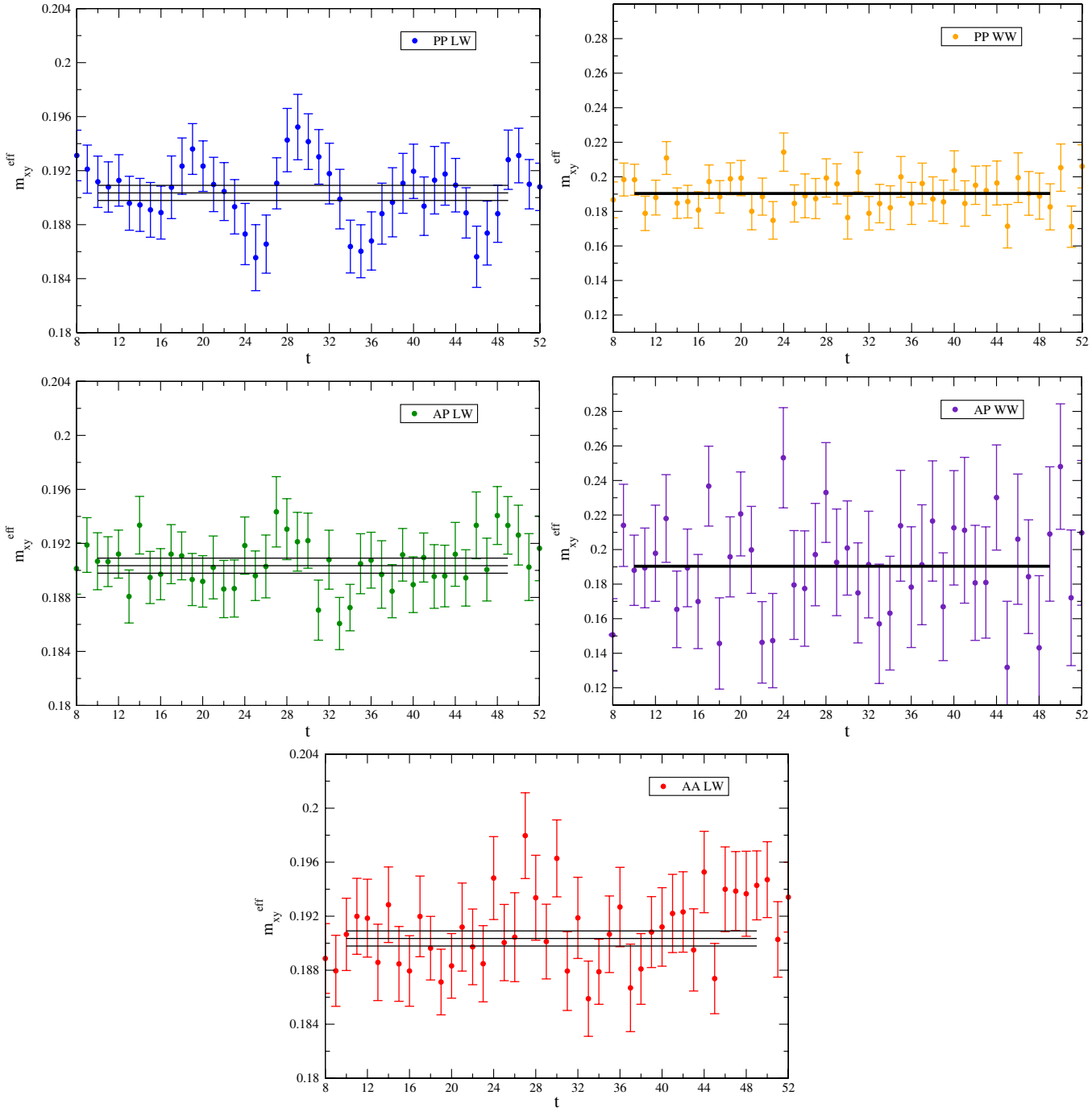

FIG. 11 (color online). Effective pion masses from the PP LW correlator (top-left), PP WW correlator (top-right), AP LW correlator (center-left), AP WW (center-right), and AA LW correlator (bottom). Note the different vertical scale for the WW correlators. The horizontal bands represent the result for the mass from a simultaneous fit.

where V_0, α, and σ are constants. These fits are illustrated in Fig. 15, which shows the fit to the time dependence of the Wilson loop $W(r = 2.45, t)$ at the physical strange-quark mass, and also the subsequent fit over the potential. The strange-quark mass dependence of the scales r_0 and r_1 is small and cannot be resolved within our statistics.

Nucleon and Δ masses

A detailed study of the baryon mass spectrum, including the continuum and chiral extrapolations, is postponed to a separate paper. The one exception is the Ω baryon, whose mass is used in the definition of the scaling trajectory and which is therefore studied in detail together with the properties of pseudoscalar mesons. In this subsection

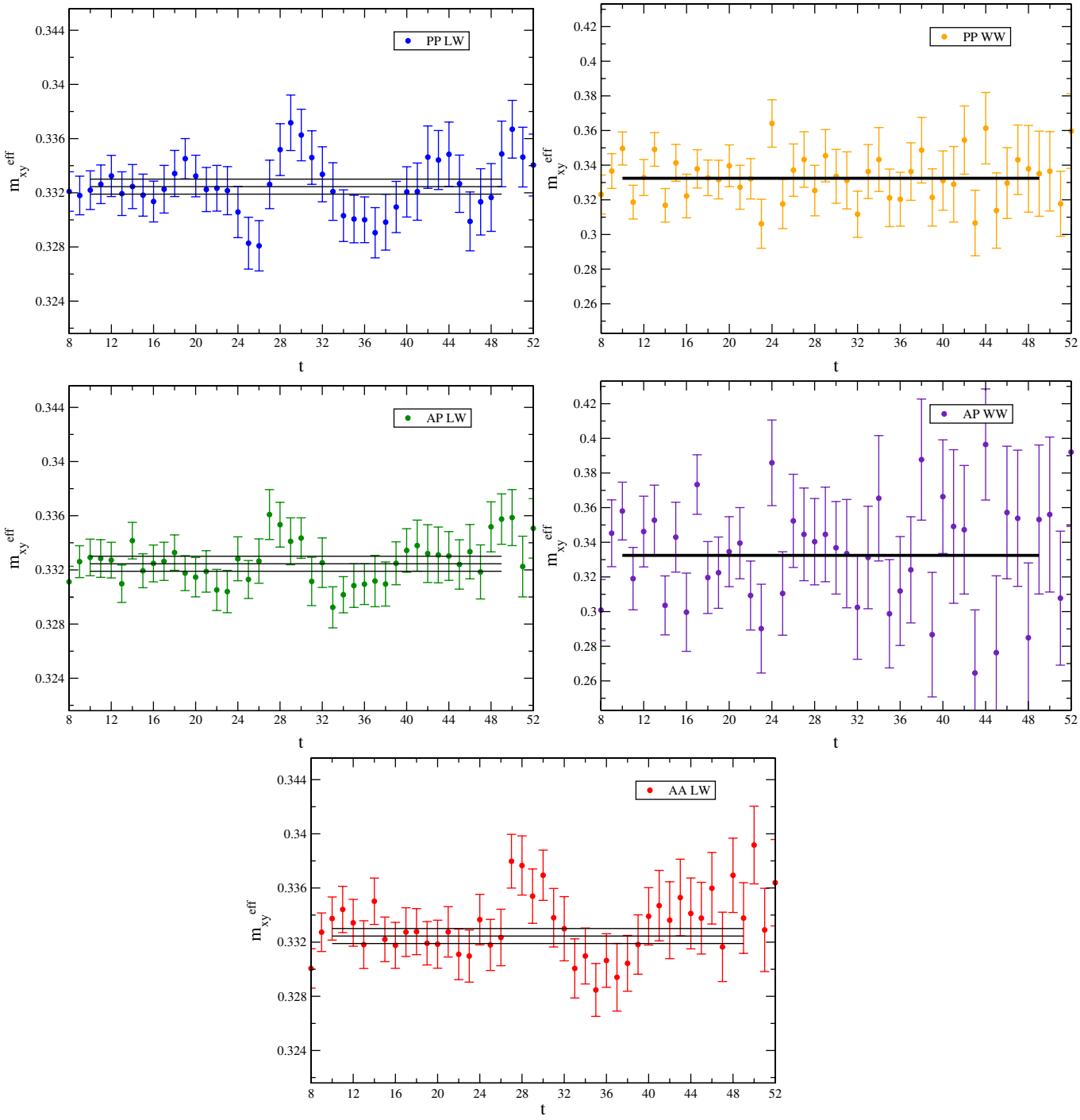

FIG. 12 (color online). Effective kaon masses from the PP LW correlator (top-left), PP WW correlator (top-right), AP LW correlator (center-left), AP WW (center-right), and AA LW correlator (bottom). Note the different vertical scale for the WW correlators. The horizontal bands represent the result for the mass from a simultaneous fit.

we briefly discuss our experiences in extracting the masses of the nucleons and Δ baryons using different sources and present the results for these masses on each ensemble, starting here with those from the 24^3 ensembles. The baryon spectrum from the 32^3 ensembles will be discussed below. We start however, with some general comments about our procedures which are relevant to both sets of ensembles.

We use the standard operator, $N = \epsilon_{abc}(u_a^T C\gamma_5 d_b)u_c$, to create and annihilate nucleon states and $\Delta = \epsilon_{abc}(u_a^T C\gamma_\mu u_b)u_c$ for the flavor decuplet Δ states. On an antiperiodic lattice of size N_t in the time direction, the

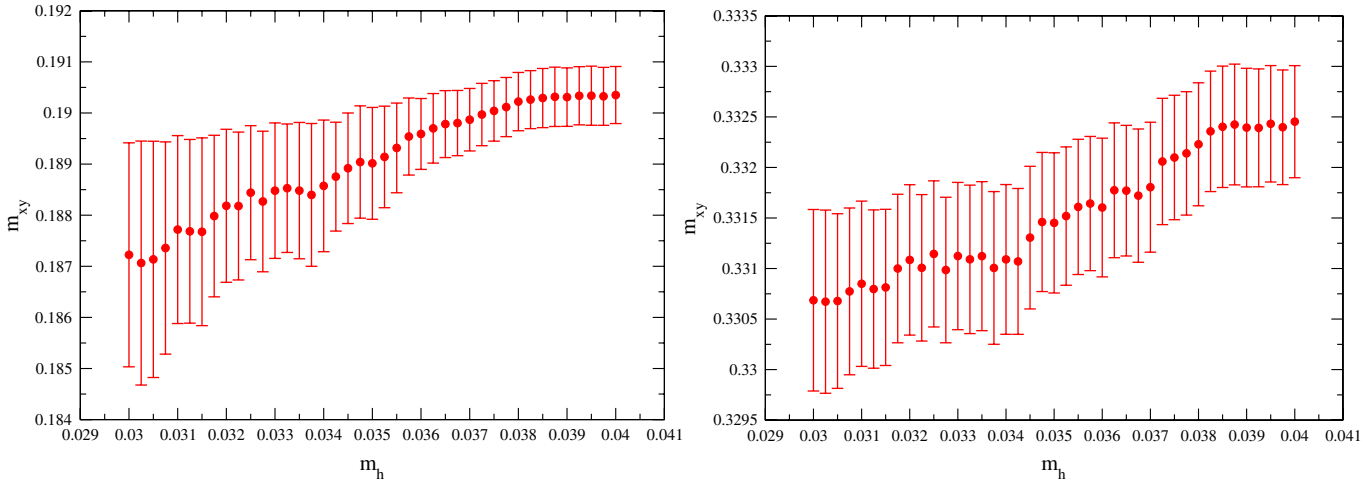

FIG. 13 (color online). We illustrate the m_h dependence of the unitary pion (left panel) and kaon (right panel) masses on the $m_l = 0.005$, 24^3 ensemble. The values are obtained by reweighting around the simulated value ($m_h = 0.04$).

zero-momentum two-point correlation function, $C(t)$, calculated with one of these baryonic operators at its source and sink, takes the following asymptotic form for sufficiently large time, t:

$$C(t) = Z[(1 + \gamma_4)e^{-Mt} - (1 - \gamma_4)e^{-M(N_t - t)}], \qquad (25)$$

corresponding to particle and antiparticle propagation, respectively. Conventionally one chooses an appropriate range in time where the excited-state contributions can be neglected so that this form is valid, and extracts the ground-state mass, M, by fitting the numerical data to the function in Eq. (25). This is indeed what we do to extract baryon masses from the 24^3 ensembles. Alternatively we can try to fit the correlation function to a sum of two exponentials, representing the ground- and excited-state contributions. As will be reported below, this is the method we use for the 32^3 ensembles.

The determination of baryon masses can be made more effective by an appropriate choice of smearing at the source and/or sink. We use several different choices of the smearing of these operators, wall, box, and gauge-invariant Gaussian [39,40], in an attempt to obtain a better overlap with the ground state; our choices are summarized

TABLE IX. Pseudoscalar masses $m_{xy}(m_l)$ and decay constants $f_{xy}(m_l)$ on the 24^3 ensembles at the simulated strange-quark mass ($m_h = 0.04$) are shown.

m_x	m_y	$m_{xy}(0.005)$	$m_{xy}(0.01)$	$f_{xy}(0.005)$	$f_{xy}(0.01)$
0.04	0.04	0.4317(4)	0.4344(4)	0.1063(6)	0.1087(6)
0.03	0.04	0.4051(4)	0.4080(4)	0.1034(6)	0.1059(6)
0.02	0.04	0.3772(5)	0.3802(4)	0.1002(5)	0.1028(5)
0.01	0.04	0.3478(5)	0.3509(5)	0.0967(5)	0.0996(6)
0.005	0.04	0.3325(6)	0.3358(5)	0.0949(5)	0.0982(6)
0.001	0.04	0.3199(7)	0.3233(7)	0.0937(6)	0.0975(7)
0.03	0.03	0.3771(4)	0.3800(4)	0.1006(5)	0.1031(5)
0.02	0.03	0.3472(5)	0.3502(4)	0.0974(5)	0.1001(5)
0.01	0.03	0.3152(5)	0.3184(4)	0.0939(5)	0.0969(5)
0.005	0.03	0.2983(5)	0.3016(5)	0.0920(5)	0.0954(6)
0.001	0.03	0.2843(6)	0.2877(6)	0.0908(6)	0.0946(6)
0.02	0.02	0.3149(5)	0.3179(4)	0.0943(5)	0.0971(5)
0.01	0.02	0.2794(5)	0.2826(5)	0.0908(5)	0.0938(5)
0.005	0.02	0.2603(5)	0.2636(5)	0.0889(5)	0.0923(5)
0.001	0.02	0.2440(6)	0.2475(6)	0.0876(5)	0.0915(6)
0.01	0.01	0.2389(5)	0.2422(5)	0.0872(5)	0.0905(5)
0.005	0.01	0.2161(5)	0.2195(5)	0.0853(5)	0.0889(5)
0.001	0.01	0.1960(6)	0.1997(6)	0.0840(5)	0.0879(5)
0.005	0.005	0.1904(6)	0.1940(6)	0.0834(5)	0.0871(5)
0.001	0.005	0.1669(6)	0.1709(6)	0.0819(5)	0.0858(5)
0.001	0.001	0.1391(6)	0.1434(7)	0.0802(5)	0.0840(5)

TABLE X. Pion masses $m_{xy}(m_l)$ and decay constants $f_{xy}(m_l)$ on the 24^3 ensembles at the physical strange-quark mass $m_s = 0.0348(11)$ are shown.

m_x	m_y	$m_{xy}(0.005)$	$m_{xy}(0.01)$	$f_{xy}(0.005)$	$f_{xy}(0.01)$
0.01	0.01	0.2378(8)	0.2420(7)	0.0867(5)	0.0900(6)
0.005	0.01	0.2149(9)	0.2192(7)	0.0848(6)	0.0882(6)
0.001	0.01	0.1948(10)	0.1994(8)	0.0833(6)	0.0871(6)
0.005	0.005	0.1891(10)	0.1936(8)	0.0828(5)	0.0863(6)
0.001	0.005	0.1656(11)	0.1704(8)	0.0813(6)	0.0850(6)
0.001	0.001	0.1377(12)	0.1427(9)	0.0796(6)	0.0832(7)

TABLE XI. Kaon masses $m_{xh}(m_l)$ and decay constants $f_{xh}(m_l)$ on the 24^3 ensembles at the physical strange-quark mass $m_s = 0.0348(11)$ are shown.

m_x	$m_{xh}(0.005)$	$m_{xh}(0.01)$	$f_{xh}(0.005)$	$f_{xh}(0.01)$
0.01	0.330(4)	0.334(4)	0.0947(7)	0.0978(8)
0.005	0.314(4)	0.318(4)	0.0928(7)	0.0963(9)
0.001	0.301(4)	0.305(4)	0.0915(8)	0.0955(10)

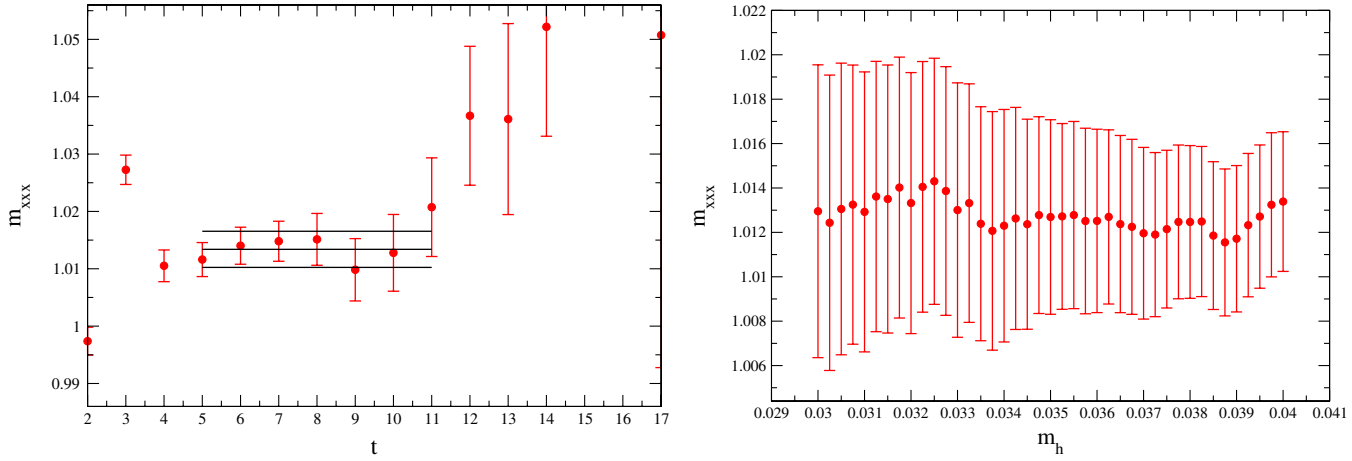

FIG. 14 (color online). Fit to the Ω baryon mass with valence strange mass $m_x = 0.04$ on the $m_l = 0.005$, $m_h = 0.04$, 24^3 ensemble showing the quality of the fit with our box source (left panel). We also show the weak dependence of the Ω baryon mass with fixed valence mass $m_x = 0.04$ on our simulated m_h inferred by the reweighting procedure on the $m_l = 0.005$, 24^3 ensemble (right panel).

in Table XIV. The wall source, used for the 32^3 ensembles, is Coulomb-gauge fixed. A box source of size 16, also Coulomb-gauge fixed, is used for the 24^3 ensembles. The Gaussian-source radius is set to 7 lattice units and 100 smearing steps are used for the 24^3 ensembles, while the radius is 6 in the 32^3 ensembles: these choices are optimized for our nucleon-structure calculations [7–9].

As can also be seen from the table, several steps are taken to reduce the statistical error. For each configuration, as many as four different time slices are used for the sources, usually separated by 16 lattice units, but occasionally fewer. Measurements are made as frequently as every tenth trajectory and are averaged into bins of 40 hybrid Monte Carlo time units.

We now turn to the results obtained specifically on the 24^3 ensembles. The unitary nucleon and Δ effective masses are plotted in Figs. 16 and 17 for each choice of quark mass. For the nucleon, both Gaussian and box sources are shown. Plateaus for the effective masses obtained with the box source appear quickly, suggesting a strong overlap with the ground state. The corresponding plateaus obtained with the Gaussian source appear more slowly, from above. Both sets of results agree reasonably well for sufficiently large t. For the Δ the correlators were only computed using the box source and the plateaus for the effective masses again appear quickly. The results for the masses, obtained using fully correlated fits, are summarized in Table XV. Note such fully correlated fits work well for extracting baryon masses as the procedure involves much shorter ranges in time than for the meson observables discussed in the rest of this paper. As expected from the effective mass plots, nucleon masses obtained using different sources agree fairly well when the fits are performed over appropriate ranges. All values of χ^2 per degree of freedom (χ^2/dof) are close to 1 or smaller, except for the box-source nucleon fit at $m_f = 0.02$ which is about 2.5.

Some of these results have been reported earlier at Lattice 2008 [41], and also partially in related papers on nucleon structure [8,9]. A preliminary report on a bootstrap correlated analysis with a frozen correlation matrix was presented at Lattice 2009 [42] and the results agree with the updated ones given here.

TABLE XII. Omega baryon masses on the 24^3 ensembles at the simulated strange-quark mass $m_h = 0.04$ (first two rows) and at the physical strange-quark mass (third row) are shown.

m_y	m_h	$m_\Omega(0.005)$	$m_\Omega(0.01)$
0.04	0.04	1.013(3)	1.028(4)
0.03	0.04	0.963(4)	0.978(4)
0.0348	0.0348	0.988(9)	1.001(7)

TABLE XIII. The quantities r_0, r_1, and r_1/r_0 at the simulated ($m_h = 0.04$) and physical ($m_h = 0.0348$) strange-quark masses on the 24^3 ensembles. $Q(m_l)$ denotes the quantity measured with light-quark mass m_l.

Quantity	$m_h = 0.04$		$m_h = 0.0348$	
	$Q(0.005)$	$Q(0.01)$	$Q(0.005)$	$Q(0.01)$
r_0	4.16(2)	4.10(2)	4.15(2)	4.12(3)
r_1	2.82(3)	2.70(2)	2.83(3)	2.72(3)
r_1/r_0	0.678(8)	0.657(6)	0.682(9)	0.661(10)

IV. RESULTS FROM THE 32^3 ENSEMBLES

The results for masses, decay constants, r_0 and r_1 obtained directly on the 32^3 lattice are presented in the same format as those from the 24^3 ensembles in Sec. III and the available measurements are also summarized in Table IV. The results are presented for three values of the sea light-quark mass $m_l = 0.004$, 0.006, and 0.008 which correspond to unitary pion masses in the range 290 MeV–400 MeV which we had found to be consistent with

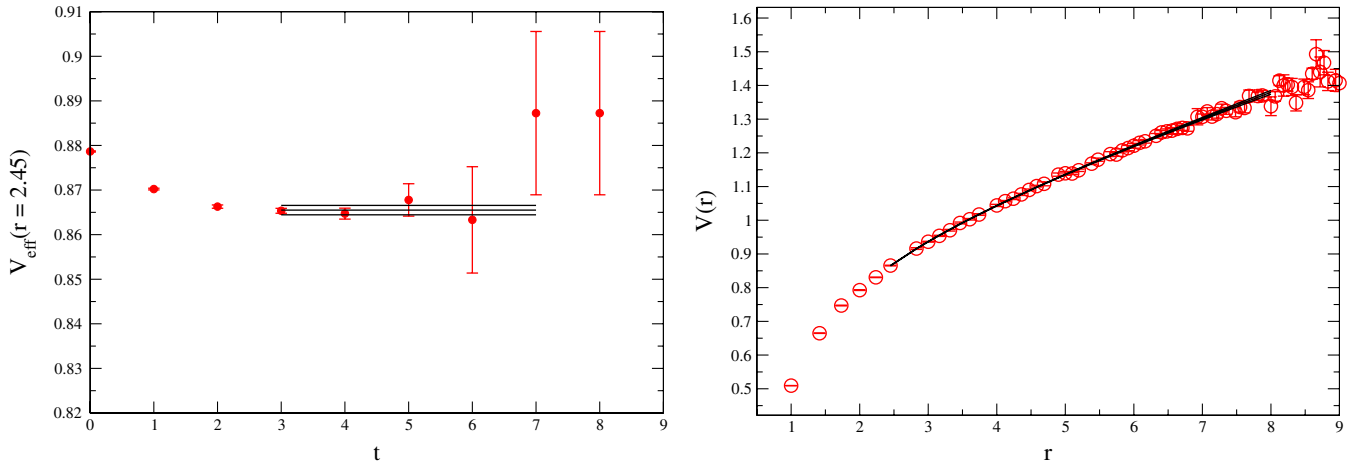

FIG. 15 (color online). The effective potential of the Wilson loops with a spatial extent of $r = 2.45$ on the 24^3, $m_l = 0.005$ ensemble at the physical strange-quark mass, overlaid by the fit to the range $t = 3$–7 (left panel). The right panel shows the static interquark potential $V(r)$ on this ensemble, again at the physical strange-quark mass, as a function of the spatial extent of the Wilson loops, overlaid by the fit to the Cornell form over the range $r = 2.45$–8.

SU(2) chiral perturbation theory on the 24^3 lattice [1]. The valence-quark masses used in the analysis are $m_{x,y} = 0.002$, 0.004, 0.006, 0.008, 0.025, and 0.03. For pseudoscalar quantities we use 305, 312, and 252 measurements separated by 20 trajectories on the 0.004, 0.006, and 0.008 ensembles, respectively, (see Table IV). For the 32^3 lattices, we have used a single-source technique for our measurements of pseudoscalar quantities, which differs from the two-source method for the 24^3 ensembles. Recall that for the 24^3 ensembles, as discussed in Sec. III, we placed Coulomb gauge-fixed wall sources at $t = 5$ and at $t = 57$. For the 32^3 ensembles we have used a single source and calculated both periodic and antiperiodic propagators from this one source. The source is placed at $t = 0$ on the first configuration used for measurements, and the position of the source is then increased by 16 for every subsequent measurement so that $t_{\rm src} = 16n \bmod 64$ where n is the measurement index, which starts from zero. Moving the source in this way helps to decorrelate measurements. We always place the antiperiodic boundary condition on the links in the time direction going from the hyperplane with $t = t_{\rm src} - 1$ to $t = t_{\rm src}$. Clearly the number of propagators to calculate for the single-source method is half that for the two-source method.

For meson two-point functions, as given in Eq. (18), the single-source method is identical to the two-source method, except for having half the number of measurements per configuration. For the light-quark masses on our 32^3 ensembles we do see around-the-world effects at the fraction of a percent level, so fits of the form in Eq. (19) must be used. We also perform measurements using three-point functions of the type $\langle P(x)O(y)P(z)\rangle$, where $P(x)$ and $P(z)$ are pseudoscalar interpolating fields and $O(y)$ is an operator whose matrix element we wish to measure. Here

TABLE XIV. A summary of the configurations used in the calculation of the baryon spectrum is shown.

Size	m_l	Source type	Correlators	Source time slices	Configurations
24^3	0.005	Gaussian	N	0, 8, 16, 19, 32, 40, 48, 51	647
	0.005	Box	Δ, Ω	0, 32	90
	0.01	Gaussian	N	0, 8, 16, 19, 32, 40, 48, 51	357
	0.01	Box	Δ, Ω	0, 32	90
	0.02	Gaussian	N	0, 8, 16, 19, 32, 40, 48, 51	99
	0.02	Box	Δ, Ω	0, 32	43
	0.03	Gaussian	N	0, 8, 16, 19, 32, 40, 48, 51	106
	0.03	Box	Δ, Ω	0, 32	44
32^3	0.004	Gaussian	N, Δ	10, 26, 42, 58	264
	0.004	Wall	N, Δ	0, 16, 32, 48	305
	0.006	Wall	N, Δ	0, 16, 32, 48	224
	0.008	Gaussian	N, Δ	10, 26, 42, 58	169
	0.008	Wall	N, Δ	0, 16, 32, 48	254

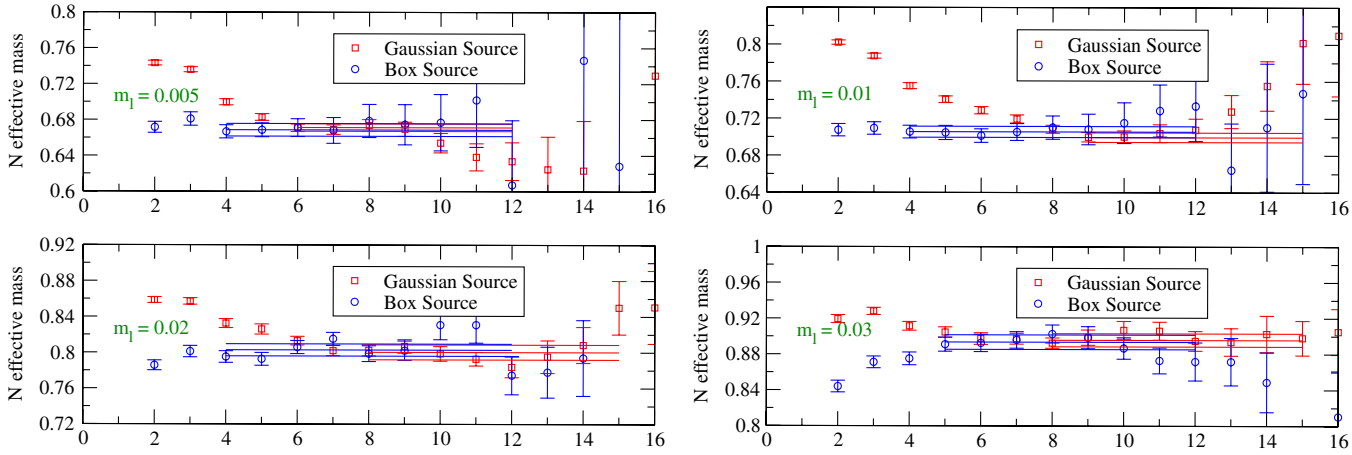

FIG. 16 (color online). Nucleon effective mass plots from the 24^3 ensembles. Results obtained using the Gaussian source are marked by red squares and those from the box source by blue circles. The four plots correspond to unitary light-quark masses 0.005 (top-left), 0.01 (top-right), 0.02 (bottom-left), and 0.03 (bottom-right).

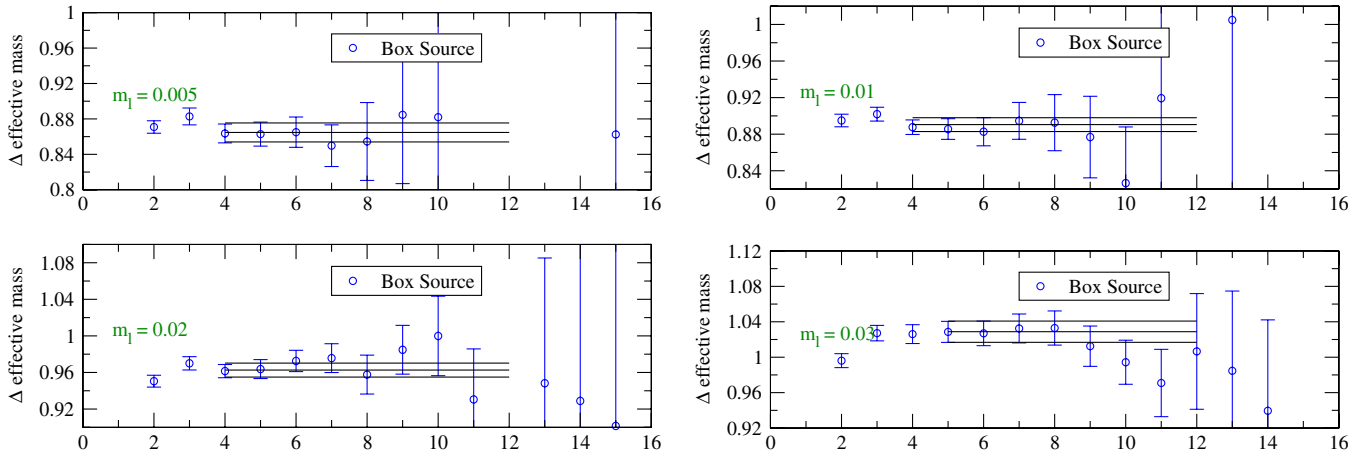

FIG. 17 (color online). Effective mass plots for the Δ baryon from the 24^3 ensembles. The results were obtained using the box source. The four plots correspond to unitary light-quark masses 0.005 (top-left), 0.01 (top-right), 0.02 (bottom-left), and 0.03 (bottom-right).

$P(x)$ is made out of propagators of the form $D^{-1}_{P+A,0} = 1/2(D^{-1}_{P,0} + D^{-1}_{A,0})$ in the notation of Eq. (17) and $P(z)$ is composed of $D^{-1}_{P-A,0} = 1/2(D^{-1}_{P,0} - D^{-1}_{A,0})$ propagators. This means that the time separation between $P(x)$ and $P(z)$ is N_t, the time extent of our lattice. We performed tests on our 24^3 ensembles, comparing the single-source and two-source methods and found that, for the same number of inversions, the single-source methods gave at least as small an error as the two-source methods. The single-source method allows us to measure on more configurations for the same computer time and so we chose this method. Although we do not discuss three-point measurements in this paper, sharing propagators between them and the two-point measurements discussed here has helped to define our measurement strategy.

TABLE XV. Baryon mass in lattice units from the $\beta = 2.13$, 24^3 ensembles. {} denotes the fit range.

m_l	N (Gaussian)		N (Box)		Δ (Box)	
0.005	0.671(4)	{6–12}	0.669(7)	{4–12}	0.865(11)	{4–12}
0.01	0.699(5)	{9–15}	0.706(6)	{4–12}	0.891(8)	{4–12}
0.02	0.800(8)	{8–15}	0.803(7)	{4–12}	0.963(8)	{4–12}
0.03	0.896(7)	{8–15}	0.894(8)	{5–12}	1.029(12)	{5–12}

The measured values of the residual mass $m^l_{\rm res}$ at each pair of valence and sea light-quark masses (m_x, m_l) used in this work are given in Table XVI; in this table the strange-quark mass is the one used in the simulation $m_h = 0.03$. Table XVII contains the corresponding results obtained after reweighting to the physical strange mass [$m_s = 0.0273(7)$] determined later in the analysis and presented in Sec. V. The residual mass in the unitary two-flavor chiral limit is given in Table VII and Fig. 9.

TABLE XVI. m'_{res} on the 32^3 ensemble set at the simulated strange-quark mass $m_h = 0.03$ is shown.

m_x	m_l		
	0.004	0.006	0.008
0.002	0.000 676 1(35)	0.000 668 8(34)	0.000 682 2(37)
0.004	0.000 669 7(34)	0.000 665 1(31)	0.000 679 1(36)
0.006	0.000 662 2(33)	0.000 658 9(30)	0.000 673 6(35)
0.008	0.000 655 0(32)	0.000 652 4(29)	0.000 667 6(34)
0.025	0.000 609 0(24)	0.000 608 9(21)	0.000 621 8(25)
0.03	0.000 599 3(23)	0.000 599 7(20)	0.000 611 5(24)

TABLE XVII. m'_{res} on the 32^3 ensemble set at the physical strange-quark mass is shown.

m_x	m_l		
	0.004	0.006	0.008
0.002	0.000 671 8(39)	0.000 667 1(36)	0.000 678 1(44)
0.004	0.000 665 8(39)	0.000 663 3(33)	0.000 675 1(42)
0.006	0.000 658 6(37)	0.000 656 9(31)	0.000 669 6(40)
0.008	0.000 651 5(36)	0.000 650 3(30)	0.000 663 6(39)
0.025	0.000 606 3(26)	0.000 605 8(24)	0.000 618 0(31)
0.03	0.000 596 7(24)	0.000 596 6(22)	0.000 608 0(29)

The results for Z_A for the 32^3 ensembles obtained from the ratios of matrix elements of $\mathcal{A}_4$ and A_4 are given in Table XVIII. We obtain $Z_A = 0.744\,75(12)$ in the chiral limit with the simulated sea strange mass and $Z_A = 0.744\,68(13)$ when reweighted to the nearby physical strange mass. This is illustrated in Fig. 18. As explained in Sec. III and Appendix B, however, in this paper we use $Z_V/Z_{\mathcal{V}} = 0.7396(17)$ as the normalization factor for the local axial current when calculating the central values of physical quantities.

In order to illustrate the quality of the fits, we present sample effective mass plots for the unitary simulated pion on the $m_l = 0.004$, $m_h = 0.03$ ensemble in Fig. 19 and for the kaon in Fig. 20. The analysis is performed as a simultaneous constrained fit to the five pseudoscalar channels as for the 24^3 ensembles (see Sec. III). The fits are performed between $t_{\mathrm{min}} = 12$ and $t_{\mathrm{max}} = 51$. We give an example of the reweighted m_h dependence of the unitary pion and kaon masses in Fig. 21.

Table XIX contains the measured pseudoscalar masses and decay constants at the simulated strange-quark mass $m_h = 0.03$. Reweighting to the estimated physical strange-quark mass $m_h = 0.0273(7)$, we obtain the masses and decay constants of the pions and kaons in Tables XX and XXI, respectively.

We use a gauge-fixed box source of size 24 for the Ω baryon using the same configurations as for our pion measurements with valence strange-quark masses $m_x = 0.03$ and $m_x = 0.025$ to enable an interpolation to the physical strange-quark mass. We display the fit to the $m_x = 0.03$ Ω baryon mass on the $m_l = 0.004$, $m_h = 0.03$ ensemble in Fig. 22, along with the dependence of this mass on the dynamical strange mass under reweighting. We take our fitting range between $t_{\mathrm{min}} = 7$ and $t_{\mathrm{max}} = 13$.

The results for the masses of the Ω baryon and the scales r_0, r_1 and r_1/r_0 are given in Tables XXII and XXIII, respectively. r_0 and r_1 were determined again using Wilson loops formed from products of temporal gauge links with Coulomb gauge-fixed closures in spatial directions, with an exponential fit from $t = 4$ to $t = 8$ and the resulting potential fit to the Cornell form in the range $r = 2.45 - 10$. An example of the fit to the time dependence of the Wilson loops at the physical strange-quark mass is given in Fig. 23. This figure also shows the fit to the potential. On these ensembles, the strange-quark mass dependence of r_0 and r_1 can be resolved within the statistics, but remains small.

Nucleon and Δ masses

Baryon effective masses from the 32^3 ensembles are plotted in Figs. 24 and 25. The Gaussian-source correlators give good effective mass signals, while the wall-source correlators are much noisier; indeed it is hard to identify a plateau in effective mass signals from the latter. While for nucleons effective mass signals from the wall source seem to eventually settle at the same values as from Gaussian-source correlators, for the Δ baryons a plateau cannot be identified from the wall source except for the lightest up/down mass. Nevertheless fully correlated fits using two exponentials to represent the contributions of the ground and first-excited states can be performed for both the nucleon and Δ, yielding the results summarized in Table XXIV. In addition to this fully correlated two-exponential fit, we have tried two other fit methods: uncorrelated and bootstrap correlated with frozen correlation matrix [42]. While those earlier analyses were conducted on smaller statistics, they agree with the two-state fully correlated fits within 2 standard deviations (see Table XXV.) We use the results from the two-state fully correlated fits as our best values of the baryon masses.

TABLE XVIII. Z_A on the 32^3 ensembles at the simulated and physical strange sea-quark masses is shown.

m_h	Z_A (chiral)	$Z_A(m_l = 0.004)$	$Z_A(m_l = 0.006)$	$Z_A(m_l = 0.008)$
$m_h^{\mathrm{sim}} = 0.03$	0.744 75(12)	0.745 053(54)	0.745 222(45)	0.745 328(48)
m_h^{phys}	0.744 69(13)	0.745 059(52)	0.745 239(47)	0.745 384(56)

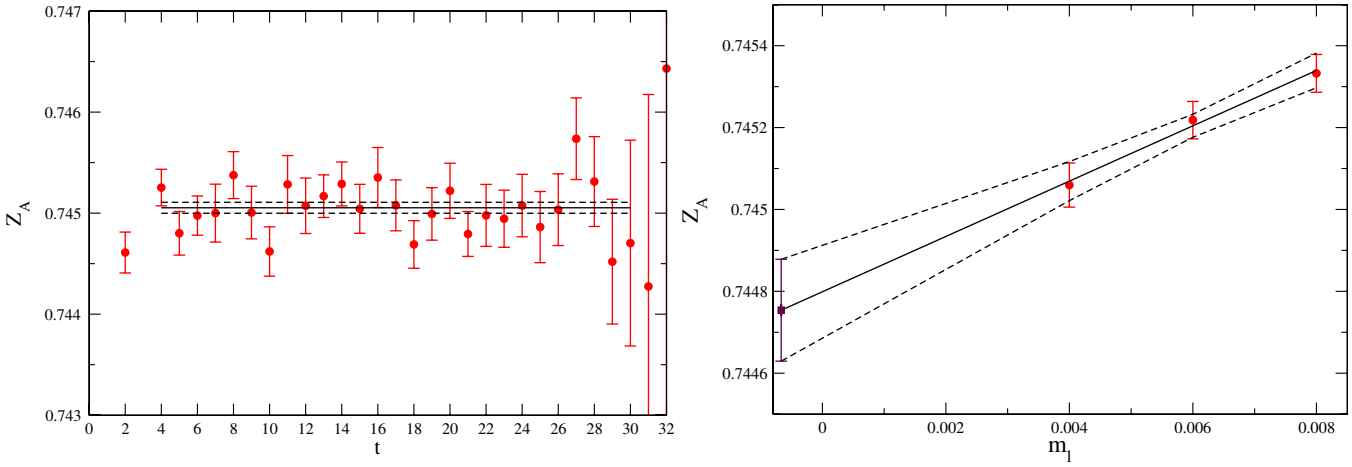

FIG. 18 (color online). Measurement of Z_A for $m_f = 0.004$ on the $m_l = 0.004$, $m_h = 0.03$ ensemble (left panel) and the unitary chiral extrapolation of Z_A for the 32^3 ensemble set (right panel). The results do not change significantly under reweighting to the physical strange mass.

They also broadly agree with an independent analysis of baryon masses from our ensembles by the LHP Collaboration [43] within 2 standard deviations.

V. COMBINED CONTINUUM AND CHIRAL FITS

We now turn to the main objective of this paper which is to use the results obtained on the 24^3 and 32^3 ensembles, as discussed in the previous two sections, to determine physical hadron and quark masses and mesonic decay constants in the continuum limit, for physical values of the light and strange-quark masses. Since we are reporting our first results obtained at a second lattice spacing, we present a careful discussion of our approach to taking the continuum limit and the relation between evaluating the continuum limit and determining the physical quark masses. We start in Sec. V A with a discussion of what we mean by a *scaling trajectory* scaling trajectory and explain in some detail the choice of scaling trajectory which we use in the following. In Sec. V B we describe our power-counting scheme, in which we treat the $O(a^2)$ terms in our two ensembles and the next-to-leading order (NLO) terms in SU(2) chiral perturbation theory as being of comparable size. In order to gain insights into the uncertainties associated with the chiral extrapolation, in addition to SU(2) chiral perturbation theory, we introduce an analytic ansatz which is a simple first-order Taylor expansion in the light-quark mass. This is explained in Sec. V C. We then discuss the specific fitting procedure which implements this power-counting strategy in Sec. V D and in Sec. V E we present and discuss the results.

A. Defining the scaling trajectory

Although ultimately we will combine the continuum and chiral extrapolations by performing *global fits* as described in Sec. V A 3 and in the following subsections, we start by focussing on the approach to the continuum limit and discussing the definition and choice of scaling trajectory. For the purposes of this subsection we imagine that we can perform lattice computations for any choice of quark masses and envision performing a series of lattice simulations for a range of values of β, the inverse square of the bare lattice coupling. As $\beta \to \infty$ the lattice spacing, measured in physical units, will vanish along with all discretization errors. We refer to such a one-dimensional path through the space of possible lattice theories as a scaling trajectory. For $2 + 1$ flavor QCD we must vary the bare lattice mass $m_{ud}(\beta)$ of the up and down quarks and $m_s(\beta)$ of the strange quark so that this trajectory describes physically equivalent theories up to order a^2 errors. The functions $m_{ud}(\beta)$ and $m_s(\beta)$ can be determined by requiring two mass ratios (or two other dimensionless quantities) to remain fixed as β varies. Because of the presence of $O(a^2)$ discretization errors, using a different pair of mass ratios will yield a different trajectory of lattice theories, whose low-momentum Green's functions will be equivalent to those of the first up to $O(a^2)$ corrections.

In Ref. [1], where we obtained results from simulations at a single value of β, we found that using the masses of the π and K mesons and the Ω baryon to determine the lattice spacing a and the bare values of m_{ud} and m_s was an effective procedure. A natural choice of scaling trajectory would therefore be to keep the ratios m_π/m_Ω and m_K/m_Ω fixed as β varies. Thus, these ratios would be chosen to take their continuum values for all β with no a^2 corrections. This choice of scaling trajectory then fixes the functions $m_{ud}(\beta)$ and $m_s(\beta)$. In addition, we will identify an inverse lattice spacing, expressed in GeV, with each point on this scaling trajectory. To do this we use the mass of the Ω^- baryon and define $1/a = 1.672/m_\Omega$ GeV where 1.672 GeV is the physical mass of this baryon and m_Ω is the mass of the Ω^- as measured along our trajectory in lattice units.

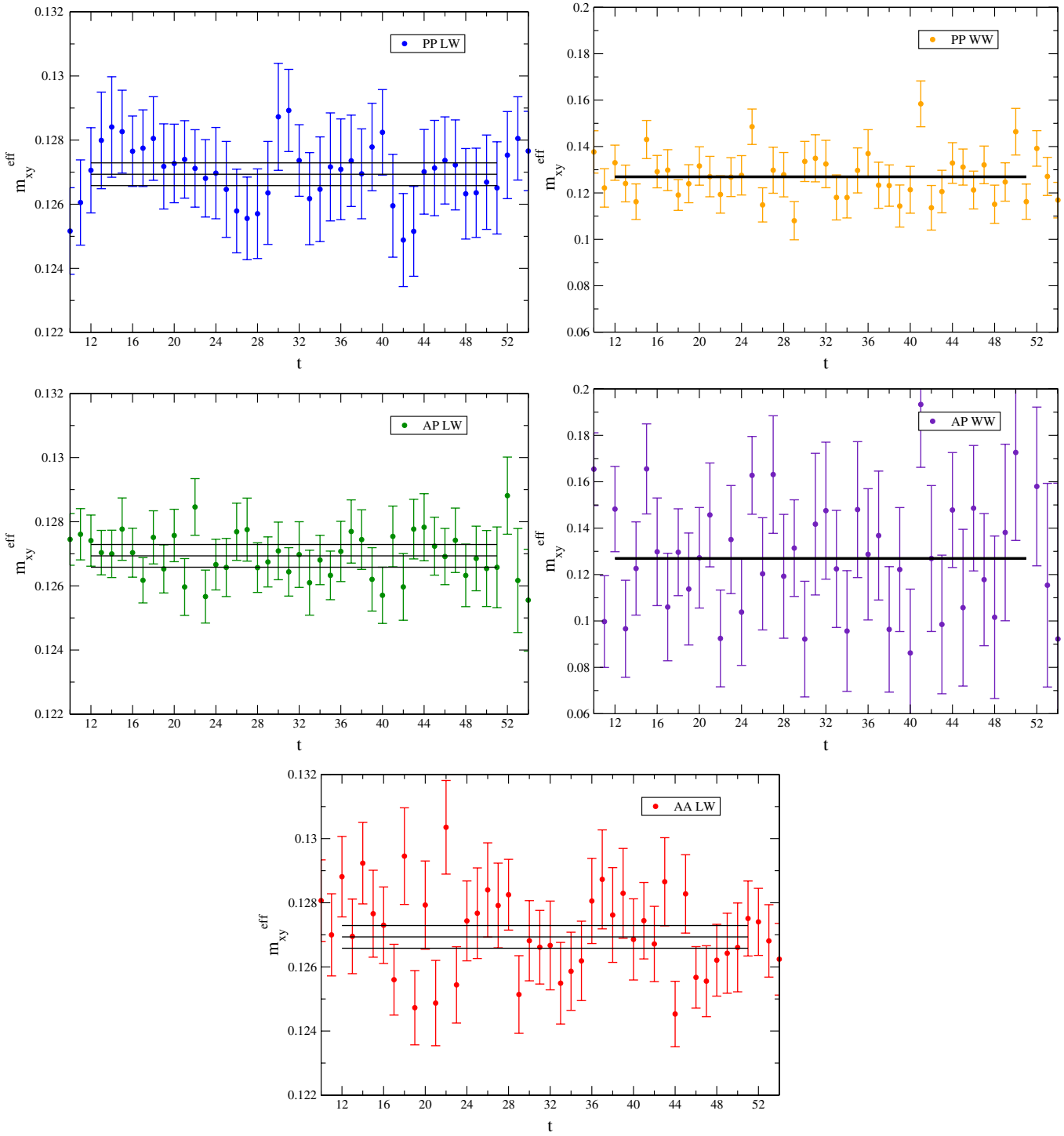

FIG. 19 (color online). Effective pion masses from the PP LW correlator (top-left), PP WW correlator (top-right), AP LW correlator (center-left), AP WW (center-right), and AA LW correlator (bottom). Note the different vertical scale for the WW correlators. The horizontal bands represent the result for the mass from a simultaneous fit.

Having defined the scaling trajectory and determined the lattice spacing at each β by fixing the ratios m_π/m_Ω, m_K/m_Ω, and the mass of the Ω baryon to their physical values, we are in a position to make predictions for other physical quantities. The results obtained at a particular value of β will differ from the physical ones by terms of $O(a^2)$. We imagine eliminating these artefacts by extrapolating results obtained at several values of β to the continuum limit. In order to discuss this continuum extrapolation it is convenient to introduce some notation.

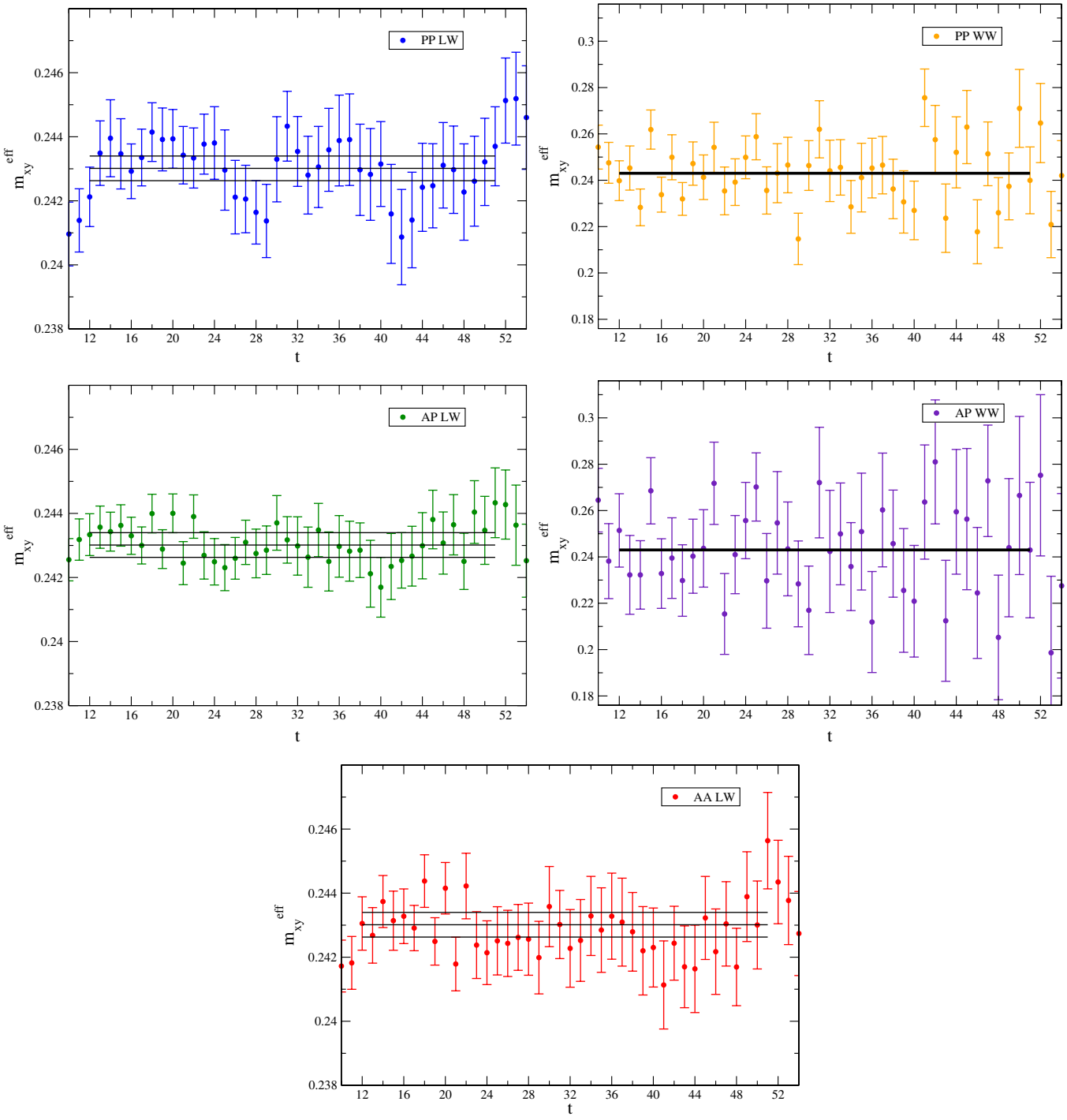

FIG. 20 (color online). Effective kaon masses from the PP LW correlator (top-left), PP WW correlator (top-right), AP LW correlator (center-left), AP WW (center-right), and AA LW correlator (bottom). Note the different vertical scale for the WW correlators. The horizontal bands represent the result for the mass from a simultaneous fit.

Let us assume that we have performed lattice calculations at a series of N values of β, $\{\beta^{\mathbf{e}}\}_{1\le\mathbf{e}\le N}$ corresponding to points along the scaling trajectory defined above (in the present study $N = 2$). This will determine a series of bare-quark masses $m_f^{\mathbf{e}} = m_f(\beta^{\mathbf{e}})$ where $f = ud$ or s. On each of the lattices we compute a number of physical quantities, e.g., the kaon leptonic decay constant $f_K^{\mathbf{e}}$, and our prediction for the physical value of f_K is the value obtained by extrapolating to the continuum limit.

Of course, as already mentioned above, the scaling trajectory and the assigned value of the lattice spacing at a particular β are not unique. Had we used three different

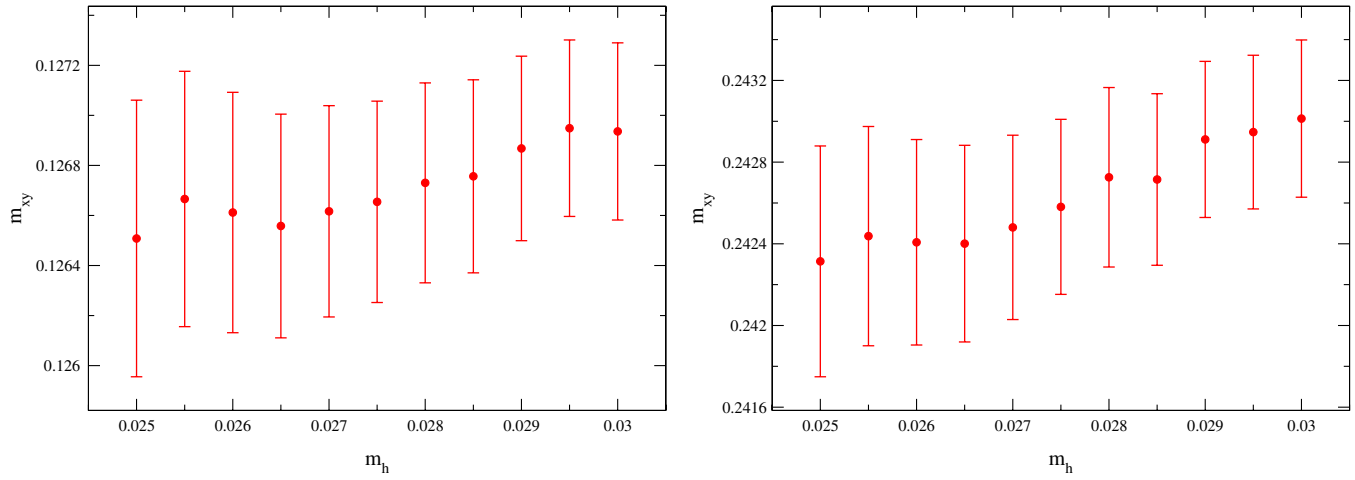

FIG. 21 (color online). We illustrate the m_h dependence of the unitary pion (left panel) and kaon (right panel) masses on the $m_l = 0.004$, 32^3 ensemble. The values are obtained by reweighting around the simulated value ($m_h = 0.03$).

physical quantities to calibrate the lattice at each β and then used the resulting bare-quark masses and lattice spacing to compute m_π/m_Ω, m_K/m_Ω, and the mass of the Ω baryon, we would find results which differed from the physical ones by terms of $O(a^2)$. Although there is a choice of the quantities used to define and determine the scaling trajectory and the value of the lattice spacing at each β, for a $2 + 1$ flavor theory the number of conditions is always $3N$, where N is the number of different β values used in the simulations and the factor 3 corresponds to the fact that at each β there are three parameters, the bare masses m_{ud} and m_s and the lattice spacing a.

In the above presentation we have tried to provide a pedagogical introduction to the determination of scaling trajectories and chose to decouple issues related to the extrapolations in the mass of the light quark (chiral extrapolations) from the discussion. Of course, in practice at present we are unable to perform simulations at physical quark masses, i.e., with masses which give the physical values of m_π/m_Ω and m_K/m_Ω, and so chiral extrapolations

TABLE XIX. Pseudoscalar masses $m_{xy}(m_l)$ and the decay constants $f_{xy}(m_l)$ on the 32^3 ensembles at the simulated strange-quark mass ($m_h = 0.03$) are shown.

m_x	m_y	$m_{xy}(0.004)$	$m_{xy}(0.006)$	$m_{xy}(0.008)$	$f_{xy}(0.004)$	$f_{xy}(0.006)$	$f_{xy}(0.008)$
0.03	0.03	0.3212(3)	0.3216(2)	0.3224(3)	0.0801(3)	0.0804(3)	0.0809(3)
0.025	0.03	0.3073(3)	0.3078(2)	0.3086(3)	0.0786(3)	0.0789(3)	0.0794(3)
0.008	0.03	0.2561(3)	0.2565(2)	0.2579(4)	0.0723(3)	0.0729(3)	0.0738(3)
0.006	0.03	0.2496(3)	0.2500(3)	0.2516(4)	0.0715(3)	0.0721(3)	0.0731(3)
0.004	0.03	0.2430(4)	0.2434(3)	0.2452(5)	0.0707(3)	0.0714(3)	0.0725(3)
0.002	0.03	0.2363(5)	0.2367(3)	0.2388(6)	0.0701(3)	0.0709(4)	0.0723(4)
0.025	0.025	0.2930(3)	0.2934(2)	0.2943(3)	0.0770(3)	0.0775(3)	0.0780(3)
0.008	0.025	0.2392(3)	0.2396(2)	0.2410(4)	0.0709(3)	0.0715(3)	0.0724(3)
0.006	0.025	0.2323(3)	0.2327(3)	0.2342(4)	0.0701(3)	0.0707(3)	0.0717(3)
0.004	0.025	0.2252(4)	0.2256(3)	0.2273(5)	0.0693(3)	0.0700(3)	0.0711(3)
0.002	0.025	0.2180(4)	0.2184(3)	0.2203(5)	0.0686(3)	0.0695(3)	0.0708(4)
0.008	0.008	0.1708(3)	0.1714(2)	0.1727(4)	0.0649(3)	0.0657(3)	0.0666(3)
0.006	0.008	0.1610(3)	0.1616(3)	0.1629(4)	0.0641(3)	0.0648(3)	0.0659(3)
0.004	0.008	0.1506(3)	0.1513(3)	0.1526(4)	0.0633(3)	0.0640(3)	0.0651(3)
0.002	0.008	0.1395(4)	0.1403(3)	0.1417(4)	0.0625(3)	0.0634(3)	0.0646(4)
0.006	0.006	0.1505(3)	0.1512(3)	0.1525(4)	0.0633(3)	0.0640(3)	0.0651(3)
0.004	0.006	0.1393(3)	0.1400(3)	0.1413(4)	0.0624(3)	0.0632(3)	0.0643(3)
0.002	0.006	0.1271(4)	0.1280(3)	0.1293(4)	0.0615(3)	0.0624(3)	0.0637(4)
0.004	0.004	0.1269(4)	0.1278(3)	0.1291(4)	0.0614(3)	0.0623(3)	0.0634(3)
0.002	0.004	0.1133(4)	0.1144(3)	0.1156(4)	0.0605(3)	0.0614(3)	0.0627(4)
0.002	0.002	0.0976(4)	0.0989(4)	0.1001(5)	0.0595(3)	0.0603(3)	0.0617(4)

TABLE XX. Pion masses $m_{xy}(m_l)$ and decay constants $f_{xy}(m_l)$ computed on the 32^3 ensembles at the physical strange-quark mass $m_h = 0.0273(7)$ are shown.

m_x	m_y	$m_{xy}(0.004)$	$m_{xy}(0.006)$	$m_{xy}(0.008)$	$f_{xy}(0.004)$	$f_{xy}(0.006)$	$f_{xy}(0.008)$
0.008	0.008	0.1706(3)	0.1711(3)	0.1725(5)	0.0645(3)	0.0653(3)	0.0662(4)
0.006	0.008	0.1608(4)	0.1613(3)	0.1628(5)	0.0636(3)	0.0645(4)	0.0654(4)
0.004	0.008	0.1503(4)	0.1510(3)	0.1526(5)	0.0628(4)	0.0636(4)	0.0647(4)
0.002	0.008	0.1392(4)	0.1401(3)	0.1417(5)	0.0620(4)	0.0630(4)	0.0641(4)
0.006	0.006	0.1503(4)	0.1509(3)	0.1524(5)	0.0628(4)	0.0636(4)	0.0646(4)
0.004	0.006	0.1390(4)	0.1398(3)	0.1414(5)	0.0619(4)	0.0628(4)	0.0638(4)
0.002	0.006	0.1268(4)	0.1278(3)	0.1295(5)	0.0611(4)	0.0620(4)	0.0632(4)
0.004	0.004	0.1267(4)	0.1276(3)	0.1292(5)	0.0609(4)	0.0618(4)	0.0630(4)
0.002	0.004	0.1131(4)	0.1142(4)	0.1158(5)	0.0601(4)	0.0610(4)	0.0622(4)
0.002	0.002	0.0974(4)	0.0988(4)	0.1003(5)	0.0590(4)	0.0598(4)	0.0612(5)

are necessary. It will therefore be useful in the following to discuss the scaling behavior of a general $2 + 1$ flavor theory in which the masses of the pion and kaon differ from those in nature. Following the conventions defined elsewhere in this paper, we will use m_l and m_h for the quark masses in the DWF lattice action which correspond to the usual ud and s quarks, and $\tilde{m}_l$ and $\tilde{m}_h$ for the corresponding multiplicatively renormalizable bare-quark masses $\tilde{m}_l = m_l + m_{\rm res}$ and $\tilde{m}_h = m_h + m_{\rm res}$ specific to the DWF action. In the next subsection we review the origin of the a^2 errors as described by the Symanzik effective theory for DWF and in the following subsection present our treatment of scaling for this more general theory.

1. Symanzik effective theory and $a^2 \to 0$ extrapolation

Symanzik's effective theory provides a powerful framework in which to discuss the approach to the continuum limit. For any finite value of β we expect the low-momentum Green's functions in our lattice theory to agree with those in a corresponding effective continuum theory. The effective action for this theory contains not only the usual dimension-3 and 4 terms standard in QCD but also higher-dimension operators. If the quark masses and the coefficients of these higher-dimension operators are properly chosen then the low-energy Green's functions of the lattice and effective theories will agree through $O(a^{d-4})$ provided the effective theory includes all necessary terms of dimension up to and including d. This implies that the low-energy Green's functions of the lattice theory and the usual continuum theory will differ by the matrix elements of these dimension-5 and higher operators which of course are not present in the standard continuum theory.

For the domain wall fermion calculation presented here the leading corrections come from operators of dimension 6. While the dimension-5 Pauli term $\bar{q}\sigma^{\mu\nu}F^{\mu\nu}q$ is present, its chiral properties imply that it is generated by chirality violation due to propagation between the left and right domain walls. This same residual breaking of chiral symmetry gives rise to the residual mass $m_{\rm res}$, the coefficient of the dimension-3 mass term which remains when

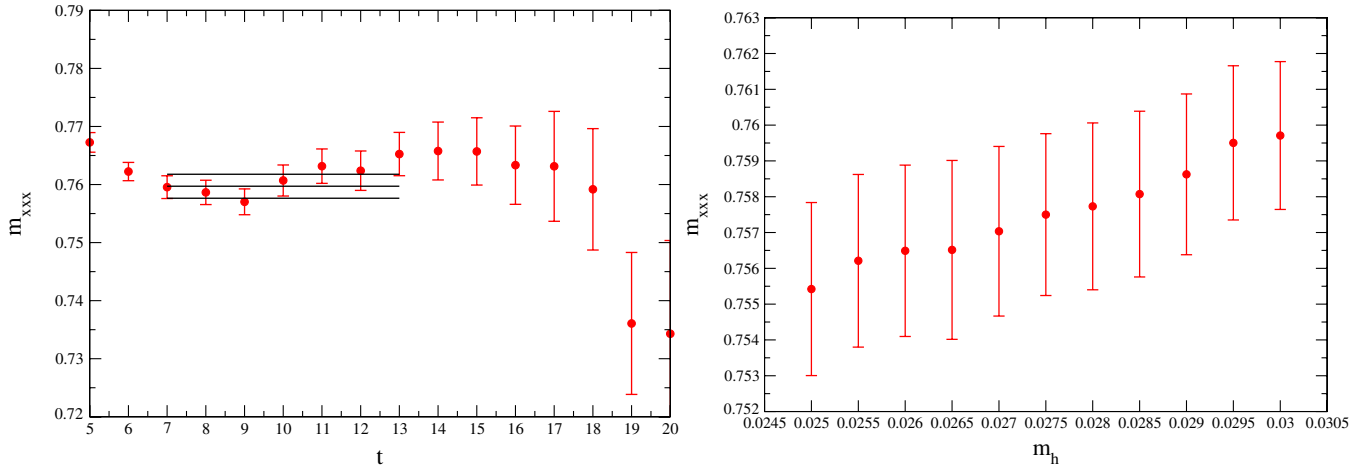

FIG. 22 (color online). We display the fit to the Ω baryon mass with valence strange mass $m_x = 0.03$ on the $m_l = 0.004$, $m_h = 0.03$, 32^3 ensemble showing the quality of the fit with our box source (left panel). We also show the weak dependence of the Ω baryon mass with fixed valence mass $m_x = 0.03$ on our simulated m_h inferred by the reweighting procedure on the $m_l = 0.004$, 32^3 ensemble (right panel).

TABLE XXI. Kaon masses $m_{xh}(m_l)$ and decay constants $f_{xy}(m_l)$ on the 32^3 ensembles at the physical strange-quark mass $m_h = 0.0273(7)$ are shown.

m_x	$m_{xh}(0.004)$	$m_{xh}(0.006)$	$m_{xh}(0.008)$	$f_{xh}(0.004)$	$f_{xh}(0.006)$	$f_{xh}(0.008)$
0.008	0.247(2)	0.247(3)	0.249(3)	0.0712(4)	0.0718(5)	0.0727(5)
0.006	0.240(2)	0.240(3)	0.242(3)	0.0703(4)	0.0710(5)	0.0720(5)
0.004	0.233(3)	0.234(3)	0.235(3)	0.0695(4)	0.0703(5)	0.0713(5)
0.002	0.226(3)	0.227(3)	0.229(3)	0.0687(5)	0.0698(5)	0.0710(6)

the input quark mass is set equal to zero. The largest value for $m_{\rm res}$ found in our current calculation, $m_{\rm res} = 0.003\,152(43)$, is suppressed from unity by more than 2 orders of magnitude. Since a similar suppression for this dimension 5 operator is expected, the combination of chiral symmetry and the small value of $a\Lambda_{\rm QCD} \sim 0.2$ suggest this term can be ignored and that the largest finite lattice-spacing errors that we should expect are $O(a^2)$.

We require that for our choice of scaling trajectory the matrix elements of these $O(a^2)$ Symanzik terms behave as a^2, allowing a linear extrapolation in a^2 to give the continuum limit. This implies that the coefficients of these operators remain reasonably constant along our trajectory. This is typically achieved by varying only β and quark masses along the trajectory so the only variation in the coefficients of these $O(a^2)$ terms comes from the variations in β which are quite small in present scaling studies [44].

2. Scaling and the quark masses

In the present calculation we obtain results using a number of light-quark masses, all of which are significantly larger than the physical quark masses that were used in the introductory remarks above to describe a physical scaling trajectory in which m_π/m_Ω, m_K/m_Ω, and m_Ω were fixed at their physical values. However, we can easily generalize our notion of a scaling trajectory to include families of choices for the parameters $(\beta, \tilde{m}_l, \tilde{m}_h)$ for which, in an obvious notation, the ratios m_{ll}/m_{hhh} and m_{lh}/m_{hhh} are held fixed. In the language used earlier, we require that the N triplets of parameters $(\beta^{\mathbf{e}}, \tilde{m}_l^{\mathbf{e}}, \tilde{m}_h^{\mathbf{e}})$, $1 \le \mathbf{e} \le N$, lie on the same scaling trajectory if

$$\frac{m_{ll}(\beta^{\mathbf{e}}, \tilde{m}_l^{\mathbf{e}}, \tilde{m}_h^{\mathbf{e}})}{m_{hhh}(\beta^{\mathbf{e}}, \tilde{m}_l^{\mathbf{e}}, \tilde{m}_h^{\mathbf{e}})} = \frac{m_{ll}(\beta^{\mathbf{e}'}, \tilde{m}_l^{\mathbf{e}'}, \tilde{m}_h^{\mathbf{e}'})}{m_{hhh}(\beta^{\mathbf{e}'}, \tilde{m}_l^{\mathbf{e}'}, \tilde{m}_h^{\mathbf{e}'})}, \tag{26}$$

$$\frac{m_{lh}(\beta^{\mathbf{e}}, \tilde{m}_l^{\mathbf{e}}, \tilde{m}_h^{\mathbf{e}})}{m_{hhh}(\beta^{\mathbf{e}}, \tilde{m}_l^{\mathbf{e}}, \tilde{m}_h^{\mathbf{e}})} = \frac{m_{lh}(\beta^{\mathbf{e}'}, \tilde{m}_l^{\mathbf{e}'}, \tilde{m}_h^{\mathbf{e}'})}{m_{hhh}(\beta^{\mathbf{e}'}, \tilde{m}_l^{\mathbf{e}'}, \tilde{m}_h^{\mathbf{e}'})}, \tag{27}$$

for each pair $\mathbf{e}$ and $\mathbf{e}'$. The ratio of lattice spacings for such a pair would be defined as

$$\frac{a^{\mathbf{e}}}{a^{\mathbf{e}'}} = \frac{m_{hhh}(\beta^{\mathbf{e}}, \tilde{m}_l^{\mathbf{e}}, \tilde{m}_h^{\mathbf{e}})}{m_{hhh}(\beta^{\mathbf{e}'}, \tilde{m}_l^{\mathbf{e}'}, \tilde{m}_h^{\mathbf{e}'})}. \tag{28}$$

The scaling trajectory determines two functions $\tilde{m}_l(\beta)$ and $\tilde{m}_h(\beta)$, where these bare masses are nontrivial functions of β. While a portion of their β dependence should reflect their naive mass dimension, these quantities also carry a logarithmic dependence on a characteristic of the anomalous dimension of the mass operator $\bar{q}q$ in QCD. Thus, even when expressed as dimensionless ratios, e.g., $\tilde{m}_l(\beta)/m_\Omega$ and $\tilde{m}_h(\beta)/m_\Omega$, these parameters will have singular continuum limits (in fact, the sign of the anomalous dimension of $\bar{q}q$ is such that these ratios vanish in the continuum-limit).

The mass parameters $\tilde{m}_l$ and $\tilde{m}_h$ are short-distance quantities whose definition is free of infrared singularities. For example, they could be specified by examining high-momentum, infrared safe Green's functions with no need to compute low-energy masses which are dependent upon the low-energy, nonperturbative behavior of QCD. While

TABLE XXII. Omega baryon masses on the 32^3 ensembles at the simulated strange-quark mass $m_h = 0.03$ (first two rows) and at the physical strange-quark mass (third row) are shown.

m_y	m_h	$m_\Omega(0.004)$	$m_\Omega(0.006)$	$m_\Omega(0.008)$
0.03	0.03	0.760(2)	0.765(2)	0.766(3)
0.025	0.03	0.733(2)	0.739(2)	0.740(3)
0.0273	0.0273	0.743(6)	0.749(5)	0.753(4)

TABLE XXIII. The quantities r_0, r_1, and r_1/r_0 at the simulated ($m_h = 0.03$) and physical ($m_h = 0.0273$) strange-quark masses on the 32^3 ensembles. $Q(m_l)$ denotes the quantity measured with light-quark mass m_l.

Quantity	$m_h = 0.03$			$m_h = 0.0273$		
	$Q(0.004)$	$Q(0.006)$	$Q(0.008)$	$Q(0.004)$	$Q(0.006)$	$Q(0.008)$
r_0	5.52(2)	5.50(2)	5.53(2)	5.52(2)	5.52(2)	5.55(2)
r_1	3.738(9)	3.718(8)	3.707(9)	3.754(12)	3.728(9)	3.723(10)
r_1/r_0	0.678(2)	0.676(2)	0.670(2)	0.680(2)	0.675(2)	0.670(2)

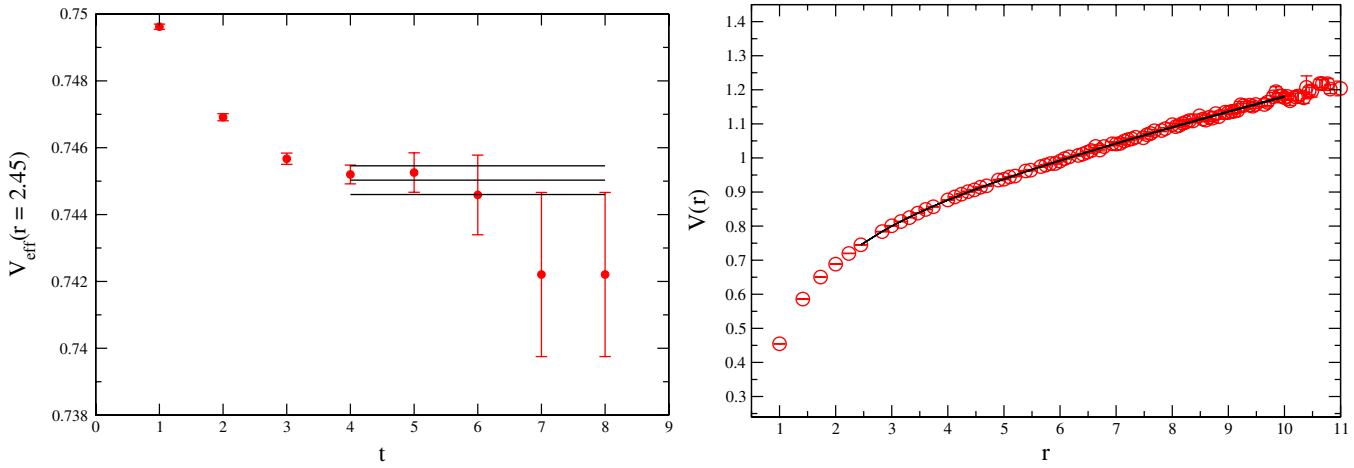

FIG. 23 (color online). The effective potential of the Wilson loops with a spatial extent of $r = 2.45$ on the $m_l = 0.004$ ensemble at the physical strange-quark mass, overlaid by the fit to the range $t = 4$–8 (left panel). The right panel shows the static interquark potential $V(r)$ on this ensemble, again at the physical strange-quark mass, as a function of the spatial extent of the Wilson loops, overlaid by the fit to the Cornell form over the range $r = 2.45$–10.

the individual masses $\tilde{m}_l(\beta)$ and $\tilde{m}_h(\beta)$ do not have a continuum limit, both the naive and anomalous scale dependence cancels in their ratio $\tilde{m}_l(\beta)/\tilde{m}_h(\beta)$, which is well defined in the continuum limit and agrees with the corresponding ratio in conventional renormalization schemes, such as the regularization independent momentum scheme (RI/MOM) [45] or $\overline{\text{MS}}$.

Let us now assume that we have performed lattice calculations at a series of N values of β, $\{\beta^{\mathbf{e}}\}_{1\le\mathbf{e}\le N}$, corresponding to points along the scaling trajectory defined above. This will determine a series of quark masses $\tilde{m}_f^{\mathbf{e}} = \tilde{m}_f(\beta^{\mathbf{e}})$ where $f = l$ or h. It is natural to introduce a series of factors which relate the lattice spacings and quark masses between these N ensembles. For convenience, we identify a primary ensemble **1**, and introduce $3(N-1)$ factors relating each ensemble **e** to the ensemble **1** as follows:

$$R_a^{\mathbf{e}} = \frac{a^{\mathbf{1}}}{a^{\mathbf{e}}} = \frac{m_{hhh}^{\mathbf{1}}}{m_{hhh}^{\mathbf{e}}}, \tag{29}$$

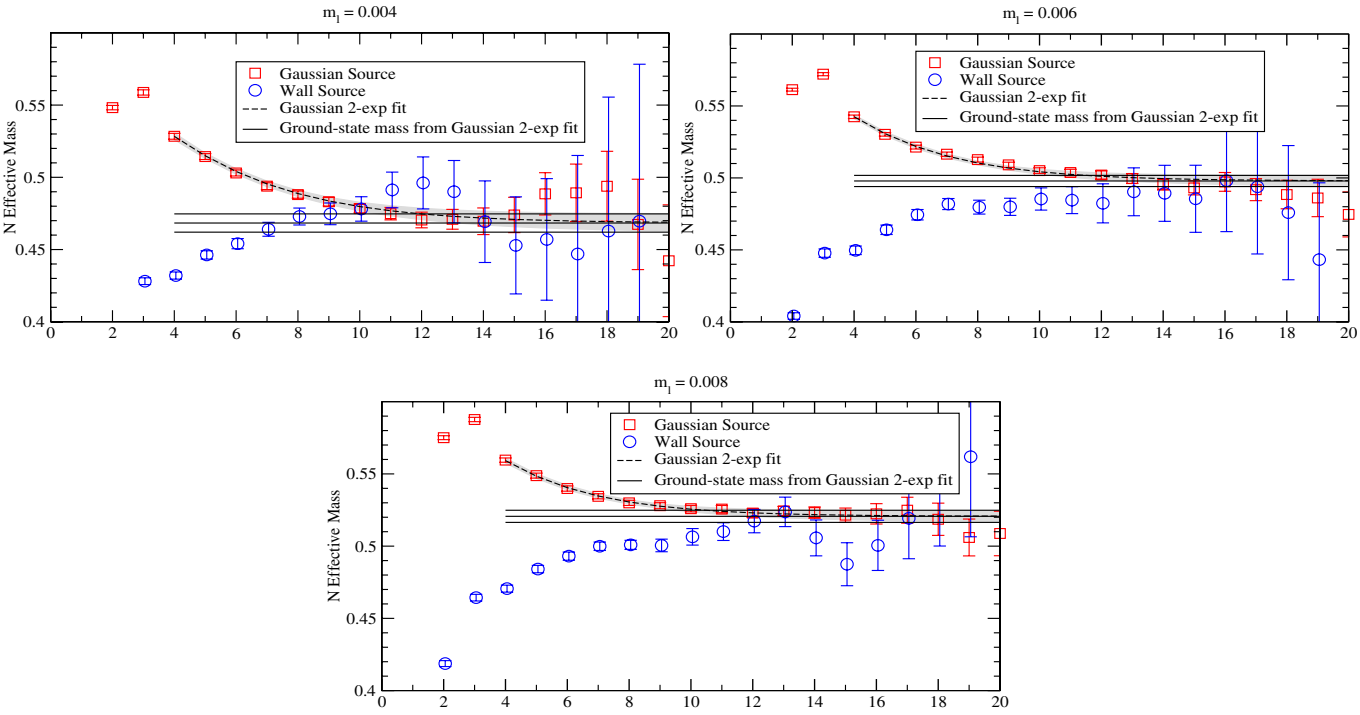

FIG. 24 (color online). Nucleon effective mass plots from the 32^3 ensembles are shown.

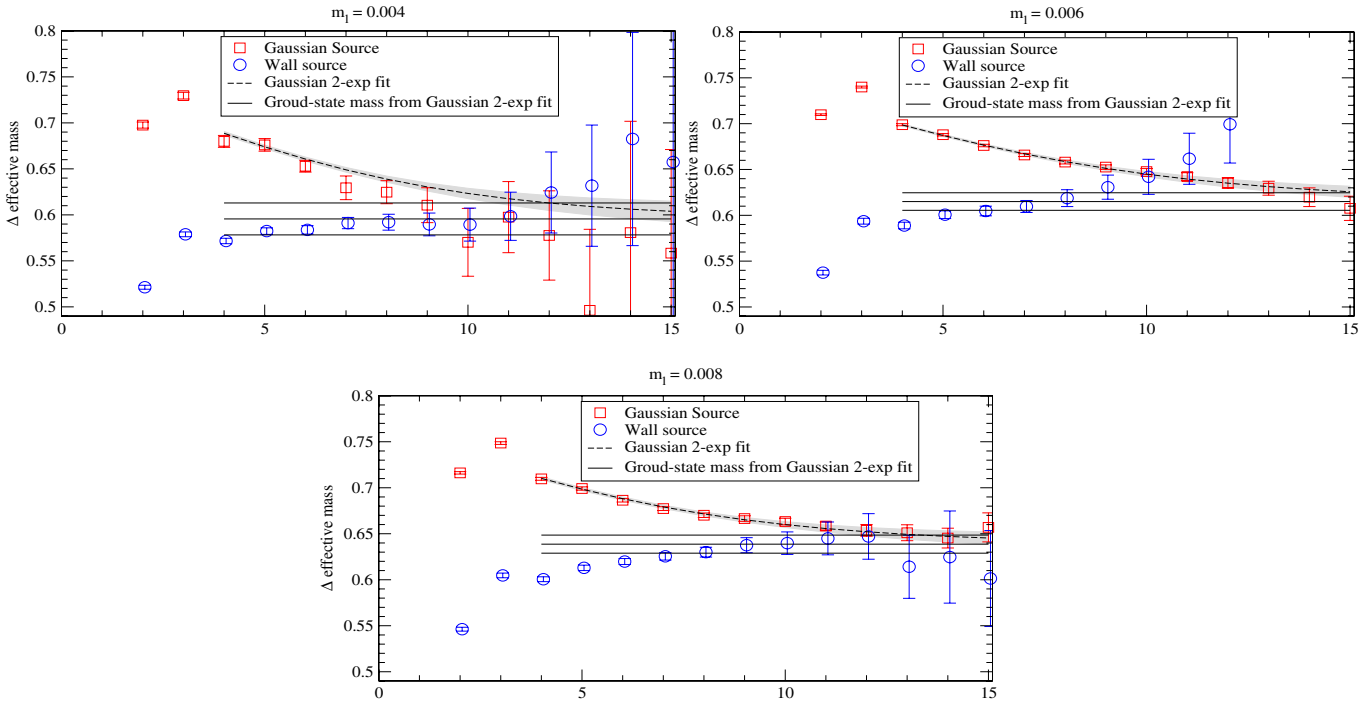

FIG. 25 (color online). Δ effective mass plots from the 32^3 ensembles are shown.

$$Z_f^{\mathbf{e}} = \frac{1}{R_a^{\mathbf{e}}} \frac{\tilde{m}_f^{\mathbf{1}}}{\tilde{m}_f^{\mathbf{e}}} \quad \text{for } f = l \quad \text{or} \quad h. \tag{30}$$

Since the ratio $\tilde{m}_l/\tilde{m}_h$ is well defined in the continuum limit, the corresponding ratio for each of these ensembles $\tilde{m}_l^{\mathbf{e}}/\tilde{m}_h^{\mathbf{e}}$ differs from that limit by a term proportional to $(a^{\mathbf{e}})^2$. This $O(a^2)$ correction represents the discrepancy between our choice of scaling trajectory with m_{ll}/m_{lh} fixed as we vary β and an alternative choice where instead $\tilde{m}_l^{\mathbf{e}}/\tilde{m}_h^{\mathbf{e}}$ is held fixed. Since these trajectories differ at $O(a^2)$, we expect that

$$\frac{\tilde{m}_l^{\mathbf{e}}}{\tilde{m}_h^{\mathbf{e}}} = \lim_{\beta\to\infty}\left(\frac{\tilde{m}_l(\beta)}{\tilde{m}_h(\beta)}\right)(1 + c_m(\Lambda_{\mathrm{QCD}} a^{\mathbf{e}})^2). \tag{31}$$

The term proportional to c_m arises from the shifts in m_{ll}^2 and m_{lh}^2 caused by the first-order effects of dimension-6 terms in the Symanzik effective action. While c_m must vanish as $\tilde{m}_l^{\mathbf{e}} \to \tilde{m}_h^{\mathbf{e}}$, we prefer not to write c_m as proportional to the difference $\tilde{m}_l^{\mathbf{e}} - \tilde{m}_h^{\mathbf{e}}$ because of possible nonanalytic terms in the quark masses (e.g. possible logarithms of $m_l^{\mathbf{e}}$) that may appear in the low-energy matrix elements of these dimension-6 operators. If we divide Eq. (31) evaluated for our primary ensemble **1** by the same equation applied to the ensemble **e** and Taylor expand in the lattice spacing, we obtain the following useful relation between $Z_h^{\mathbf{e}}$ and $Z_l^{\mathbf{e}}$:

$$Z_h^{\mathbf{e}} = Z_l^{\mathbf{e}}(1 + c_m \Lambda_{\mathrm{QCD}}^2[(a^{\mathbf{e}})^2 - (a^{\mathbf{1}})^2]), \tag{32}$$

implying the $2(N-1)$ Z factors associated with the quark masses actually depend on N quantities through order a^2 (e.g. we can take the $(N-1)$ $Z_l^{\mathbf{e}}$ and c_m as the independent quantities). The constraints implied by Eq. (32) do not simplify the $N = 2$ case addressed in the present paper where we would simply be trading the two parameters $Z_h^{\mathbf{2}}$ and $Z_l^{\mathbf{2}}$ for the alternative pair of parameters $Z_l^{\mathbf{2}}$ and c_m.

Equation (32) provides an explicit estimate of how scaling violations revise the standard expectation that all quark masses will scale with a common Z factor as the cutoff is varied. As we will see from our simulation results presented below, the terms proportional to c_m are small and difficult to resolve from zero given our statistical errors.

TABLE XXIV. Nucleon and Δ masses in lattice units from the 32^3 ensembles obtained by two-exponential correlated fits to Gaussian-source correlators. {} denotes the fit range.

m_l	N		Δ	
0.004	0.468(6)	{4–20}	0.596(15)	{4–15}
0.006	0.498(4)	{4–20}	0.615(9)	{4–15}
0.008	0.521(4)	{4–20}	0.639(10)	{4–15}

TABLE XXV. A comparison of nucleon mass results from different analyses on the same 32^3 ensembles is shown.

m_l	Fully correlated	Uncorrelated	Bootstrap[a]	LHP[b]
0.004	0.477(4)	0.465(5)	0.469(4)	0.474(4)
0.006	0.498(2)	0.486(10)	0.489(7)	0.501(2)
0.008	0.517(3)	0.524(4)	0.5254(16)	0.522(2)

[a]Denotes Ref. [42], where a frozen correlation matrix was used.
[b]Denotes Ref. [43].

Since we are now using formulas in which the lattice spacing $a^{\mathbf{e}}$ appears alone rather than in a ratio, e.g., as $a^{\mathbf{e}}/a^{\mathbf{e}'}$, it may be useful to explain how we intend this to be determined. It is natural to start by considering the physical scaling trajectory discussed in Sec. VA on which $m_{ll}/m_{hhh} = m_\pi/m_\Omega$ and $m_{lh}/m_{hhh} = m_K/m_\Omega$. For this physical trajectory, the actual value of the Omega mass measured in GeV can be used to define the lattice spacing for any point $\beta^{\mathbf{e}}$ on that trajectory using $a^{\mathbf{e}} = m^{\mathbf{e}}_{hhh}/(1.672\,45(0.29)\ \text{GeV})$. In our present study, in order to reach the physical trajectory a chiral extrapolation must be performed from the quark masses used in our simulation. Ultimately of course, when we present results for dimensionful quantities in physical units, it will be necessary to perform the chiral extrapolation and this is the subject of the following subsections. For the present discussion of scaling it is sufficient simply to imagine that the lattice spacing has been determined in this way and this is the most straightforward way of interpreting the $O((a^{\mathbf{e}})^2)$ terms appearing in equations in this subsection. We stress however, that even this is not strictly necessary. We can consider a scaling trajectory defined by fixed, but unphysical, values of m_{ll}/m_{hhh} and m_{lh}/m_{hhh} and define the lattice spacing by assigning an arbitrary value to M_{hhh}, the mass of the hhh baryon on the trajectory in "physical" units, $a^{\mathbf{e}} \equiv m^{\mathbf{e}}_{hhh}/M_{hhh}$. While the value of $a^{\mathbf{e}}$ defined in this way depends, of course, on the choice of M_{hhh}, this arbitrariness is simply absorbed by a change in constants such as c_m in (31). For the discussion in this subsection it is sufficient to note that such a definition of the lattice spacing is possible in principle, the numerical determination of $a^{\mathbf{e}}$ does not actually have to be performed.

In the analysis to follow we will examine a family of nearby scaling trajectories in which $\tilde{m}_l$ and $\tilde{m}_h$ vary over limited ranges (specifically, $\tilde{m}_l$ varies up to about 0.013 on our coarser lattice and $\tilde{m}_h$ varies by up to 20% around $\tilde{m}_s$). Consider two such trajectories, defined by keeping the ratios m_{ll}/m_{hhh} and m_{lh}/m_{hhh} fixed along each trajectory, but taking different values on the two trajectories. Let $m_{ll}/m_{hhh} = r_{ll}$ and $m_{lh}/m_{hhh} = r_{lh}$ on the first trajectory and $m_{ll}/m_{hhh} = r'_{ll}$ and $m_{lh}/m_{hhh} = r'_{lh}$ on the second. As $\beta \to \infty$, the ratio of bare-quark masses on the two trajectories will approach a limit up to $O(a^2)$ corrections:

$$\frac{\tilde{m}^{\mathbf{e}}_f(r_{ll}, r_{lh})}{\tilde{m}^{\mathbf{e}}_f(r'_{ll}, r'_{lh})} = \lim_{\beta\to\infty}\left(\frac{\tilde{m}_f(\beta)}{\tilde{m}'_f(\beta)}\right)(1 + d_{m,f}(\Lambda_{\text{QCD}}a^{\mathbf{e}})^2), \quad (33)$$

where $f = l$ or h, and $\tilde{m}^{\mathbf{e}}_l(r_{ll}, r_{lh})$ and $\tilde{m}^{\mathbf{e}}_h(r_{ll}, r_{lh})$ [$\tilde{m}^{\mathbf{e}}_l(r'_{ll}, r'_{lh})$ and $\tilde{m}^{\mathbf{e}}_h(r'_{ll}, r'_{lh})$] are the values of the bare-quark masses on ensemble $\mathbf{e}$ such that $m_{ll}/m_{hhh} = r_{ll}$ and $m_{lh}/m_{hhh} = r_{lh}$ [$m_{ll}/m_{hhh} = r'_{ll}$ and $m_{lh}/m_{hhh} = r'_{lh}$]. The ratios $R_a = m^{\mathbf{1}}_{hhh}(\tilde{m}^{\mathbf{1}}_l(r_{ll}, r_{lh}), \tilde{m}^{\mathbf{1}}_h(r_{ll}, r_{lh}))/m^{\mathbf{e}}_{hhh}(\tilde{m}^{\mathbf{e}}_l(r_{ll}, r_{lh}), \tilde{m}^{\mathbf{e}}_h(r_{ll}, r_{lh}))$ and $R'_a = m^{\mathbf{1}}_{hhh}(\tilde{m}^{\mathbf{1}}_l(r'_{ll}, r'_{lh}), \tilde{m}^{\mathbf{1}}_h(r'_{ll}, r'_{lh}))/m^{\mathbf{e}}_{hhh}(\tilde{m}^{\mathbf{e}}_l(r'_{ll}, r'_{lh}), \tilde{m}^{\mathbf{e}}_h(r'_{ll}, r'_{lh}))$ each describe the change in lattice scale as the bare coupling changes from $\beta^{\mathbf{1}}$ to $\beta^{\mathbf{e}}$. In the limit of small bare coupling, this change of scale can be determined entirely from the short-distance part of the theory and must be the same for our two trajectories up to order a^2 corrections since these two trajectories differ only in the choice of quark masses. Thus, we can write

$$\frac{R_a}{R'_a} = 1 + d_a\Lambda^2_{\text{QCD}}((a^{\mathbf{e}})^2 - (a^{\mathbf{1}})^2), \quad (34)$$

where we have explicitly represented the fact that each ratio and hence the ratio of ratios must approach unity as $a^{\mathbf{e}} \to a^{\mathbf{1}}$. Both the coefficients $d_{m,f}$ and d_a will vanish when the primed and unprimed trajectories that are being compared become identical.

Taking the ratio of two versions of Eq. (33), one for $\beta^{\mathbf{e}}$ and the other for our primary ensemble $\beta^{\mathbf{1}}$ and using Eq. (34), we obtain an expression for the change in the factors Z_f between these two trajectories:

$$\frac{Z^{\mathbf{e}}_f}{Z^{\mathbf{e}\prime}_f} = (1 + (d_{m,f} + d_a)\Lambda^2_{\text{QCD}}[(a^{\mathbf{1}})^2 - (a^{\mathbf{e}})^2]). \quad (35)$$

Since the changes in $\tilde{m}_l$ and $\tilde{m}_h$ between these two trajectories which we wish to compare are small, the resulting coefficients $d_{m,f}$ and d_a will also be small and we will neglect the $O(a^2)$ correction on the right-hand side of Eq. (35). Thus, we will use the same values for Z_l and Z_h for this family of nearby trajectories, i.e., we drop lattice artefacts proportional to $\tilde{m}_l$ and $(\tilde{m}_h - \tilde{m}_s)$ and so neglect the mass dependence of Z_l and Z_h in this limited range of masses. In the following we will refer to this range for $\tilde{m}_l$ and $\tilde{m}_h$ as their "allowed range."

3. Fitting strategies

We exploit the above relations between numerical results obtained at the two values of β for which we have performed simulations in two ways. The first we label the "fixed-trajectory" method. In this approach we determine R_a, Z_l, and Z_h by matching results obtained at a single pair of equivalent quark masses [46]. For example, the masses used at one value of β may correspond to values at which a simulation was actually performed. The corresponding set of masses for the other β might be determined by linear interpolation to make the two ratios m_{ll}/m_{hhh} and m_{lh}/m_{hhh} agree with those on the first ensemble. The ratio of lattice spacings and the two Z_f factors are then determined from Eqs. (29) and (30). It will be important to recall that Z_l and Z_h are constant in the allowed range of quark masses. Finally, knowing the three factors R_a, Z_l, and Z_h we make a common fit to the mass dependence of physical quantities computed for both values of β.

In the final step, we adopt an ansatz for the mass dependence that is expected to be accurate both for the points in our calculation and for the physical values to which we wish to extrapolate, specifically a NLO chiral expansion about the chiral limit or a simple Taylor expansion about

the physical point. Each ansatz for the continuum theory, when combined with the three scaling factors R_a, Z_l, and Z_h and with any required a^2 corrections, will then provide a set of formulas which should describe all of our data for both β values. For example, in the chiral fits described in the next section we can use a common set of LECs to fit both sets of data provided we scale the values used on one set by the required factors of R_a, Z_l, and Z_h before we use them on the other. Where explicit $O(a^2)$ terms are required, these can be added with unknown coefficients which are also scaled appropriately between our two values of β. In such a combined chiral and a^2 expansion we adopt a power-counting scheme, described below, so that only effects of a similar minimum size are consistently included.

During the initial process of determining R_a, Z_l, and Z_h we cannot assign a physical value to the lattice spacing. The original trajectory being used does not correspond to physical masses so no notion of "GeV" exists for that case. Of course, the further fitting to the quark mass dependence of the two ensembles is introduced to allow extrapolation to physical values for the ratios m_{ll}/m_{hhh} and m_{lh}/m_{hhh}. When m_Ω is evaluated at this same physical point, its value can be compared with 1.672 GeV to determine the lattice scale.

This fixed-trajectory method is intended to cover a wider range of possible scaling trajectories than the example discussed above where the trajectory passes precisely through one of the simulation points. If we wish, we can adopt an ansatz for the quark mass dependence of m_π, m_K, and m_Ω and perform this fixed-trajectory scaling with the parameters R_a, Z_l, and Z_h allowed to vary and fix their values from Eqs. (29) and (30) at values of m_l and m_h for which the ratios m_{ll}/m_{hhh} and m_{lh}/m_{hhh} take their physical values.

The second approach, termed "generic scaling," introduces the factors R_a, Z_l and Z_h as parameters into the ansatz being used to fit the quark mass dependence. In this approach we perform a fit to all our data for m_π, m_K, and m_Ω over a range of quark masses for which the fitting ansatz is accurate and for which the use of fixed values for R_a, Z_l, and Z_h is legitimate. In this generic scaling approach, our choice of scaling trajectory with fixed hadron mass ratios m_{ll}/m_{hhh} and m_{lh}/m_{hhh} and with m_{hhh} determining the lattice scale is realized somewhat indirectly. The three conditions associated with this choice of scaling trajectory are realized by omitting possible a^2 corrections from the expressions used to fit m_{ll}, m_{lh}, and m_{hhh}. The resulting trajectory can therefore be interpreted as being the one along which the masses of the pion, kaon, and Ω baryon take their physical values, as was the case in the discussion of Sec. V A. The difference of course, is that whereas in Sec. V A we envisaged (unrealistically at present) being able to simulate directly at the physical value of m_l, we now reach the physical point after an extrapolation in quark masses. The detailed discussion of the ChPT functions used in describing the quark mass dependence of the pion and kaon masses is given in Sec. V B and those for the analytic ansatz in Sec. V C below. However, both our ChPT and Taylor expansion ansätze stipulate that to the order being studied m_{hhh} is a linear function of $\tilde{m}_l$ and $\tilde{m}_h$. It is instructive to explore this case here.

Included among the equations used to determine the low-energy constants and the scaling factors R_a, Z_l, and Z_h are two equations for m_{hhh} on our two ensembles:

$$m^{\mathbf{1}}_{hhh}(\tilde{m}_l, \tilde{m}_h) = m^{\mathbf{1}}_{hhh}(0, \tilde{m}_{h0}) + c^{\mathbf{1}}_{m_\Omega m_l}\tilde{m}_l + c^{\mathbf{1}}_{m_\Omega m_h}(\tilde{m}_h - \tilde{m}_{h0}), \tag{36}$$

$$\begin{aligned} m^{\mathbf{2}}_{hhh}(\tilde{m}_l, \tilde{m}_h) &= \frac{1}{R_a} m^{\mathbf{1}}_{hhh}(R_a Z_l \tilde{m}_l, R_a Z_h \tilde{m}_h) \\ &= \frac{1}{R_a}[m^{\mathbf{1}}_{hhh}(0, \tilde{m}_{h0}) + c^{\mathbf{1}}_{m_\Omega m_l} R_a Z_l \tilde{m}_l \\ &\quad + c^{\mathbf{1}}_{m_\Omega m_h}(R_a Z_h \tilde{m}_h - \tilde{m}_{h0})]. \end{aligned} \tag{37}$$

Here **1** is our primary ensemble, for us that is the one with $\beta = 2.25$ and the $32^3 \times 64$ volume, while the second ensemble is the one with the coarser lattice spacing and is labeled **2**. $m^{\mathbf{e}}_{hhh}(\tilde{m}_l, \tilde{m}_h)$ are the hhh-baryon masses corresponding to bare-quark masses $\tilde{m}_l$ and $\tilde{m}_h$ on ensemble **e**. Although we have written $\tilde{m}_{h0}$ as a general constant, we have in mind to use the equations with $\tilde{m}_{h0}$ in the allowed range of the physical bare strange-quark mass in the primary ensemble. Equations (36) and (37) define the three constants $m^{\mathbf{1}}_{hhh}(0, \tilde{m}_{h0})$, $c^{\mathbf{1}}_{m_\Omega m_l}$, and $c^{\mathbf{1}}_{m_\Omega m_h}$ which are related to the physical Ω^- mass and its physical dependence on the quark masses. The absence of $O(a^2)$ corrections to Eqs. (36) and (37) implements our choice that m_Ω is being used to set the scale and hence by construction contains no finite lattice-spacing errors. While part of a larger set of equations which are being used to determine the low-energy constants as well as R_a, Z_l and Z_h, the leading-order effect of these two equations is to determine R_a. Note that this is identical to imposing Eq. (29) in the fixed-trajectory method at the point $\tilde{m}_l = 0$, $\tilde{m}_h = \tilde{m}_{h0}$. Since the variation of R_a as $\tilde{m}_l$ and $\tilde{m}_h$ change over their allowed range is of the same size as the variation of Z_l and Z_h over this same range it can also be neglected, so any particular choice of $\tilde{m}_h$ is equivalent to any other within this allowed range.

The fixed trajectory and generic scaling methods are similar in nature. Both require that an ansatz be adopted to allow the quark mass dependence of lattice quantities to be described in order to define the scaling parameters R_a, Z_l, and Z_h and to extrapolate to the physical point. Both assume that the scaling relations between the two ensembles defined by R_a, Z_l, and Z_h hold over the allowed range of masses. The fixed-trajectory method corresponds most closely to our original definition of a scaling trajectory and

decouples the matching of the two lattices from the chiral extrapolation. It requires however, the introduction of a convenient but arbitrary point at which the matching between the two ensembles is performed. The generic method avoids this arbitrary choice and applies these assumptions uniformly over the entire range of allowed masses. The fixed-trajectory method determines R_a, Z_l, and Z_h in an iterative fashion as explained in Sec. V D. The generic approach determines the coefficients in the adopted ansatz from a single χ^2 minimization. The physical quark masses are then determined by inverting the resulting equations which give m_π, m_K, and m_Ω in terms of $\tilde{m}_l$ and $\tilde{m}_h$.

The detailed discussion and results presented in this paper correspond to the fixed-trajectory method; fits using the generic scaling approach were performed to monitor the consistency of the results and estimated errors.

B. Scaling and chiral perturbation theory

At the start of Sec. V A we discussed the continuum extrapolation in an idealized situation in which we can perform simulations at any value of the quark mass m_l. In reality this is not the case; for example, the lightest unitary pion appearing in the current study has mass 290 MeV. In order to compare our results with nature we therefore need to extrapolate to lighter quark masses and this was already acknowledged when discussing the fitting strategies in Sec. V A 3 above. We now explain how we combine the continuum and chiral extrapolations in global fits. We start in this section by using SU(2) chiral perturbation theory for the mass dependence, with the expectation that the extrapolation will be made more precise if constrained by the theoretically known behavior of QCD in the chiral limit [1]. However, in order to estimate possible systematic errors associated with this extrapolation and to obtain a more complete understanding of the implications of our calculation, we also examine a simpler analytic extrapolation to physical quark masses [47] and this is explained in the following subsection. Although later we will perform extrapolations using partially quenched ensembles, for the purposes of this introduction we restrict the discussion to the unitary theory in which the valence and sea-quark masses are equal.

We now explain the power-counting scheme we employ to identify NLO corrections to the chiral and continuum limits. Since the pion mass and decay constant are central to SU(2) ChPT, we begin by considering the predictions of continuum NLO ChPT for these two quantities:

$$m_{ll}^2 = \chi_l + \chi_l \cdot \left\{ \frac{16}{f^2}((2L_8^{(2)} - L_5^{(2)}) + 2(2L_6^{(2)} - L_4^{(2)}))\chi_l + \frac{1}{16\pi^2 f^2}\chi_l \log\frac{\chi_l}{\Lambda_\chi^2} \right\}, \quad (38)$$

$$f_{ll} = f + f \cdot \left\{ \frac{8}{f^2}(2L_4^{(2)} + L_5^{(2)})\chi_l - \frac{\chi_l}{8\pi^2 f^2}\log\frac{\chi_l}{\Lambda_\chi^2} \right\}. \quad (39)$$

Here m_{ll} and f_{ll} are the mass and decay constant of the pseudoscalar meson composed of two light quarks, f, L_4, L_5, L_6, and L_8 are the conventional low-energy constants and Λ_χ is the usual chiral scale. The quantity χ_l comes directly from the lowest order chiral symmetry breaking term in the effective chiral theory and is proportional to the QCD light-quark mass. It is conventionally written $\chi_l = 2B\tilde{m}_l$, where B is another low-energy constant.

We now discuss how we apply these formulas to describe the low-energy behavior of lattice theories which lie on a scaling trajectory. For a sequence of ensembles $\{\mathbf{e}\}_{1\le\mathbf{e}\le N}$ lying on such a scaling trajectory not only will the quark masses and lattice units, $(\tilde{m}_l^{\mathbf{e}}, \tilde{m}_h^{\mathbf{e}}, a^{\mathbf{e}})$ be related, but also, when expressed in physical units, the quantities f, L_4, L_5, L_6, and L_8 should take the same values up to $O(a^2)$ corrections. The same is true for the renormalization independent combination $\chi_l = 2B\tilde{m}_l$ (see the discussion below). As detailed in Ref. [1], chiral perturbation theory at finite lattice spacing for domain wall fermions involves a simultaneous expansion in the explicit bare quark mass, m_l, the squared lattice spacing, a^2, and the residual chiral symmetry breaking arising from the finite separation, L_s, between the two four-dimensional walls in the fifth dimension. We will denote this last quantity by $e^{-\lambda L_s}$, suggesting the exponential decrease in such residual chiral symmetry breaking found in perturbation theory for DWF. (The actual behavior is a sum of exponential and inverse power dependence on L_s.) No new terms need to be added to the resulting effective low-energy theory to describe the resulting Green's functions to NLO in the parameters $\tilde{m}_l$, a^2, and $e^{-\lambda L_s}$. Thus, we can use equations with the form of Eqs. (38) and (39) to describe the lattice results for m_{ll} and f_{ll} along a scaling trajectory, provided we work to NLO in a power-counting scheme which treats the quantities $\chi_l/(4\pi f)^2$, $a^2\Lambda_{\mathrm{QCD}}^2$, and $e^{-\lambda L_s}$ as equivalent and keep a single power of any of these quantities as a correction. We must now determine how the parameters appearing in these equations must be adjusted to describe lattice results at finite a^2.

Since the scale Λ_χ can be freely varied if the other analytic terms are appropriately changed, we will choose this quantity to be constant if measured in physical units. Thus, for each point on our physical scaling trajectory we will choose $\Lambda_\chi = m_\Omega \cdot 1/1.672$, giving it the value of 1 GeV. Because of their proportionality to the NLO factor χ_l all of the parameters which appear in the large curly brackets on the right-hand side of Eqs. (38) and (39) can be given their continuum values, dropping possible $O(a^2)$ terms as being of next-to-next-to-leading order (NNLO) in our power-counting scheme. Thus, within those brackets the quantities f, L_4, L_5, L_6 and L_8, when expressed in

physical units, can be given identical values for the ensembles on the scaling trajectory.

In contrast, when Eq. (39) is used to describe our finite lattice-spacing results, the LO quantity $f^{\mathbf{e}}$ determined on ensemble $\mathbf{e}$, expressed in physical units, depends on $\beta^{\mathbf{e}}$. However, it approaches its continuum limit with $O(a^2)$ corrections and so we write $f^{\mathbf{e}} = f + c_f(a^{\mathbf{e}})^2$.

Given the definition of a scaling trajectory, the variation of the quantity $\chi_l^{\mathbf{e}}$ needed to apply Eq. (38) to the ensemble $\mathbf{e}$ is actually trivial. Because our choice of quark mass $\tilde{m}_l^{\mathbf{e}}$ gives the same value for m_{ll} for each ensemble $\mathbf{e}$ on our scaling trajectory, all of the quantities in Eq. (38) with the possible exception of the $\chi_l^{\mathbf{e}}$ which we are now considering, are the same when expressed in physical units for all points on the scaling trajectory. Thus, $\chi_l^{\mathbf{e}} = 2B^{\mathbf{e}}\tilde{m}_l^{\mathbf{e}}/(a^{\mathbf{e}})^2$ must be a constant as well, where $B^{\mathbf{e}}$ and $\tilde{m}_l^{\mathbf{e}}$ are explicitly left in lattice units. Since we know how the quantities $\tilde{m}_l$ and a^2 are related between an ensemble $\mathbf{e}$ and our primary ensemble $\mathbf{1}$, we can determine the $N-1$ constants $B^{\mathbf{e}}$ in terms of the single constant $B^{\mathbf{1}}$:

$$B^{\mathbf{e}} = \frac{Z_l^{\mathbf{e}}}{R_a^{\mathbf{e}}} B^{\mathbf{1}}, \tag{40}$$

without any a^2 corrections. Because of the complex scaling behavior of the mass, we will treat $B^{\mathbf{1}}$ as one of the LECs to be determined in our fitting and not relate it to a physical continuum quantity whose definition would require introducing a continuum mass renormalization scheme.

We conclude that our lattice results for light pseudoscalar masses and decay constants obtained from a series of ensembles $\{\mathbf{e}\}$ can be described through NLO by the formulas:

$$(m_{ll}^{\mathbf{e}})^2 = \chi_l^{\mathbf{e}} + \chi_l^{\mathbf{e}} \cdot \left\{ \frac{16}{f^2}((2L_8^{(2)} - L_5^{(2)}) + 2(2L_6^{(2)} - L_4^{(2)}))\chi_l^{\mathbf{e}} + \frac{1}{16\pi^2 f^2}\chi_l^{\mathbf{e}} \log\frac{\chi_l^{\mathbf{e}}}{\Lambda_\chi^2} \right\}, \tag{41}$$

$$f_{ll}^{\mathbf{e}} = f[1 + c_f(a^{\mathbf{e}})^2] + f \cdot \left\{ \frac{8}{f^2}(2L_4^{(2)} + L_5^{(2)})\chi_l^{\mathbf{e}} - \frac{\chi_l^{\mathbf{e}}}{8\pi^2 f^2} \log\frac{\chi_l^{\mathbf{e}}}{\Lambda_\chi^2} \right\}, \tag{42}$$

with

$$\chi_l^{\mathbf{e}} = \frac{Z_l^{\mathbf{e}}}{R_a^{\mathbf{e}}} \frac{B^{\mathbf{1}}\tilde{m}_l^{\mathbf{e}}}{(a^{\mathbf{e}})^2}, \tag{43}$$

where all quantities in Eqs. (41) and (42) are expressed in physical units [except for $B^{\mathbf{1}}$ and $\tilde{m}_l^{\mathbf{e}}$ in Eq. (43) which are given in lattice units].

Two important refinements should be mentioned. First, for the case of a physical scaling trajectory, i.e., one which terminates in the physical masses m_π, m_K, and m_Ω, these physical units are naturally GeV. However, for other scaling trajectories appropriate physical units to use can be those in which the Omega mass is unity. Second, for simplicity in Eqs. (38), (39), (41), and (42) we have treated the heavy-quark mass as fixed and not displayed the dependence of the quantities f, B, L_4, L_5, L_6, and L_8 on m_h. In practice we can easily generalize these equations to describe the dependence of m_{ll} and f_{ll} on m_h as well. Provided we limit the variation of m_h to a small range about an expansion point $\tilde{m}_{h0}$, this variation can be described by including a linear term in $m_h - \tilde{m}_{h0}$ and treating this term as NLO in our power-counting scheme. Thus, such extra linear terms will only be introduced into the leading-order terms in Eqs. (41) and (42).

Next we present the corresponding formulas for the quantities m_K and m_Ω which are used in the determination of the scaling trajectory and in the assignment of a lattice spacing at each value of β:

$$(m_{lh}^{\mathbf{e}})^2 = (m^{(K)})^2 + (m^{(K)})^2\left\{\frac{\lambda_1 + \lambda_2}{f^2}\chi_l^{\mathbf{e}}\right\}, \tag{44}$$

$$m_{hhh}^{\mathbf{e}} = m^{(\Omega)} + m^{(\Omega)} c_{m_\Omega, m_l}\chi_l^{\mathbf{e}}. \tag{45}$$

Here $m^{(K)}$ and $m^{(\Omega)}$ are the mass of the lh meson and the hhh baryon, respectively, in the SU(2) chiral limit, i.e., with $\tilde{m}_l = 0$, for the value of $\tilde{m}_h$ used in the simulation. Similarly the LECs $\lambda_{1,2}$ and c_{m_Ω,m_l} depend on $\tilde{m}_h$ and we are using the notation for the LECs $\lambda_{1,2}$ which we introduced in [1]. [Note that c_{m_Ω,m_l}, whose value is given in Table XXVII below, should be distinguished from the related parameter $c^{\mathbf{1}}_{m_\Omega m_l}$ which appears in Eqs. (36) and (37) above.] The absence of any corrections of $O(a^2)$ on the right-hand sides of Eqs. (44) and (45) follows from the same argument which justified omitting an $O(a^2)$ correction from the right-hand side of Eq. (41). For masses $\tilde{m}_l^{\mathbf{e}}$

TABLE XXVI. Values of the quark mass ratios Z_l and Z_h and the lattice-spacing ratio R_a determined by matching at five points over both ensemble sets. The quark masses here are quoted without the additive $m_{\rm res}$ correction. The ensemble $\mathbf{e} \neq \mathbf{M}$.

$\mathbf{M}$	$(am_l)^{\mathbf{M}}$	$(am_h)^{\mathbf{M}}$	$(am_l)^{\mathbf{e}}$	$(am_h)^{\mathbf{e}}$	Z_l	Z_h	R_a
32^3	0.004	0.03	0.003 13(13)	0.038 12(80)	0.980(15)	0.976(11)	0.7617(72)
32^3	0.006	0.03	0.005 83(12)	0.038 39(51)	0.981(9)	0.974(7)	0.7583(46)
32^3	0.008	0.03	0.008 60(19)	0.038 69(64)	0.979(10)	0.972(8)	0.7545(58)
24^3	0.005	0.04	0.005 45(11)	0.031 48(51)	0.985(12)	0.978(9)	0.7620(57)
24^3	0.01	0.04	0.008 97(18)	0.030 74(57)	0.974(11)	0.968(9)	0.7517(70)

TABLE XXVII. Parameters of the global fit to our ensembles using NLO ChPT without finite-volume corrections (second column) and with finite-volume corrections (third column). For the unitary theory the parameters are defined in Sec. V B and for the partially quenched theory in Appendix B of Ref. [1].

Parameter	No FV corrections	With FV corrections
B	4.12(7) GeV	4.03(7) GeV
f	0.110(2) GeV	0.112(2) GeV
c_f	0.05(7) GeV^2	0.04(7) GeV^2
$L_4^{(2)}$	−0.000 00(7)	−0.000 05(7)
$L_5^{(2)}$	0.00050(5)	0.00047(5)
$L_6^{(2)}$	−0.000 03(4)	−0.000 05(4)
$L_8^{(2)}$	0.000 55(2)	0.000 59(2)
$m^{(K)}$	0.4856(4) GeV	0.4854(4) GeV
$f^{(K)}$	0.141(3) GeV	0.143(3) GeV
$c_{f^{(K)}}$	0.01(6) GeV^2	0.01(6) GeV^2
λ_1	0.0043(9)	0.0046(10)
λ_2	0.023(1)	0.024(1)
λ_3	−0.0018(9)	−0.0016(10)
λ_4	0.0058(2)	0.0057(2)
$m^{(\Omega)}$	1.666(2) GeV	1.666(2) GeV
c_{m_Ω,m_l}	0.20(6) GeV^{-2}	0.20(6) GeV^{-2}

and $\tilde{m}_h^{\mathbf{e}}$ lying on a scaling trajectory the left-hand sides of these equations must all be the same because of our definition of scaling trajectory. Because of our power-counting scheme, no a^2 corrections need to be included in the NLO terms proportional to $\chi_l^{\mathbf{e}}$ on the right-hand side of these two equations. Therefore the leading-order terms $m^{(K)}$ and $m^{(\Omega)}$ must also be the same for all ensembles when expressed in physical units and no $O(a^2)$ correction can appear. As discussed above, these equations can be generalized to describe the NLO dependence on $\tilde{m}_h$ varying about an expansion point $\tilde{m}_{h0}$. In fact, for the Ω baryon this more general case for Eq. (45) was described in the previous subsection in the equivalent Eqs. (36) and (37).

Note that the coefficient of the chiral logarithm in Eq. (41) includes a factor which depends on f, the pion decay constant in the SU(2) chiral limit [all other factors of f in Eqs. (41) and (44) can be absorbed into a redefinition of LECs which in any case are determined by fitting]. This low-energy constant f can be determined from the measured values of f_{ll} using Eq. (42), but to NLO it can also be replaced by the measured values of f_{ll}.

As described in Sec. V A 3, these ChPT formulas can now be used to determine physical results in the continuum limit from those obtained on our two lattice spacings. We can employ the fixed-trajectory method, finding the ratios Z_l and Z_h which relate a specific choice of quark masses on one ensemble to those on the other which lie on the same scaling trajectory. The corresponding ratio of values of m_{hhh} determines R_a. These three quantities then allow a single set of LECs to be used to extrapolate the results of both ensembles to the continuum limit and to the physical value of the light-quark mass using Eqs. (41), (42), (44), and (45). As a result we learn the physical values of $\tilde{m}_{ud}(\beta^{\mathbf{e}})$, $\tilde{m}_s(\beta^{\mathbf{e}})$, and $a^{\mathbf{e}}$ on our two ensembles. In other words, we determine the quark masses and lattice spacings for our two ensembles which lie on the physical scaling trajectory.

Alternatively, we can use the generic fitting approach and introduce the three parameters (Z_l, Z_h, R_a) into the four equations, Eqs. (41), (42), (44), and (45), and obtain a fit to the lattice data from both ensembles for which the quark masses lie in the allowed range. The resulting values of the LECs and (Z_l, Z_h, R_a) then determine the functions $m_{ll}^{\mathbf{e}}(\tilde{m}_l, \tilde{m}_h)$, $m_{lh}^{\mathbf{e}}(\tilde{m}_l, \tilde{m}_h)$, and $m_{hhh}^{\mathbf{e}}(\tilde{m}_l, \tilde{m}_h)$. The physical quark masses on each ensemble, $m_{ud}^{\mathbf{e}} = m_{ud}(\beta^{\mathbf{e}})$ and $m_s^{\mathbf{e}} = m_s(\beta^{\mathbf{e}})$, are then obtained by solving the equations:

$$\frac{m_{ll}^{\mathbf{e}}(\tilde{m}_{ud}^{\mathbf{e}}, \tilde{m}_s^{\mathbf{e}})}{m_{hhh}^{\mathbf{e}}(\tilde{m}_{ud}^{\mathbf{e}}, \tilde{m}_s^{\mathbf{e}})} = \frac{m_\pi}{m_\Omega} \quad \text{and} \quad \frac{m_{lh}^{\mathbf{e}}(\tilde{m}_{ud}^{\mathbf{e}}, \tilde{m}_s^{\mathbf{e}})}{m_{hhh}^{\mathbf{e}}(\tilde{m}_{ud}^{\mathbf{e}}, \tilde{m}_s^{\mathbf{e}})} = \frac{m_K}{m_\Omega}, \tag{46}$$

where on the right-hand sides the ratios take their physical values.

Having determined $m_{ud}(\beta^{\mathbf{e}})$, $m_s(\beta^{\mathbf{e}})$, and $a^{\mathbf{e}}$ as described above, we are in a position to compute other physical quantities. For example, at NLO in our power counting the behavior of the kaon decay constant f_K is

$$f_{lh}^{\mathbf{e}} = f^{(K)}[1 + c_{f^{(K)}}(a^{\mathbf{e}})^2] + f^{(K)}\left\{\frac{\lambda_3 + \lambda_4}{f^2}\chi_l^{\mathbf{e}} - \frac{1}{(4\pi f)^2}\frac{3}{4}\chi_l^{\mathbf{e}} \log\frac{\chi_l^{\mathbf{e}}}{\Lambda_\chi^2}\right\}, \tag{47}$$

where $f^{(K)}$ is the result in the SU(2) chiral limit ($\tilde{m}_l = 0$), $\lambda_{3,4}$ are m_h-dependent low-energy constants and $c_{f^{(K)}}$ is a constant. For each $\beta^{\mathbf{e}}$, having determined $\tilde{m}_s(\beta^{\mathbf{e}})$ we measure $f_{lh}^{\mathbf{e}}$ for $\tilde{m}_h^{\mathbf{e}} = \tilde{m}_s(\beta^{\mathbf{e}})$ as a function of $\tilde{m}_l$; fit the measured values at all $\beta^{\mathbf{e}}$ to determine the LECs and $c_{f^{(K)}}$ in Eq. (47) and finally obtain the physical value of f_K by setting $a = 0$ and $\tilde{m}_l = \tilde{m}_{ud}$. Such a procedure is then generalized to the other physical quantities we wish to compute.

C. Scaling combined with an analytic ansatz for the chiral dependence

While we know that the ansatz based on chiral perturbation theory described in the previous subsection is valid in the limit of small u and d quark masses, we do not know the precision with which it holds over the range of masses which we analyze in this paper (corresponding to data in the range 240 MeV $\lesssim m_\pi \lesssim$ 420 MeV). Indeed it is precise lattice simulations which will answer such questions. In order to obtain some understanding of the corresponding systematic uncertainties, in addition to the procedures based on chiral perturbation theory described in Sec. V B, we consider an ansatz based on a first-order Taylor expansion about a nonzero quark mass, in the style

of Refs. [47,48]. Within this approach, since we do not include chiral logarithms, we are not able to take the chiral limit and only assume the validity of the analytic ansatz between the physical point (to which we extrapolate) and the region where we have data. In this work we only consider linear, first-order fits and are therefore insensitive to the choice of expansion point which we take to be the same as that at which we match the ensembles when using the fixed-trajectory method. This simplifies the discussion below of the simultaneous expansion in a^2 and mass differences. Beyond first order, convergence may be improved by considering an expansion point between the region in which we have data and the physical point, but this is beyond the scope of our current analysis.

Using the analytic ansatz for m_π^2 as a function of the quark mass m_q, we find numerically that the constant (mass-independent) term is consistent with zero, indicating that the tangent of $m_\pi^2(m_q)$ in the unitary case does pass through the origin. Thus, at our statistical precision, no significant chiral curvature is needed to satisfy Goldstone's theorem, however we retain the view that we are indeed using a model which is valid only in a restricted region of nonzero quark masses.

Goldstone's theorem also applies in the partially quenched theory and the pion mass vanishes as the valence-quark masses are taken to zero while keeping the sea-quark masses fixed. In this case however, our linear fit extrapolates to a nonzero pion mass for massless valence quarks, and this naturally implies that some form of curvature is required at smaller masses. This is consistent with enhanced chiral logarithms in the partially quenched theory. However, the fits do not necessarily imply that chiral logarithms at NLO correctly represent the quark mass dependence between the simulated range of masses and the physical point. Instead, in this approach the sum over multiple orders of chiral perturbation theory is assumed to be approximated by a linear dependence in the relevant range of masses. It is also possible of course that the simulated range of masses is outside the useful domain of chiral perturbation theory and that, for example, phenomenological models based on combining NLO chiral perturbation theory with arbitrary analytic subsets of terms which appear at NNLO and NNNLO are less well motivated than our linear ansatz.

For m_π^2 and f_π it is convenient to define the average valence-quark mass $\tilde{m}_v = \frac{\tilde{m}_x + \tilde{m}_y}{2}$. As in Sec. V B, we apply a power-counting rule in a double expansion in $m_x - m^m$, $m_y - m^m$, $m_l - m^m$, and a^2, where m^m is the mass at which we match the ensembles which we also choose to be the point around which we perform the Taylor expansion and we recall that $m_{x,y}$ and m_l are the valence and sea light-quark masses, respectively, (here we allow for partial quenching). For the pion mass we use the ansatz

$$m_{xy}^2 = C_0^{m_\pi} + C_1^{m_\pi}(\tilde{m}_v - \tilde{m}^m) + C_2^{m_\pi}(\tilde{m}_l - \tilde{m}^m), \quad (48)$$

where we use our standard notation in which the subscripts xy imply that the two valence quarks have mass m_x and m_y, respectively. By the definition of our scaling trajectory, there is no $O(a^2)$ term at the match point and so there is no correction to $C_0^{m_\pi}$. Within our power counting we could equivalently use

$$m_{xy}^2 = C_0^{m_\pi} + C_1^{m_\pi}\tilde{m}_v + C_2^{m_\pi}\tilde{m}_l, \quad (49)$$

where for convenience we redefine $C_0^{m_\pi}$ between Eqs. (48) and (49).

In searching for evidence of chiral logarithms it is conventional to plot the ratio $m_{xy}^2/\tilde{m}_v$ as a function of the quark masses. With the ansatz proposed in Eq. (49)

$$\frac{m_{xy}^2}{\tilde{m}_v} = \frac{C_0^{m_\pi}}{\tilde{m}_v} + C_1^{m_\pi} + \frac{C_2^{m_\pi}\tilde{m}_l}{\tilde{m}_v}, \quad (50)$$

and we note that an observed deviation of the mass dependence of $\frac{m_{xy}^2}{\tilde{m}_v}$ from a constant in the finite range of quark masses which can be simulated, is not in itself unambiguous evidence of a nonanalytic structure.

For decay constants, which do not vanish in the chiral limit, the $O(a^2)$ term is not sensitive to the choice of expansion point:

$$f_{xy} = C_0^{f_\pi}[1 + C_{f_\pi}a^2] + C_1^{f_\pi}(\tilde{m}_v - \tilde{m}^m) + C_2^{f_\pi}(\tilde{m}_l - \tilde{m}^m), \quad (51)$$

$$\equiv C_0^{f_\pi}[1 + C_f a^2] + C_1^{f_\pi}\tilde{m}_v + C_2^{f_\pi}\tilde{m}_l, \quad (52)$$

where again we have redefined $C_0^{f_\pi}$ between the first and second lines.

Following a similar argument, at a fixed strange-quark mass, we take the light-quark mass dependence of the kaon mass and decay constant and the mass of the Ω baryon to be given by

$$m_{xh}^2(a, m_l) = C_0^{m_K} + C_1^{m_K}\tilde{m}_x + C_2^{m_K}\tilde{m}_l, \quad (53)$$

$$f_{xh}(a, m_l) = C_0^{f_K}[1 + C_{f_K}a^2] + C_1^{f_K}\tilde{m}_x + C_2^{f_K}\tilde{m}_l, \quad (54)$$

$$m_{hhh}(a, m_l) = C_0^{m_\Omega} + C_2^{m_\Omega}\tilde{m}_l. \quad (55)$$

We stress that the constants $C_n^{m_\pi}$, $C_n^{f_\pi}$, C_f, $C_n^{m_K}$, $C_n^{f_K}$, C_{f_K}, and $C_n^{m_\Omega}$ implicitly depend on the strange-quark mass.

D. Procedure for combined scaling and chiral fitting

Having introduced the theoretical framework behind our combined scaling and chiral fits in Secs. V B and V C we now explain its practical implementation. The formulas given above which describe the combined behavior are valid only for a fixed strange-quark mass and we are faced with the problem that the physical strange mass is not known *a priori* but is an output of the calculation. The procedure for performing the combined chiral-continuum

fits is therefore necessarily iterative. As explained in more detail below, we start with some initial values for the lattice spacings and quark masses, perform the fits, and then use linear interpolations in m_h to obtain updated estimates. The process terminates when the updated estimates converge. During this iterative procedure we use reweighting (see Sec. II D) to adjust all pionic observables to the new strange-quark mass on each ensemble. For kaon and Ω observables a linear interpolation between the unreweighted unitary measurement, and measurements with a second valence strange quark (reweighted-to-be-unitary) suffice to obtain that observable for $m_y = m_h = m_s^{\text{guess}}$.

For the remainder of this subsection we explain further the procedure which we use to match lattices with different β and present results for the ratios $R_a^{\mathbf{e}}$ and $Z_f^{\mathbf{e}}$ defined in Eqs. (29) and (30) for our ensembles using the fixed-trajectory method explained in Sec. V A 3. We start by taking a specific value of $(m_l, m_h)^{\mathbf{M}}$ on the ensemble $\mathbf{M}$ to which the other ensembles are matched. We refer to this as the matching point. The ensemble set $\mathbf{M}$ may be the same as the primary ensemble $\mathbf{1}$, but does not need to be. As discussed in Sec. V A, the matching to other ensembles $\mathbf{e} \neq \mathbf{M}$ is performed by requiring that the ratios of hadronic masses $\frac{m_{ll}}{m_{hhh}}$ and $\frac{m_{lh}}{m_{hhh}}$ are the same on all lattices at the matching point. Although the final physical predictions do not depend upon the choice of matching point, certain choices are favored due to the quality of the data at the matching point and the range over which the data must be interpolated/extrapolated on the other ensembles to perform the matching. The ideal point has as small a statistical error as possible and lies within the range of simulated data on all of the matched ensembles such that only a small interpolation is required. In practice, the errors on the mass ratios at the matching point can be reduced by fitting to all partially quenched simulated data on the ensemble set $\mathbf{M}$ and interpolating to the matching point along the unitary curve. We use linear fitting functions for the light-quark mass dependence of the pseudoscalar mesons and the Ω baryon in these short interpolations:

$$m_{xy}^2 = c_0 + c_l m_l + c_v(m_x + m_y), \tag{56}$$

$$m_{xh}^2 = d_0 + d_l m_l + d_v m_x, \tag{57}$$

$$m_{hhh} = e_0 + e_l m_l, \tag{58}$$

where as elsewhere x, y (l) represent the light valence (sea) quarks and h represents the heavy-quark. Equations (56)–(58) are written in lattice units. Although the linear behavior in Eqs. (56)–(58) is similar to that used in the analytic ansatz, Eqs. (49), (53), and (55), we stress that the meaning is different. When using the analytic ansatz we assume its validity in the full range of masses between the physical ones and those we simulate. Equations (56)–(58) on the other hand, are only assumed to represent the mass behavior in the short intervals between the matching and simulated points on ensembles $\mathbf{e} \neq \mathbf{M}$, independently of whether we subsequently use chiral perturbation theory or the analytic ansatz to perform the chiral extrapolation.

Once a matching point has been chosen, the matching proceeds as follows:

(1) For each set of ensembles $\mathbf{e} \neq \mathbf{M}$, we perform an independent partially quenched linear fit to the simulated pion, kaon, and Omega masses using the forms given in Eqs. (56)–(58).
(2) We make a first estimate of the pair of quark masses $(m_l, m_h)^{\mathbf{e}}$ on each ensemble set $\mathbf{e} \neq \mathbf{M}$ that corresponds to the matching point.
(3) We then interpolate the three hadronic masses to the estimated $m_l^{\mathbf{e}}$ for each value of the simulated unitary heavy-quark mass.
(4) We linearly interpolate each quantity to the estimated value of $m_h^{\mathbf{e}}$.
(5) Next we calculate the ratios $R_l^{\mathbf{e}} = \frac{m_{ll}^{\mathbf{e}}}{m_{hhh}^{\mathbf{e}}}$ and $R_h^{\mathbf{e}} = \frac{m_{lh}^{\mathbf{e}}}{m_{hhh}^{\mathbf{e}}}$.
(6) Using the measured slopes of $m_{ll}^{\mathbf{e}}$ and $m_{hhh}^{\mathbf{e}}$ with respect to $m_l^{\mathbf{e}}$, by comparing $R_l^{\mathbf{e}}$ to the corresponding value $R_l^{\mathbf{M}}$ at the matching point we obtain an updated estimate of $m_l^{\mathbf{e}}$.
(7) Similarly, by comparing the ratio $R_h^{\mathbf{e}}$ to $R_h^{\mathbf{M}}$ we obtain an updated estimate of $m_h^{\mathbf{e}}$.
(8) With these updated estimates of the quark masses $(m_l, m_h)^{\mathbf{e}}$, we return to step 3 and iterate the steps until the process converges.

Once this procedure has converged, we have a set of bare-quark masses $(m_l, m_h)^{\mathbf{e}}$ which, in physical units, are equivalent to the masses $(m_l, m_h)^{\mathbf{M}}$. Following the discussion in Sec. V A 2, we choose a primary ensemble $\mathbf{1}$ and determine the ratios of quark masses $Z_f^{\mathbf{e}}$ in ensembles $\mathbf{1}$ and $\mathbf{e}$ as in Eq. (30) with the corresponding ratios of lattice spacing R_a given in Eq. (29).

In the above we assumed that for each ensemble $\mathbf{e}$ we had performed simulations at several values of $m_h^{\mathbf{e}}$. In our present study the simulations were performed at a single value of $m_h^{\mathbf{e}}$ and the dependence on the heavy-quark mass is obtained by reweighting as explained in Sec. II D.

The above discussion was deliberately presented in a general case where there are an arbitrary number of ensembles. In our case we only have two sets, i.e., the 24^3 and 32^3 lattices. For the primary ensemble we choose the finer 32^3 lattice. As we have only one other ensemble set (24^3), from now on we drop the superscript on the ratios of lattice spacings (R_a) and quark masses (Z_l and Z_h).

In Table XXVI we give results for Z_l, Z_h, and R_a obtained by matching at several matching points on both ensemble sets $\mathbf{M} \in \{\mathbf{24^3}, \mathbf{32^3}\}$. Since we prefer to have a matching point within the range of simulated data on both ensembles, we can discard the first and last entries in the

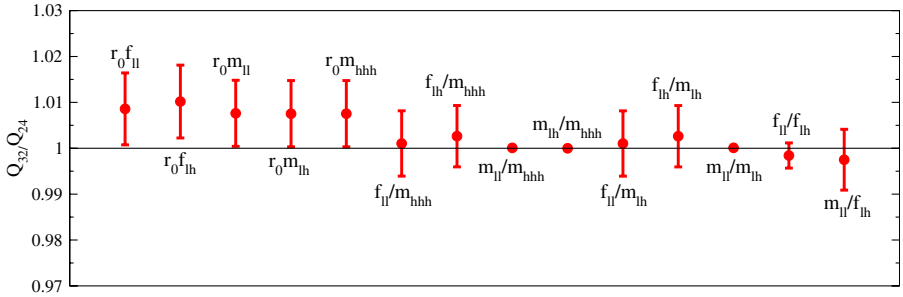

FIG. 26 (color online). Ratios of dimensionless combinations of lattice quantities Q (listed in the figure) between the 32^3 and 24^3 lattices at the matching point corresponding to $m_l = 0.006$, $m_h = 0.03$ on the 32^3 lattice. A value of unity indicates perfect scaling. The ratios m_{ll}/m_{hhh} and m_{lh}/m_{hhh} (and consequently m_{ll}/m_{lh}) are defined to scale perfectly at these quark masses as a consequence of our choice of scaling trajectory.

table. From the remaining 3 possibilities, we choose as our final values $Z_l = 0.981(9)$, $Z_h = 0.974(7)$, and $R_a = 0.7583(46)$ from the second entry with $\mathbf{M = 32^3}$ and $(m_l, m_h)^{32^3} = (0.006, 0.03)$.

Having chosen to perform the matching of the lattices at the two lattice spacings by requiring that m_{ll}/m_{hhh} and m_{lh}/m_{hhh} take the same values at the matching point, we expect to see lattice artefacts in ratios of other physical quantities. This is illustrated in Fig. 26 in which we show the ratios of several other dimensionless combinations of lattice quantities between the two lattices at the quark masses used in the matching procedure above. The figure shows that we can expect only small scaling violations on the order of 1%–2% for the other quantities used in our global fits, and also confirms that other dimensionless combinations of lattice quantities would be equally suitable choices for the definition of the scaling trajectory.

E. Results of combined scaling and chiral fits

Using the matching factors Z_l, Z_h, and R_a determined as described in the previous section we are ready to perform a simultaneous fit of all our pion, kaon and Ω mass and decay constant data to either the NLO forms in chiral perturbation theory, Eq. (41) to Eq. (45), or the analytic forms Eq. (49) to Eq. (55). We also correct for finite-volume (FV) effects in NLO PQChPT by substituting the chiral logarithms with the corresponding finite-volume sum of Bessel functions [49]. The iterative procedure is the same for each of these three fit ansätze. For each iteration i, we:

(1) estimate the physical strange-quark masses, m_s^i, from the $(i-1)$-th iteration;
(2) interpolate and reweight the data to m_s^i;
(3) fit the m_x, m_y, m_l dependence of the light pseudoscalar mass and decay constant;
(4) fit the m_x, m_l dependence of kaon quantities at $m_h = m_s^i$;
(5) fit the m_l dependence of the Omega mass for $m_h = m_s^i$;
(6) by comparing to the physical values of m_π/m_Ω and m_K/m_Ω, determine the iterated predictions for the physical strange-quark masses m_s^{i+1}.

This process is repeated until it converges and a self consistent set of quark masses, lattice spacings, and results in the continuum limit are obtained.

For the fits based on NLO chiral perturbation theory we use Eqs. (41) and (42) for the pion mass and decay constant, respectively, and Eqs. (44) and (47) for the kaon mass and decay constant. In our earlier work [1] we found that we had to apply cuts to keep the pion mass below around 420 MeV in order for NLO SU(2) ChPT to give an acceptable description of our data. All the additional data introduced in this work satisfies this cut and we include all the data for pions with valence masses m_x, $m_y \leq 0.01$ on the two 24^3 ensembles and all data for pions with valence masses m_x, $m_y \leq 0.008$ for the three 32^3 ensembles. For kaons we include all the valence light-quark masses in the above range for each fixed strange-quark mass. For this infinite-volume SU(2) NLO global fit the fitted parameters are presented in the second column of Table XXVII. The χ^2/dof for all the fits discussed here are given in Table XXVIII. We also perform the corresponding fits using the finite-volume chiral logarithm composed of a sum of Bessel functions [49]; resummed expressions are not available for our partially quenched fits. The parameters of the fit are presented in the third column of Table XXVII. In terms of the conventional LECs $\bar{l}_3$ and $\bar{l}_4$ the results are

$$\bar{l}_3 = 2.82(16), \quad \bar{l}_4 = 3.76(9) \quad \text{(Infinite Volume ChPT)}, \tag{59}$$

$$\bar{l}_3 = 2.57(18), \quad \bar{l}_4 = 3.83(9) \quad \text{(Finite Volume ChPT)}. \tag{60}$$

In Table XXIX we present the parameters of the fit with the analytic ansatz over the same mass range as for the fits using SU(2) chiral perturbation theory, as explained in the previous paragraph. We find that analytic fits including a

TABLE XXVIII. Fit ansatze, mass ranges, and uncorrelated χ^2/dof obtained in our analyses are shown. The fits were performed for pion masses less than 420 MeV.

Ansatz	χ^2/dof
NLO	0.72(46)
NLO-fv	1.07(47)
Analytic	0.60(44)

TABLE XXIX. Parameters of the global fit to our ensembles using the analytic ansatz. The parameters are defined in Eqs. (49) –(55).

Parameter	Value	Parameter	Value
$C_0^{m_\pi}$	$-0.001(1)$ GeV^2	$C_1^{m_K}$	3.67(4) GeV
$C_1^{m_\pi}$	7.45(9) GeV	$C_2^{m_K}$	0.7(1) GeV
$C_2^{m_\pi}$	0.43(8) GeV	$C_0^{f_K}$	0.149(2) GeV
$C_0^{f_\pi}$	0.123(2) GeV	C_{f_K}	0.02(6) GeV^2
C_{f_π}	0.04(7) GeV^2	$C_1^{f_K}$	0.34(1)
$C_1^{f_\pi}$	0.85(2)	$C_2^{f_K}$	0.52(10)
$C_2^{f_\pi}$	0.56(9)	$C_0^{m_\Omega}$	1.666(2) GeV
$C_0^{m_K}$	0.2353(8) GeV^2	$C_2^{m_\Omega}$	2.7(9)

larger range of pseudoscalar masses give an acceptable uncorrelated χ^2/dof but then the lightest data points were consistently missed by the fit by about 1 standard deviation. The utility of such extended fits for extrapolating to the physical point was therefore compromised and we decided to restrict the range of masses used in the analytic fits.

The global fit to many ensembles of partially quenched data is naturally a high dimensional space and so the exposition of the fits is best performed by looking at portions of the data in turn. In order to illustrate the quality of the fits, in the following subsections we display the fit and data for each physical quantity in turn. In total we have analyzed five ensembles at two lattice spacings, and each ensemble has measurements at many partially quenched valence-quark masses. As it is only feasible to present a subset of possible plots, in the following we display the

TABLE XXX. Unrenormalized physical quark masses in lattice units and the values of the inverse lattice spacing a^{-1} for the 32^3 and 24^3 ensembles are shown.

	NLO	NLO fv	Analytic
$\tilde{m}_l(32^3)$	0.001 00(3)	0.001 02(3)	0.001 05(6)
$\tilde{m}_s(32^3)$	0.0280(7)	0.0280(7)	0.0279(7)
$a^{-1}(32^3)$	2.280(28) GeV	2.281(28) GeV	2.282(28) GeV
$\tilde{m}_l(24^3)$	0.001 34(4)	0.001 36(4)	0.001 41(9)
$\tilde{m}_s(24^3)$	0.0379(11)	0.0379(11)	0.0378(11)
$a^{-1}(24^3)$	1.729(25) GeV	1.729(25) GeV	1.730(25) GeV

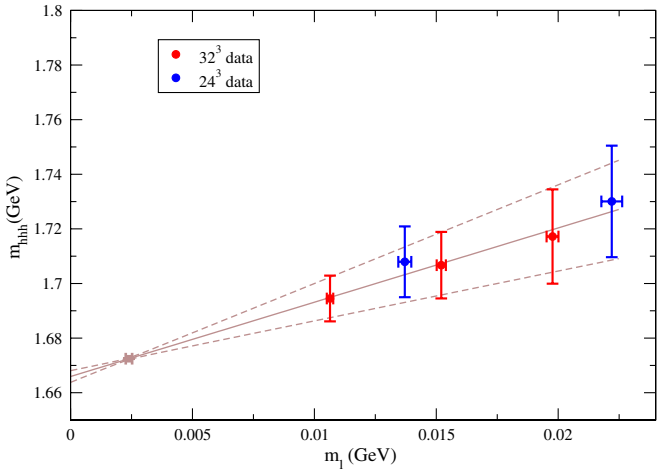

FIG. 27 (color online). The fit to the light-quark mass behavior of the Ω-baryon in the continuum limit obtained using the analytic ansatz. The corresponding plots using the infinite and finite-volume SU(2) ChPT ansatz are almost indistinguishable, differing only slightly in the estimates of the physical quark masses and the lattice spacings. Of the five data points, the first, third, and fourth from the left (denoted in red) correspond to the 32^3 ensembles and the remaining 2 (denoted in blue) correspond to the 24^3 ones.

dependence of each quantity on the valence-quark masses at the lightest sea-quark mass ($m_l = 0.005$ for the 24^3 ensembles and $m_l = 0.004$ on the 32^3 ensembles). The exception of course, is the mass of the Omega baryon m_{hhh} which does not depend on the light valence-quark masses. We also display the unitary subset of data on both lattice spacings along with the mass dependence we infer from our fits in the unitary continuum limit.

Before discussing the chiral and continuum behavior of hadronic masses and decay constants in detail, we present in Table XXX our results for the unrenormalized physical quark masses and the lattice spacings obtained from the three fits. In this table the quark masses are given in lattice units. The nonperturbative renormalization of the masses will be discussed in Sec. VI where the values of the renormalized quark masses in the $\overline{\text{MS}}$ scheme will be presented.

1. Chiral and continuum behavior of the Ω baryon

The Ω mass is fitted using Eq. (45) [or equivalently (55)]. The fit form for the Ω baryon does not change between the different ansätze and only very small differences arise from the different estimates of physical quark masses and hence of the lattice spacings. For illustration, Fig. 27 shows the extrapolation of the Ω mass using the analytic ansatz.

2. Chiral and continuum behavior of the pion mass

We display the fits of the partially quenched pion masses using infinite-volume NLO SU(2) partially quenched ChPT [i.e. to the partially quenched generalization of

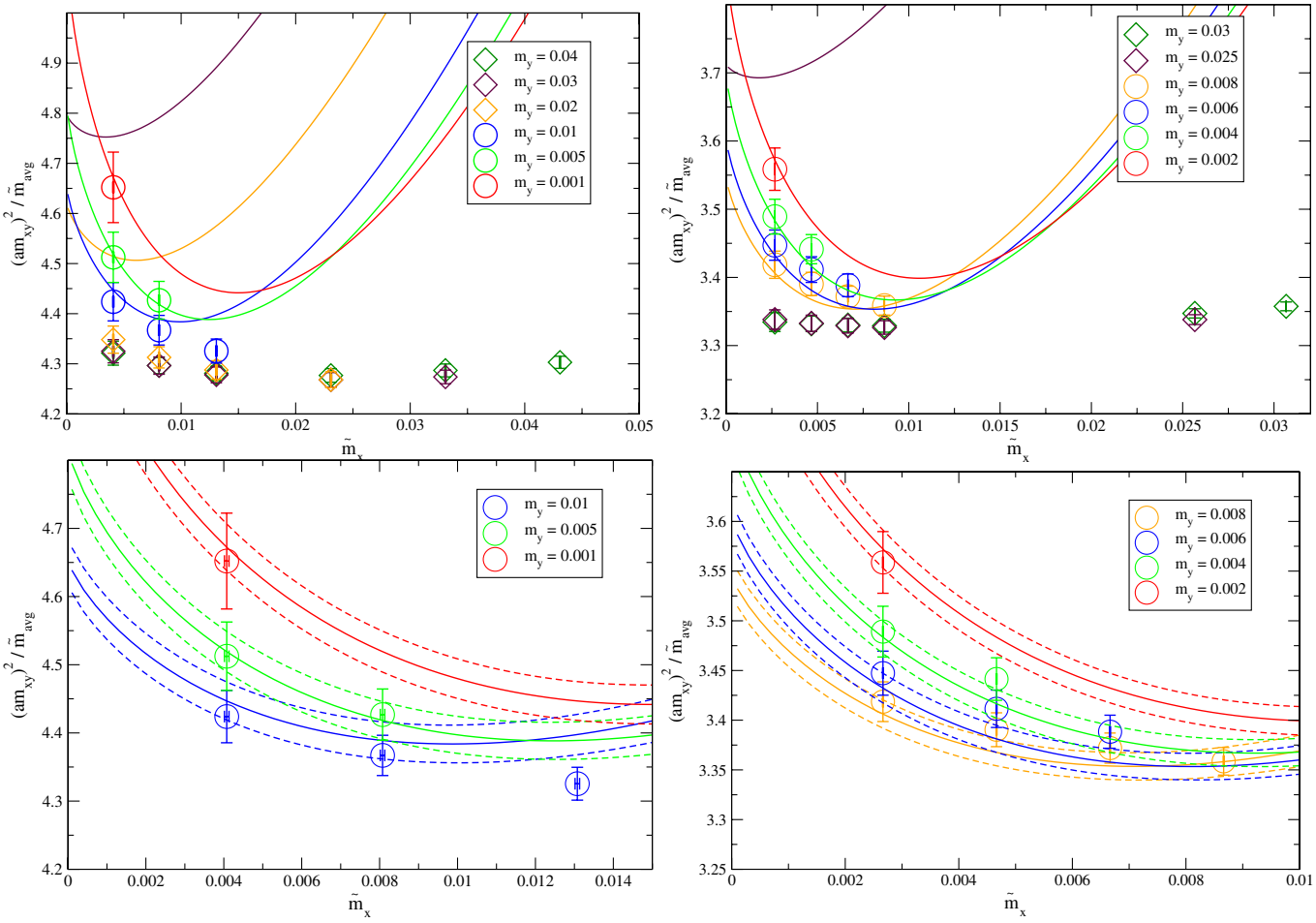

FIG. 28 (color online). Global fits obtained using infinite-volume NLO SU(2) chiral perturbation theory for the pion mass. The top-left panel includes the partially quenched data from the $m_l = 0.005$ ensemble on the 24^3 lattice and the data points in the top-right panel are from the $m_l = 0.004$ ensemble from the 32^3 lattice. In each case the curves correspond to the appropriate value of the lattice spacing. The points marked by the circles were included in the fit, whereas those marked by the diamonds were not. In the bottom two panels we zoom into the low-mass region, illustrating the fits to the points which were included (24^3 points on the left and 32^3 points on the right). [For fixed $\tilde{m}_x$, m_y decreases as $(am_{xy})^2/\tilde{m}_{\rm avg}$ increases.]

Eq. (38) given in Eq. (B.32) of Ref. [1]] in Fig. 28 for the lightest 24^3 and 32^3 ensembles. As discussed in Sec. V C, we divide by the average valence-quark mass with the intention of enhancing the visibility of chiral logarithms. Figure 29 displays the corresponding fit of the same data but including finite-volume corrections.

It is apparent that the infinite-volume and finite-volume NLO fits diverge rapidly from our data at larger masses, and this indeed is the reason why we were compelled to introduce the upper cutoff of 420 MeV for this analysis [1].

We now consider the chiral extrapolation of the pion mass using the analytic form of Eq. (49) which is shown in Fig. 30. Comparing Figs. 28 and 29 with Fig. 30 suggests that data at substantially larger masses can be described by the analytic expansion, without any curvature terms in the ansatz. The division by the average valence-quark mass in the plots, coupled to allowing the tangent not to pass through the origin (i.e. that the extrapolated m_π^2 at $m_x = m_y = 0$ may not be equal to zero) allows the analytic fit to reproduce a structure that might otherwise be attributed to chiral logarithms.

We emphasize that admitting the possibility that the constant term $C_0^{m_\pi} \neq 0$ allows for a pole in Fig. 30 in the unitary chiral limit. In fact we find that $C_0^{m_\pi}$ is numerically small and consistent with zero, $C_0^{m_\pi} = -0.001(1)$ GeV^2. We stress again that while Goldstone's theorem implies the vanishing of the pion mass in the SU(2) chiral limit, this does not necessarily imply that $C_0^{m_\pi} = 0$. Our model is that the linear ansatz is valid in the region between that where we have data and the physical point, and that if $C_0^{m_\pi} \neq 0$ then it is the curvature due to chiral logarithms below the physical pion mass which will force the pion mass to zero in the chiral limit. Nevertheless, from the fits we found that $C_0^{m_\pi}$ is consistent with zero. This is illustrated by the flat behavior (within the statistical precision) for the chiral behavior of the unitary points for m_π^2/m_l in the continuum

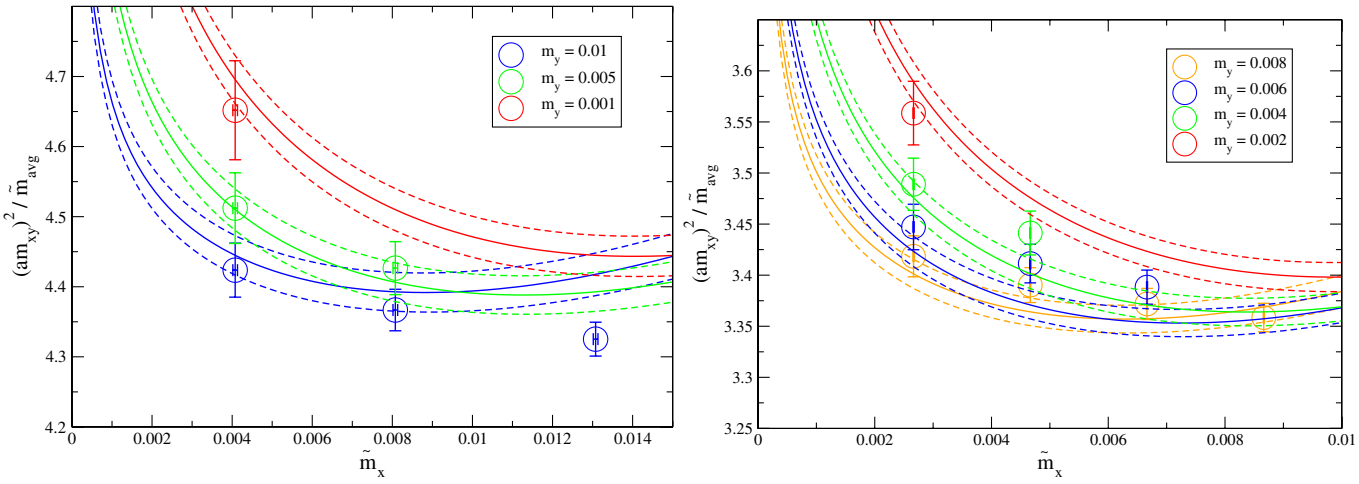

FIG. 29 (color online). Global fits for the pion mass obtained using NLO SU(2) chiral perturbation theory with finite-volume corrections. In this case we only include the points which were included in the fit ($m_l = 0.005$, 24^3 points on the left and $m_l = 0.004$, 32^3 points on the right) since the finite-volume corrections at larger masses are small. [For fixed $\tilde{m}_x$, m_y decreases as $(am_{xy})^2/\tilde{m}_{\rm avg}$ increases.]

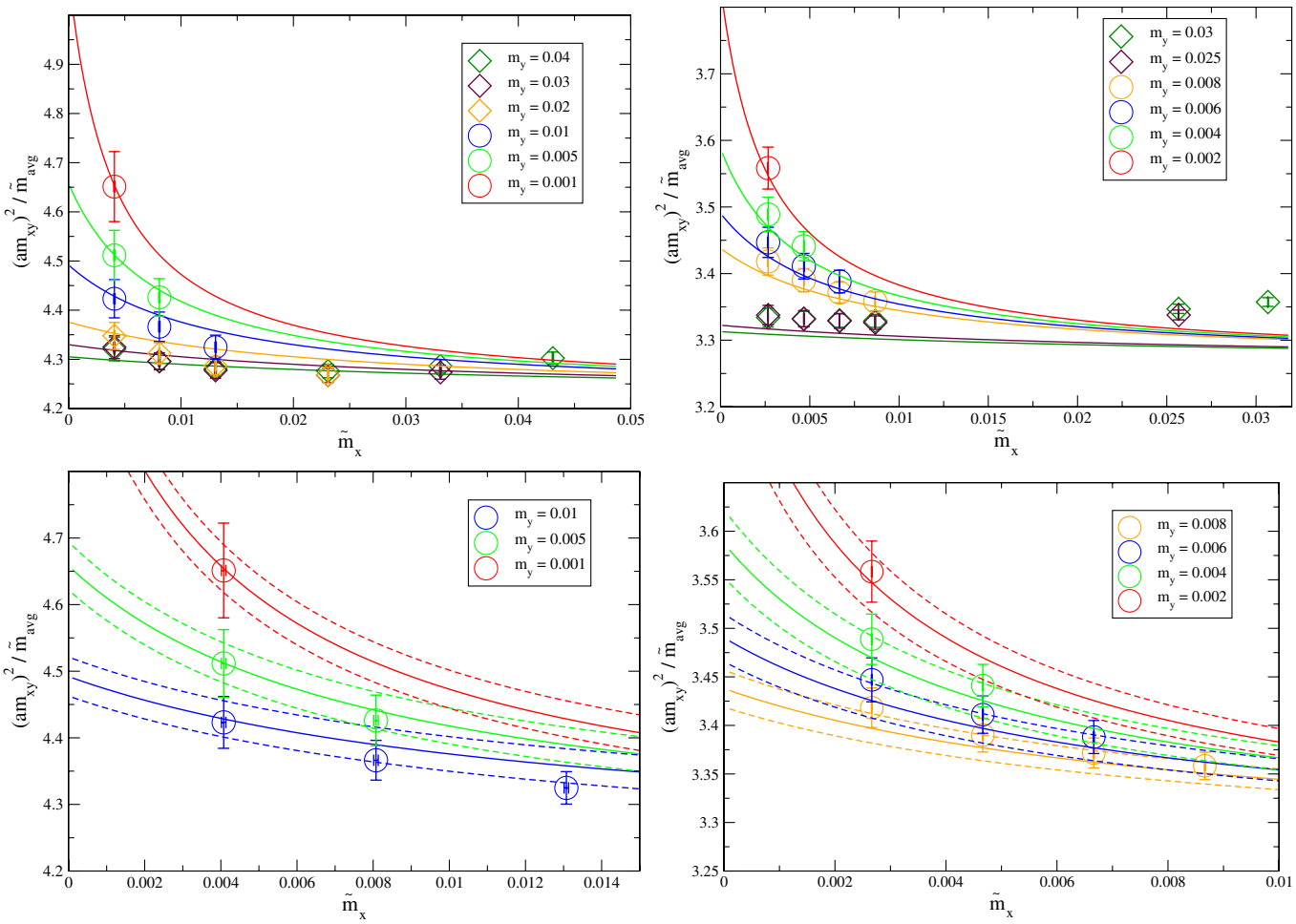

FIG. 30 (color online). Global fit curves obtained using the analytic fit ansatz (49) overlaying the simulated pion masses on the $m_l = 0.005$, 24^3 ensemble (top-left) and the $m_l = 0.004$, 32^3 ensemble (top-right). Points marked by circles were included in the fit, those marked by diamonds were not. The simple linear expansion replicates the entire range of lattice data reasonably well with the description being rather better than NLO chiral perturbation theory at our larger masses. In the bottom two panels we zoom into the low-mass region, illustrating the fits to the points which were included (24^3 points on the left and 32^3 points on the right). [For fixed $\tilde{m}_x$, m_y decreases as $(am_{xy})^2/\tilde{m}_{\rm avg}$ increases.]

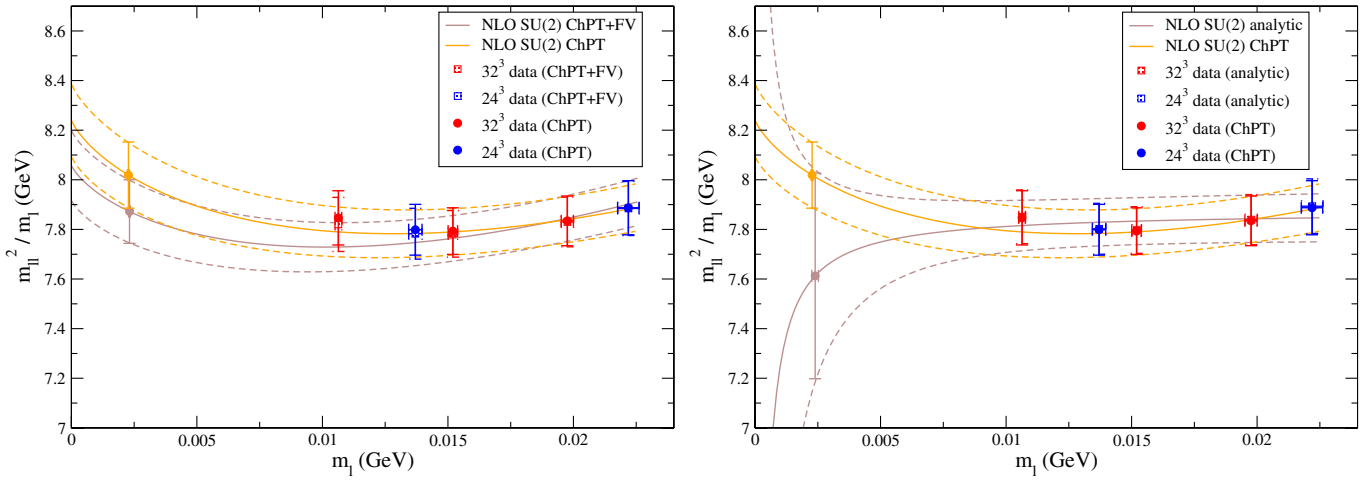

FIG. 31 (color online). Left panel: Pion mass fit for the SU(2) NLO fit form in the continuum limit, both with and without finite-volume logarithms. We adjust the data points to the continuum limit using the a^2 dependence in our fit form and overlay these. Right panel: Chiral extrapolation of the pion mass using the analytic (52) and infinite-volume NLO ChPT ansätze. In both panels the first, third, and fourth data points from the left (denoted in red) correspond to the 32^3 ensembles and the remaining 2 (denoted in blue) correspond to the 24^3 ones.

limit shown in the right panel in Fig. 31. Allowing for a nonzero value of $C_0^{m_\pi}$ does, however, lead to an amplified error for m_π^2/m_l at the physical point. The left panel of Fig. 31 shows the corresponding plots for the infinite and finite-volume ChPT fits.

Goldstone's theorem equally applies at vanishing valence-quark mass ($m_x = m_y = 0$) but with a nonzero sea-quark mass ($m_l > 0$). In contrast with the unitary case discussed in the previous paragraph where $C_0^{m_\pi}$ was consistent with zero, in the partially quenched direction we find that the corresponding constant $C_0^{m_\pi} + C_2^{m_\pi} m_l$ is nonzero, specifically $C_2^{m_\pi} = 0.43(8)$ GeV. This value for $C_2^{m_\pi}$ is much larger than might be created by propagating the mass dependence in $m_{\mathrm{res}}^l(m)$ through the term involving $C_1^{m_\pi}$; the greatest mass dependence in m_{res}^l occurs on our 24^3 ensembles in the partially quenched direction, but can at most generate a 1% correction to $\tilde{m}$ and produces a term much smaller than the measured $C_2^{m_\pi}$. Further, the residual chiral symmetry breaking is 4 times smaller for the 32^3 ensemble which is also included in the global fit. Our results from this global analytic fit, therefore, require a curvature, most likely from partially quenched chiral logarithms which are known to be larger than in the unitary direction, in order for Goldstone's theorem to be satisfied.

It is also worth emphasizing that the *discovery* of chiral logarithms in lattice data from plots such as those in Figs. 28 to 30 is to a certain extent artificial. Inconsistency with LO chiral perturbation theory is certainly indicated. Our linear fits suggest that the transformations made in displaying the data render even conclusions of genuine curvature, let alone unambiguous demonstration of logarithmic mass dependence, to be somewhat optimistic. In order to prove logarithmic behavior, one should really change quark masses substantially on a logarithmic scale; our present lattice data supports only the weaker claim of consistency with logarithmic behavior in the partially quenched direction.

3. Chiral and continuum behavior of the pion decay constant

We now turn to the chiral behavior of f_π and the extrapolation to the physical point. The leading term in all the fits contains an a^2 correction and we display the fits performed at nonzero lattice spacing combined with the unmodified lattice data and also our continuum predictions combined with the lattice data extrapolated to the continuum limit using the results of the fits.

We display our fits obtained using infinite-volume NLO SU(2) partially quenched ChPT in Fig. 32. The corresponding fits including finite-volume corrections are shown in Fig. 33. Finally Fig. 34 displays the fits obtained using our analytic ansatz. Having performed the fits, we adjust our unitary data to the continuum limit using the fitting functions with the determined parameters and display the adjusted data in Fig. 35 together with the finite and infinite-volume NLO SU(2) ChPT fits (left panel) and the analytic fit (right panel). The effect of the adjustment to the continuum limit is illustrated in Fig. 36 where the fits are superimposed on the unadjusted unitary data. It can be seen from Figs. 35 and 36 that the adjustment to the continuum limit for the pion decay constant is very small.

The predictions for f_π extrapolated to the physical quark masses for each of the fits is given in Table XXXI. We anticipate the discussion of the global fits for f_K which are presented in Sec. V E 6 and mention that the predictions for f_K extrapolated to the physical quark masses are given in Table XXXII, and the predictions for f_K/f_π extrapolated to the physical quark masses are given in Table XXXIII.

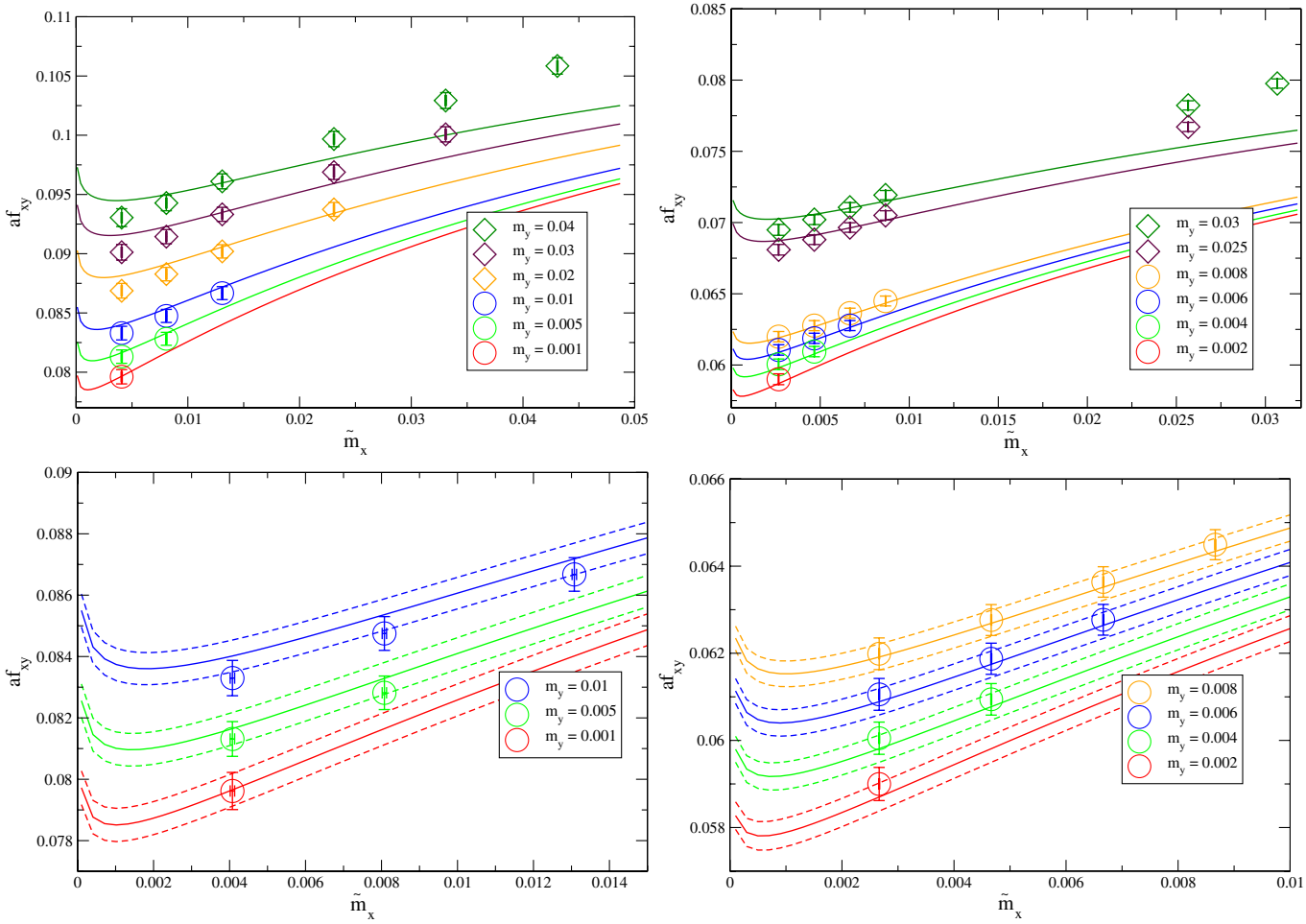

FIG. 32 (color online). Global fits to the lattice data for the pion decay constant obtained using infinite-volume NLO SU(2) chiral perturbation theory. The top-left and top-right panels correspond to the 24^3, $m_l = 0.005$ and 32^3, $m_l = 0.004$ ensembles, respectively. Points marked by circles are included in the fits, while those with heavier masses marked by diamonds are not. In the bottom two panels we zoom into the low-mass region, illustrating the fits to the points which were included (24^3 points on the left and 32^3 points on the right). (For fixed $\tilde{m}_x$, m_y increases as af_{xy} increases.)

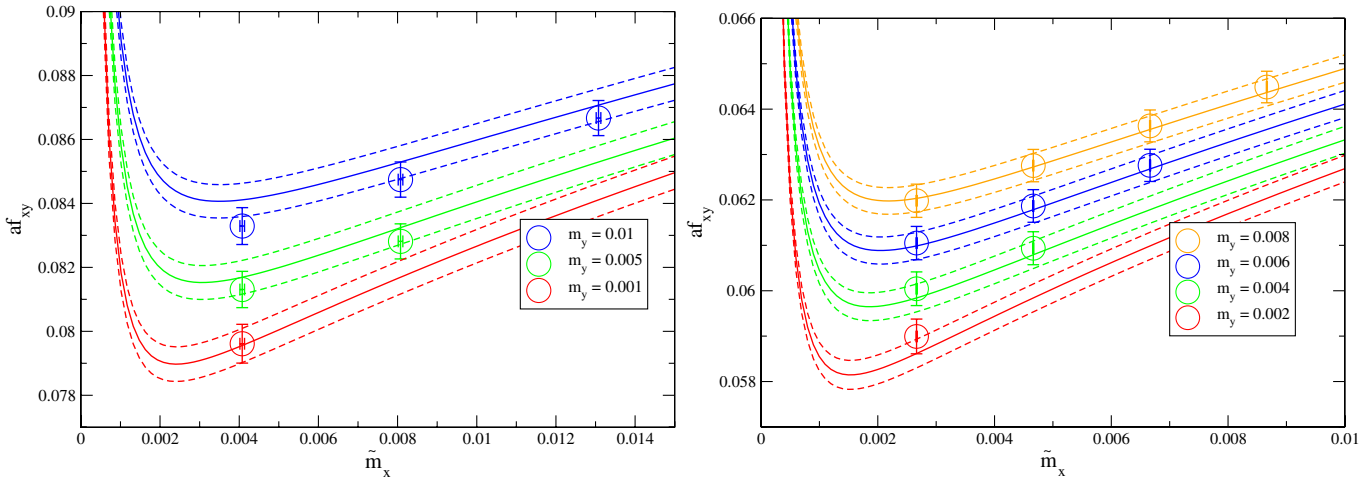

FIG. 33 (color online). Global fits to the lattice data for the pion decay constant obtained using NLO SU(2) chiral perturbation theory with finite-volume corrections. In this case we only include the points which were included in the fit ($m_l = 0.005$, 24^3 points on the left and $m_l = 0.004$, 32^3 points on the right) since the finite-volume corrections at larger masses are small. (For fixed $\tilde{m}_x$, m_y increases as af_{xy} increases.)

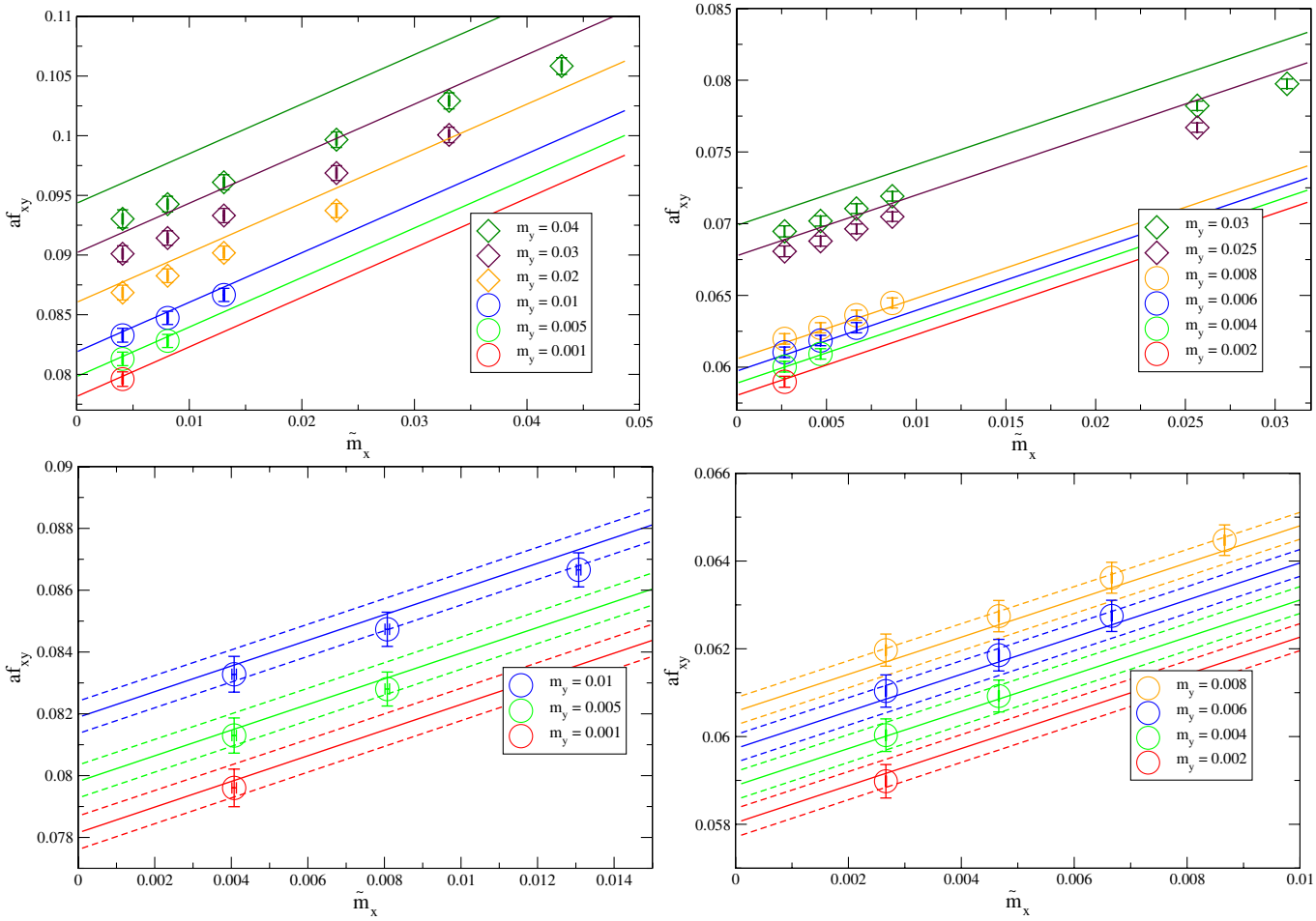

FIG. 34 (color online). Global fits to the lattice data for the pion decay constant obtained using the analytic ansatz in Eq. (52). The top-left and top-right panels correspond to the 24^3, $m_l = 0.005$ and 32^3, $m_l = 0.004$ ensembles, respectively. Points marked by circles are included in the fits, while those with heavier masses marked by diamonds are not. In the bottom two panels we zoom into the low-mass region, illustrating the fits to the points which were included (24^3 points on the left and 32^3 points on the right). (For fixed $\tilde{m}_x$, m_y increases as af_{xy} increases.)

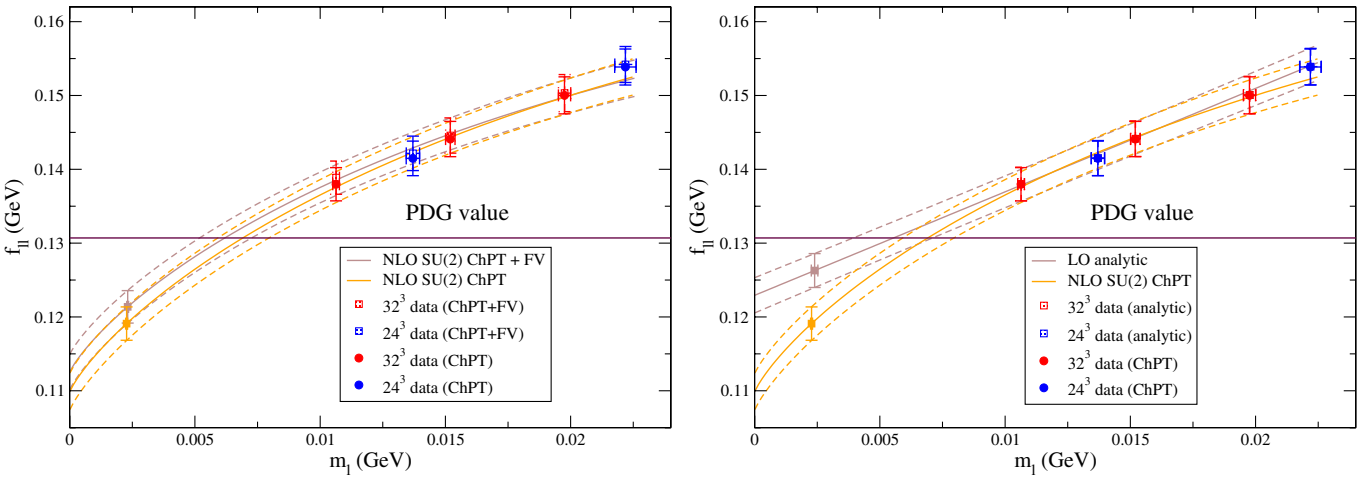

FIG. 35 (color online). Unitary data for f_π adjusted to the continuum limit using each of the fit ansätze. The left panel compares the infinite-volume and finite-volume forms of the NLO SU(2) fit, while the right panel compares the analytic fit to the infinite-volume NLO SU(2) fit. The horizontal solid line indicates the value $f_{\pi^-} = 130.4$ MeV [the authors of Ref. [62] quote $f_{\pi^-} = (130.4 \pm 0.04 \pm 0.2)$ MeV]. In both panels the first, third, and fourth data points from the left (denoted in red) correspond to the 32^3 ensembles and the remaining 2 (denoted in blue) correspond to the 24^3 ones.

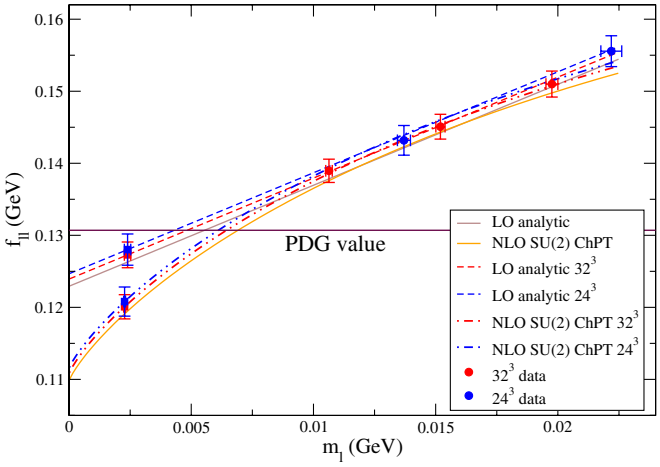

FIG. 36 (color online). Chiral extrapolation of the pion decay constant using the analytic (52) and ChPT (42) fit ansätze. Here, the lattice results from the 24^3 (first and fourth points from the right denoted in blue) and 32^3 (remaining 3 points denoted in red) ensembles are shown along with the mass dependence we infer both at each lattice spacing and in the continuum limit. The consistency of the two ensembles with each other and with this continuum limit is indicative of the size of lattice artefacts. The horizontal solid line indicates the value $f_{\pi^-} = (130.4 \pm 0.04 \pm 0.2)$ MeV [62].

We find that the NLO SU(2) fits underestimate the physical value at our simulated lattice spacings, and that this discrepancy is amplified a little by the extrapolation to the continuum limit. At each of our two lattice spacings, the analytic ansatz extrapolates close to the physical value of f_π, but, with our ansatz for the form of the a^2 effects, the result becomes statistically inconsistent in the continuum limit.

From the above discussion we see that using NLO ChPT to perform the chiral extrapolation for f_π results in a value which is significantly smaller than the physical one. We recall that only data limited to $m_\pi < 420$ MeV was used in the analysis and note that the fits were performed using the chiral expansion with f, the decay constant in the SU(2) chiral limit, included in the expansion parameter $\chi_l/(4\pi f)^2$. The downward curvature at low masses seen in Fig. 35 can, of course, be reduced by replacing the mass-independent f by an artificial larger parameter such as the physical f_π or $f_{ll}(\tilde{m}_l)$ measured at each quark mass used in the simulation. The curvature can also be partially absorbed by using a subset of terms that arise at NNLO. We have experimented with NNLO fits [50] but find that the low-energy constants are insufficiently constrained by our data to be of practical use. Thus the resulting predictions for the physical value of f_π depend strongly on the model assumptions used at NNLO.

The observed $O(10\%)$ deviation found using NLO chiral perturbation theory is broadly consistent with the size of NNLO terms one might expect to be present at masses in the region of our data. Our data for f_π vary from about 20% to 40% above the value of f obtained from our extrapolations and the square of these terms can be taken as being indicative of the expected NNLO terms. We might therefore expect them to be around 5%–15% within our simulated mass range.

The discrepancy of the prediction for the physical value of f_π from the analytic fits is smaller than that found with NLO ChPT, but is nevertheless visible. The results at each of the two lattice spacings are statistically consistent with f_π but lead to an underestimate in the continuum limit. Given the sign of the chiral logarithms at NLO, one might expect a linear ansatz to overestimate rather than underestimate the prediction for the physical value. It is nevertheless striking that one cannot admit any significant nonlinearity in this extrapolation and retain consistency with the physical value for f_π. The simple analytic form used here appears to be a successful phenomenological model which is simpler and has fewer parameters than approaches based on ChPT with arbitrarily chosen analytic subsets of NNLO and NNNLO terms.

It is of interest to pose the scientific question whether any of the fit ansätze could in principal be consistent with the experimentally measured pion decay constant? To answer this question we update the analysis of Ref. [51] and include an artificially created data point for each ensemble that represents the experimental result in the continuum limit but includes our fitted a^2 correction at

TABLE XXXI. Predictions for f_π in GeV for each global fit ansatz at each simulated lattice spacing and in the continuum limit are shown.

	NLO	NLO fv	Analytic
$f_\pi^{24^3}$	0.121(2)	0.123(2)	0.128(2)
$f_\pi^{32^3}$	0.120(2)	0.122(2)	0.127(2)
$f_\pi^{\text{continuum}}$	0.119(2)	0.121(2)	0.126(2)

TABLE XXXII. Predictions for f_K in GeV for each global fit ansatz at each simulated lattice spacing and in the continuum limit are shown.

	NLO	NLO fv	Analytic
$f_K^{24^3}$	0.147(2)	0.148(2)	0.152(2)
$f_K^{32^3}$	0.147(2)	0.148(2)	0.151(2)
$f_K^{\text{continuum}}$	0.146(2)	0.147(2)	0.151(2)

TABLE XXXIII. Predictions for f_K/f_π for each global fit ansatz at each simulated lattice spacing and in the continuum limit are shown.

	NLO	NLO fv	Analytic
$(f_K/f_\pi)^{24^3}$	1.216(9)	1.205(9)	1.184(9)
$(f_K/f_\pi)^{32^3}$	1.221(6)	1.209(6)	1.188(6)
$(f_K/f_\pi)^{\text{continuum}}$	1.229(8)	1.215(7)	1.194(7)

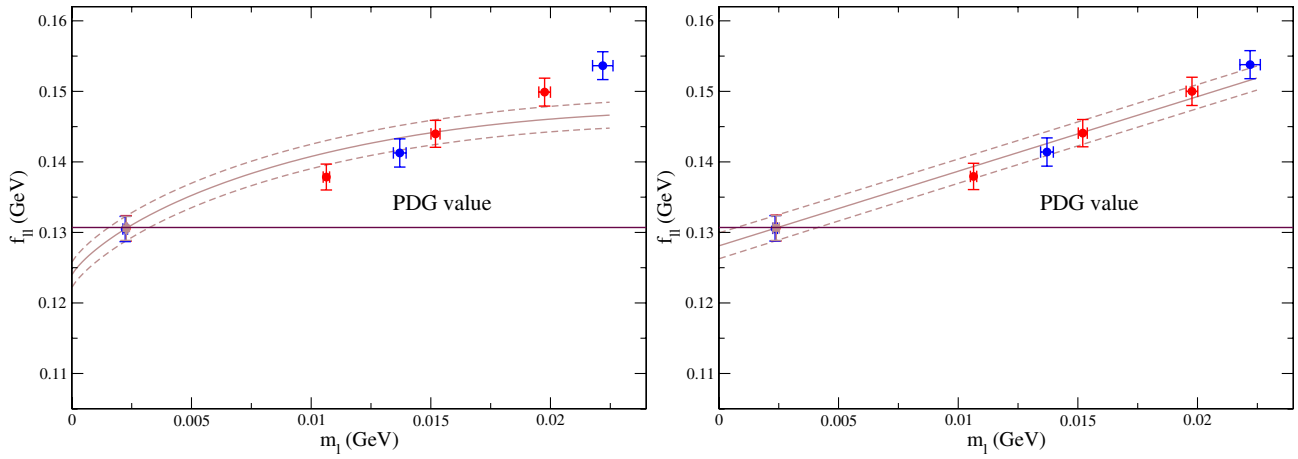

FIG. 37 (color online). An artificial data point (the left-most data point in each panel) corresponding to the physical value of f_π [62], but including our uncertainties in the lattice spacing, is added to the data for the pion decay constant from the five ensembles. The left-hand panel corresponds to the NLO SU(2) ChPT fits and the right-hand panel to the analytic ansatz. In both panels the first, third, and fourth data points from the left (denoted in red) correspond to the 32^3 ensembles and the remaining 2 (denoted in blue) correspond to the 24^3 ones.

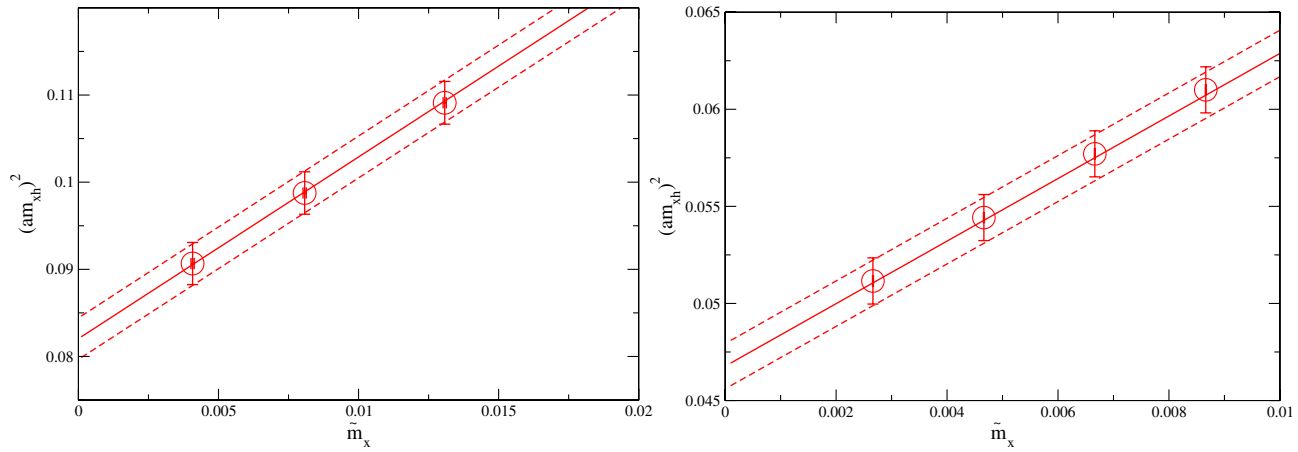

FIG. 38 (color online). Dependence of the kaon mass on the mass of the light valence quark with fits performed using infinite-volume NLO partially quenched ChPT. The left panel shows the results from the 24^3, $m_l = 0.005$ ensemble and the right panel from the 32^3, $m_l = 0.004$ ensemble. In each case the results are for the physical strange-quark mass.

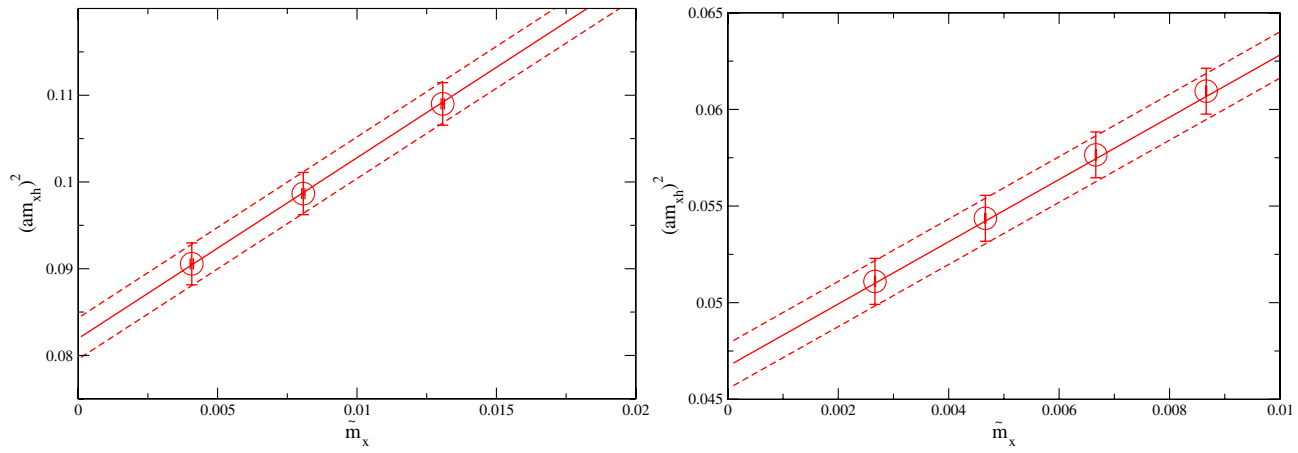

FIG. 39 (color online). Dependence of the kaon mass on the mass of the light valence quark with fits performed using finite-volume NLO partially quenched ChPT. The left panel shows the results from the 24^3, $m_l = 0.005$ ensemble and the right panel from the 32^3, $m_l = 0.004$ ensemble. In each case the results are for the physical strange-quark mass.

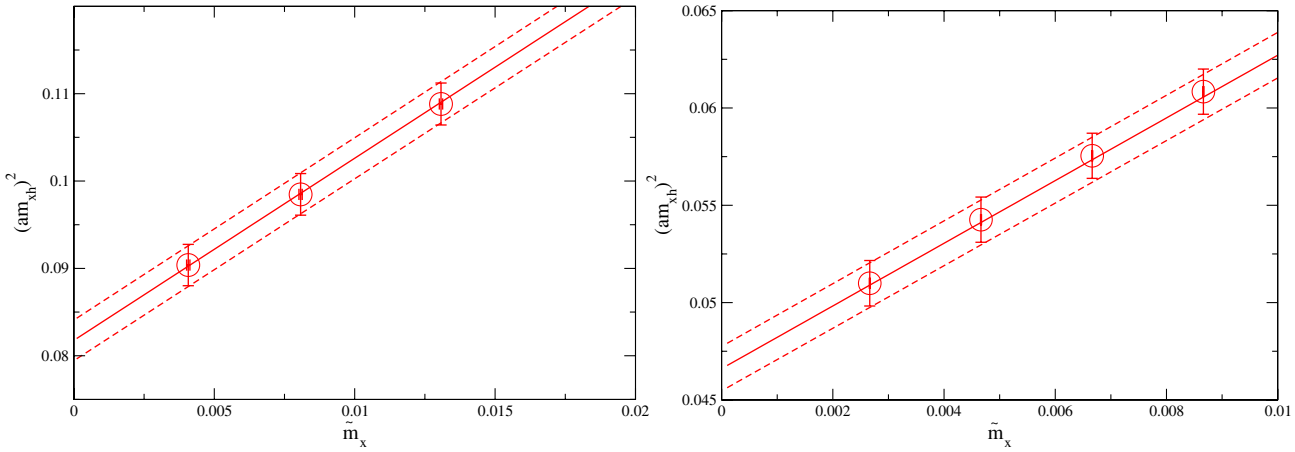

FIG. 40 (color online). Dependence of the kaon mass on the mass of the light valence quark with fits performed using the analytic fit ansatz. The left panel shows the results from the 24^3, $m_l = 0.005$ ensemble and the right panel from the 32^3, $m_l = 0.004$ ensemble. In each case the results are for the physical strange-quark mass.

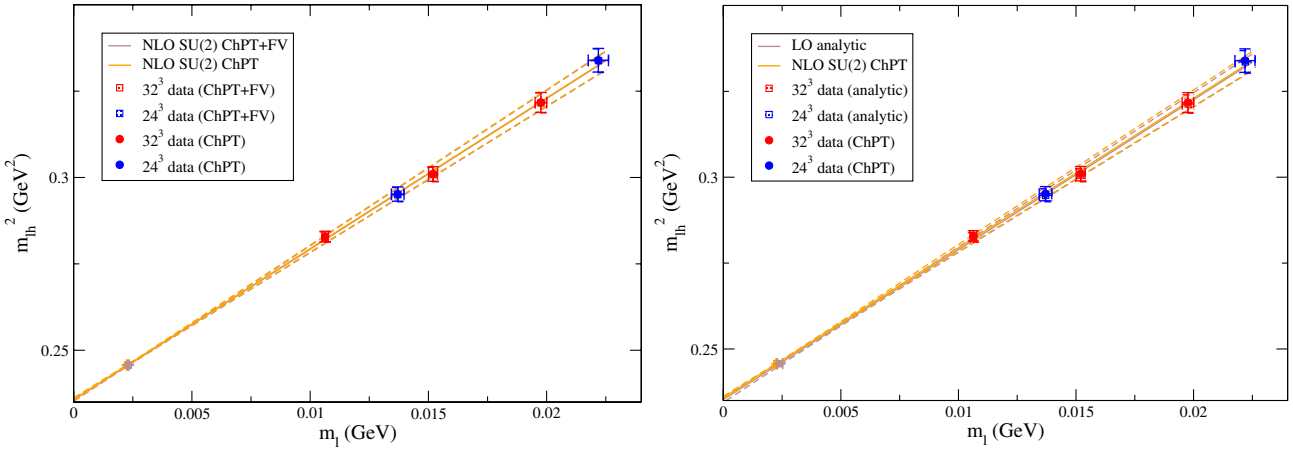

FIG. 41 (color online). Chiral extrapolation of the kaon mass using unitary data points adjusted to the continuum limit by the fitting ansätze. Here we compare results obtained using the infinite-volume NLO ChPT ansatz to that using finite-volume logarithms (left panel) and to the analytic ansatz (right panel). In both panels the first, third, and fourth data points from the left (denoted in red) correspond to the 32^3 ensembles and the remaining 2 (denoted in blue) correspond to the 24^3 ones.

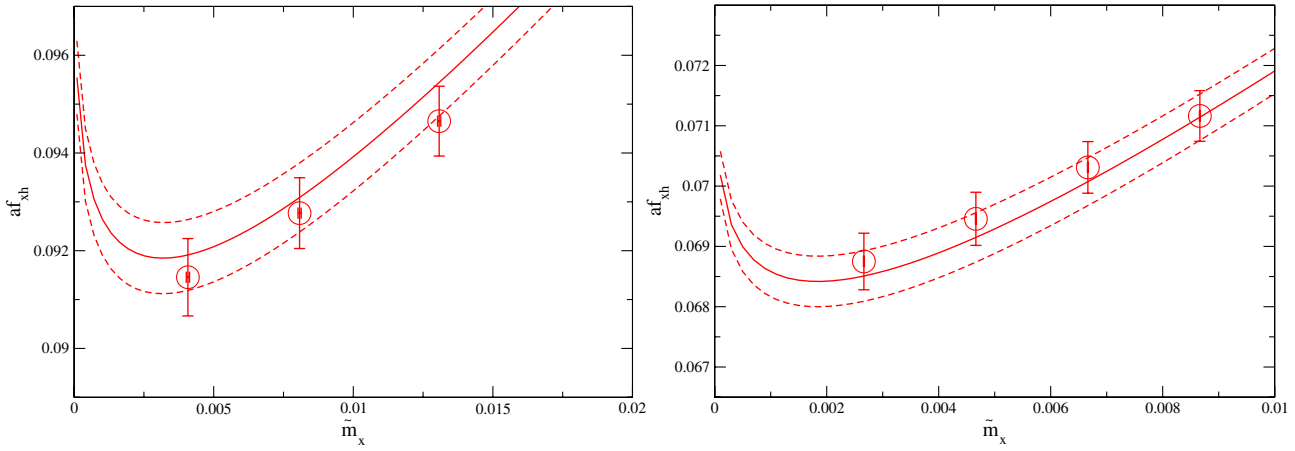

FIG. 42 (color online). Dependence of the kaon decay constant on the mass of the light valence quark with fits performed using infinite-volume partially quenched NLO ChPT. The left panel shows the results from the 24^3, $m_l = 0.005$ ensemble and the right panel from the 32^3, $m_l = 0.004$ ensemble. In each case the results are for the physical strange-quark mass.

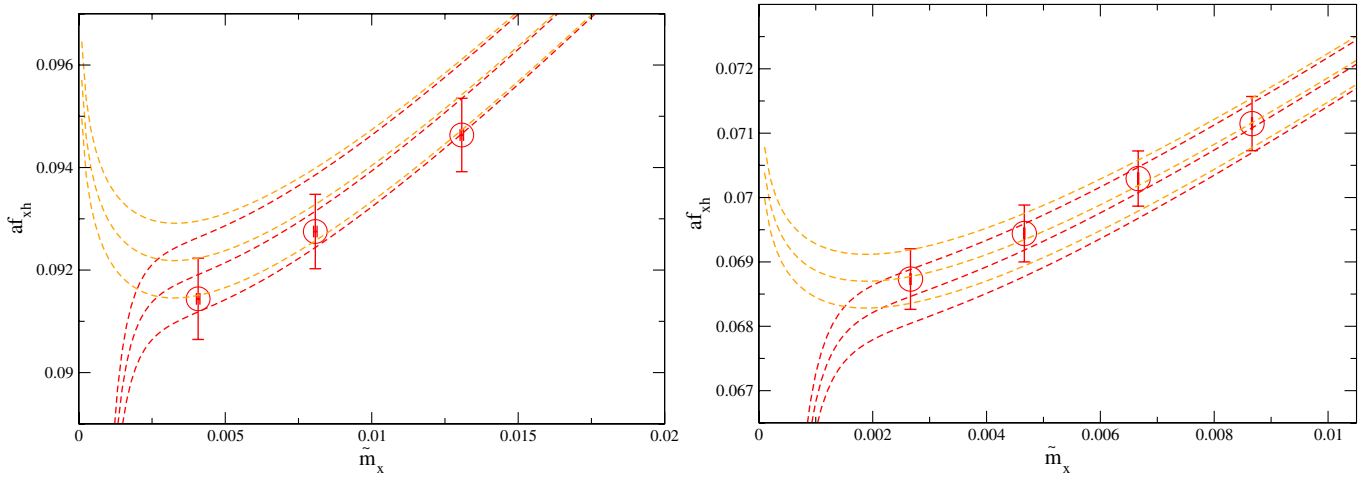

FIG. 43 (color online). Dependence of the kaon decay constant on the mass of the light valence quark. The left panel shows the results from the 24^3, $m_l = 0.005$ ensemble and the right panel from the 32^3, $m_l = 0.004$ ensemble. In each case the results are for the physical strange quark mass. There are two curves plotted. The orange curve which turns up at low masses is the result one infers for the infinite volume, while the red curve which turns down at low masses is the result we obtain on the finite volume. As we do not adjust our data for finite volume effects, the finite-volume curve should go through our data. The infinite-volume curve also goes through our data which is an indication that the finite-volume effects in our data are substatistical, and the difference between the two curves at lighter masses indicates that one should expect substantial finite-volume effects *if* one were to simulate at these lighter masses without changing our present volume.

each nonzero lattice spacing. This is displayed in Fig. 37 and we find that the analytic ansätze could be consistent with an uncorrelated $\chi^2/\text{dof} = 1.9(7)$, while NLO ChPT would fail to simultaneously fit our data and the physical point, with $\chi^2/\text{dof} = 6(1)$ (infinite volume) and $\chi^2/\text{dof} = 5(1)$ (finite volume).

Of course, improved statistical errors, simulations at a third lattice spacing and larger physical volumes would give us better control of the continuum extrapolation and finite-volume effects. However, our main conclusion is that it is imperative to simulate with masses substantially nearer to the physical point; this will constrain both fit forms to give more consistent predictions. Ultimately simulations will be performed directly at physical quark masses and will eliminate this error completely. We are currently generating new ensembles with a coarser lattice spacing, with a substantially larger volume and with very much lighter pion masses (for a preliminary discussion of these configurations see Ref. [52]) precisely to address this issue.

As an estimate of the systematic uncertainties in physical quantities we take the difference between the results obtained using linear and finite-volume NLO ChPT analyses. This allows for the possible validity of the full NLO nonanalyticity in the region of masses between the data and the physical point but also recognizes that part of this extrapolation may be outside the range of validity of

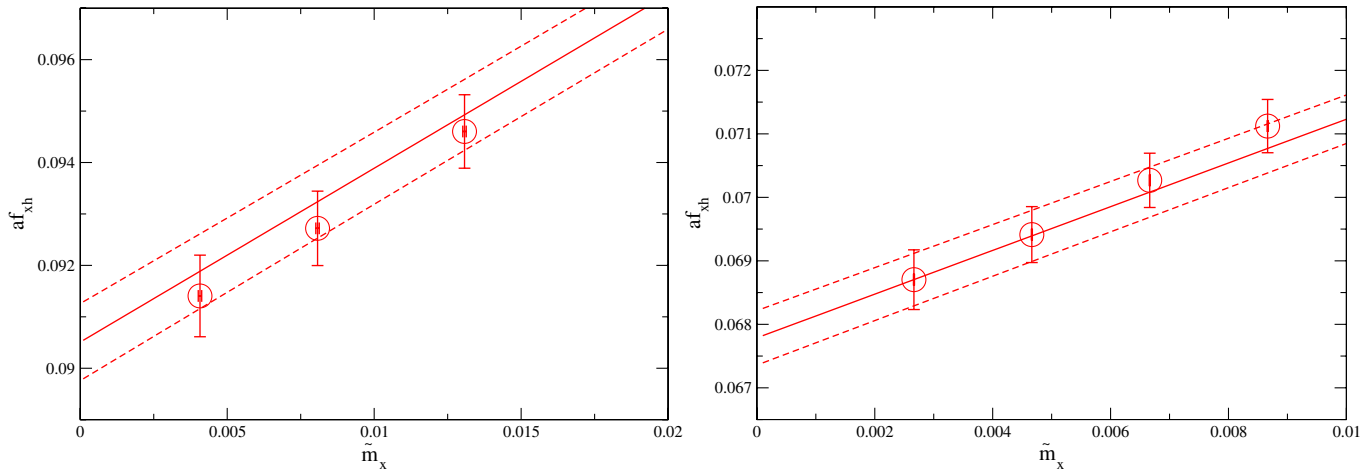

FIG. 44 (color online). Dependence of the kaon decay constant on the mass of the light valence quark with fits performed using the analytic fit ansatz. The left panel shows the results from the 24^3, $m_l = 0.005$ ensemble and the right panel from the 32^3, $m_l = 0.004$ ensemble. In each case the results are for the physical strange-quark mass.

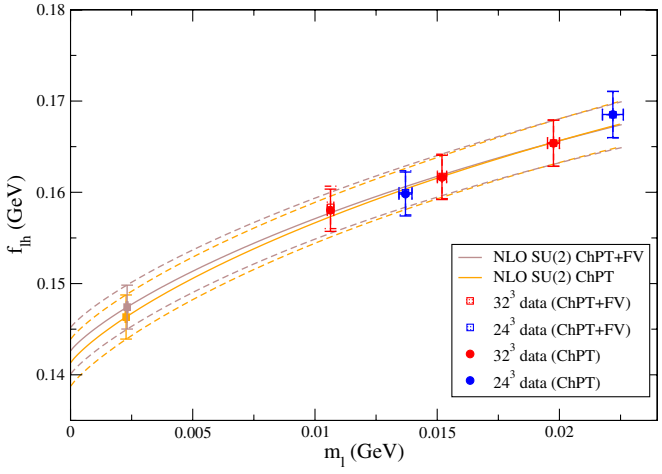

FIG. 45 (color online). Chiral extrapolation of the kaon decay constant for unitary data in the continuum limit. We compare the NLO ChPT ansatz to the corresponding ansatz with finite-volume logarithms. Of the five data points, the first, third, and fourth from the left (denoted in red) correspond to the 32^3 ensembles and the remaining 2 (denoted in blue) correspond to the 24^3 ones.

NLO ChPT as suggested by the observation that the present data is surprisingly consistent with linear behavior. Guided by the results for f_π discussed above, we take as our central values for phenomenological predictions the average of the results obtained from our finite-volume NLO ChPT fits and our analytic fits.

4. Chiral and continuum behavior of the mass of the kaon

We display our fits using infinite-volume NLO SU(2) partially quenched ChPT in Fig. 38. Figure 39 displays the corresponding fits of the same data with the finite-volume corrections included, while the analytic fits are displayed in Fig. 40. The corresponding unitary view of the data in the continuum limit is shown in Fig. 41. All these plots are for results at the physical sea strange-quark mass.

5. Chiral and continuum behavior of f_K

We next discuss f_K, the decay constant of the kaon. We display our fits using infinite-volume NLO SU(2) partially quenched ChPT in Fig. 42. The following two figures display fits of the same partially quenched data to ChPT with finite-volume corrections (Fig. 43) and to the global analytic fit ansatz (Fig. 44). The NLO ChPT fit ansätze, both with and without finite-volume logarithms, are displayed for the unitary data adjusted to the continuum limit in Fig. 45.

The two panels in Fig. 46 display the chiral behavior of the actual unitary data from the two sets of ensembles (left panel) as well as of the data adjusted to the continuum limit (right panel).

From these fits our final predictions for f_K are given in Table XXXII, and the corresponding results for $\frac{f_K}{f_\pi}$ in Table XXXIII.

6. Predictions

We now present our results for f_π, f_K and their ratio as well as for the physical bare-quark masses. As discussed above, our central value for any physical quantity is taken to be the average of the results obtained from analyses using the NLO SU(2) ChPT fit with finite-volume corrections and those from the analytic fit. The difference between the analytic and finite-volume NLO SU(2) fits is taken as a systematic error. This procedure includes a NLO finite-volume correction, estimated from the difference between results obtained using NLO ChPT at infinite and

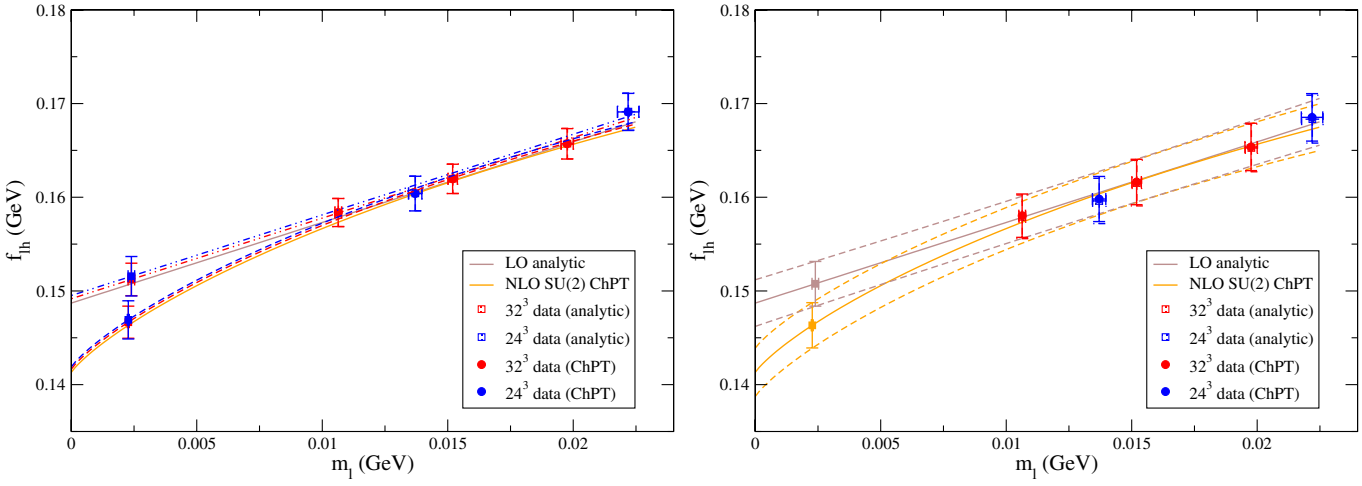

FIG. 46 (color online). Chiral extrapolation of the kaon decay constant for unitary data in the continuum limit. We compare the NLO ChPT ansatz to the analytic ansatz. The left panel displays the data and fits at nonzero lattice spacing, while the right panel displays the predicted results and correspondingly adjusted data points for the continuum limit. In both panels the first, third, and fourth data points from the left (denoted in red) correspond to the 32^3 ensembles and the remaining 2 (denoted in blue) correspond to the 24^3 ones.

finite volumes, and which is much smaller than the total systematic error here.

Our predictions for pseudoscalar decay constants therefore contain systematic errors for finite-volume effects, the chiral extrapolation, and residual chiral symmetry breaking, while the discretization error is included indirectly by the fitting procedure:

$$f_\pi^{\text{continuum}} = 124(2)(5)\ \text{MeV}, \tag{61}$$

$$f_K^{\text{continuum}} = 149(2)(4)\ \text{MeV}, \tag{62}$$

$$(f_K/f_\pi)^{\text{continuum}} = 1.204(7)(25), \tag{63}$$

where we display the statistical and systematic errors separately. We note that the known, experimental value of f_π influenced our choice to take the central value of physical quantities as the average of the results from the analytic and finite-volume NLO ChPT ansätze. The prediction for f_π cannot therefore be considered unbiased, however, as our aim is to select the most likely central value for phenomenologically important quantities such as f_K/f_π and B_K our procedure is both appropriate and contains a prudent systematic error.

Applying the same procedure to obtain predictions for the physical bare-quark masses for the $\beta = 2.25$ 32^3 ensembles, we find:

$$\tilde{m}_{ud} = 2.35(8)(9)\ \text{MeV} \quad \text{and} \quad \tilde{m}_s = 63.7(9)(1)\ \text{MeV}, \tag{64}$$

and these will be renormalized in the following section. The corresponding bare masses for the $\beta = 2.13$ 24^3 ensembles can be obtained by dividing the results in (64) by the values of Z_l and Z_h in Table XXVI.

7. Chiral and continuum behavior of r_0 and r_1

Finally, in this section we apply the combined chiral/continuum extrapolation procedure to the scales r_0 and r_1. Assuming a linear dependence for the light sea-quark mass dependence, and including a leading-order a^2 term as before, the scales are independently fit to the form

$$r_i = c_{r_i} + c_{r_i,a}a^2 + c_{r_i,m_l}\tilde{m}_l, \tag{65}$$

where $i = 0, 1$. Prior to the fit, the data are linearly interpolated to each of the physical strange-quark masses obtained from the global fits and presented in Table XXX, and the fit and the subsequent extrapolation are performed using the corresponding physical light-quark mass and lattice spacings.

The parameters and χ^2/d.o.f of the fits are given in Tables XXXIV and XXXV, respectively, and plots showing the fits overlaying the data in the continuum limit are shown in Fig. 47. The fits to r_0 appear to describe the data well by eye, and have a reasonable (uncorrelated) χ^2/d.o.f for the central value, but with a large deviation across the superjackknife distribution. The fits to r_1 also appear to describe the data reasonably well, although there does seem to be a tension with the heaviest point on the 24^3 ensembles, which is likely responsible for the larger χ^2/d.o.f. As there are only five data points it is difficult

TABLE XXXIV. Parameters of the chiral/continuum fits to r_0 and r_1 are shown.

(a) r_0

Parameter	ChPT	ChPT fv	Analytic
c_{r_0}	2.468(41) GeV^{-1}	2.468(41) GeV^{-1}	2.467(41) GeV^{-1}
$c_{r_0,a}$	−0.25(14) GeV	−0.25(14) GeV	−0.25(14) GeV
c_{r_0,m_l}	0.42(1.23) GeV^{-2}	0.44(1.23) GeV^{-2}	0.47(1.23) GeV^{-2}

(b) r_1

Parameter	ChPT	ChPT-fv	Analytic
c_{r_1}	1.694(29) GeV^{-1}	1.694(29) GeV^{-1}	1.693(29) GeV^{-1}
$c_{r_1,a}$	−0.15(11) GeV	−0.15(11) GeV	−0.15(12) GeV
c_{r_1,m_l}	−1.76(64) GeV^{-2}	−1.76(64) GeV^{-2}	−1.76(64) GeV^{-2}

TABLE XXXV. χ^2/d.o.f of the chiral/continuum fits to r_0 and r_1 is shown.

Quantity	ChPT	ChPT-fv	Analytic
r_0	1.35(1.66)	1.34(1.65)	1.31(1.63)
r_1	2.69(2.39)	2.68(2.38)	2.66(2.37)

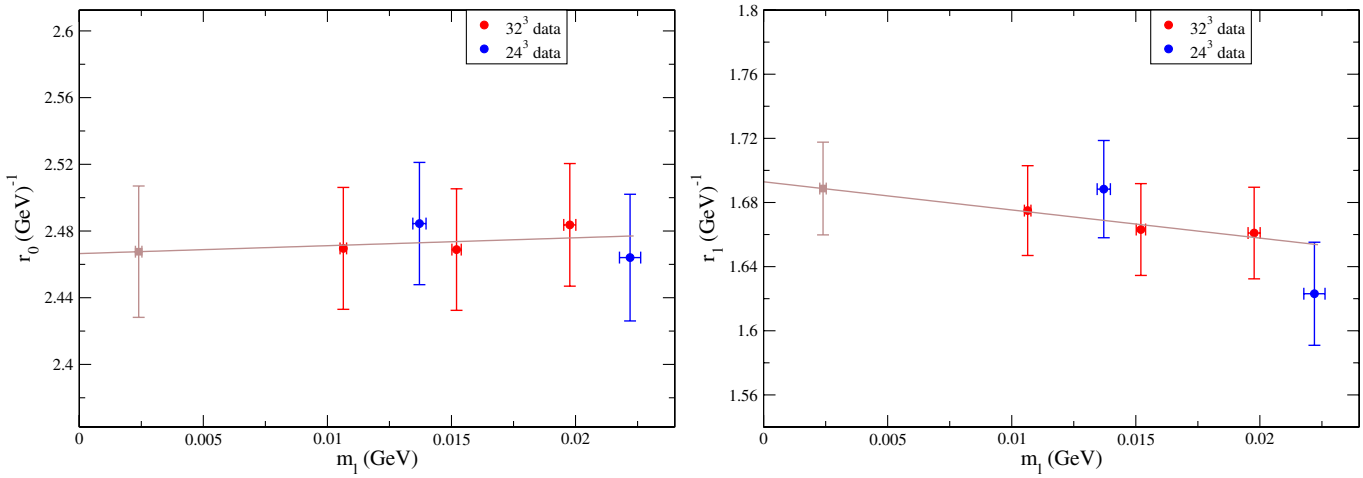

FIG. 47 (color online). The scales r_0 (left) and r_1 (right) corrected to the continuum limit, overlaid by the chiral/continuum fit. Of the five data points, the first, third and fourth from the left (denoted in red) correspond to the 32^3 ensembles and the remaining 2 (denoted in blue) correspond to the 24^3 ones. The extrapolated point at the physical light-quark mass is shown as the grey cross on the left. Here the lattice spacings and physical light-quark mass were obtained from the global fits using the analytic ansatz. The fits using the quantities obtained with the ChPT and ChPT-fv global fit ansätze are almost indistinguishable from those shown in these figures.

to reach any stronger conclusions regarding the data: more ensembles and better statistics are needed. For the purpose of quoting a final result, we apply a PDG scale factor of $\sqrt{\chi^2/\text{d.o.f}}$ to the statistical errors on each of the results. In order to retain the correlations between these quantities when the ratio is taken, the scale factor is applied to the difference of each jackknife sample from the mean.

The continuum results for r_0, r_1 and their ratio at physical quark masses are given in Table XXXVI. Using the procedure for combining the results obtained using the different chiral ansätze outlined in Sec. V E 3 and applying the PDG scale factor as above, gives

$$\begin{aligned} r_0 &= 2.468(45)_{\text{stat}}(1)_{\text{FV}}(1)_{\chi}\ \text{GeV}^{-1} \\ &= 0.4870(89)_{\text{stat}}(2)_{\text{FV}}(2)_{\chi}\ \text{fm}, \\ r_1 &= 1.689(47)_{\text{stat}}(0)_{\text{FV}}(1)_{\chi}\ \text{GeV}^{-1} \\ &= 0.3333(93)_{\text{stat}}(1)_{\text{FV}}(2)_{\chi}\ \text{fm}, \\ \text{and} \quad r_1/r_0 &= 0.684(15)_{\text{stat}}(0)_{\text{FV}}(0)_{\chi}, \end{aligned} \tag{66}$$

where the finite-volume error arising from the different determinations of the lattice spacings and quark masses is smaller than the quoted precision on the ratio. χ labels the error due to the chiral extrapolation. For comparison, the MILC Collaboration recently obtained $r_1 = 0.3117(6)(^{+12}_{-31})$ fm $[\simeq 1.580(3)(^{+6}_{-16})\ \text{GeV}^{-1}]$ [53], and also $r_1 = 0.317(7)(3)$ fm $[\simeq 1.61(4)(2)\ \text{GeV}^{-1}]$ and $r_0 = 0.462(11)(4)$ fm $[\simeq 2.34(6)(2)\ \text{GeV}^{-1}]$ from an earlier study [54]. At this time we do not have an explanation of the discrepancy between our results in (66) and those of the MILC Collaboration beyond noting the very different approaches to setting the scale and performing the chiral extrapolation.

VI. LIGHT-QUARK MASSES

The quark masses quoted in Eq. (64) are the bare masses for the lattice action which we are using on the 32^3 ensembles with $\beta = 2.25$ corresponding to a lattice spacing $a^{-1} \simeq 2.28$ GeV. In order to be useful in phenomenological applications these results must be translated into renormalized masses in some standard continuum scheme. Therefore in Sec. VI A we determine the renormalization constants relating the bare masses in (64) to those renormalized in the $\overline{\text{MS}}$ scheme at a renormalization scale of 2 GeV. In Sec. VI B we then combine these renormalization constants with the bare masses in (64) to obtain the renormalized masses, the LO LEC $B^{\overline{\text{MS}}}(2\ \text{GeV})$ and the chiral condensate.

TABLE XXXVI. Continuum values of r_0 and r_1 and the ratio r_1/r_0 at physical quark masses determined from a chiral/continuum fit using the lattice spacings and quark masses obtained from the global fits are shown.

Quantity	ChPT	ChPT-fv	Analytic
r_0	2.469(39) GeV^{-1}	2.469(39) GeV^{-1}	2.468(39) GeV^{-1}
r_1	1.690(29) GeV^{-1}	1.690(29) GeV^{-1}	1.689(29) GeV^{-1}
r_1/r_0	0.6844(96)	0.6844(97)	0.6843(97)

A. Nonperturbative renormalization for quark masses

The quark mass renormalization factor which relates the lattice bare quark mass to that in the $\overline{\mathrm{MS}}$ scheme is determined using nonperturbative renormalization (NPR) with the RI/SMOM schemes proposed in Ref. [15] as intermediate schemes. This is an extension of the Rome-Southampton NPR program in which the RI/MOM scheme was defined [45]. Quark masses renormalized in the symmetric MOM scheme (RI/SMOM) defined in [15] or the original RI/MOM scheme [45] are obtained entirely nonperturbatively. Since it is not possible to simulate in a noninteger number of dimensions, continuum perturbation theory is needed to match the results in either the RI/SMOM or the RI/MOM scheme and the target $\overline{\mathrm{MS}}$ scheme. We stress however, that we completely avoid the use of lattice perturbation theory which often converges more slowly than continuum perturbation theory (PT). Since RI/MOM and any of the schemes proposed in [15] are legitimate renormalization schemes, we exploit the freedom to choose an intermediate scheme to reduce its effect on the final result for the renormalized quark mass in the $\overline{\mathrm{MS}}$ scheme and to have a better understanding of this uncertainty.

Our earlier study [14], used to normalize the quark mass on the 24^3 ensembles, applied the RI/MOM scheme to renormalize the quark masses and suffered from sizable systematic errors with two dominant sources. One of these is the truncation error in the perturbative continuum matching between the RI/MOM and $\overline{\mathrm{MS}}$ schemes. This was estimated to be 6% for $\mu = 2$ GeV from the relative size of the highest-order term used (3 loop). The other is a nonperturbative effect arising because the strange-quark mass is fixed close to its physical value, and the chiral limit is not taken for this quark. We estimated the corresponding systematic error on the quark mass renormalization factor for $a^{-1} = 1.73$ GeV and $\mu = 2$ GeV to be about 7%. As the strange-quark mass and the typical scale of spontaneous chiral symmetry breaking are almost the same, this error can be viewed as a general error due to contamination of nonperturbative effects (NPE). It was shown in Ref. [14] that changing the kinematics of momenta used to define the NPR scheme greatly reduces the contamination from unwanted nonperturbative effects and this will be discussed below. The actual implementation of the schemes with unconventional kinematics has been done in Ref. [15] carefully ensuring that the Ward-Takahashi chiral identities are satisfied. A pilot study [55] using the new schemes demonstrated that it is a promising alternative to the conventional RI/MOM scheme with reduced systematic errors. In the present article we use two RI/SMOM schemes proposed in Ref. [15]. Preliminary results have been reviewed in Ref. [56].

An important technical improvement introduced since the previous study [14] is the use of volume momentum sources for the quark propagators. This helps to reduce the statistical error greatly and in addition reduces the systematic error due to the dependence on the position of the local source used in [14]. More details about the use of momentum sources can be found in Ref. [35].

The mass renormalization factor Z_m is conveniently calculated using the relation

$$Z_m = 1/Z_S = 1/Z_P, \tag{67}$$

where Z_m, Z_S, Z_P are the quark mass, flavor nonsinglet scalar, and pseudoscalar renormalization factors, respectively. Here we are exploiting the important chiral symmetry properties of DWF. Our convention is that the renormalization factors multiply the bare quantities to yield renormalized ones:

$$m_R = Z_m \tilde{m}, \quad P_R^a = Z_P P^a, \quad S_R^a = Z_S S^a, \tag{68}$$

where the left-hand sides are the renormalized mass, pseudoscalar and scalar densities, and a is a flavor label. $\tilde{m}$ in Eq. (68) is in physical units. The relations in Eq. (67) are necessary for the Ward-Takahashi identities to hold for the renormalized operators. The RI/MOM renormalization condition on the amputated scalar vertex Π_S reads

$$\frac{Z_S}{Z_q}\frac{1}{12}\,\mathrm{Tr}[\Pi_S \cdot I] = 1. \tag{69}$$

Z_q is the wave function renormalization factor, which can be determined using the trace condition on the local vector operator,

$$\frac{Z_V}{Z_q}\frac{1}{48}\,\mathrm{Tr}[\Pi_{V_\mu} \cdot \gamma_\mu] = 1. \tag{70}$$

The vertex functions Π depend on the incoming and outgoing momenta on the two fermion lines, $\Pi(p_{\mathrm{in}}, p_{\mathrm{out}})$. The conventional RI/MOM scheme is defined using the forward vertex with $p_{\mathrm{in}} = p_{\mathrm{out}} = p$. The renormalization conditions, Eqs. (69) and (70), are applied by setting the renormalization scale μ to be the off-shell external momentum, $\mu^2 = p^2$, in the chiral limit.

It is in principle possible to determine $Z_S(= Z_P)$ using the pseudoscalar vertex function instead of the scalar one in Eq. (69). However, with the original RI/MOM choice for the external momenta, the pseudoscalar vertex couples to the zero-momentum pion, and the Green function diverges as $1/m_q$ as the quark mass $m_q \to 0$ at fixed p [57]. Therefore the pseudoscalar vertex cannot be used without some manipulation of the divergence (see, e.g., [58]) and has not been considered in our previous publication [14]. This is in contrast with the RI/SMOM schemes described below which do not have such a pole as $m_q \to 0$. Similarly, the axial-vector vertex can be used to determine Z_q because $Z_V = Z_A$. However, Z_q obtained using the vector and axial-vector vertices at large but finite p^2 will differ because of the coupling of the axial current to the Goldstone boson [45]. These differences are known to be of $O(1/p^2)$ at high momentum from the operator product expansion [45,57] or from Weinberg's theorem of power counting for

a Feynman diagram [14]. In Ref. [14], the average of the vector and the axial-vector vertex was used to determine Z_q and the difference was included in the systematic error, though the corresponding 1% error is subdominant.

The caveats mentioned in the two preceding paragraphs are both connected to the RI/MOM scheme and its channel with an "exceptional momentum"; specifically, the momentum transfer $q \equiv p_{\rm in} - p_{\rm out} = 0$. This is the reason for the large NPE error. It was demonstrated that the use of nonexceptional momenta $p_{\rm in} - p_{\rm out} \neq 0$ reduces the NPE effect significantly. The RI/SMOM schemes are designed so that all channels have nonexceptional momenta. For quark bilinear operators we choose to have $p_{\rm in}^2 = p_{\rm out}^2 = q^2$ and hence introduce the name "symmetric MOM" (SMOM) schemes. The two schemes RI/SMOM and RI/SMOM$_{\gamma_\mu}$ are defined with this kinematical choice but differ in the Γ-projection operators which are used to define the wave function renormalization. For the vector (axial-vector) vertex function the projector $\not{q} q_\mu/q^2$ ($\gamma_5 \not{q} q_\mu/q^2$) is used in the RI/SMOM scheme and γ_μ ($\gamma_5\gamma_\mu$) as in Eq. (70) is used for RI/SMOM$_{\gamma_\mu}$. The standard I (γ_5) spinor projector is used for the scalar (pseudoscalar) vertex in both new schemes.

The conversion factors from the RI/SMOM and RI/SMOM$_{\gamma_\mu}$ schemes to $\overline{\rm MS}$ have been calculated at one-loop order in Ref. [15] and recently to two-loop order [16,17]:

$$\begin{aligned} &C_m(\mathrm{RI/SMOM} \to \overline{\mathrm{MS}}, \mu) \\ &= 1 - \left(\frac{\alpha_s(\mu)}{4\pi}\right) 0.646 \\ &\quad - \left(\frac{\alpha_s(\mu)}{4\pi}\right)^2 (22.608 + 4.014 n_f) \ldots, \end{aligned} \tag{71}$$

$$\begin{aligned} &C_m(\mathrm{RI/SMOM}_{\gamma_\mu} \to \overline{\mathrm{MS}}, \mu) \\ &= 1 - \left(\frac{\alpha_s(\mu)}{4\pi}\right) 1.979 - \left(\frac{\alpha_s(\mu)}{4\pi}\right)^2 (55.032 + 6.162 n_f) \ldots, \end{aligned} \tag{72}$$

where the coefficients have been rounded to the third decimal place. Evaluating these factors at $\mu = 2$ GeV we have

$$\begin{aligned} &C_m(\mathrm{RI/SMOM} \to \overline{\mathrm{MS}}, \mu = 2\ \mathrm{GeV}, n_f = 3) \\ &\quad = 1 - 0.015 - 0.006 \ldots, \end{aligned} \tag{73}$$

$$\begin{aligned} &C_m(\mathrm{RI/SMOM}_{\gamma_\mu} \to \overline{\mathrm{MS}}, \mu = 2\ \mathrm{GeV}, n_f = 3) \\ &\quad = 1 - 0.046 - 0.020 \ldots. \end{aligned} \tag{74}$$

In the RI/MOM and RI′/MOM schemes the conversion factors are known to three-loop order [59,60]:

$$\begin{aligned} &C_m(\mathrm{RI/MOM} \to \overline{\mathrm{MS}}, \mu = 2\ \mathrm{GeV}, n_f = 3) \\ &\quad = 1 - 0.123 - 0.070 - 0.048 + \ldots, \end{aligned} \tag{75}$$

$$\begin{aligned} &C_m(\mathrm{RI'/MOM} \to \overline{\mathrm{MS}}, \mu = 2\ \mathrm{GeV}, n_f = 3) \\ &\quad = 1 - 0.123 - 0.065 - 0.044 + \ldots. \end{aligned} \tag{76}$$

We note that, at least up to two-loop order, the convergence of the series relating the new SMOM schemes to $\overline{\rm MS}$ is considerably better than for the RI/MOM scheme. As already mentioned, the truncation error of the RI/MOM scheme was estimated from the size of the highest-order term available (3 loop). Having, in addition, two intermediate SMOM schemes, we can expect to have a more reliable estimate of the truncation error.

We now turn to the numerical evaluation of the renormalization factors. At each value of β, we use data obtained at the three light-quark masses: $m_l = 0.004$, 0.006, and 0.008 for the finer 32^3 lattice and $m_l = 0.005$, 0.01, and 0.02 for the coarser 24^3 lattice. 20 configurations were analyzed for each point. The ratio of quark wave function and local axial current renormalization factors is calculated from the average of vector and axial-vector vertex functions,

$$\frac{Z_q}{Z_V} = \frac{1}{2}(\Lambda_V + \Lambda_A), \tag{77}$$

with projected and traced vertex functions:

$$\begin{aligned} \Lambda_V^{\mathrm{RI/SMOM}} &= \frac{1}{12\hat{q}^2}\,\mathrm{Tr}[\Pi_{V_\mu} \cdot \hat{\not{q}} \hat{q}_\mu] \quad \text{and} \\ \Lambda_A^{\mathrm{RI/SMOM}} &= \frac{1}{12\hat{q}^2}\,\mathrm{Tr}[\Pi_{A_\mu} \cdot \gamma_5 \hat{\not{q}} \hat{q}_\mu], \end{aligned} \tag{78}$$

for the RI/SMOM scheme. Here q_μ in the continuum RI/SMOM scheme [15] has been replaced with the $\hat{q}_\mu = \sin(q_\mu)$, as the derivative for the divergence of the current in the continuum theory is naturally replaced by the symmetric difference on the lattice. A remarkable feature of the RI/SMOM scheme is that in the chiral limit $\Lambda_V = \Lambda_A$ holds nonperturbatively, in contrast to $\Lambda_V \neq \Lambda_A$ for the RI/MOM scheme due to spontaneous symmetry breaking. In principle there could still be a small difference for the lattice RI/SMOM scheme with nonzero $m_{\rm res}$, which, however, is negligible in the momentum range we use [55]. Using the continuum Ward-Takahashi identities, one can also show the equivalence of Z_q in the RI/SMOM and RI′/MOM schemes [15].

The RI/SMOM$_{\gamma_\mu}$ scheme is defined using the conventional projectors,

$$\Lambda_V^{\mathrm{RI/SMOM}_{\gamma_\mu}} = \tfrac{1}{48}\mathrm{Tr}[\Pi_{V_\mu} \cdot \gamma_\mu] \quad \text{and}$$
$$\Lambda_A^{\mathrm{RI/SMOM}_{\gamma_\mu}} = \tfrac{1}{48}\mathrm{Tr}[\Pi_{A_\mu} \cdot \gamma_5\gamma_\mu]. \tag{79}$$

Although these projectors are superficially the same as those used in the RI/MOM scheme, it should be remembered that the kinematics is different in the two cases with no exceptional channels in the Green functions used to define the $\mathrm{RI/SMOM}_{\gamma_\mu}$ scheme.

The product of mass and wave function renormalization factors is calculated from the average of scalar and pseudoscalar vertex functions,

$$Z_m Z_q = \tfrac{1}{2}(\Lambda_S + \Lambda_P), \tag{80}$$

with

$$\Lambda_S = \tfrac{1}{12}\mathrm{Tr}[\Pi_S \cdot 1] \quad \text{and} \quad \Lambda_P = \tfrac{1}{12}\mathrm{Tr}[\Pi_P \cdot \gamma_5], \tag{81}$$

again defined with the SMOM kinematics for the vertex functions. While $\Lambda_S = \Lambda_P$ holds to all orders in perturbation theory with naive dimensional regularization, by using Weinberg's power-counting scheme we see that they can in general differ by terms of $O(1/p^6)$ [14]. The difference $\Lambda_P - \Lambda_S$ after the chiral extrapolation is plotted in Fig. 48 as a function of p^2 (in physical units) for both the 24^3 and 32^3 lattices. The figure confirms the expected approximate $1/p^6$ scaling. The unwanted nonperturbative effect from spontaneous symmetry breaking is small and the introduction of nonexceptional momenta has had the expected effect. This is in contrast to the RI/MOM scheme with the exceptional channel, where the same difference behaves as $1/(mp^2)$, and thus diverges in the chiral limit at finite p^2.

The mass renormalization factor Z_m^σ, with $\sigma =$ RI/SMOM or $\mathrm{RI/SMOM}_{\gamma_\mu}$, is given by combining Eqs. (77) and (80),

$$Z_m^\sigma = \frac{1}{Z_V}\frac{\Lambda_S + \Lambda_P}{\Lambda_V^\sigma + \Lambda_A^\sigma}. \tag{82}$$

In calculating the ratio of vertex functions in Eq. (82) we take the average of S and P or V and A for each light-quark mass and then fit with a quadratic $[c + c'(m_l + m_{\mathrm{res}})^2]$ or linear $[c + c''(m_l + m_{\mathrm{res}})]$ formula to obtain the value c in the chiral limit for the numerator and denominator. For illustration, the extrapolation for the numerator using the quadratic formula is shown in Fig. 49, where the observed mass dependence is seen to be very small. Because of the very mild mass dependence, to the precision with which we quote our results and errors, the quadratic and linear extrapolation formulas lead to exactly the same quark mass renormalization factor and error. Finally, taking the ratio and combining with Z_V gives the mass renormalization factor in the RI/SMOM schemes. The renormalization factor in the $\overline{\mathrm{MS}}$ scheme at a scale $\mu = 2$ GeV is obtained by first matching the scheme σ to $\overline{\mathrm{MS}}$ at $\mu^2 = p_{\mathrm{in}}^2 = p_{\mathrm{out}}^2 = q^2$ using Eqs. (71) and (72) and then running to 2 GeV using the three-loop anomalous dimension in the $\overline{\mathrm{MS}}$ scheme. We use the four-loop QCD beta functions [61] to calculate $\alpha_s^{(3)}(\mu)$ for running and matching as shown in Appendix A of Ref. [14]. The relevant parameters taken from the 2008 Particle Data Group [62] are

$$\alpha_s^{(5)}(m_Z) = 0.1176, \qquad m_Z = 91.1876 \text{ GeV},$$
$$\bar{m}_b = 4.20 \text{ GeV}, \quad \text{and} \quad \bar{m}_c = 1.27 \text{ GeV}, \tag{83}$$

where the quark masses are in the $\overline{\mathrm{MS}}$ scheme at the scale of the mass itself, e.g., $\bar{m}_b = m_b^{\overline{\mathrm{MS}}}(\bar{m}_b)$.

In Fig. 50 we plot $Z_m^{\mathrm{SMOM}_{\gamma_\mu}}(\mu)$ and $Z_m^{\mathrm{SMOM}}(\mu)$ in the SU(2) chiral limit as functions of $\mu^2 = p^2$ for the 32^3 ensembles. In addition we also plot $Z_m^{\overline{\mathrm{MS}}}(2\text{ GeV})$ as functions of

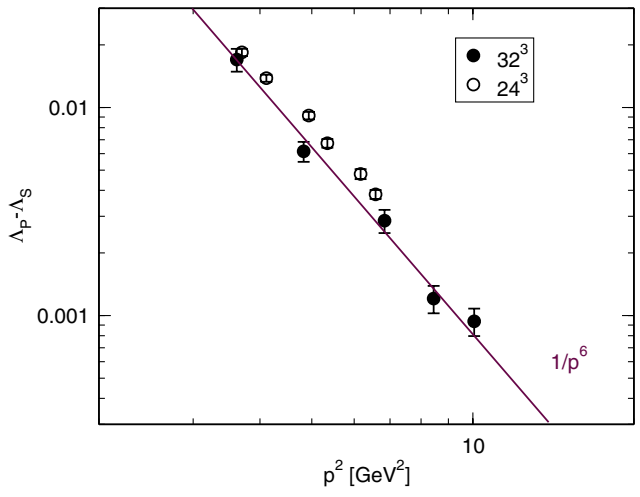

FIG. 48 (color online). $\Lambda_P - \Lambda_S$ as a function of p^2 [GeV^2] for fine (32^3) and coarse (24^3) lattices. A straight line with $1/p^6$ slope but arbitrary normalization is drawn to guide the eye.

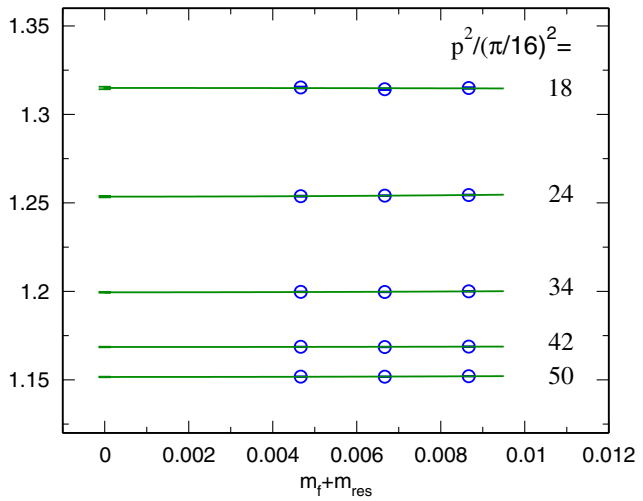

FIG. 49 (color online). The chiral extrapolation of $(\Lambda_P + \Lambda_S)/2$ for the fine (32^3) lattice for each p^2 point is shown.

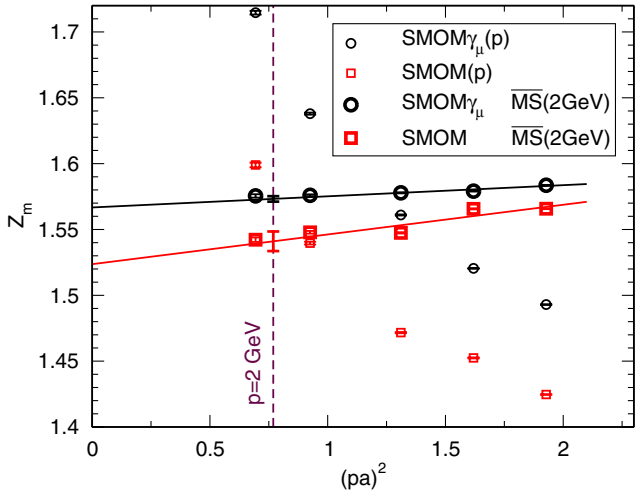

FIG. 50 (color online). $Z_m^{\mathrm{SMOM}_{\gamma_\mu}}(\mu)$ and $Z_m^{\mathrm{SMOM}}(\mu)$ as functions of $\mu^2 = p^2$, and $Z_m^{\overline{\mathrm{MS}}}(2\ \mathrm{GeV})$ from the SMOM or $\mathrm{SMOM}_{\gamma_\mu}$ schemes as a function of matching scale squared p^2 for the fine lattice. The interpolation points are shown with the error bar at $p^2 = (2\ \mathrm{GeV})^2$.

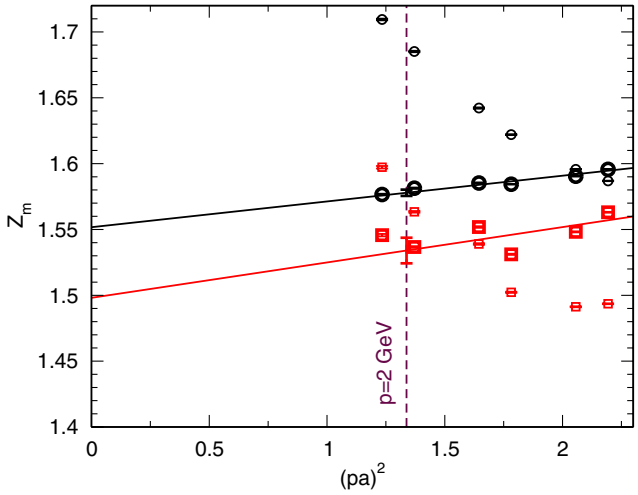

FIG. 51 (color online). The same figure as Fig. 50, but for the coarse 24^3 lattice is shown.

the matching scale p^2 obtained with SMOM and $\mathrm{SMOM}_{\gamma_\mu}$ as the intermediate schemes. In an ideal situation, i.e., one in which the errors due to NPE contamination, truncation of perturbation theory and lattice artifacts are all small, the results obtained using the two intermediate schemes would give the same results for $Z_m^{\overline{\mathrm{MS}}}(2\mathrm{GeV})$, and the results would be independent of $(pa)^2$. Since we have observed that the NPE error is small, the difference between the two sets of results is mostly due to the truncation of perturbation theory and lattice discretization errors. The observed decrease in this difference as p^2 increases is consistent with the expected behavior of the truncation error. Conversely, since the truncation error increases as p^2 decreases, taking the limit $(pa)^2 \to 0$, which is a typical treatment to eliminate the discretization error, is not an appropriate procedure. We therefore choose instead to evaluate Z_m by taking an intermediate reference point $p^2 = (2\ \mathrm{GeV})^2$, for both the 24^3 and 32^3 lattices. In this way, as we take the continuum limit of the renormalized quark mass, the leading $(pa)^2$ discretization error associated with the nonperturbative renormalization will be removed.

There is a subtlety due to lattice artefacts which are not $O(4)$ invariant and which are responsible for the non-smooth $(pa)^2$ dependence in the figure. A term like $a^2\sum_\mu (p_\mu)^4/p^2$, whose presence has been demonstrated in the conventional RI/MOM scheme for Wilson quarks [63], could exist also in the SMOM schemes. Such a term would manifest itself as scattered data around a smooth curve in p^2, and the size of the scatter is expected to be comparable to the leading $(pa)^2$ error as both are of the same order in a^2. This appears to be compatible to what is shown in the figure. Of course, it would be very helpful to know these terms, but in the absence of this knowledge we include this scatter in the systematic error by inflating the error by a factor $\sqrt{\chi^2/\mathrm{dof}}$. The results are

$$Z_m^{\overline{\mathrm{MS}}(32)}(\mu = 2\ \mathrm{GeV}, n_f = 3; \mathrm{SMOM}_{\gamma_\mu}) = 1.573(2), \tag{84}$$

$$Z_m^{\overline{\mathrm{MS}}(32)}(\mu = 2\ \mathrm{GeV}, n_f = 3; \mathrm{SMOM}) = 1.541(7). \tag{85}$$

The final arguments on the left-hand sides denote the choice of intermediate scheme. The error on the right-hand sides is the combination of the statistical fluctuations and the scatter of the points around the linear fit. The central values and errors are shown in the figure at the reference point, $p^2 = (2\ \mathrm{GeV})^2$.

The 24^3 coarser lattice has been analyzed similarly for the $m_l = 0.005$, 0.01 and 0.02 ensembles and the results are shown in Fig. 51. The mass renormalization factors on the 24^3 lattice for the two intermediate SMOM schemes are

$$Z_m^{\overline{\mathrm{MS}}(24)}(\mu = 2\ \mathrm{GeV}, n_f = 3; \mathrm{SMOM}_{\gamma_\mu}) = 1.578(2), \tag{86}$$

$$Z_m^{\overline{\mathrm{MS}}(24)}(\mu = 2\,\mathrm{GeV}, n_f = 3; \mathrm{SMOM}) = 1.534(10). \tag{87}$$

In Eq. (64) we have presented the bare-quark masses for the fine 32^3 lattice and in Table XXVI we give the ratios of equivalent bare masses on the 24^3 and 32^3 lattices. Because of the different $O(a^2)$ artefacts for the light and heavy-quark masses, there are two such ratios Z_l for the ud quarks and Z_h for the s quark. These ratios Z_l and Z_h are also the scheme-independent ratios of the renormalization constants on the course and fine lattices. We now use these ratios to estimate the difference of the $\overline{\mathrm{MS}}$ renormalized masses with the SMOM and $\mathrm{SMOM}_{\gamma_\mu}$ schemes in the continuum limit. The continuum extrapolation of $Z_m^{(32)}$

TABLE XXXVII. The systematic error budget for $Z_m^{\overline{\rm MS}}(2\ {\rm GeV})$ with intermediate RI/SMOM schemes (this work) and RI/MOM scheme [14].

Ensemble Intermediate scheme	Fine (32^2) RI/SMOM	Course (24^3) RI/SMOM	Course (16^3) [14] RI/MOM
PT truncation error	2.1%	2.1%	6%
$m_s \neq 0$	0.1%	0.2%	7%
$(\Lambda_P - \Lambda_S)/2$	0.5%	0.6%	N.A. (∞)
$(\Lambda_A - \Lambda_V)/2$	0.0%	0.0%	1%
total	2.2%	2.2%	9%

and $Z_m^{(24)}/Z_l$ or $Z_m^{(24)}/Z_h$ will remove the $(pa)^2$ error in the nonperturbative renormalization. Thus, if a difference is found, it can largely be attributed to the truncation error of the perturbative matching. Performing such an extrapolation we find

$$Z_{ml}^{\overline{\rm MS}(32)c}(\mu = 2\ {\rm GeV}, n_f = 3; {\rm SMOM}_{\gamma_\mu}) = 1.527(6), \tag{88}$$

$$Z_{ml}^{\overline{\rm MS}(32)c}(\mu = 2\ {\rm GeV}, n_f = 3; {\rm SMOM}) = 1.511(22), \tag{89}$$

for the ud quark, and

$$Z_{mh}^{\overline{\rm MS}(32)c}(\mu = 2\ {\rm GeV}, n_f = 3; {\rm SMOM}_{\gamma_\mu}) = 1.510(6), \tag{90}$$

$$Z_{mh}^{\overline{\rm MS}(32)c}(\mu = 2\ {\rm GeV}, n_f = 3; {\rm SMOM}) = 1.495(22), \tag{91}$$

for the s quark. Note that because these factors multiply $\tilde{m}_{ud}(32^3)/a(32^3)$ or $\tilde{m}_s(32^3)/a(32^3)$ presented in Eq. (64) to give the $\overline{\rm MS}$ mass in the continuum limit, they are made to absorb the $O(a^2(32^3))$ discretization error in these bare-quark masses on the fine lattice. Because of this, as well as the fact that the Z_m's are free from $O(a^2)$ errors originating from the SMOM nonperturbative renormalization, we have put additional suffix "c" as "continuum" to distinguish them from $Z_m^{\overline{\rm MS}(32)}$. The existence of a mass dependent contribution to the $O(a^2)$ artefacts gives rise to the different Z_m for the light and heavy-quark masses. From the two different estimates of the $\overline{\rm MS}$ renormalization factors with the SMOM and ${\rm SMOM}_{\gamma_\mu}$ intermediate nonperturbative schemes, we choose to take ${\rm SMOM}_{\gamma_\mu}$ for our central value. The reason is that the scatter about the linear behavior observed for the SMOM scheme in Figs. 50 and 51 is much larger. Although the effect of the scatter has been taken into account in the error, we consider the continuum extrapolation from the SMOM scheme to be less reliable. The difference in the central values of $Z_{ml}^{\overline{\rm MS}(32)c}$ in Eqs. (88) and (89) is about 1%, and this is also the case for the difference between the central values of $Z_{mh}^{\overline{\rm MS}(32)c}$ in Eqs. (90) and (91). These differences of about 1% give an indication of the possible size of the truncation error of the perturbative two-loop matching to $\overline{\rm MS}$ (it should be noted however, that the errors in the renormalization factors in the SMOM scheme are even a little larger). Another estimate of the truncation error of the matching is obtained by evaluating the size of the two-loop term in Eq. (74), resulting in 2.1% for the ${\rm SMOM}_{\gamma_\mu}$ scheme. In order to be conservative, we shall take the latter as our estimate. Other systematic errors arise from the fact that the simulated strange mass is nonzero and from the small difference in the scalar and pseudoscalar vertices due to the residual spontaneous symmetry breaking effects. The first error is estimated from the response of scalar and pseudoscalar vertex functions to the variation of the light-quark mass [14]. From the flat behavior of $\Lambda_P + \Lambda_S$ on the light-quark mass in Fig. 49 it can be seen that this uncertainty is small. The error estimates are compiled in Table XXXVII. In the table, the corresponding errors from the RI/MOM analysis [14] are shown for comparison. All errors have become significantly smaller for the new SMOM schemes. Now our final values for the $\overline{\rm MS}$ renormalization factor read

$$Z_{ml}^{\overline{\rm MS}(32)c}(\mu = 2\ {\rm GeV}, n_f = 3) = 1.527(6)(33), \tag{92}$$

$$Z_{mh}^{\overline{\rm MS}(32)c}(\mu = 2\ {\rm GeV}, n_f = 3) = 1.510(6)(33), \tag{93}$$

where the first error is the statistical uncertainty inflated to take into account the scatter about the linear behavior due to $O(4)$ noninvariant effects (as explained above) and the second is due to the remaining systematic effects and is dominated by the 2.1% truncation error of the perturbative matching. Here we have not taken into account the statistical fluctuation of Z_V, which will be properly included in the calculation of the renormalized quark masses described in the next subsection. The corresponding renormalization factor for the light-quark mass on the coarse 24^3 lattice is $Z_{ml}^{\overline{\rm MS}(24)c}(\mu = 2\ {\rm GeV}, n_f = 3) = Z_l \cdot Z_{ml}^{\overline{\rm MS}(32)c}(\mu = 2\ {\rm GeV}, n_f = 3) = 1.498(6)(33)$. This value is consistent with our earlier estimate of the same quantity using RI/MOM as the intermediate scheme, 1.656(157) [14], but now with a considerably reduced error.

B. Renormalized quark masses

After the detailed discussion of the quark mass renormalization, it is now straightforward to combine the renormalization constants in Eqs. (92) and (93) with the physical bare-quark masses on the 32^3 lattice in Eq. (64) to obtain the light and strange-quark masses renormalized in $\overline{\text{MS}}$ scheme:

$$\begin{aligned} m_{ud}^{\overline{\text{MS}}}(2\text{ GeV}) &= Z_{ml}^{\overline{\text{MS}}(32)c}(\mu = 2\text{ GeV}, n_f = 3) \\ &\quad \cdot \tilde{m}_{ud}(32^3) \cdot a^{-1}(32^3) \\ &= 3.59(13)_{\text{stat}}(14)_{\text{sys}}(8)_{\text{ren}}\text{ MeV}, \end{aligned} \tag{94}$$

$$\begin{aligned} m_{s}^{\overline{\text{MS}}}(2\text{ GeV}) &= Z_{mh}^{\overline{\text{MS}}(32)c}(\mu = 2\text{ GeV}, n_f = 3) \\ &\quad \cdot \tilde{m}_{s}(32^3) \cdot a^{-1}(32^3) \\ &= 96.2(1.6)_{\text{stat}}(0.2)_{\text{sys}}(2.1)_{\text{ren}}\text{ MeV}, \end{aligned} \tag{95}$$

where the three errors on the right-hand side correspond to the statistical uncertainty, the systematic uncertainty due to the chiral extrapolation and finite volume, and the error in the renormalization factor. We recall that for the error due to the chiral extrapolation we conservatively take the full difference of the results obtained using the finite-volume NLO SU(2) and analytic fits and for the central value we take the average of these results. We estimate the finite-volume effects from the difference of the results obtained using finite-volume and infinite-volume NLO ChPT fits and combine these errors in quadrature. The finite-volume errors prove to be small. The error in the renormalization factor includes those in Eqs. (92) and (93).

The ratio of the s and ud quark masses is

$$\frac{m_s}{m_{ud}} = 26.8(0.8)_{\text{stat}}(1.1)_{\text{sys}}. \tag{96}$$

We end this section by presenting our results for the leading-order LEC B and the chiral condensate. Using the finite-volume NLO ChPT fits we find

$$\begin{aligned} B^{\overline{\text{MS}}}(2\text{ GeV}) &= Z_{ml}^{\overline{\text{MS}}(32)-1}(\mu = 2\text{ GeV}, n_f = 3) \\ &\quad \cdot B(32^3) \cdot a^{-1}(32^3) \\ &= 2.64(6)_{\text{stat}}(6)_{\text{sys}}(6)_{\text{ren}}\text{ GeV}. \end{aligned} \tag{97}$$

Combining this result with the pion decay constant in the chiral limit, also obtained using the finite-volume NLO ChPT fits the chiral condensate is found to be

$$\begin{aligned} [\Sigma^{\overline{\text{MS}}}(2\text{ GeV})]^{1/3} &= [f^2 B(2\text{ GeV})/2]^{1/3} \\ &= 256(5)_{\text{stat}}(2)_{\text{sys}}(2)_{\text{ren}}\text{ MeV}. \end{aligned} \tag{98}$$

In Eqs. (97) and (98) the second error is only due to finite-volume corrections estimated from the difference of finite and infinite-volume NLO ChPT fits.

VII. TOPOLOGICAL SUSCEPTIBILITY

The topological charge Q, defined on a single Euclidean space-time configuration, and its susceptibility, χ_Q, are interesting quantities to calculate. While Q depends only indirectly on the quark masses, leading-order SU(2) ChPT [64,65] predicts a strong dependence of χ_Q on the light with χ_Q vanishing linearly as $m_l \to 0$, suggesting that χ_Q may show important dynamical quark mass effects.

In the continuum Q and χ_Q are defined by

$$Q = \frac{g^2}{16\pi^2}\int d^4x G_{\mu\nu}(x)\tilde{G}_{\mu\nu}(x) \quad \text{and} \quad \chi_Q = \langle Q^2\rangle/V, \tag{99}$$

where V is the four-volume of the lattice, $G_{\mu\nu}(x)$ is the gluon field strength tensor and $\tilde{G}_{\mu\nu}(x)$, its dual. In the continuum, Q is integer valued and related to exact chiral zero modes of the massless Dirac operator by the Atiyah-Singer index theorem [66]. For sufficiently smooth gauge fields it is possible to find a lattice expression which will always evaluate to an integer [67], as in the continuum limit. However, in the calculation reported here the necessary smoothness condition is not obeyed and we instead replace the right-hand side of Eq. (99) by a sum of Wilson loops chosen to approximate the $G_{\mu\nu}(x)\tilde{G}_{\mu\nu}(x)$ product in Eq. (99). Specifically we employ the "five-loop improved" definition of the topological charge proposed in Ref. [68]

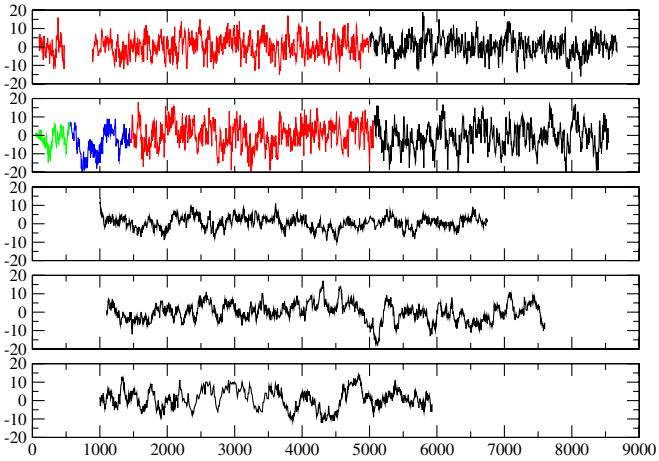

FIG. 52 (color online). Monte Carlo time histories of the topological charge. The light sea-quark mass increases from top to bottom, [0.005 and 0.01, 24^3 (top two panels), and 0.004-0.008, 32^3]. Data for the 24^3 ensembles up to trajectory 5000 were reported originally in [1]; the results for later trajectories and for the 32^3 ensembles are new and are plotted in black. Most of the data was generated using the RHMC II algorithm (red and black lines). The exceptions are the trajectories up to 1455 for the $m_l = 0.01$, 24^3ensemble for which the RHMC 0 (for the first 550 trajectories, green line) and RHMC I (for remaining trajectories up to 1455, blue line) were used. The small gap in the top panel represents missing measurements which are irrelevant since observables are always calculated starting from trajectory 1000.

which at tree level is accurate through order a^4. However, before evaluating this lattice expression for the topological charge, we smooth the links in the lattice by performing a series of APE smearing steps [69,70]. The smearing parameter was set to 0.45, and 60 smearing sweeps were performed before measuring Q. The results are insensitive to the choice of these parameters.

In Fig. 52 the Monte Carlo time history of Q is shown for each ensemble of gauge fields in our study. For each case, the update algorithm RHMC II [1] was used, except for the first 1455 configurations for the $m_l = 0.01$ ensemble where the RHMC 0 and RHMC I algorithms were used. In [1] it was shown that RHMC II is more effective in changing the gauge field topology, and therefore produces shorter autocorrelation times. The data for the first half (up to trajectory 5000) of both 24^3 ensembles is repeated from [1]. Figure 52 shows clearly the expected slowing of the rate of change of topological charge when moving towards the continuum [71] and, to a lesser degree, when decreasing the quark mass. The integrated autocorrelation times for Q for the smaller lattice-spacing ensembles are shown in Fig. 2. While this figure is consistent with the autocorrelation times reaching a plateau of about 80 time units when integrated over an interval of about 200 time units, the exploding errors make this conclusion highly uncertain. Scanning Fig. 52 by eye, one might argue that the autocorrelations could be 500 time units, or longer. For example, note the large fluctuation to negative Q beginning around time unit 4750 for $m_l = 0.006$.

The distributions of topological charge for each ensemble are shown in Fig. 53. The distributions become narrower as the quark mass is decreased. For the smaller lattice spacing, they also appear to exhibit non-Gaussian-like tails, or humps at large $|Q|$.

Because of the parity symmetry of our calculation, the average of the pseudoscalar quantity $\langle Q \rangle$ vanishes. However, χ_Q remains nonzero and at leading order in SU(2) chiral perturbation theory [64,65] is given by

$$\chi_Q = \Sigma\left(\frac{1}{m_u} + \frac{1}{m_d}\right)^{-1} = \Sigma\frac{m_u m_d}{m_u + m_d}, \tag{100}$$

where $\Sigma = Bf^2/2$ is the chiral condensate coming from a single flavor in the limit of vanishing up and down quark mass.

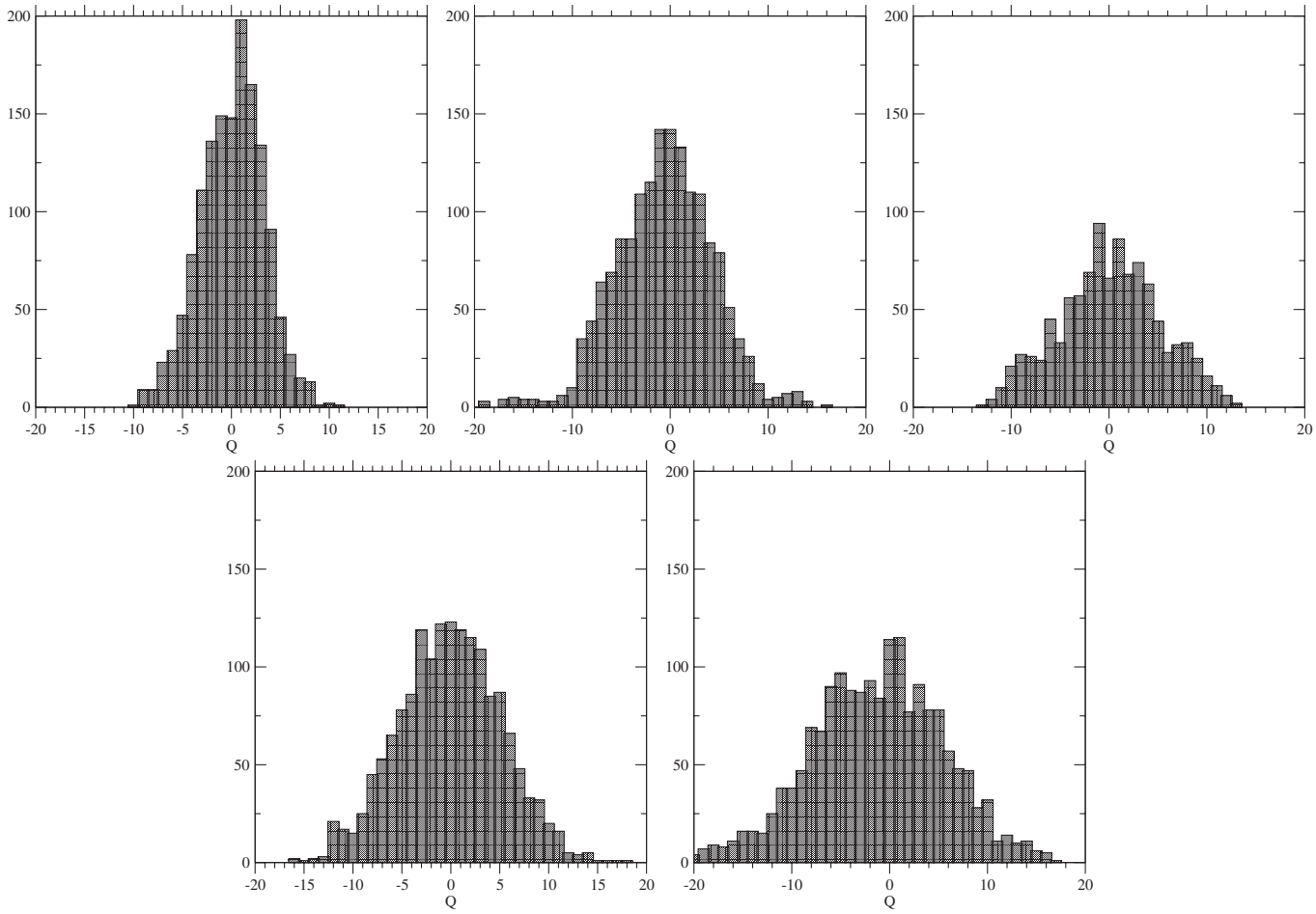

FIG. 53. Topological charge distributions are shown. Top: 32^3, $m_l = 0.004$–0.008, left to right. Bottom: 24^3, $m_l = 0.005$ and 0.01.

At one-loop in chiral perturbation theory [72],

$$\chi_Q = \Sigma\left(\frac{1}{m_u}+\frac{1}{m_d}\right)^{-1}\times\left(1-\frac{3}{(4\pi f)^2}m_\pi^2\log\frac{m_\pi^2}{\Lambda^2} + K_6(m_u+m_d)+2(2K_7+K_8)\frac{m_u m_d}{m_u+m_d}\right), \quad (101)$$

$$= \Sigma\frac{m_l}{2}\left(1-\frac{3}{(4\pi f)^2}m_{ll}^2\log\frac{m_{ll}^2}{\Lambda^2}+(2K_6+2K_7+K_8)m_l\right), \quad (102)$$

where $K_i = 128\Sigma L_i/f^4$ are proportional to the Gasser-Leutwyler NLO LECs [72], and in the last line the formula is evaluated for degenerate quarks. In contrast to other quantities considered in this paper, we do not attempt to characterize or evaluate the corrections to Eqs. (101) or (102) which come from nonzero lattice spacing. That interesting question is left for future work.

In Table XXXVIII values of $\langle Q\rangle$ and χ_Q for each ensemble of configurations are summarized. To test for the expected autocorrelations, the data were blocked into bins of various sizes ranging from 10 to 600 time units. The quoted values of the statistical errors resulted when the block sizes were taken large enough that the errors no longer changed significantly. The block sizes are given in Table XXXVIII. For all cases the first 1000 time units were discarded for thermalization.

The dependence of χ_Q on the light-quark mass is shown in Fig. 54. All of the data points lie above the LO curve (dashed line), all but the lightest significantly so. The result of the fit ($\chi^2/\text{dof} \approx 13/4 \approx 3$) to the NLO formula, Eq. (102), is also shown. Since we have not determined K_7 in Eq. (102) from other means, we treat the linear combination of LECs as a single, new, free parameter in the fit and find $(2K_6 + 2K_7 + K_8) = 19.8(6.3)$. Except for the lightest data point, there is scant evidence for large $O(a^2)$ errors, though the statistical errors on the heavier two points with $a^{-1} = 2.284$ are somewhat large. Omitting the former point in the fit leads to a more acceptable value of $\chi^2/\text{dof} \approx 1.5$, suggesting the lightest point may be systematically low due to long autocorrelations in Q that are not well resolved in our finite Markov chain of configurations. Despite these limitations, the data appear to show a dependence on the light quark mass that is consistent with the dictates of NLO SU(2) ChPT.

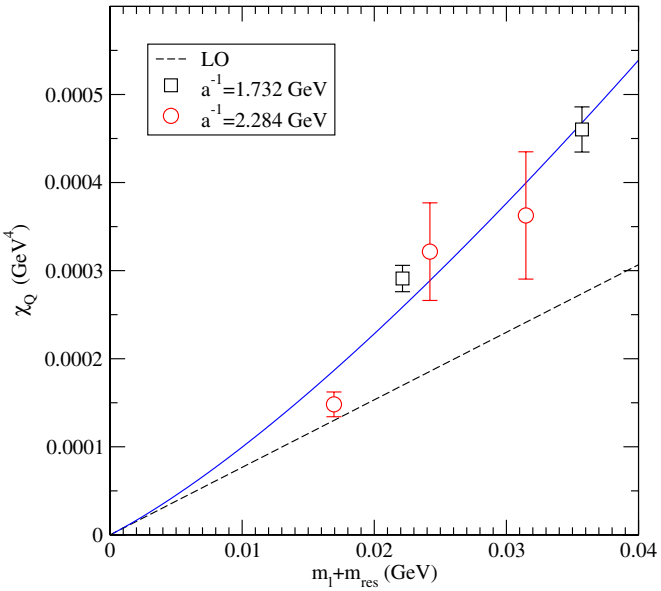

FIG. 54 (color online). Topological susceptibility [24^3 (squares), 32^3 (circles)]. The dashed line is the prediction from LO SU(2) chiral perturbation theory [Eq. (100)] with the chiral condensate computed from the finite-volume LECs given in Table XXVII. The solid line denotes the result of the single-parameter fit to the NLO formula given in Eq. (102).

VIII. CONCLUSIONS

We have presented results from simulations using DWF and the Iwasaki gauge action for lattice QCD at two values of the lattice spacing [$a^{-1} = 1.73(3)$ GeV and $a^{-1} = 2.28(3)$ GeV] and for unitary pion masses in the range 290–420 MeV (225–420 MeV for the partially quenched pions). The raw data obtained at each of the two values of β was presented in Secs. III and IV respectively and the chiral behavior of physical quantities on the 24^3 and 32^3 lattices separately was studied in Appendix A. The main aim of this paper, however, was to combine the data obtained at the two values of the lattice spacing into global chiral-continuum fits in order to obtain results in the continuum limit and at physical quark masses and we explain

TABLE XXXVIII. Topological charge and susceptibility. The measurement frequency, "meas. freq.", and "block size" are given in units of Monte Carlo time.

m_l	Measurement frequency	Block size	$\langle Q\rangle$	$\langle Q^2\rangle$	χ (GeV^4)
0.005	5	50	0.49 (25)	28.6 (1.4)	0.000 290 (14)
0.01	5	50	−0.22(37)	45.2 (2.5)	0.000 458 (25)
0.004	4	200	0.59 (42)	11.4 (1.1)	0.000 148 (14)
0.006	4	200	−0.07(64)	24.8 (4.3)	0.000 322 (55)
0.008	4	400	0.64 (100)	27.9 (5.6)	0.000 363 (72)

our procedure in Sec. V. In that section we define our scaling trajectory, explain how we match the parameters at the different lattice spacings so that they correspond to the same physics and discuss how we perform the extrapolations. We consider this discussion to be a significant component of this paper and believe that this will prove to be a good approach in future efforts to obtain physical results from lattice data. Although we apply the procedures to our data at two values of the lattice spacing, we stress that the discussion is more general and can be used with data from simulations at an arbitrary number of different values of β. In the second half of Sec. V we then perform the combined continuum-chiral fits in order to obtain our physical results for the decay constants, physical bare-quark masses (which are renormalized in Sec. VI) and for the quantities r_0 and r_1 defined from the heavy-quark potential. For the discussion below, it is important to recall that we use the physical pion, kaon, and Ω masses to determine the physical quark masses and the values of the lattice spacing and we then make predictions for other physical quantities.

In contrast to most other current lattice methods, the DWF formulation gives our simulations good control over chiral symmetry, nonperturbative renormalization factors, and flavor symmetry. This control allows us to measure and use, as either inputs or predictions: pseudoscalar decay constants, as well as their ratios; pseudoscalar masses; baryon masses; weak matrix elements and static potential values, limited only by the statistics achievable for these observables. The ability to predict many observables from the same simulations, provides evidence for the general reliability of the underlying methods. The good properties of DWF also allow us to test scaling, over this wide range of observables, at unphysical quark masses, since there are no flavor or chiral symmetry breaking effects to distort a test of scaling. We find scaling violations at the percent level, which supports including scaling corrections in only the leading-order terms in our light-quark expansions.

As we reduce the quark masses used in the simulations, it is frustrating that there remains a doubt as to the best ansatz to use for the chiral extrapolation. We know of course that for sufficiently light u and d masses the behavior is given by SU(2) ChPT; what we do not know is what "sufficiently light" means in practice. While in the range of quark masses accessible in our simulations, corresponding to 290–420 MeV for unitary pions and 225–420 MeV for partially quenched pions, our data are consistent with NLO SU(2) ChPT, we have seen that they are also consistent with a simple analytic ansatz leading to an inherent uncertainty in how best to perform the chiral extrapolation. This is particularly well illustrated in the study of f_π, see Fig. 35 for example, where the data is well represented by all three ansätze [including NLO SU(2) ChPT with finite-volume corrections], but the extrapolated values differ as seen in Table XXXI $f_\pi = 121(2)$ MeV from the NLO ChPT analysis with finite-volume corrections and $f_\pi = 126(2)$ MeV using the analytic ansatz. Since a complete NNLO ChPT analysis is not possible with the available data, we have resisted the temptation to introduce model dependence by including only some of the higher order corrections and for our current "best" results we take the average of the two values and include the full difference in the systematic uncertainty obtaining $f_\pi = 124(2)(5)$ MeV. In Sec. V E 3 we investigated the increase in χ^2/dof if the fits are required to pass through the physical value 130.7(4) MeV up to corrections from lattice artefacts and found $\chi^2 = 1.9(7)$ for the analytic ansatz and an unacceptably large value of 5(1) for the NLO ChPT with finite-volume corrections. In the future, it will be very interesting to see how the different ansätze for the chiral extrapolation become constrained or invalidated as we perform simulations with even lighter masses. We point out that the difference in the results from the analyses using the finite-volume ChPT and analytic ansätze is much smaller for the other quantities studied in this paper than for f_π.

The main physical results of this study are

$$\begin{aligned} f_\pi &= 124(2)(5)\ \text{MeV}, \\ f_K &= 149(2)(4)\ \text{MeV}, \\ \frac{f_K}{f_\pi} &= 1.204(7)(25), \\ m_s^{\overline{\text{MS}}}(2\ \text{GeV}) &= (96.2 \pm 2.7)\ \text{MeV}, \\ m_{ud}^{\overline{\text{MS}}}(2\ \text{GeV}) &= (3.59 \pm 0.21)\ \text{MeV}, \\ [\Sigma^{\overline{\text{MS}}}(2\ \text{GeV})]^{1/3} &= 256(6)\ \text{MeV}, \\ r_0 &= 0.487(9)\ \text{fm}, \quad \text{and} \\ r_1 &= 0.333(9)\ \text{fm}. \end{aligned} \tag{103}$$

For convenience, in order to help the reader find the corresponding discussion, we now list the equation numbers where the results were presented earlier in this paper. They are (61) for f_π, (62) for f_K, (63) for f_K/f_π, (95) for $m_s^{\overline{\text{MS}}}$, (94) for $m_{ud}^{\overline{\text{MS}}}$, (98) for $\Sigma^{\overline{\text{MS}}}$, and (66) for r_0 and r_1. All the results in Eq. (103) were obtained after reweighting the strange-quark mass to its physical value at each β, and the renormalized quark masses were obtained using nonperturbative renormalization with nonexceptional momenta as described in Sec. VI. The low-energy constants obtained by fitting our data to NLO chiral perturbation theory can be found in Sec. V E.

The configurations and results presented in this paper are being used in many of our current studies in particle physics phenomenology, including the determination of the B_K parameter of neutral-kaon mixing in the continuum limit [35]. In parallel to these studies we are exploiting configurations generated at almost physical pion masses on lattices with a large physical volume (~ 4.5 fm) but at the

expense of an increased lattice spacing. Preliminary results obtained for the meson spectrum and decay constants and for $\Delta I = 3/2$ $K \to \pi\pi$ decay amplitudes were recently presented in Refs. [52,73]. Having access to data with excellent chiral and flavor properties with a range of lattice spacings and quark masses makes this an exciting time indeed for studies in lattice phenomenology.

ACKNOWLEDGMENTS

The calculations reported here were performed on the QCDOC computers [80–82] at Columbia University, Edinburgh University, and at the Brookhaven National Laboratory (BNL). At BNL, the QCDOC computers of the RIKEN-BNL Research Center and the USQCD Collaboration were used. Most important were the computer resources of the Argonne Leadership Class Facility (ALCF) provided under the Incite Program of the U.S. DOE. The very large-scale capability of the ALCF was critical for carrying out the challenging calculations reported here. We also thank the University of Southampton for access to the Iridis computer system used in the calculations of the nonperturbative renormalization factors (with support from UK STFC Grant No. ST/H008888/1). The software used includes: the CPS QCD codes http://qcdoc.phys.columbia.edu/chulwoo/index.html, supported in part by the U.S. DOE SciDAC program; the BAGEL http://www.ph.ed.ac.uk/ paboyle/bagel/Bagel.html assembler kernel generator for many of the high-performance optimized kernels [25]; and the UKHADRON codes. Y. A. is partially supported by JSPS Kakenhi Grant No. 21540289. R. A., P. A. B., B. J. P., and J. M. Z. were partially supported by UK STFC Grant No. ST/G000522/1. T. B. and R. Z. were supported by U.S. DOE Grant No. DE-FG02-92ER40716. D. B., J. M. F., and C. T. S. were partially supported by UK STFC Grant No. ST/G000557/1 and by EU Contract No. MRTN-CT-2006-035482 (Flavianet). N. H. C., M. L., and R. D. M. were supported by U.S. DOE Grant No. DE-FG02-92ER40699. C. J., T. I., and A. S. are partially supported by the U.S. DOE under Contract No. DE-AC02-98CH10886. E. E. S. is partly supported by DFG SFB/TR 55 and by the Research Executive Agency of the European Union under Grant No. PITN-GA-2009-238353 (ITN STRONGnet).

TABLE XXXIX. Results from the SU(2) ChPT fits to the 24^3 data (without and with finite-volume corrections) compared to those from [1] obtained with lower statistics (without finite-volume corrections). We also quote in the lower part of the table the SU(2) ChPT fit parameters aB, af, $L_i^{(2)}$ (at the scale $\Lambda_\chi = 1$ GeV), and bare-quark masses $a\tilde{m}_{ud,s}$ in lattice units. Only statistical uncertainties are quoted except for quark masses and the LEC B renormalized in the $\overline{\text{MS}}$ scheme at 2 GeV where also the systematic uncertainty from the renormalization constant is quoted. [Mass renormalization constant at $1/a = 1.731(19)$ GeV: $Z_m = 1.546(0.002)_{\text{stat}}(0.044)_{\text{ren}}$ and at $1/a = 1.784(44)$ GeV: $Z_m = 1.559(0.003)_{\text{stat}}(0.047)_{\text{ren}}$.]

	Allton *et al.* [1]	Increased statistics		
	No FV correlated	No FV corrrelated		Including FV correlated
	Ω: $m_l \leq 0.03$	Ω: $m_l \leq 0.03$	Ω: $m_l \leq 0.01$	Ω: $m_l \leq 0.01$
$1/a$ [GeV]	1.729(28)	1.731(19)	1.784(44)	1.784(44)
$B^{\overline{\text{MS}}}$(2 GeV) [GeV]	$2.52(0.11)(0.23)_{\text{ren}}$	$2.63(0.06)(0.07)_{\text{ren}}$	$2.69(0.09)(0.08)_{\text{ren}}$	$2.63(0.09)(0.08)_{\text{ren}}$
f [MeV]	114.8(4.1)	111.5(2.9)	114.8(4.0)	117.1(4.0)
$\bar{l}_3$	3.13(0.33)	2.76(0.24)	2.82(0.24)	2.59(0.27)
$\bar{l}_4$	4.43(0.14)	4.54(0.10)	4.61(0.10)	4.57(0.11)
f_π [MeV]	124.1(3.6)	121.2(2.5)	124.4(3.6)	126.4(3.6)
f_K [MeV]	149.6(3.6)	147.9(2.6)	151.0(3.7)	152.1(3.7)
f_K/f_π	1.205(0.018)	1.220(0.011)	1.214(0.012)	1.204(0.012)
$m_{ud}^{\overline{\text{MS}}}$(2 GeV) [MeV]	$3.72(0.16)(0.33)_{\text{ren}}$	$3.56(0.08)(0.10)_{\text{ren}}$	$3.48(0.12)(0.10)_{\text{ren}}$	$3.55(0.12)(0.11)_{\text{ren}}$
$m_s^{\overline{\text{MS}}}$(2GeV) [MeV]	$107.3(4.4)(9.7)_{\text{ren}}$	$101.0(1.9)(2.9)_{\text{ren}}$	$99.0(3.0)(3.0)_{\text{ren}}$	$98.8(3.0)(3.0)_{\text{ren}}$
$\tilde{m}_{ud}$: $\tilde{m}_s$	1:28.8(0.4)	1:28.37(0.27)	1:28.44(0.26)	1:27.89(0.28)
aB	2.414(61)	2.348(43)	2.349(44)	2.298(45)
af	0.0665(21)	0.0644(14)	0.0643(14)	0.0656(14)
$L_4^{(2)} \times 10^4$	1.3(1.3)	2.2(0.9)	2.5(0.9)	2.2(0.9)
$L_5^{(2)} \times 10^4$	5.16(0.73)	5.00(0.47)	5.50(0.47)	5.36(0.48)
$(2L_6^{(2)} - L_4^{(2)}) \times 10^4$	−0.71(0.62)	−0.09(0.45)	0.03(0.45)	0.01(.49)
$(2L_8^{(2)} - L_5^{(2)}) \times 10^4$	4.64(0.43)	4.86(0.30)	4.36(0.38)	5.34(0.33)
$a\tilde{m}_{ud}$	0.001 300(58)	0.001 331(43)	0.001 251(71)	0.001 274(72)
$a\tilde{m}_s$	0.0375(16)	0.0377(11)	0.0356(19)	0.0355(19)

APPENDIX A: SEPARATE FITS TO 24^3 AND 32^3 DATA

In this section we report on results obtained by fitting the data from the 24^3 runs at $\beta = 2.13$ and from the 32^3 runs at $\beta = 2.25$ separately to the predictions of SU(2) $\times$ SU(2) ChPT. This complements the material presented in Secs. III and IV in which we presented the results for masses and decays constants at each set of quark masses but did not perform the chiral extrapolations and also that in Sec. V in which we performed simultaneous chiral and continuum fits to the data at both lattice spacings. Our main motivation for studying separate fits here is to be able to compare directly our results obtained with the new data to those in our previous publication [1]. For that reason in this appendix we will be using the same renormalization constant Z_A as in our previous publication, which differs from the one used in the global analysis presented in the main part of this paper, see the discussion in Sec. III and Appendix B for details. We use the same method of iterated fits as outlined in our earlier publication [1]; at each lattice spacing we iterate the combined fits of the meson masses and decay constants with $m_x \leq 0.01$ to the SU(2)-ChPT formulas, using kaon SU(2) ChPT to fit the kaon mass and decay constants and the extrapolation in the Ω-baryon mass until convergence. The pion, kaon, and Ω masses are used to fix the physical bare-quark masses m_{ud}, m_s, and the lattice scale $1/a$. Predictions for the remaining physical quantities are then obtained by extrapolation to these physical quark masses. For further details see [1]. In the case of the 24^3

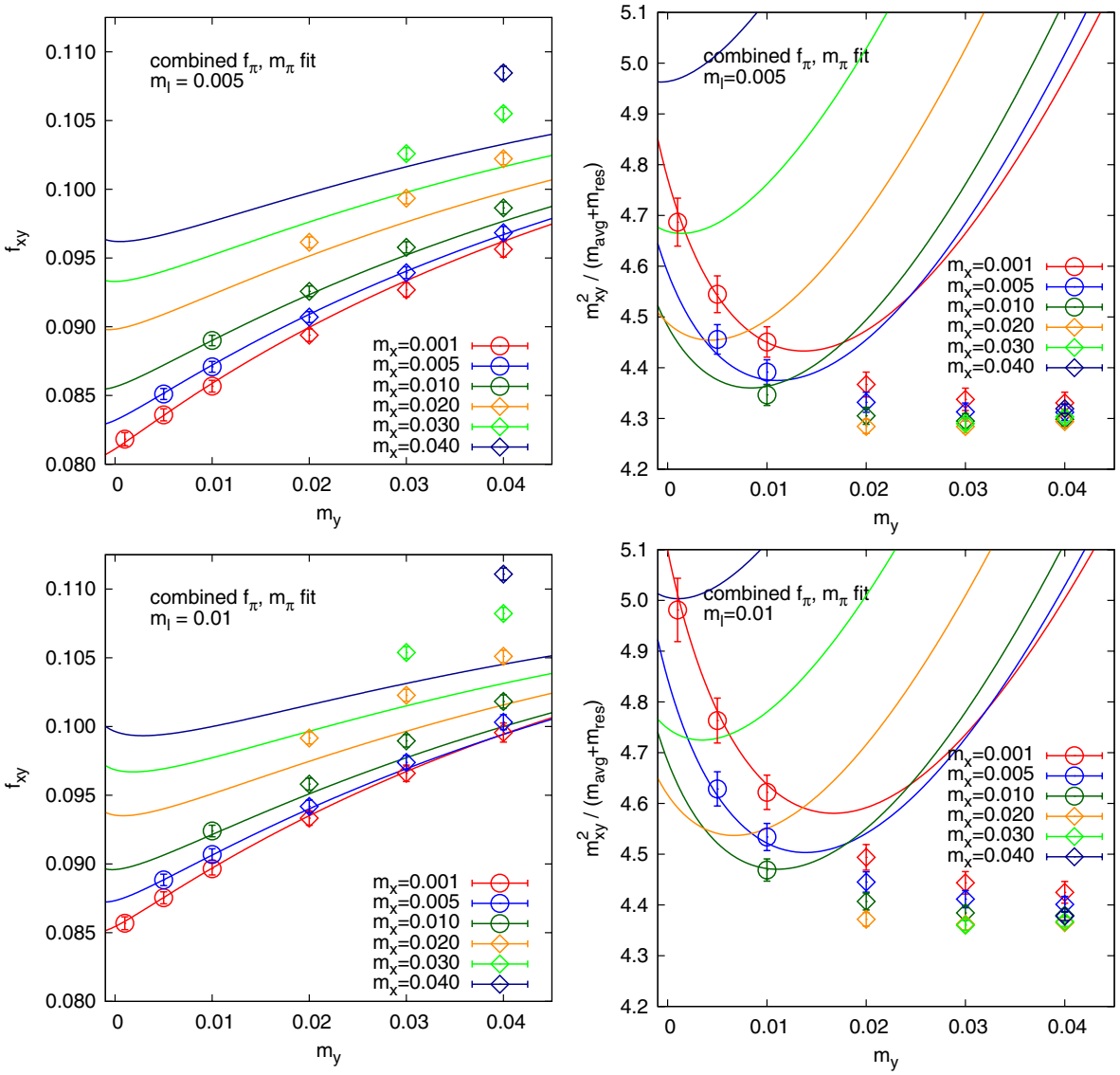

FIG. 55 (color online). Combined SU(2) ChPT fits (without finite-volume corrections) for the meson decay constants (left column) and masses (right column) on the 24^3 data set at $m_l = 0.005$ (top row) and 0.01 (bottom row). Only points marked with circles, corresponding to the range $(m_x + m_y)/2 \leq 0.01$, are included in the fits.

TABLE XL. Comparison of the pion and kaon decay constants and their ratios at finite lattice spacing from separate (see Tables XXXIX and XLI) and global fits using our previous definition of Z_A.

			f_π [MeV]	f_K [MeV]	f_K/f_π
No FV correlated	24^3, $\beta = 2.13$	separate	124.4(3.6)	151.0(3.7)	1.214(0.012)
		global	123(2)	150(2)	1.215(0.009)
	32^3, $\beta = 2.25$	separate	120.4(1.9)	147.1(2.0)	1.222(0.007)
		global	121(2)	147(2)	1.222(0.006)
Including FV correlated	24^3, $\beta = 2.13$	separate	126.4(3.6)	152.1(3.7)	1.204(0.012)
		global	126(2)	151(2)	1.204(0.009)
	32^3, $\beta = 2.25$	separate	122.3(1.9)	148.1(2.0)	1.212(0.007)
		global	123(2)	149(2)	1.210(0.006)

ensembles, the runs have been extended since the publication of [1] (see Sec. II and especially Table I for details) so that a direct comparison of the results from the previous (smaller) data set with the new extended data set is possible. We quote results from fits with and without corrections due to finite-volume effects. When including the finite-volume corrections, the terms described in Appendix C of [1] are included in the SU(2) ChPT in the pion sector (both for the meson masses and decay constants). We also include the correction terms containing the chiral logarithm of the light-quark masses in the kaon decay constant [74] and note that up to NLO in the light-quark masses, no finite-volume corrections arise in the masses of the kaon and Ω baryon. Below we present the physical results in the infinite-volume limit, i.e., after removing the corrections. Finally, we will perform a naive continuum extrapolation of the results obtained by the separate fits at the two lattice spacings, which can then be compared to results from the combined chiral-continuum extrapolations using the global fits described in Sec. V. Note that in this appendix also for the combined chiral-continuum extrapolations we are going to quote results obtained using our previous definition of Z_A. For that reason the results reported here differ slightly from those in the main part of this paper.

1. SU(2)-ChPT fits to 24^3 data

In Table XXXIX we summarize our results from the iterative fits to the masses and decay constants measured on the 24^3 ensembles (see Sec. III for details) and compare them to our earlier results obtained with lower statistics [1]. We have performed two kinds of fits: one including the Ω-baryon masses determined at all the simulated light-quark masses, $m_l = 0.005$, 0.01, 0.02, and 0.03, (as was done originally) and one where only the Ω-baryon masses at the two lightest dynamical quark masses $m_l = 0.005$ and 0.01 are included. The latter, limited range is also the one used in the combined chiral-continuum extrapolations in Sec. V and in the separate fits to the 32^3 data in the next subsection. In Fig. 55 we plot the combined SU(2) ChPT fits (without finite-volume corrections) to the meson masses and decay constants in the pion sector. It is evident that over the fit range $(m_x + m_y)/2 \leq 0.01$, corresponding to a maximum meson mass of about 420 MeV, the data is well described by SU(2) ChPT. This is also true for the fits including the finite-volume corrections (not shown).

We note that by comparing the results in the first two columns of Table XXXIX, which have been obtained using the same (large) mass-range for the chiral extrapolation of the Ω-baryon mass, the results obtained with the increased statistics (for each dynamical light-quark mass the statistics has nearly been doubled, see Sec. III) nicely agree with those from our previous publication [1] within the statistical uncertainty. Furthermore, we observe the expected reduction in the statistical error. For the remainder of the discussion, we focus on the fits in which only the two lightest dynamical masses have been included in the extrapolation of the Ω-baryon mass, i.e., the last two columns of Table XXXIX. The major difference resulting from this change in the fit range is in the value of the lattice scale $1/a$, but within 1.4 standard deviations (statistical error only, taking into account correlations) the results still show agreement. Including the finite-volume effects results in higher values for the decay constants (both in the chiral limit and at the physical point), which is a statistically significant effects (taking the correlations into account). In Table XL we compare the decay constants and their ratio obtained from the separate fits with the corresponding results from the global analysis at the simulated, finite value of the lattice-spacing (i.e. not extrapolated to the continuum, see Sec. V and especially Tables XXXI, XXXII, and XXXIII but note the difference due to the use of our previous definition of Z_A here). We are reassured by the observed agreement between the results obtained using the global fits with those obtained using our previous strategy in Ref. [1] which was developed at that time to describe data at only a single lattice spacing.

2. SU(2)-ChPT fits to 32^3 data

The results of a separate fit on the 32^3 data set are summarized in Table XLI. Here we only included the Ω-baryon masses from the $m_l = 0.004$, 0.006, and 0.008

TABLE XLI. Results from the SU(2) ChPT fits to the 32^3 data (without and with finite-volume corrections). We also quote in the lower part of the table the SU(2) ChPT fit parameters aB, af, $L_i^{(2)}$ (at the scale $\Lambda_\chi = 1$ GeV) and quark masses $a\tilde{m}_{ud,s}$ in lattice units. Only statistical uncertainties are quoted except for quark masses and the LEC B renormalized in the $\overline{\text{MS}}$ scheme at 2 GeV where also the systematic uncertainty from the renormalization constant is quoted. [Mass renormalization constant at $1/a = 2.221(29)$ GeV: $Z_m = 1.550(0.002)_{\text{stat}} \times (0.034)_{\text{ren}}$.]

	No FV correlated	FV correlated included
$1/a$ [GeV]	2.221(29)	2.221(29)
$B^{\overline{\text{MS}}}$(2 GeV) [GeV]	$2.62(0.05)(0.06)_{\text{ren}}$	$2.57(0.05)(0.06)_{\text{ren}}$
f [MeV]	111.4(2.2)	113.7(2.2)
$\bar{l}_3$	2.84(0.21)	2.61(0.24)
$\bar{l}_4$	4.18(0.09)	4.10(0.09)
f_π [MeV]	120.4(1.9)	122.3(1.9)
f_K [MeV]	147.1(2.0)	148.1(2.0)
f_K/f_π	1.222(0.007)	1.212(0.007)
$m_{ud}^{\overline{\text{MS}}}$(2 GeV) [MeV]	$3.58(0.07)(0.08)_{\text{ren}}$	$3.64(0.07)(0.08)_{\text{ren}}$
$m_s^{\overline{\text{MS}}}$(2 GeV) [MeV]	$100.6(1.7)(2.2)_{\text{ren}}$	$100.4(1.7)(2.2)_{\text{ren}}$
$\tilde{m}_{ud}$: $\tilde{m}_s$	1:28.08(0.19)	1:27.60(0.20)
aB	1.826(0.024)	1.790(0.025)
af	0.0502(0.0007)	0.0512(0.0007)
$L_4^{(2)} \times 10^4$	−0.75(0.79)	−1.21(.82)
$L_5^{(2)} \times 10^4$	5.14(0.40)	4.87(0.41)
$(2L_6^{(2)} - L_4^{(2)}) \times 10^4$	−0.93(0.42)	−1.03(0.45)
$(2L_8^{(2)} - L_5^{(2)}) \times 10^4$	6.22(0.23)	7.37(0.24)
$a\tilde{m}_{ud}$	0.001 040(31)	0.001 057(32)
$a\tilde{m}_s$	0.0292(08)	0.0292(08)

ensembles. In Fig. 56 we show the fits for the meson masses and decay constants in the pion sector (without finite-volume corrections). Again, over the fit range $[(m_x + m_y)/2 \leq 0.008]$, corresponding to a maximum pion mass of about 400 MeV, the data is well described by SU(2) ChPT.

As was already the case for the 24^3 ensembles, taking finite-volume corrections into account also leads to a good description of the data and results in higher values for the decay constants at the physical point and in the chiral limit. Again, taking the correlations into account, we note that this is a statistically significant effect. As was also the case on the 24^3 ensembles, we observe a good agreement for the decay constants and their ratio between the results of the separate fits to the 32^3 data and the results from the global fits at finite lattice spacing, see Table. XL.

3. Extrapolation to the continuum limit

With the results obtained from separate chiral extrapolations on the 24^3 (extended statistics) and the 32^3 data sets (see the two previous subsections, respectively) we can perform a naive continuum limit extrapolation assuming a^2 scaling. Of course, with only two lattice spacings available, we are not able to confirm this scaling behavior. Further caveats include the fact that here, for simplicity, we did not use reweighting and so the dynamical strange-quark mass is not tuned to exactly the same value on the two data sets and indeed is not exactly the physical one on either set. Also, the dynamical light-quark mass ranges are a little different at the two lattice spacings, corresponding to unitary pion masses in the range 330–420 MeV on the coarser 24^3 lattices and 290–400 MeV on the finer 32^3 lattices (a similar statement is true for the partially quenched masses). One might therefore expect a larger uncertainty in the chiral extrapolation of the 24^3 results. In the naive continuum ansatz followed here, we are not taking into account this effect. Because of this, and maybe more importantly, since two separate chiral extrapolations have been performed (one at each of the two values of the lattice spacing), the continuum extrapolation is not completely disentangled from the chiral extrapolation. Recall that in our procedure for the global fits described in the main part of this paper, these two extrapolations are indeed disentangled. There this is achieved by adding $O(a^2)$ terms into the two functions, such that the chiral and continuum extrapolations are performed simultaneously and independently from each other.

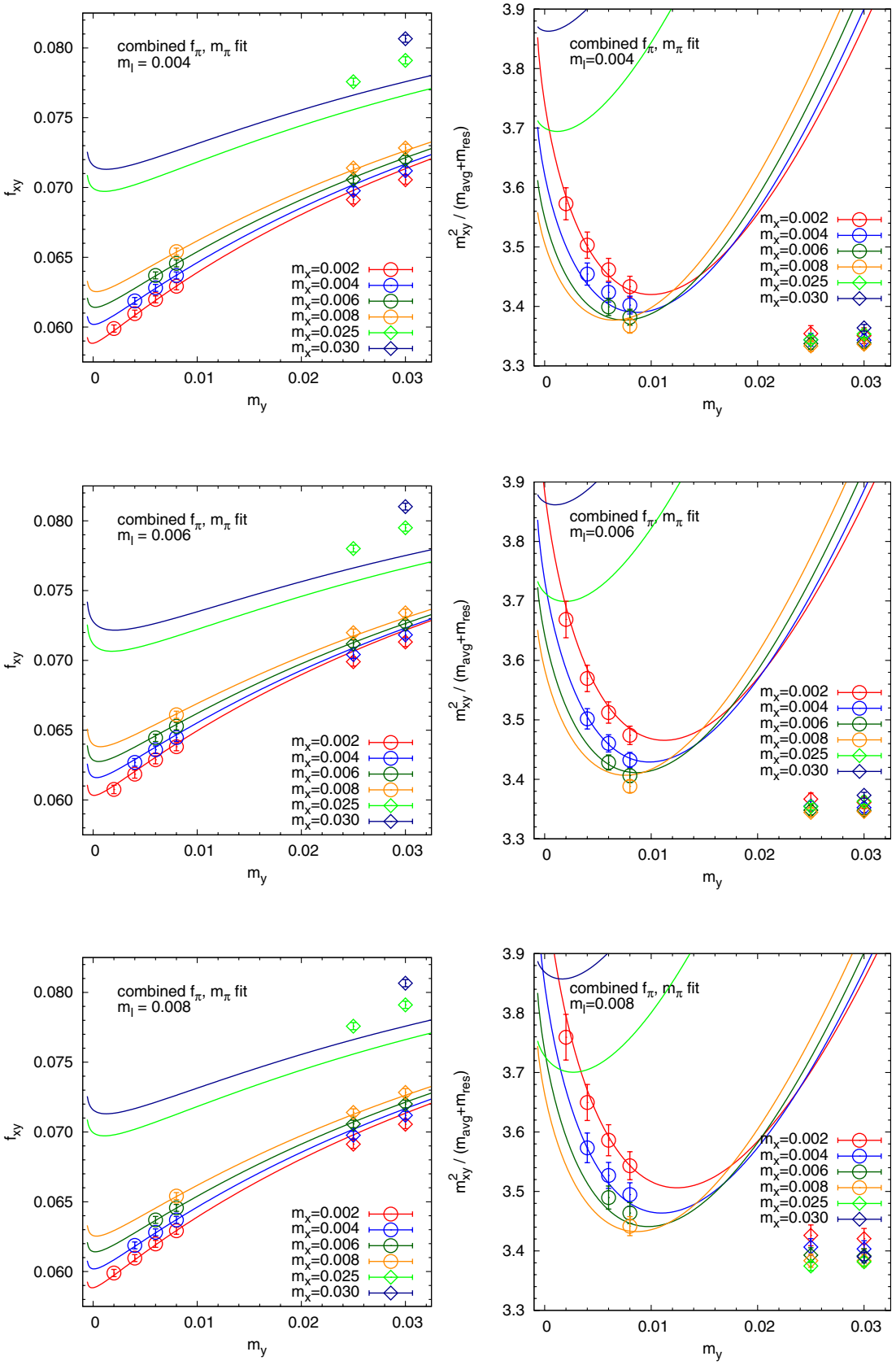

FIG. 56 (color online). Combined SU(2) ChPT fits (without finite-volume corrections) for the meson decay constants (left column) and masses (right column) on the 32^3 data set at $m_l = 0.004$ (top row), 0.006 (middle row), and 0.008 (bottom row). Only points marked with circles, corresponding to the range $(m_x + m_y)/2 \leq 0.008$ are included in the fits.

TABLE XLII. Selected results from separate fits to the 24^3 and 32^3 data sets (Ω masses from $m_l \leq 0.1$ for 24^3 data set, cf. Tables XXXIX and XLI) and their naive continuum limit assuming a^2 scaling (see Fig. 57) compared to results from the combined chiral-continuum extrapolation using the previous definition of Z_A. The top table contains results without finite-volume corrections whereas the results in the bottom table were obtained by including finite-volume effects.

	No FV correlated			
	Separate fits		Naive CL	Combined chiral/CL
	24^3, $\beta = 2.13$	32^3, $\beta = 2.25$		
a [fm]	0.1106(27)	0.0888(12)	$\rightarrow 0$	$\rightarrow 0$
f [MeV]	114.8(4.0)	111.4(2.2)	105.2(10.4)	107(2)
$\bar{l}_3$	2.82(0.24)	2.84(0.21)	2.87(0.74)	2.81(0.16)
$\bar{l}_4$	4.61(0.10)	4.18(0.09)	3.39(0.36)	3.76(0.08)
f_π [MeV]	124.4(3.6)	120.4(1.9)	113.0(9.5)	117(2)
f_K [MeV]	151.0(3.7)	147.1(2.0)	139.9(9.6)	144(2)
f_K/f_π	1.214(0.012)	1.222(0.007)	1.236(0.030)	1.233(0.008)

	Including FV correlated			
	Separate fits		naive CL	Combined chiral/CL
	24^3, $\beta = 2.13$	32^3, $\beta = 2.25$		
a [fm]	0.1106(27)	0.0888(12)	$\rightarrow 0$	$\rightarrow 0$
f [MeV]	117.1(4.0)	113.7(2.2)	107.4(10.3)	110(2)
$\bar{l}_3$	2.59(0.27)	2.61(0.24)	2.64(0.83)	2.55(0.18)
$\bar{l}_4$	4.57(0.11)	4.10(0.09)	3.26(0.38)	3.83(0.09)
f_π [MeV]	126.4(3.6)	122.3(1.9)	114.8(9.4)	119(2)
f_K [MeV]	152.1(3.7)	148.1(2.0)	140.9(9.6)	145(2)
f_K/f_π	1.204(0.012)	1.212(0.007)	1.226(0.029)	1.219(0.007)

In Table XLII we repeat the results obtained at the two different lattice spacings (with and without finite-volume corrections) and give the values extrapolated to the continuum limit assuming a^2 scaling. Figure 57 illustrates the continuum extrapolation of the various quantities (only results obtained without taking into account finite-volume corrections are shown there). Note, that the two points at the different lattice spacings are completely uncorrelated, the only correlation in the data for the continuum extrapolation is between the uncertainty in the lattice spacing (the "x" datum) and the quantity itself at that lattice spacing (the "y" datum). These correlations were treated by the superjackknife method which we have been using in our earlier work and which is clearly explained in [75,76]. For comparison, Table XLII also contains our results from the combined continuum-chiral extrapolation as described in the main part of this paper but here using our previous definition of Z_A. As one can see, the combined continuum-chiral extrapolation gives a substantially smaller (up to a factor of 5) statistical uncertainty compared to the naive continuum extrapolation. The main reason, of course, is the correlation in the combined fits between the two data sets at different lattice spacings. This correlation occurs because we require the fitted parameters to be the same on both data sets and only include $O(a^2)$ corrections for the leading-order terms, as is consistent with our power-counting scheme. In this way, the continuum extrapolation in the combined fits is also more constrained, leading to a smaller statistical uncertainty. Comparing the results of the naive continuum extrapolation and the combined continuum-chiral extrapolation for the quantities in Table XLII we observe agreement better than 0.5-σ (taking into account correlations) for all quantities except for $\bar{l}_4$, where the agreement still holds at the 1- or 1.5-σ level (without and with taking FV corrections into account, respectively). It is reassuring, that the results from the two methods agree well, although the value of this statement is limited, given the large (statistical) uncertainty of almost 10% for the decay constants or even more in case of the LECs from the naive method. However, it should be noted that the same agreement holds, not only for the continuum values, but also for the results obtained in the separate fits as compared to the predictions of the global fit made for the finite lattice spacings. This has already been discussed in the previous subsections and is shown in Table XL.

APPENDIX B: DETERMINING $Z_{\mathcal{A}}$

As pointed out by Sharpe [18] and refined in Ref. [1], the normalization of the partially conserved axial current defined for domain wall fermions [77] is expected to deviate

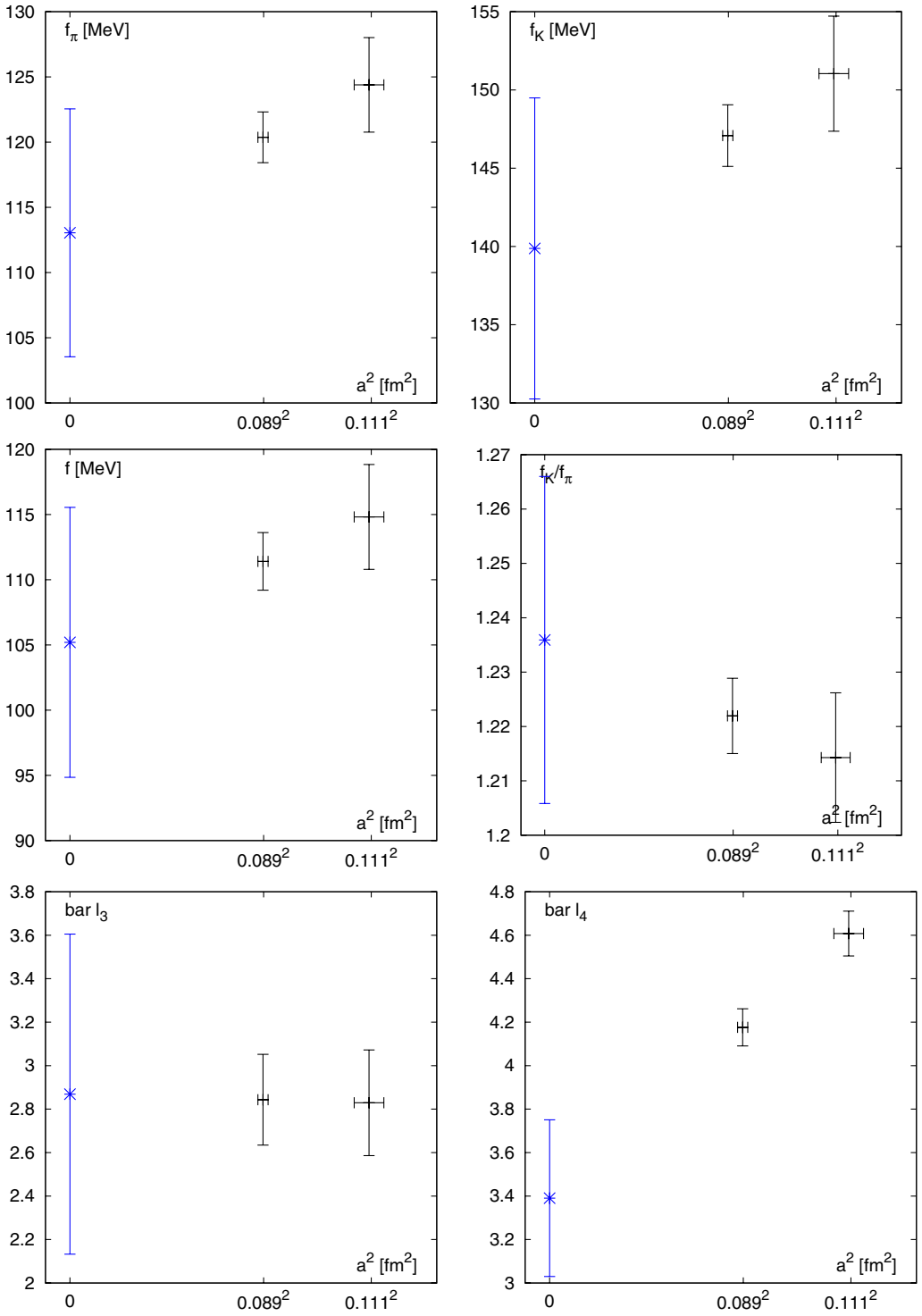

FIG. 57 (color online). Results from separate fits (without finite-volume corrections) to the 24^3 and 32^3 data sets (black points) and the naive continuum-limit extrapolation (blue asterisks) for selected quantities assuming a^2 scaling. For details see Appendix A 3 and Table XLII.

from that of the conventionally normalized continuum current by an amount of order $m_{\mathrm{res}}a$. Here and below, when making such estimates we will introduce the explicit lattice spacing a and express the residual mass in physical units in order to make the comparison of various terms in a Symanzik expansion in powers of a easier to recognize. Since such a deviation can be viewed as $O(ma)$ which is formally larger than the $O(ma^2)$ which we neglect in our power-counting scheme and because the normalization of this axial current plays a central role in our determination

of the important quantities f_π and f_K, we have calculated this normalization factor $Z_{\mathcal{A}}$ numerically. We explain our method and result in this appendix. The first subsection contains a discussion of the theoretical issues and explains the basis for our method of determining $Z_{\mathcal{A}}$. The second subsection describes the actual calculation and results.

1. Determining the normalization of $\mathcal{A}_\mu$

To determine the normalization of $\mathcal{A}_\mu$ we compare the matrix element of four distinct domain wall fermion currents. The first two are the conserved/partially conserved vector and axial currents $\mathcal{V}^a_\mu(x)$ and $\mathcal{A}^a_\mu(x)$, respectively, where a and μ are flavor and space-time indices. These currents were introduced by Furman and Shamir [77] and involve fermion fields evaluated on each of the L_s 4-dimensional hyperplanes and at both the space-time points x and $x + \hat{e}_\mu$ where $\hat{e}_\mu$ is a unit vector pointing the μ-th direction. Thus, these currents are local but distributed in the fifth dimension and one-link nonlocal in space-time. While this vector current is exactly conserved, the divergence of the axial current contains the usual mass term and a midpoint term J^a_{5q}. In the long-distance limit this midpoint term can be decomposed into the residual mass term, a piece that is conveniently written as $(1 - Z_{\mathcal{A}})$ times the divergence of the same axial current and a final term of dimension five which we write out explicitly as the sum of the dimension-five, chiral rotation of the usual clover term and the four-dimensional Laplacian applied to the pseudoscalar density:

$$J^a_{5q} = m_{\rm res}\bar{q}\gamma^5\lambda^a q + \frac{1 - Z_{\mathcal{A}}}{2}\Delta_\mu \mathcal{A}^a_\mu + c_1\bar{q}\sigma^{\mu\nu}F^{\mu\nu}\lambda^a q + c_2\partial_\mu\partial_\mu\bar{q}\gamma^5\lambda^a q. \tag{B1}$$

In Eq. (B1) λ^a is the generator which acts on the fermion fields corresponding to the flavor index a while $q(x)$ and $\bar{q}(x)$ are the physical, four-dimensional quark fields obtained by evaluating the five-dimensional domain wall fields on the $s = 0$ and $s = L_s - 1$ boundaries. [See Eqs. (11) and (12) in Ref. [1].]

The second pair of currents which we will need in this appendix is the local vector and axial currents, $V^a_\mu(x)$ and $A^a_\mu(x)$, constructed in the standard way from the four-dimensional quark fields, $q(x)$ and $\bar{q}(x)$. These currents are localized in all five dimensions and neither is conserved.

Finally, it will also be convenient to introduce the scalar densities $\bar{q}(x)q(x)$, $\bar{q}(x)\lambda^a q(x)$ from which the domain fermion mass is constructed and their chiral transforms $\bar{q}(x)\gamma^5 q(x)$, $\bar{q}(x)\lambda^a\gamma^5 q(x)$. These four classes of operators will be labeled $S(x)$, $S^a(x)$, $P(x)$, and $P^a(x)$.

Following Symanzik, we can add improvement terms to each of these six operators to insure that their Green's functions, when evaluated with an appropriately improved action, will agree with the corresponding continuum Green's functions up to errors of order a^n. For our present purposes, accuracy up to $O(am)$ where m is a quark mass in physical units, will be sufficient. Since $m_{\rm res}$ and m have a similar size, we are explicitly attempting to control the $m_{\rm res}a$ corrections described above. We do not attempt to explicitly remove $O(a^2)$ terms since these will be eliminated by the final linear extrapolation $a^2 \to 0$.

In the discussion to follow we will recognize constraints on the required Symanzik improvement terms and relations between the various renormalization constants by applying the approximate chiral symmetry of domain wall fermions to Green's functions containing these various operators. For such arguments to be valid we will assume that these Green's functions are evaluated at sufficiently small distances that the effects of the vacuum chiral symmetry breaking of QCD can be ignored but at sufficiently large distances that the Symanzik improvement program can be applied. Since this discussion is a theoretical one, constraining the form of the Symanzik improvement terms, we need not be concerned about practical questions regarding the degree to which such conditions can be realized in our present calculation.

Using the notation V^{Sa}_μ, A^{Sa}_μ, S^{Sa}, and P^{Sa} for the Symanzik-improved vector current, axial current, scalar density, and pseudoscalar density, respectively, keeping improvement terms which are nominally of order a and imposing charge conjugation symmetry, we find

$$V^{Sa}_\mu = Z_{\mathcal{V}}\mathcal{V}^a_\mu + C_{\mathcal{V}}\partial_\nu\bar{q}\sigma^{\mu\nu}\lambda^a q, \tag{B2}$$

$$A^{Sa}_\mu = Z_{\mathcal{A}}\mathcal{A}^a_\mu + C_{\mathcal{A}}\partial_\mu P^a, \tag{B3}$$

$$V^{Sa}_\mu = Z_V V^a_\mu + C_V\partial_\nu\bar{q}\sigma^{\mu\nu}\lambda^a q, \tag{B4}$$

$$A^{Sa}_\mu = Z_A A^a_\mu + C_A\partial_\mu P^a, \tag{B5}$$

$$S^{Sa} = Z_S S^a, \tag{B6}$$

$$P^{Sa} = Z_P P^a. \tag{B7}$$

In contrast to the Symanzik-improved current operators, we have not specified a normalization convention for the operators S^{Sa} and P^{Sa}. Adopting definitive conventions for S^{Sa} and P^{Sa} is not needed here beyond the requirement that those conventions are consistent with $S^{Sa} \pm P^{Sa}$ belonging to the $(\bar{3}, 3)/(3, \bar{3})$ representations of the $\mathrm{SU}(3)_L \times \mathrm{SU}(3)_R$ flavor symmetry.

Because the operators S and P contain no vector indices, any correction terms must increase the dimension by two and we have chosen to neglect such $O(a^2)$ contributions. Thus, Eqs. (B6) and (B7) are particularly simple. However, we can also drop the dimension-four, $O(a)$ correction terms to Eqs. (B2)–(B5). This can be established by considering the chiral structure of the Symanzik and conserved/partially conserved current operators. Ignoring

effects of order m, the Symanzik currents will couple to pairs of quarks which are either left- or right-handed. Likewise the domain wall conserved/partially conserved current operators couple to a pair of quarks with the same value of the coordinate s in the fifth dimension. For $s = 0$ these are left-handed fermions while for $s = L_s - 1$ they are right-handed. As the coordinate s moves into the fifth-dimensional bulk, the amplitude for coupling to such physical modes decreases until when $s \approx L_s/2$ the amplitude will be suppressed by two traversals halfway through the fifth dimension which implies a suppression of order $m_{\rm res}a$. Of course, the $s \approx 0$ and $s \approx L_s - 1$ terms will dominate. The character of the local vector and axial currents is simpler since they contain quark field strictly limited to $s = 0$ and $L_s - 1$. Since the four, dimension-four improvement terms included in Eqs. (B2)–(B5) involve pairs of quarks with opposite handedness, such terms require a complete propagation across the fifth dimension if they are to couple to the conserved/partially conserved or local currents. This is true even for the terms with general s which appear in the former currents. Thus, these correction terms involve an additional power of $m_{\rm res}a$ and are of order $m_{\rm res}a^2$ and can be neglected in our power-counting scheme.

With this simplification, we can demonstrate that to this order the following relations hold:

$$Z_{\mathcal{V}} = 1, \tag{B8}$$

$$Z_V = Z_A, \tag{B9}$$

$$Z_S = Z_P. \tag{B10}$$

Equation (B8) follows easily from the fact that $\mathcal{V}_\mu^a$ is conserved at finite lattice spacing and has been given the conventional normalization. Equations (B9) and (B10) can each be shown using essentially the same argument which we will now review.

In the massless continuum theory the operators $\bar{q}^c \lambda^a \gamma^\mu (1 \pm \gamma^5) q^c$ are independent involving only right-handed/left-handed degrees of freedom. Here the label c indicates *continuum*. This implies the vanishing of the Symanzik-improved Green's function:

$$\langle (V_\mu^{\mathbf{S}a} + A_\mu^{\mathbf{S}a})(x)(V_\nu^{\mathbf{S}a} - A_\nu^{\mathbf{S}a})(y)\rangle = 0. \tag{B11}$$

This same property is obeyed by the local domain wall currents up to order $(m_{\rm res}a)^2$ since nonvanishing terms which can contribute to the DWF version of Eq. (B11) must connect both fermion degrees of freedom between the left and right walls requiring two-traversals of the fifth dimension and hence are of order $(m_{\rm res}a)^2$ [18,78]. It is then easy to see that these two behaviors can be consistent through order $m_{\rm res}a$ only if $Z_V = Z_A$ through order $m_{\rm res}a$. We need only examine the mixing between $V_\mu^{\mathbf{S}a} \pm A_\mu^{\mathbf{S}a}$ that is generated by $Z_V - Z_A$:

$$\begin{aligned}
&\langle (V_\mu^{Sa} + A_\mu^{Sa})(x) \cdot (V_\nu^{Sa} - A_\nu^{Sa})(y)\rangle \\
&= \langle (Z_V V_\mu^a + Z_A A_\mu^a)(x) \cdot (Z_V V_\nu^a - Z_A A_\nu^a)(y)\rangle \\
&= \tfrac{1}{4}\langle [(Z_V + Z_A)(V_\mu^a + A_\mu^a)(x) + (Z_V - Z_A) \\
&\quad \times (V_\mu^a - A_\mu^a)(x)] \cdot [(Z_V + Z_A)(V_\nu^a - A_\nu^a)(y) \\
&\quad + (Z_V - Z_A)(V_\nu^a + A_\nu^a)(y)]\rangle.
\end{aligned} \tag{B12}$$

The product of the left-most operators in the square brackets on the right-hand side of Eq. (B12) cannot mix at order $m_{\rm res}$ because of their construction from domain wall quark fields as explained above. Likewise the product of the right-most terms also vanishes. However, the two cross terms have nonzero correlators implying that for the entire expression to be of order $m_{\rm res}^2$, the difference $Z_V - Z_A$ must be of order $(m_{\rm res}a)^2$, demonstrating the intended result. A very similar argument can be constructed which shows that $Z_S = Z_P$ through order $m_{\rm res}a$. One must invoke the flavor structure and, for example, consider correlators between $(S^1 - iS^2)(x) + (P^1 - iP^2)(x))$ and $(S^1 + iS^2) \times (y) + (P^1 + iP^2)(y))$ which also must vanish in the chiral limit. Here $a = 1, 2$ is a specific choice of the eight octet indices $a = 1$–8.

The relations in Eqs. (B8)–(B10) were established by considering the domain wall and continuum theories in a limit in which the physical quark masses could be neglected, at sufficiently short distances that vacuum chiral symmetry breaking could be ignored but at sufficiently long distances that the Symanzik effective theory could be applied. While this is an excellent regime in which to establish these theoretical constraints, it is not a practical one for calculations. Thus, we will now employ these relations at low energies where vacuum chiral symmetry breaking is important in order to provide a practical method to compute $Z_{\mathcal{A}}$.

Since at low energies the left- and right-hand sides of Eqs. (B4) and (B5) must have identical matrix elements, the ratio of long-distance correlators computed with the Symanzik and local currents must give identical constants: $Z_V = Z_A$. Thus, we have established

$$\frac{\langle V_i^{Sa}(x) V_i^a(y)\rangle}{\langle V_i^a(x) V_i^a(y)\rangle} = \frac{\langle A_0^{Sa}(x) P^a(y)\rangle}{\langle A_0^a(x) P^a(y)\rangle}, \tag{B13}$$

where we have introduced the fixed spatial index i, the temporal index 0 and sources $V_i^a(y)$ and $P^a(y)$ that will correspond to those used in our actual calculation. Next we can use the long-distance equality represented by Eqs. (B2) and (B3) to write

$$1 = \frac{\langle V_i^{Sa}(x) V_i^a(y)\rangle}{\langle \mathcal{V}_i^a(x) V_i^a(y)\rangle}, \tag{B14}$$

$$Z_{\mathcal{A}} = \frac{\langle A_0^{Sa}(x) P^a(y)\rangle}{\langle \mathcal{A}_0^a(x) P^a(y)\rangle}. \tag{B15}$$

Then we can combine Eqs. (B13)–(B15) to yield an equation for $Z_{\mathcal{A}}$ which does not involve the Symanzik currents:

$$Z_{\mathcal{A}} = \frac{\langle A_0^a(x) P^a(y)\rangle}{\langle \mathcal{A}_0^a(x) P^a(y)\rangle} \cdot \frac{\langle \mathcal{V}_i^a(x) V_i^a(y)\rangle}{\langle V_i^a(x) V_i^a(y)\rangle}, \tag{B16}$$

which determines $Z_{\mathcal{A}}$ in terms of four correlators which we have evaluated directly in our lattice calculation.

In order to relate the discussion of the Symanzik-improved operators given in Eqs. (B2)–(B7) with the operators appearing in Eq. (B1), we should recognize that the quantity $Z_{\mathcal{A}}$ has been introduced in two places. The most important is in the relation between the Symanzik current and the partially conserved domain wall operator in Eq. (B3). It is this quantity that is determined in Eq. (B16) and which is needed to give a physical normalization to the axial current matrix elements determined in our calculation. However, the quantity $Z_{\mathcal{A}}$ also appears in the expression for J_{5q} given in Eq. (B1). For completeness, we will now demonstrate that these two quantities are in fact the same up to order $(m_{\text{res}}a)^2$.

This is easily done by introducing a flavor-breaking mass term $\bar{q}Mq$ into the DWF action, examining the divergence equations obeyed by $\mathcal{V}_\mu^a$ and $\mathcal{A}_\mu^a$ and using the relation $Z_S = Z_P$ established above. With the additional mass term the conserved/partially conserved vector and axial currents obey the lattice divergence equations, through $O(m_{\text{res}}a)$:

$$\Delta^\mu \mathcal{V}_\mu^a = \bar{q}[\lambda^a, M]q, \tag{B17}$$

$$\Delta^\mu \mathcal{A}_\mu^a = \bar{q}\{\lambda^a, M\}\gamma^5 q + 2m_{\text{res}}\bar{q}\gamma^5 q - (Z_{\mathcal{A}} - 1)\Delta^\mu \mathcal{A}_\mu^a. \tag{B18}$$

Taking the $Z_{\mathcal{A}} - 1$ term to the left-hand side and recognizing that the scalar and pseudoscalar operators S^a and P^a are symmetrically normalized ($Z_S = Z_P$), we can conclude that the operators $\mathcal{V}_\mu^a$ and $Z_{\mathcal{A}}\mathcal{A}_\mu^a$ must be related to the corresponding Symanzik currents by the same factor. This establishes that our two definitions of $Z_{\mathcal{A}}$ are consistent.

We will conclude this analysis with a brief discussion of the effects of the explicit quark mass, m_f, on the operator product expansion represented by Eq. (B1) and on the Symanzik-improved operators given in Eqs. (B2)–(B7). Although m_f explicitly connects the $s = 0$ and $s = L_s - 1$ walls, it can combine with the midpoint operator J_{5q} appearing on the left-hand side of Eq. (B1) to create effects with arbitrary chiral properties. Thus, we expect multiplicative corrections of the form $(1 + b_i m_f a)_{1\le i\le 4}$ to each of the four terms on the right-hand side of Eq. (B1). In the case of the left-most term the correction is of order $m_f m_{\text{res}} a$ while for the remaining three terms the corrections are of order $m_f m_{\text{res}} a^2$ or $m_f m_{\text{res}} a^3$, all beyond the level of accuracy of the current paper. The conclusion that $Z_{\mathcal{V}} = 1$ through order $m_{\text{res}}a^2$ (and order $m_f a^2$) prevents the appearance of a factor $1 + b(m_f a)$ multiplying the $Z_{\mathcal{V}}$ in Eq. (B2). The argument that $Z_A = Z_V$ and $Z_S = S_P$ with corrections of order $(m_{\text{res}}a)^2$ applies equally well to the left-right mixings created by m_f but again the allowed $m_f m_{\text{res}} a^2$ and $(m_f a)^2$ terms are negligible within our present power-counting scheme so Eqs. (B4)–(B7) need no $O(m_f a)$ corrections. Lastly, consider adding a factor of the form $(1 + b(mfa))$ multiplying the $Z_{\mathcal{A}}$ on the right-hand side of Eq. (B3). As explained above, a similar correction to $Z_{\mathcal{A}}$ appearing in Eq. (B1) carries the additional suppression of one power of $m_{\text{res}}a$. Since the equality derived above between the $Z_{\mathcal{A}}$ factors appearing in the divergence equation, Eq. (B1), and the Symanzik-improved current $\mathcal{A}_\mu^a$, in Eq. (B3), holds at order $m_f a$ such a $1 + b(m_f a)$ factor is not allowed in Eq. (B3). Thus, no $m_f a$ terms need to be introduced into the equations presented in this appendix.

2. Computational method and results

We have evaluated the two factors in Eq. (B16) to determine $Z_{\mathcal{A}}$ on both the $32^3 \times 64$, $\beta = 2.25$ ($m_l = 0.004$, 0.006, and 0.008) and the $24^3 \times 64$, $\beta = 2.13$ ($m_l = 0.005$, 0.01 and 0.02) ensembles. We used a small subset of

TABLE XLIII. Results for the ratios $Z_A/Z_{\mathcal{A}}$, $Z_V/Z_{\mathcal{V}}$, and $Z_{\mathcal{V}}/Z_{\mathcal{A}}$ computed on six ensembles. The rows with quark mass $-m_{\text{res}}$ contain the chiral extrapolation to the light-quark mass $m_l = -m_{\text{res}}$. The left-hand portion of the fit range gives that used for the axial current ratio while the right-hand portion that for the vector current. For the $Z_V/Z_{\mathcal{V}}$ calculation the data at t and $63 - t$ were combined for $0 \le t < 32$.

β	m_l	$Z_A/Z_{\mathcal{A}}$	$Z_V/Z_{\mathcal{V}}$	$Z_{\mathcal{V}}/Z_{\mathcal{A}}$	Fit range	N_{meas}
2.13	0.02	0.719 00(20)	0.6956(17)	1.0336(25)	9–54/9–17	50
2.13	0.01	0.71759(16)	0.6998(20)	1.0254(29)	9–54/9–17	50
2.13	0.005	0.71743(30)	0.6991(17)	1.0262(25)	9–54/10–19	105
2.13	$-m_{\text{res}}$	0.71615(36)	0.7019(26)	1.0208(40)		
2.25	0.008	0.745 26(12)	0.738 02(55)	1.0098(7)	9–54/9–20	85
2.25	0.006	0.745 23(12)	0.738 53(64)	1.0090(9)	9–54/9–18	76
2.25	0.004	0.74513(15)	0.73871(77)	1.0087(10)	9–54/10–19	166
2.25	$-m_{\text{res}}$	0.744 99(34)	0.7396(17)	1.0073(23)		

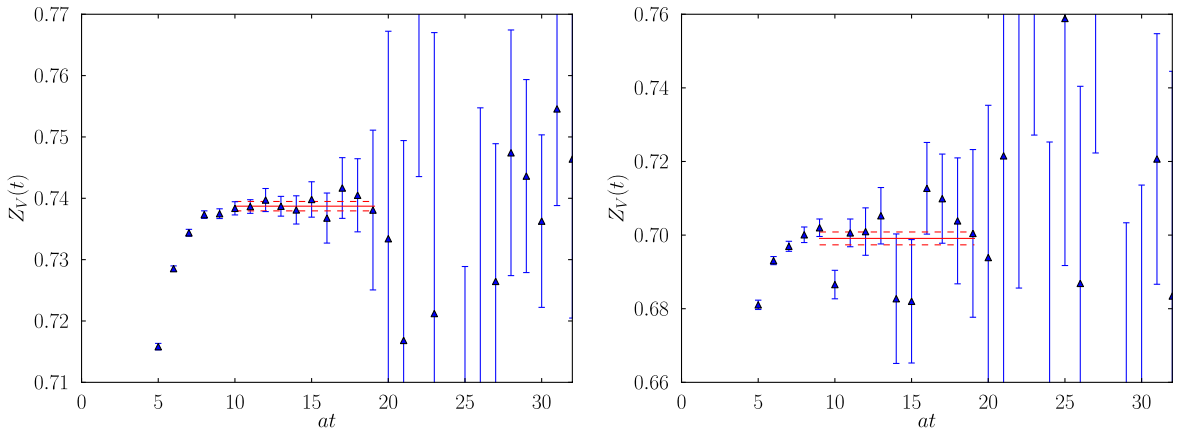

FIG. 58 (color online). Plots of the correlator ratio which determines the renormalization factor $Z_V/Z_{\mathcal{V}}$ as a function of time. The left panel shows results from the 32^3, $m_l = 0.004$ ensemble while the right panel shows the result from the 24^3, $m_l = 0.005$ ensemble. The horizontal line with error bands in each panel shows the fitting range and the result obtained in each case.

these six ensembles and obtained the results given in Table XLIII. The results presented for $Z_A/Z_{\mathcal{A}}$ duplicate those from the calculation of Z_A described in Secs. III and IV. In this appendix we add the factor $Z_{\mathcal{A}}$ in the denominator because we are now determining the deviation of this factor from unity. We do not simply use the results presented earlier in the paper because our calculation of $Z_V/Z_{\mathcal{V}}$ has been performed on a subset of the configurations analyzed earlier and results for $Z_A/Z_{\mathcal{A}}$ are needed on this same subset of configurations if ratios with meaningful jackknife errors are to be determined.

The ratio $Z_A/Z_{\mathcal{A}}$ was computed from the same ratio of current-pseudoscalar correlators studied in Secs III and IV, using the method specified in Ref. [79]. Similar methods are used to compute $Z_V/Z_{\mathcal{V}}$ using the ratio of vector correlators

$$\frac{Z_V}{Z_{\mathcal{V}}} = \frac{\sum_{i=1}^{3}\sum_{\vec{x}}\langle \mathcal{V}_i^a(\vec{x},t)V_i^a(\vec{0},0)\rangle}{\sum_{i=1}^{3}\sum_{\vec{x}}\langle V_i^a(\vec{x},t)V_i^a(\vec{0},0)\rangle}, \tag{B19}$$

an equation expected to be valid for time separations t much larger than 1 lattice spacing: $t \gg a$. Figure 58 shows the right-hand side of Eq. (B19) as a function of time for the case of the lightest mass for each of the 32^3 and 24^3 ensembles. A constant fit to plateau regions identified by the horizontal lines was then used to determine the $Z_V/Z_{\mathcal{V}}$ on the left-hand side of this equation. Figure 59 displays the chiral extrapolation of the two quantities $Z_A/Z_{\mathcal{A}}$ and $Z_V/Z_{\mathcal{V}}$ on both sets of ensembles.

Two useful results follow from this appendix. First, the ratio $Z_{\mathcal{V}}/Z_{\mathcal{A}}$ differs from unity on our two ensembles and that difference decreases more rapidly than a^2 with increasing β. Thus, we will obtain more accurate results in our continuum extrapolation from both matrix elements of the local axial current and our NPR calculations which are normalized using off-shell Green's functions containing the local vector and axial currents if we convert the normalization of these local currents to the usual continuum normalization by using the ratio $Z_V/Z_{\mathcal{V}}$ instead of the ratio $Z_A/Z_{\mathcal{A}}$, the quantity which we have used in previous work

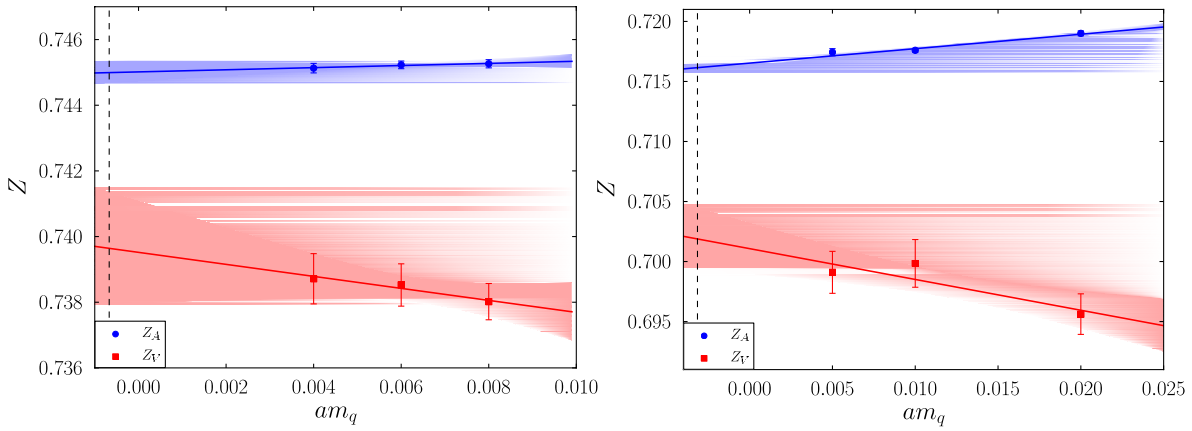

FIG. 59 (color online). The quantities $Z_A/Z_{\mathcal{A}}$ and $Z_V/Z_{\mathcal{V}}$ extrapolated to the chiral limit for the 32^3 (left panel) and 24^3 (right panel) ensembles are shown.

for such conversions. The values of $Z_V/Z_\mathcal{V}$ presented in Table XLIII are therefore used to normalize the results presented in the current paper and are the second result obtained in this appendix. Because these ratios were calculated on a smaller subset of configurations than were used for our main results, we have included their statistical fluctuations as independent within our superjackknife, statistical error analysis. Since these fluctuations are at or below the 0.5% level, this omission of possible statistical correlations is unimportant.

APPENDIX C: STATISTICAL ERRORS OF REWEIGHTED QUANTITIES

In this appendix we discuss the statistical errors that should be expected when Monte Carlo data is reweighted to obtain results for a gauge or fermion action that is different from that used to generate the data. Throughout this discussion we will make the assumption that the reweighting factors are not correlated with the data. Of course, if this assumption were exactly true then the reweighting would not be needed. However, the correlation between the data and reweighting factors is often small in practice and neglecting this correlation may well provide a reasonably accurate view of the resulting errors. As we will show, with this assumption the usual analysis of the statistical errors applies easily to reweighted data and yields a simple, useful formula which we present here.

Consider a quantity x and the corresponding ordered ensemble of N Monte Carlo configurations with corresponding measured values $\{x_n\}$, $1 \le n \le N$. For each of these N configurations we will determine a reweighting factor w_n so that the final, reweighted quantity of interest is given by

$$\langle x \rangle_N = \frac{\sum_{n=1}^N x_n w_n}{\sum_{n=1}^N w_n}. \tag{C1}$$

Here the single brackets $\langle \ldots \rangle_N$ indicate an average over a single Monte Carlo ensemble of N samples. In this appendix we are interested in how the statistical fluctuations in the quantity $\langle x \rangle_N$ are affected by the operation of reweighting. We can then express the true value for x_N as

$$\bar{x}_N = \langle\langle \langle x \rangle_N \rangle\rangle, \tag{C2}$$

where the double brackets $\langle\langle \ldots \rangle\rangle$ indicate a ''meta'' average over many equivalent Monte Carlo ensembles. The statistical fluctuation present in a particular result $\langle x \rangle_N$ can then be characterized by the average fluctuation of $\langle x \rangle_N$ about $\bar{x}_N$:

$$\text{Error}\,(x) = \sqrt{\langle\langle (\langle x \rangle_N - \bar{x}_N)^2 \rangle\rangle}. \tag{C3}$$

A quantity such as $\langle x \rangle_N$, defined in Eq. (C1) as a ratio of averages, will be a biased estimator of the physical result which must be determined in the limit $N \to \infty$. Thus, the meta average $\bar{x}_N = \langle\langle \langle x \rangle_N \rangle\rangle$ will differ from the true result by terms of order $1/N$. While these $1/N$ corrections are not difficult to enumerate and estimate from our data, these corrections are not the subject of the present appendix and will not be considered further here. Instead we will study how the size of the statistical fluctuations of $\langle x_N \rangle$ about $\bar{x}_N$ is affected by the reweighting. Thus, the quantity Error(x) defined in Eq. (C3) describes the average deviation of $\langle x \rangle_N$ from $\bar{x}_N$ not from the $N \to \infty$ limit of $\bar{x}_N$.

We will now work out an expression for Error(x) in the case that nearby measurements x_n and x_{n+l} in a single Markov chain (or reweighting factors w_n and w_{n+l}) are correlated but with the assumption that x_n and w_{n+l} are not:

$$\langle\langle (\langle x \rangle_N - \bar{x}_N)^2 \rangle\rangle = \left\langle\left\langle \left(\frac{\sum_{n=1}^N x_n w_n}{\sum_n w_n} - \bar{x}_N \right) \left(\frac{\sum_{n'=1}^N x_{n'} w_{n'}}{\sum_{n'} w_{n'}} - \bar{x}_N \right) \right\rangle\right\rangle \tag{C4}$$

$$= \left\langle\left\langle \frac{(\sum_{n=1}^N x_n w_n - \bar{x}_N \sum_{n=1}^N w_n)(\sum_{n'=1}^N x_{n'} w_{n'} - \bar{x}_N \sum_{n'=1}^N w_{n'})}{(\sum_{n=1}^N w_n)(\sum_{n'=1}^N w_{n'})} \right\rangle\right\rangle \tag{C5}$$

$$= \left\langle\left\langle \frac{(\sum_{n=1}^N (x_n - \bar{x}_N) w_n))(\sum_{n'=1}^N (x_{n'} - \bar{x}_N) w_{n'})}{(\sum_{n=1}^N w_n)(\sum_{n'=1}^N w_{n'})} \right\rangle\right\rangle \tag{C6}$$

$$= \frac{\sum_{n=1}^N \sum_{l=1-n}^{N-n} \{\langle\langle (x_n - \bar{x}_N)(x_{n+l} - \bar{x}_N) \rangle\rangle \langle\langle w_n w_{n+l} \rangle\rangle\}}{\langle\langle \sum_{n=1}^N w_n \rangle\rangle^2}, \tag{C7}$$

where in the last line we have used our assumption of the lack of correlation between the x_n and w_n to write the average of their product as the product of their separate averages. We have also assumed that our sample size N is sufficiently large that correlated fluctuations of the averages in the numerator and denominator will be sufficiently small that the average of the original ratios and products can be replaced by the corresponding ratios and products of the individual averages.

This result can be cast in a simple form if we define the three averages:

$$\delta x^2 = \langle\langle (x_n - \bar{x}_N)^2 \rangle\rangle, \tag{C8}$$

$$\bar{w} = \langle\langle w_n \rangle\rangle, \tag{C9}$$

$$\overline{w^2} = \langle\langle w_n^2 \rangle\rangle \tag{C10}$$

(where δx^2 is the usual width of the distribution of the measured quantity x_n) and the two autocorrelation functions:

$$C(l) = \frac{\langle\langle (x_n - \bar{x}_N)(x_{n+l} - \bar{x}_N) \rangle\rangle}{\delta x^2}, \tag{C11}$$

$$W(l) = \frac{\langle\langle w_n w_{n+l} \rangle\rangle}{\overline{w^2}}, \tag{C12}$$

defined so that $C(0) = W(0) = 1$. Making the conventional assumption that the range of l over which the correlation function $C(l)$ is nonzero is small compared to the sample size N and using the quantities defined above, we can rewrite Eq. (C7) as

$$\langle\langle (\langle x \rangle_N - \bar{x}_N)^2 \rangle\rangle = \frac{\delta x^2 \sum_{l=-L_{\max}}^{L_{\max}} C(l) W(l) \overline{w^2}}{N(\bar{w})^2} \tag{C13}$$

$$= \delta x^2 \frac{\tau_{\text{corr}}}{N} \frac{\overline{w^2}}{(\bar{w})^2}, \tag{C14}$$

where the autocorrelation time τ_{corr} is defined as

$$\tau_{\text{corr}} = \sum_{l=-L_{\max}}^{L_{\max}} C(l) W(l). \tag{C15}$$

The limit $L_{\max}$ is chosen to be larger than the region within which $C(l)$ is nonzero and has been introduced as a reminder that when working with a single finite sample, one must take care to evaluate the limit of large N before the limit of large $L_{\max}$. Finally, Eq. (C14) can be written in the conventional form

$$\text{Error}\,(x) = \sqrt{\frac{\delta x^2}{N_{\text{eff}}}}, \tag{C16}$$

where the effective number of configurations N_{eff} is given by

$$N_{\text{eff}} = \frac{N}{\tau_{\text{corr}}} \frac{\bar{w}^2}{\overline{w^2}}. \tag{C17}$$

This result makes precise a number of aspects of reweighting that may be useful to understand. In the case that there are no autocorrelations so $\tau_{\text{corr}} = 1$, the ratio $\bar{w}^2/\overline{w^2}$ expresses the degree to which the reweighting process selectively samples the original data and degrades the initial statistics. The general inequality $\bar{w}^2/\overline{w^2} \leq 1$ (a consequence of the Schwartz inequality) is saturated only in the case that the reweighting factors w_n do not vary with n. In the extreme case that a single sample w_n dominates the averages then $\bar{w}^2/\overline{w^2} = 1/N$ and $N_{\text{eff}} = 1$. Thus, in the case of uncorrelated data (which is the case for most of the results presented here) we should expect the statistical fluctuations to grow as the degree of reweighting increases by the factor $\overline{w^2}/\bar{w}^2$.

Including autocorrelations makes the effects of reweighting on the size of the statistical fluctuations less certain because the behavior of the factors $1/\tau_{\text{corr}}$ and $\bar{w}^2/\overline{w^2}$ in Eq. (C17) become entangled. In the limit in which the autocorrelation time associated with the measured quantity x_n alone,

$$\tau_x = \sum_{l=-L_{\max}}^{L_{\max}} C(l), \tag{C18}$$

becomes much larger than that of the reweighting factor w_n, then the majority of the sum in Eq. (C15) contributing to τ_{corr} will come from values of l where $\langle\langle w_n w_{n+l} \rangle\rangle \approx \langle\langle w \rangle\rangle^2$ so that

$$\tau_{\text{corr}} \approx \tau_x \frac{\bar{w}^2}{\overline{w^2}}. \tag{C19}$$

In this case the error given by Eq. (C16) reduces to the standard expression $\sqrt{\delta x^2 \tau_x / N}$ that holds if no reweighting is performed. Of course, this is easy to understand. When such long autocorrelation times are involved, the average over the autocorrelation time is providing an average over the reweighting factors w_n which is sufficiently precise that the error-enhancing fluctuations in the reweighting factors are averaged away. Given the large size of the fluctuations between the reweighting factors and the relatively short autocorrelation times seen in our data, it is unlikely that this averaging would be seen in the results presented here.

A second type of behavior for τ_{corr} occurs if the w_n are relatively uncorrelated and $\overline{w^2} \gg \bar{w}^2$ so that only the $l = 0$ term contributes to the sum in Eq. (C15) giving $\tau_{\text{corr}} = 1$. In this case reweighting has removed the effects of autocorrelation but increased the statistical fluctuations by the factor $\overline{w^2}/\bar{w}^2$ which was assumed to be large. Here the fluctuation-enhancing effects of autocorrelations and reweighting are not compounded.

[1] C. Allton *et al.* (RBC-UKQCD Collaboration), Phys. Rev. D **78**, 114509 (2008).
[2] D. J. Antonio *et al.* (RBC and UKQCD Collaborations), Phys. Rev. D **75**, 114501 (2007).
[3] C. Allton *et al.* (RBC and UKQCD Collaborations), Phys. Rev. D **76**, 014504 (2007).
[4] D. J. Antonio *et al.* (RBC Collaboration), Phys. Rev. Lett. **100**, 032001 (2008).
[5] P. A. Boyle *et al.*, Phys. Rev. Lett. **100**, 141601 (2008).
[6] P. Boyle, J. Flynn, A. Juttner, C. Kelly, C. Maynard *et al.*, Eur. Phys. J. C **69**, 159 (2010).
[7] T. Yamazaki *et al.* (RBC + UKQCD), Phys. Rev. Lett. **100**, 171602 (2008).
[8] T. Yamazaki *et al.*, Phys. Rev. D **79**, 114505 (2009).
[9] Y. Aoki *et al.*, Phys. Rev. D **82**, 014501 (2010).
[10] Y. Aoki *et al.* (RBC-UKQCD Collaboration), Phys. Rev. D **78**, 054505 (2008).
[11] N. Christ, C. Dawson, T. Izubuchi, C. Jung, Q. Liu *et al.*, Phys. Rev. Lett. **105**, 241601 (2010).
[12] C. Albertus *et al.*, Phys. Rev. D **82**, 014505 (2010).
[13] In this Introduction we combine the statistical and systematic errors in the results. The separate errors are presented in the following sections.
[14] Y. Aoki *et al.*, Phys. Rev. D **78**, 054510 (2008).
[15] C. Sturm *et al.*, Phys. Rev. D **80**, 014501 (2009).
[16] M. Gorbahn and S. Jager, Phys. Rev. D **82**, 114001 (2010).
[17] L. G. Almeida and C. Sturm, Phys. Rev. D **82**, 054017 (2010).
[18] S. R. Sharpe, arXiv:0706.0218.
[19] D. J. Antonio *et al.* (RBC and UKQCD Collaborations), Phys. Rev. D **77**, 014509 (2008).
[20] Y. Shamir, Nucl. Phys. **B406**, 90 (1993).
[21] Y. Iwasaki, Report No. UTHEP-118.
[22] M. Hasenbusch and K. Jansen, Nucl. Phys. **B659**, 299 (2003).
[23] T. Takaishi and P. de Forcrand, Phys. Rev. E **73**, 036706 (2006).
[24] C. Urbach, K. Jansen, A. Shindler, and U. Wenger, Comput. Phys. Commun. **174**, 87 (2006).
[25] P. A. Boyle, Comput. Phys. Commun. **180**, 2739 (2009).
[26] Y. Aoki *et al.*, Phys. Rev. D **72**, 114505 (2005).
[27] M. Luscher and F. Palombi, Proc. Sci., LATTICE2008 (2008) 049 [arXiv:0810.0946].
[28] A. Hasenfratz, R. Hoffmann, and S. Schaefer, Phys. Rev. D **78**, 014515 (2008).
[29] C. Jung, Proc. Sci., LAT2009 (2009) 002 [arXiv:1001.0941].
[30] H. Ohki *et al.*, Proc. Sci. LAT2009 (2009) 124 [arXiv:0910.3271].
[31] S. Aoki *et al.* (PACS-CS Collaboration), Phys. Rev. D **81**, 074503 (2010).
[32] R. Baron *et al.* (ETM Collaboration), Proc. Sci., LATTICE2008 (2008) 094 [arXiv:0810.3807].
[33] T. Ishikawa, Y. Aoki, and T. Izubuchi, Proc. Sci., LAT2009 (2009) 035 [arXiv:1003.2182].
[34] K. Ogawa and S. Hashimoto, Prog. Theor. Phys. **114**, 609 (2005).
[35] Y, Aoki *et al.* (RBC-UKQCD Collaboration), arXiv:1012.4178.
[36] We use the convention that the prime $\prime$ in $m'_{\rm res}(m_f)$ implies that the corresponding residual mass has been determined at a particular value of the light quark mass. $m_{\rm res}$ (without the $\prime$) is defined by $m_{\rm res} \equiv m'_{\rm res}(0)$.
[37] T. Blum *et al.* (RBC Collaboration), Phys. Rev. D **68**, 114506 (2003).
[38] E. Eichten, K. Gottfried, T. Kinoshita, K. D. Lane, and T.-M. Yan, Phys. Rev. D **17**, 3090 (1978).
[39] C. Alexandrou *et al.*, Nucl. Phys. **B414**, 815 (1994).
[40] F. Berruto, T. Blum, K. Orginos, and A. Soni, Phys. Rev. D **73**, 054509 (2006).
[41] T. Blum (RBC and UKQCD Collaborations), Proc. Sci., LATTICE2008 (2008) 096.
[42] C. M. Maynard (RBC and UKQCD Collaborations), Proc. Sci., LAT2009 (2009) 091 [arXiv:1001.5203].
[43] S. N. Syritsyn *et al.*, Phys. Rev. D **81**, 034507 (2010).
[44] Of course the varying quark masses $m_{ud}(\beta)$ and $m_s(\beta)$ will also appear in the coefficients of these $O(a^2)$ terms but when expressed in physical units such mass dependence will be of order a^4.
[45] G. Martinelli, C. Pittori, C. T. Sachrajda, M. Testa, and A. Vladikas, Nucl. Phys. **B445**, 81 (1995).
[46] Since N, the number of different β's for which we currently have results, is 2, there is only a single set of ratios R_a^2, Z_l^2, and Z_h^2. When specifically discussing our data, we therefore drop the superfix **2** and simply write R_a, Z_l and Z_h.
[47] L. Lellouch, Proc. Sci., LATTICE2008 (2009) 015 [arXiv:0902.4545].
[48] S. Durr *et al.*, Science **322**, 1224 (2008).
[49] S. R. Sharpe, Phys. Rev. D **46**, 3146 (1992).
[50] R. Mawhinney (RBC Collaboration), Proc. Sci., LAT2009 (2009) 081 [aXiv:0910.3194].
[51] E. E. Scholz, Proc. Sci. LAT2009 (2009) 005. [arXiv:0911.2191.]
[52] R. Mawhinney (RBC-UKQCD Collaboration), Proceedings of the XXVIII International Symposium on Lattice Field Theory (to be published).
[53] A. Bazavov *et al.* (MILC), Proc. Sci., LAT2009 (2009) 079 [arXiv:0910.3618].
[54] C. Aubin *et al.*, Phys. Rev. D **70**, 094505 (2004).
[55] Y. Aoki (RBC-UKQCD Collaboration), Proc. Sci., LATTICE2008 (2008) 222 [arXiv:0901.2595].
[56] Y. Aoki, Proc. Sci., LAT2009 (2009) 012 [arXiv:1005.2339].
[57] J.-R. Cudell, A. Le Yaouanc, and C. Pittori, Phys. Lett. B **454**, 105 (1999).
[58] L. Giusti and A. Vladikas, Phys. Lett. B **488**, 303 (2000).
[59] K. G. Chetyrkin and A. Retey, Nucl. Phys. **B583**, 3 (2000).
[60] J. A. Gracey, Nucl. Phys. **B662**, 247 (2003).
[61] T. van Ritbergen, J. A. M. Vermaseren, and S. A. Larin, Phys. Lett. B **400**, 379 (1997).
[62] C. Amsler *et al.* (Particle Data Group), Phys. Lett. B **667**, 1 (2008).
[63] M. Constantinou, V. Lubicz, H. Panagopoulos, and F. Stylianou, J. High Energy Phys. 10 (2009) 064.
[64] P. Di Vecchia and G. Veneziano, Nucl. Phys. **B171**, 253 (1980).

[65] H. Leutwyler and A. V. Smilga, Phys. Rev. D **46**, 5607 (1992).
[66] M. F. Atiyah and I. M. Singer, Bull. Am. Math. Soc. **69**, 422 (1963).
[67] M. Luscher, Commun. Math. Phys. **85**, 39 (1982).
[68] P. de Forcrand, M. Garcia Perez, and I.-O. Stamatescu, Nucl. Phys. **B499**, 409 (1997).
[69] M. Falcioni, M. L. Paciello, G. Parisi, and B. Taglienti, Nucl. Phys. **B251**, 624 (1985).
[70] M. Albanese *et al.* (APE Collaboration), Phys. Lett. B **192**, 163 (1987).
[71] Y. Aoki *et al.*, Phys. Rev. D **73**, 094507 (2006).
[72] Y.-Y. Mao and T.-W. Chiu (TWQCD Collaboration), Phys. Rev. D **80**, 034502 (2009).
[73] M. Lightman and E. Goode (RBC-UKQCD Collaboration), Proc. Sci. LATTICE2010 (2010) 313 [arXiv:1101.2473].
[74] For completeness, since those have not been included in Appendix C of [1], the finite-volume corrections for the kaon decay constant in SU(2)-ChPT read

$$\Delta_{xy}^{Lf_K} = -\frac{1}{4\pi f^2}\left[\frac{\chi_x+\chi_l}{2}\delta_1\left(\sqrt{\frac{\chi_x+\chi_l}{2}}L\right) + \frac{\chi_l-2\chi_x}{4}\delta_1(\sqrt{\chi_x}L)\right].$$

See Appendix C of [1] for an explanation of the notation.
[75] L. Del Debbio, L. Giusti, M. Luscher, R. Petronzio, and N. Tantalo, J. High Energy Phys. 02 (2007) 082.
[76] J. D. Bratt *et al.* (LHPC Collaboration), Phys. Rev. D **82**, 094502 (2010).
[77] V. Furman and Y. Shamir, Nucl. Phys. **B439**, 54 (1995).
[78] N. Christ (RBC and UKQCD Collaborations), Proc. Sci., LAT2005 (2006) 345.
[79] T. Blum *et al.*, Phys. Rev. D **69**, 074502 (2004).
[80] P. Boyle *et al.*, IBM J. Res. Dev. **49**, 351 (2005).
[81] P. A. Boyle, C. Jung, and T. Wettig (QCDOC), in *Computing in High Energy and Nuclear Physics 2003 Conference Proceedings*, econf C0303241, THIT003 (2003).
[82] P. A. Boyle *et al.*, J. Phys. Conf. Ser. **16**, 129 (2005).